

Liquid Metal Printing with Scanning Probe Lithography for Printed Electronics

Zur Erlangung des akademischen Grades eines

DOKTORS DER INGENIEURWISSENSCHAFTEN

(Dr.-Ing.)

von der KIT-Fakultät für Elektrotechnik und Informationstechnik des

Karlsruher Instituts für Technologie (KIT)

angenommene

DISSERTATION

von

M.Tech. Navid Hussain

aus Jhunjhunu, Indien

| | |
|-----------------------------|---|
| Tag der mündlichen Prüfung: | 05.12.2022 |
| Erstgutachterin: | Prof. Dr. Jasmin Aghassi-Hagmann, KIT |
| Zweitgutachter: | apl. Prof. Dr.-Ing. Alexander Colsmann, KIT |
| Drittgutachter | PD Dr. Dr. Michael Hirtz, KIT |



This document is licensed under a Creative Commons Attribution 4.0 International License (CC BY 4.0): <https://creativecommons.org/licenses/by/4.0/deed.en>

To my father late Dr. Mohd. Halim Khan

Navid Hussain
Hermann-von-Helmholtz-Platz 1
76344 Eggenstein-Leopoldshafen

I hereby declare that the enclosed thesis titled " Liquid Metal Printing with Scanning Probe Lithography for Printed Electronics" is a product of my own work and writing. This work was completed independently and without any unauthorized assistance. The sources used, passages taken literally or in terms of content, are identified as such and have been cited properly.

Date: 17 October,2022

Place: Eggenstein-Leopoldshafen

Navid Hussain

Acknowledgments

Most importantly, I would like to thank my supervisor PD Michael Hirtz for the support and encouragement he offered during my doctoral studies journey. The powerful discussions, valuable feedback, friendly counsel, and precious suggestions have helped me become a far more refined researcher and better person than the time I started this journey. I would also like to thank Prof. Jasmin Aghassi-Hagmann for acting as my first supervisor and for her continued kind support in the form of new project discussions and help with establishing new collaborations to use research facilities outside of KIT.

I would like to especially thank all my collaborators, Prof. Rasmus R Schröder (Heidelberg University), Prof. Peter Gumbsch (Fraunhofer IWM, Freiburg), and Chunyan Ma (Taiyuan University) for their wonderful teamwork and for letting me benefit from their facilities.

I am very thankful to my colleagues and co-workers, Dr. Gabriel Marques, Dr. Alexander Scholz, Dr. Chittaranjan Das, Dr. Torsten Scherer, Dr. Uwe Bog, Dr. Rafaela Debastiani, Tobias Spratte, Surya Abhishek Singaraju and Janis Heuer, who helped me to pursue pure refined knowledge with fruitful discussions. And also special thanks to Lukas Berner and Irene Wacker for their work at Heidelberg university. I really appreciate the help from students Mohammad Jan Nazami and Tongtong Fu for their helpful work during their internships.

Furthermore, I would also like to thank my other colleagues Sylwia Sekula-Neuner, Ravi Kumar, Hui-Yu Liu, Mahdi Dadfar, Eider Berganza Eguiarte, Chunting Zhong, Bingquan Yang, Wenwu Yang, George Mathew, Mahsa K. Saghafi, Raju and Pooja Arya for their support.

I really appreciate Sandeep, Devang, Vibhuti, Neha, Srivatsan, Abhinav, Prantik, Anirudh, Ravi Yadav, Tarachand, Neeraj, Jai Prakash, Aryan, Vinod, Praveen, and Krishan for their expert help about things in Germany, emotional support and making my stay in Karlsruhe full of fun and happiness.

I am very grateful to my family for their belief in my dreams and their constant support throughout this journey.

I feel enormously fortunate to have the chance to work at the Karlsruhe Institute of Technology, specifically at the Institute of Nanotechnology (INT) and Karlsruhe Nano Micro Facility (KNMFi). I want to thank Prof. Harald Fuchs, Prof. Horst Hahn, the whole lovely and friendly INT staff, and each and every individual who helped me in any possible way during my Ph.D. work and my stay at INT.

Abstract

In recent years, with the emergence of Industry 4.0, the Internet of Things (IoT), also referred to as the Internet of Everything, is bringing a stream of innovative and intelligent next-generation sensors-based electronics into everyday life. This also demands the fabrication of a massive number of electronic parts, including sensors, actuators, and other components. The available conventional electronics (also referred to as CE) manufacturing has become a highly complicated process requiring intensive investments. As the number of electronics and the demand for new, more advanced electronics increases, there is a greater need to find more efficient ways to produce these electronics. The printed electronics industry is a growing market that could meet this demand, reshaping the future of electronic device fabrication. It allows easy and cost-effective production and enables devices to be fabricated on paper or plastic substrates. On the fabrication side, there are a lot of methods available, and scanning probe lithography-based techniques have always been part of printed electronics and have led to innovations in the field. Although the technology is still young, and the current state of printed electronics at an industrial scale, such as complete integrated circuit fabrication, is limited, the potential applications are still vast.

A key component of the development of printed electronic circuits is the printing of conductive parts and functional materials. Most of the currently available works for conductors have focused on the use of nanoparticle-based inks. The fabrication steps based on these inks are complicated processes as they include annealing and other post-processing steps to make the printed patterns conductive. The use of gallium-based at/near room-temperature liquid metals and their direct writing for fully printed electronics is still uncommon, as the combination of the presence of an oxide layer, high surface tensions, and viscosity makes these materials difficult to handle.

To this end, this thesis aims to develop methods for printing materials, including liquid metals that are very hard to be printed with available printing methods, and use those methods to fabricate fully printed electronic devices. It also investigates solutions for the challenges during the printing process, such as the adhesion of ink to the substrate and other deposition-related issues. It also address scientific questions regarding the device stabilities of liquid metal-based printed electronic devices.

Within the presented thesis, a glass capillary-based direct-write method for printing the liquid metal Galinstan was developed. The method was implemented in two ways, first, a high-performance version based on a customized nanolithography setup, but also a high-accessibility micromanipulator-based version allowing "on-the-fly" capillary printing on a wide range of geometries, as exemplified by the example of vertical, recessed surfaces as well as stacked 3D scaffolds as hard-to-access surfaces. The thesis explores the potential use of these methods for the fabrication of fully

printed liquid metal-enabled devices, including resistors, microheaters, p–n diodes, and field effect transistors. All of these electronic devices are extensively characterized. The fabricated microheater structures are utilized for a heat-triggered microvalve to control the liquid flow in a microchannel. This demonstration and the ease of fabrication show that the concept can also be extended to other applications, e.g., on-demand microheater fabrication for in-situ scanning electron microscopy experiments.

Additionally, this work shows how PMMA encapsulation can act as an effective barrier against oxygen and moisture and is feasible mechanical protection of these liquid metal-based printed electronic devices. Overall, the single integrated fabrication flow and device functionality demonstrate that the potential of liquid metal printing in printed electronics is much greater than just the use as a connector between conventional electronic devices.

Aside from the development of printing methods and fabrication of electronic devices, the thesis also discusses corrosion and additional alloying of conventional metal electrodes in contact with liquid metal that could compromise device stability. For this, a correlated material interaction study of printed Galinstan and gold electrodes was implemented. In-depth characterization of the spreading process of liquid metal lines on gold films has been achieved through the combined application of optical microscopy, vertical scanning interferometry, scanning electron microscopy, x-ray photon spectroscopy, and atomic force microscopy. This study reveals a differential spread of the different components of the liquid metal and the formation of intermetallic nanostructures on the surrounding gold film surface. Based on the obtained time-dependent correlated characterization results, a model for the spread process based on liquid metal penetration is proposed. In addition, to provide a complementary perspective on the internal nanostructure, X-ray nanotomography is employed to examine the distribution of gold, Galinstan, and intermetallic phases in a gold wire dipped into the liquid metal. Finally, measurements of resistance on liquid metal lines connecting gold electrodes over time are conducted, which help assess the impact of material interactions on electronic applications.

Zusammenfassung der Arbeit

In den letzten Jahren hat das „Internet der Dinge“ (Englisch *Internet of Things*, abgekürzt IoT), das auch als *Internet of Everything* (Deutsch frei „Internet von Allem“) bezeichnet wird, mit dem Aufkommen der „Industrie 4.0“ einen Strom innovativer und intelligenter sensorgestützter Elektronik der neuen Generation in den Alltag gebracht. Dies erfordert auch die Herstellung einer riesigen Anzahl von elektronischen Bauteilen, einschließlich Sensoren, Aktoren und anderen Komponenten. Gleichzeitig ist die herkömmliche Elektronikfertigung zu einem hochkomplexen und investitionsintensiven Prozess geworden. In dem Maße, wie die Zahl der elektronischen Bauteile und die Nachfrage nach neuen, fortschrittlicheren elektronischen Bauteilen zunimmt, steigt auch die Notwendigkeit, effizientere und nachhaltigere Wege zur Herstellung dieser Bauteile zu finden. Die gedruckte Elektronik ist ein wachsender Markt, der diese Nachfrage befriedigen und die Zukunft der Herstellung von elektronischen Geräten neu gestalten könnte. Sie erlaubt eine einfache und kostengünstige Produktion und ermöglicht die Herstellung von Geräten auf Papier- oder Kunststoffsubstraten. Für die Herstellung gibt es dabei eine Vielzahl von Methoden. Techniken auf der Grundlage der Rastersondenlithografie waren dabei schon immer Teil der gedruckten Elektronik und haben zu Innovationen in diesem Bereich geführt. Obwohl die Technologie noch jung ist und der derzeitige Stand der gedruckten Elektronik im industriellen Maßstab, wie z. B. die Herstellung kompletter integrierter Schaltkreise, stark limitiert ist, sind die potenziellen Anwendungen enorm.

Im Mittelpunkt der Entwicklung gedruckter elektronischer Schaltungen steht der Druck leitfähiger und anderer funktionaler Materialien. Die meisten der derzeit verfügbaren Arbeiten haben sich dabei auf die Verwendung von Tinten auf Nanopartikelbasis konzentriert. Die Herstellungsschritte auf der Grundlage von Tinten auf Nanopartikelbasis sind komplizierte Prozesse, da sie das Ausglühen (Englisch *Annealing*) und weitere Nachbearbeitungsschritte umfassen, um die gedruckten Muster leitfähig zu machen. Die Verwendung von Gallium-basierten, bei/nahe Raumtemperatur flüssigen Metallen und deren direktes Schreiben für vollständig gedruckte Elektronik ist immer noch ungewöhnlich, da die Kombination aus dem Vorhandensein einer Oxidschicht, hohen Oberflächenspannungen und Viskosität ihre Handhabung erschwert.

Zu diesem Zweck zielt diese Arbeit darauf ab, Methoden zum Drucken von Materialien, einschließlich Flüssigmetallen, zu entwickeln, die mit den verfügbaren Druckmethoden nicht oder nur schwer gedruckt werden können und diese Methoden zur Herstellung vollständig gedruckter elektronischer Bauteile zu verwenden. Weiter werden Lösungen für Probleme während des Druckprozesses untersucht, wie z. B. die Haftung der Tinte auf dem Substrat und andere abscheidungsrelevante Aspekte. Es wird auch versucht, wissenschaftliche Fragen zur Stabilität von gedruckten elektronischen Bauelementen auf Flüssigmetallbasis zu beantworten.

Im Rahmen der vorliegenden Arbeit wurde eine auf Glaskapillaren basierenden Direktschreibmethode für das Drucken von Flüssigmetallen, hier Galinstan, entwickelt. Die Methode wurde auf zwei unterschiedlichen Wegen implementiert: Einmal in einer „Hochleistungsversion“, basierend auf einem angepassten Nanolithographiegerät, aber ebenfalls in einer hochflexiblen, auf Mikromanipulatoren basierenden Version. Dieser Aufbau erlaubt einen *on-the-fly* („im Fluge“) kapillarbasierten Druck auf einer breiten Palette von Geometrien, wie am Beispiel von vertikalen, vertieften Oberflächen sowie gestapelten 3D-Gerüsten als schwer zugängliche Oberflächen gezeigt wird. Die Arbeit erkundet den potenziellen Einsatz dieser Methode für die Herstellung von vollständig gedruckten durch Flüssigmetall ermöglichten Bauteilen, einschließlich Widerständen, Mikroheizer, p-n-Dioden und Feldeffekttransistoren. Alle diese elektronischen Bauelemente werden ausführlich charakterisiert. Die hergestellten Mikroheizerstrukturen werden für temperatur-geschaltete Mikroventile eingesetzt, um den Flüssigkeitsstrom in einem Mikrokanal zu kontrollieren. Diese Demonstration und die einfache Herstellung zeigt, dass das Konzept auch auf andere Anwendungen, wie z.B. die bedarfsgerechte Herstellung von Mikroheizern für in-situ Rasterelektronenmikroskop-Experimente, ausgeweitet werden kann.

Darüber hinaus zeigt diese Arbeit, wie PMMA-Verkapselung als effektive Barriere gegen Sauerstoff und Feuchtigkeit fungiert und zusätzlich als brauchbarer mechanischer Schutz der auf Flüssigmetall basierenden gedruckten elektronischen Bauteile wirken kann. Insgesamt zeigen der alleinstehende, integrierte Herstellungsablauf und die Funktionalität der Geräte, dass das Potenzial des Flüssigmetall-Drucks in der gedruckten Elektronik viel größer ist als einzig die Verwendung zur Verbindung konventioneller elektronischer Bauteile.

Neben der Entwicklung von Druckverfahren und der Herstellung elektronischer Bauteile befasst sich die Arbeit auch mit der Korrosion und der zusätzlichen Legierung von konventionellen Metallelektroden in Kontakt mit Flüssigmetallen, welche die Stabilität der Bauteile beeinträchtigen könnten. Zu diesem Zweck wurde eine korrelierte Materialinteraktionsstudie von gedruckten Galinstan- und Goldelektroden durchgeführt. Durch die kombinierte Anwendung von optischer Mikroskopie, vertikaler Rasterinterferometrie, Rasterelektronenmikroskopie, Röntgenphotonenspektroskopie und Rasterkraftmikroskopie konnte der Ausbreitungsprozess von Flüssigmetalllinien auf Goldfilmen eingehend charakterisiert werden. Diese Studie zeigt eine unterschiedliche Ausbreitung der verschiedenen Komponenten des Flüssigmetalls sowie die Bildung von intermetallischen Nanostrukturen auf der umgebenden Goldfilmoberfläche. Auf der Grundlage der erhaltenen zeitabhängigen, korrelierten Charakterisierungsergebnisse wird ein Modell für den Ausbreitungsprozess vorgeschlagen, das auf dem Eindringen des Flüssigmetalls in den Goldfilm basiert. Um eine ergänzende Perspektive auf die interne Nanostruktur zu erhalten, wurde die Röntgen-Nanotomographie eingesetzt, um die Verteilung von Gold, Galinstan und intermetallischen Phasen in einem in das Flüssigmetall getauchten Golddraht zu untersuchen. Schlussendlich werden

Langzeitmessungen des Widerstands an Flüssigmetalleitungen, die Goldelektroden verbinden, durchgeführt, was dazu beiträgt, die Auswirkungen von Materialwechselwirkungen auf elektronische Anwendungen zu bewerten.

List of publications

Peer-reviewed journal publications

During PhD phase

- **N. Hussain**, T. Scherer, C. Das, J. Heuer, R. Debastiani, P. Gumbsch, J. Aghassi-Hagmann and M. Hirtz, "Correlated Study of Material Interaction Between Capillary Printed Eutectic Gallium Alloys and Gold Electrodes," *Small*, page 2202987 (2022).
- S. Das, R. Kumar, B. Yang, S. Bag, E. Sauter, **N. Hussain**, M. Hirtz, and U. Manna, "Multiplexed Covalent Patterns on Double-Reactive Porous Coating," *Chemistry – An Asian Journal*, vol. 17, page e202200157 (2022).
- R. Jemai, M. A. Djebbi, **N. Hussain**, B. Yang, M. Hirtz, V. Trouillet, H. Ben Rhaïem, and A. Ben Haj Amara, "Activated Porous Carbon Supported Pd and ZnO Nanocatalysts for Trace Sensing of Carbaryl Pesticide in Water and Food Products," *New Journal Chemistry*, vol 46, page 13880 (2022).
- **N. Hussain**, M. Jan Nazami, C. Ma, and M. Hirtz, "High-Precision Tabletop Microplotter for Flexible on-Demand Material Deposition in Printed Electronics and Device Functionalization," *Review of Scientific Instruments*, vol. 92, page 125104 (2021).
- **N. Hussain**, T. Fu, G. Marques, C. Das, T. Scherer, U. Bog, L. Berner, I. Wacker, R. R. Schröder, J. Aghassi-Hagmann, and M. Hirtz, "High-Resolution Capillary Printing of Eutectic Gallium Alloys for Printed Electronics," *Advanced Materials Technologies*, vol. 6, no. 11, page 2100650-1-11 (2021).
- C. Das, W. Zia, C. Mortan, **N. Hussain**, M. Saliba, J. Ingo Flege, and M. Kot, "Top-Down Approach to Study Chemical and Electronic Properties of Perovskite Solar Cells: Sputtered Depth Profiling Versus Tapered Cross-Sectional Photoelectron Spectroscopies," *Solar RRL*, vol. 5, page 2100298 (2021).

During Master/Bachelor

- P. Joshi, **N. Hussain**, S. R. Ali, Rishu, and V. K. Bhardwaj, "Enhanced Activity of Trinuclear Zn (II) Complexes towards Phosphate Ester Bond Cleavage by Introducing Three-Metal Cooperativity," *New Journal Chemistry*, 42, (2018).
- **N. Hussain**, P. Joshi, S. R. Ali, and V. K. Bhardwaj, "Comparative Structure Activity Relationship for Heterogeneous Phosphatase-like Catalytic Activities of One-Dimensional Cu (II) Coordination Polymers," *RSC Advances*, vol. 6 (66), page 61528 (2016).

- **N. Hussain** and V. K. Bhardwaj, "The Influence of Different Coordination Environments on One-Dimensional Cu (II) Coordination Polymers for the Photo-Degradation of Organic Dyes," Dalton Transactions, vol. 45 (18), page 7697 (2016).

Prospective publication

- **N. Hussain**, A. Scholz, T. Spratte, C. Selhuber-Unkel, M. Hirtz and J. Aghassi-Hagmann, "Direct writing of liquid metal microheaters for microvalve applications," 2022.

Conference oral presentations

- **N. Hussain**, ..., M. Hirtz and J. Aghassi-Hagmann, "High-Resolution Capillary Printing of Eutectic Gallium Alloys for Printed Electronics," The 65th International Conference on Electron, Ion, and Photon Beam Technology and Nanofabrication *EIPBN-2022*, New Orleans, USA. (Presented online)
- **N. Hussain**, ..., M. Hirtz and J. Aghassi-Hagmann "High-Resolution Capillary Printing of Eutectic Gallium Alloys for Printed Electronics," *MNE-2022*, Leuven, Belgium.

Posters

- **N. Hussain**, U. Bog, H Fuchs, and M. Hirtz, "Liquid Metal based printed electronics by scanning probe lithography," in 50th IFF Spring School on Scattering 2019, in Jülich, Germany.

Contents

| | |
|---|------|
| Acknowledgments | iii |
| Abstract | v |
| Zusammenfassung der Arbeit | vii |
| List of publications | xi |
| Contents | xiii |
| Part I. Introduction | 1 |
| 1. Introduction to printed electronics | 3 |
| 1.1 Overview and history of printed electronics | 3 |
| 1.2 Motivation and objectives of this thesis | 7 |
| 1.3 Thesis outline | 10 |
| Part II. Theory and background | 13 |
| 2. Printable materials and printing techniques | 15 |
| 2.1 Printable materials | 15 |
| 2.2 Pre-printing processes..... | 30 |
| 2.3 Post-printing processes | 31 |
| 2.4 3D printing of conductors | 32 |
| 2.5 Liquid Metals (LMs)..... | 33 |
| 2.6 Challenges printing liquid metal | 35 |
| 2.7 Printing techniques..... | 37 |
| 3. Printed devices | 51 |
| 3.1 p-n diode | 51 |
| 3.2 Field-Effect Transistors..... | 58 |
| 3.3 Microheater | 71 |
| 3.4 Prior work/State of the art work on liquid metal printing and devices | 75 |
| Part III. Results | 79 |
| 4. Capillary printing of LM alloys | 81 |
| 4.1 LM printing setup | 81 |
| 4.2 Printing of LM structures | 85 |
| 4.3 Influence of writing parameters | 86 |
| 4.4 Characterization of LM structures | 87 |
| 4.5 Challenges during the writing..... | 90 |

| | |
|---|-----|
| 5. Tabletop microplotter for enhanced access to printing areas | 93 |
| 5.1 Printing setup | 93 |
| 5.2 Printing process | 96 |
| 5.3 Challenges during printing | 98 |
| 5.4 Enhanced access to printing areas | 99 |
| 5.5 Gold structures on glass and Kapton film | 100 |
| 5.6 Flexible on-demand interconnects for printed electronics | 103 |
| 5.7 Deposition of protein inks | 103 |
| 6. Fully printed electronic devices | 107 |
| 6.1 Fully printed LM interconnects and resistors | 107 |
| 6.2 Fully printed diode | 112 |
| 6.3 Fully printed transistor | 116 |
| 7. LM-based printed microheaters | 121 |
| 7.1 Fabrication of the microheater structures | 121 |
| 7.2 Microheater characterization | 122 |
| 7.3 Thermal parameter characterization | 127 |
| 7.4 Microvalve application | 131 |
| 8. Gallium alloys and gold interfaces | 135 |
| 8.1 Sample preparation | 135 |
| 8.2 Correlated characterization method | 136 |
| 8.3 Intermetallic nanostructures formation rate | 138 |
| 8.4 Characterization of intermetallic nanostructures | 140 |
| 8.5 Intermetallic nanostructures formation and growing mechanism | 151 |
| 8.6 Effect of temperature and humidity on intermetallic structure formation | 153 |
| 8.7 Effect of encapsulation on intermetallic structure formation | 155 |
| 8.8 Estimation of the oxide layer | 156 |
| 8.9 Electrical characterization of Galinstan-Gold contacts | 161 |
| Part IV. Summary, conclusions and outlook | 163 |
| 9. Summary | 165 |
| 10. Outlook | 169 |
| Part V. Appendix | 173 |
| A.1. Materials | 175 |
| A.2. Methods and techniques | 177 |
| Part VI. Index and references | 201 |

| | |
|---|-----|
| Glossary | 203 |
| List of Figures | 213 |
| List of Tables | 225 |
| Bibliography | 227 |
| Part VII. Personal details | 263 |

Part I. Introduction

1. Introduction to printed electronics

1.1 Overview and history of printed electronics

Four industrial revolutions have already taken place in the history of humanity [1], the first encouraging mechanization and the second founding mass production facilities. We are highly reliant on solid-state microelectronics as a result of the widespread digitalization by the third revolution. The fourth revolution (4IR or Industry 4.0) brings the internet of things (IoT), which involves various smart objects (sensors and actuators) communicating with one another and one machine to another machine without the intervention of humans. These intelligent systems can transfer data through wired or wireless communication networks. There is a growing popularity of the IoT worldwide, driving the fate of many businesses. A typical example is smart home electronic gadgetry that communicates and controls lighting and energy and also remotely accesses wearable health monitors and smartwatches. The internet, computers, and integrated circuits are the leading driving technologies. A fundamental component of microelectronic circuits is the field-effect transistor (FET), which forms the basis for integrated circuits. Miniaturization of transistor devices is also driving rapid growth in the semiconductor industry.

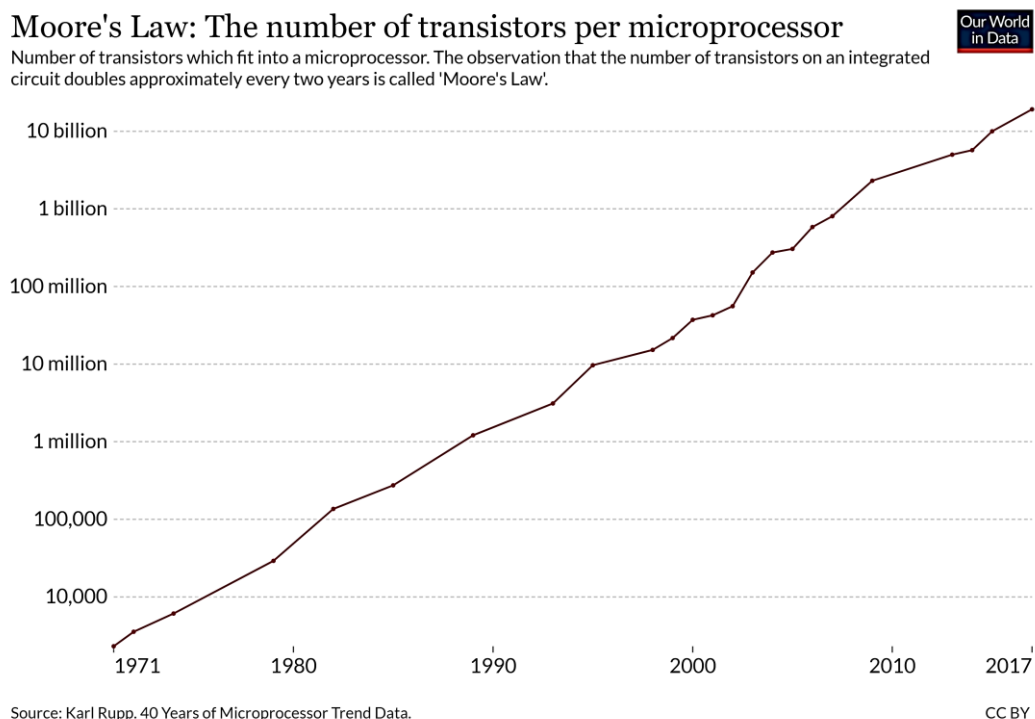


Figure 1. 1: A semi-log plot showing the evolution of transistor counts on integrated chips from 1971 to 2020 with respect to Moore's Law, which states the number of transistors on an IC chip doubles approximately every two years. Reproduced [2] under license CC-BY-4.0.

As early as 1965, Gordon E. Moore predicted that the number of components in an integrated circuit chip would double roughly every two years[3], [4]. As shown in Figure 1. 1, Transistor density continues to increase primarily due to a reduction in the feature size of transistors. The Intel 4004 was the world's first commercial microprocessor in 1971, containing 2300 transistors based on 10 μm technology[5], whereas, in 2022, Apple's ARM-based dual-die M1 Ultra system on a chip contains 114 billion transistors derived from TSMC's 5 nm FinFET N5 semiconductor manufacturing process[6]. Microelectronic devices are more energy efficient and perform better if the transistor size is reduced. It results in an increase in component density on a chip, as well as a reduction in power consumption. However, when the transistors undergo excessive scaling, their internal components begin to hinder other components' functions, leading to increased leakage currents and power consumption[7]. These miniaturizations and transformations of circuits to make intelligent systems also shorten their lifetime which in the end become significant contributors to massive e-waste produced worldwide [8], [9]. In addition to generating enormous e-waste, conventional microelectronics device manufacturing methods also suffer from industrial factors such as a reduction in material supply and rising prices. These available methods are also dependent on costly elaborative techniques that require clean rooms, which further increases the cost of the final product. In summary, these are not sustainable for fabrication in the future; therefore, new device architectures, materials, and fabrication methods must be updated for electronic device fabrication in order to satisfy the increasing demand.

Table 1.1: Difference between conventional fabrication in electronics and printed electronics.

| Factor | Conventional fabrication in electronics | Printed electronics |
|-------------------------|---|---|
| Process | Several complex subtractive steps are involved, including photolithography, etching, and cleaning | Very simple to use additive printing technology, such as direct writing of circuits |
| Substrate compatibility | Usually rigid | Rigid as well as flexible/plastic substrates are feasible |
| Throughput | Comparably low | High |
| Fabrication time | Slow as it includes mask designing or prototyping | Comparatively faster |

With Industry 4.0 (I4.0), the fourth industrial revolution transforms traditional manufacturing into intelligent manufacturing systems, thus demanding the ubiquitous use of electronic components [10]. As a result of smart manufacturing, printed electronics (PE) have emerged; as the name suggests, it uses a set of printing methods, such as additive printing technology, to create electrical devices on various substrates on demand and at low fabrication costs. It helps CE by simplifying the manufacturing process.

Table 1.1 shows the benefits of printed electronics over conventional fabrication in electronics. The main advantages of PE are low fabrication costs and less wastage of expensive metals, as functional materials are deposited using inexpensive additive process methods, also requiring fewer processing steps. Furthermore, Researchers and industry are always attracted to PE because of its more favourable properties, such as on-demand fabrication, which is complex with CE.

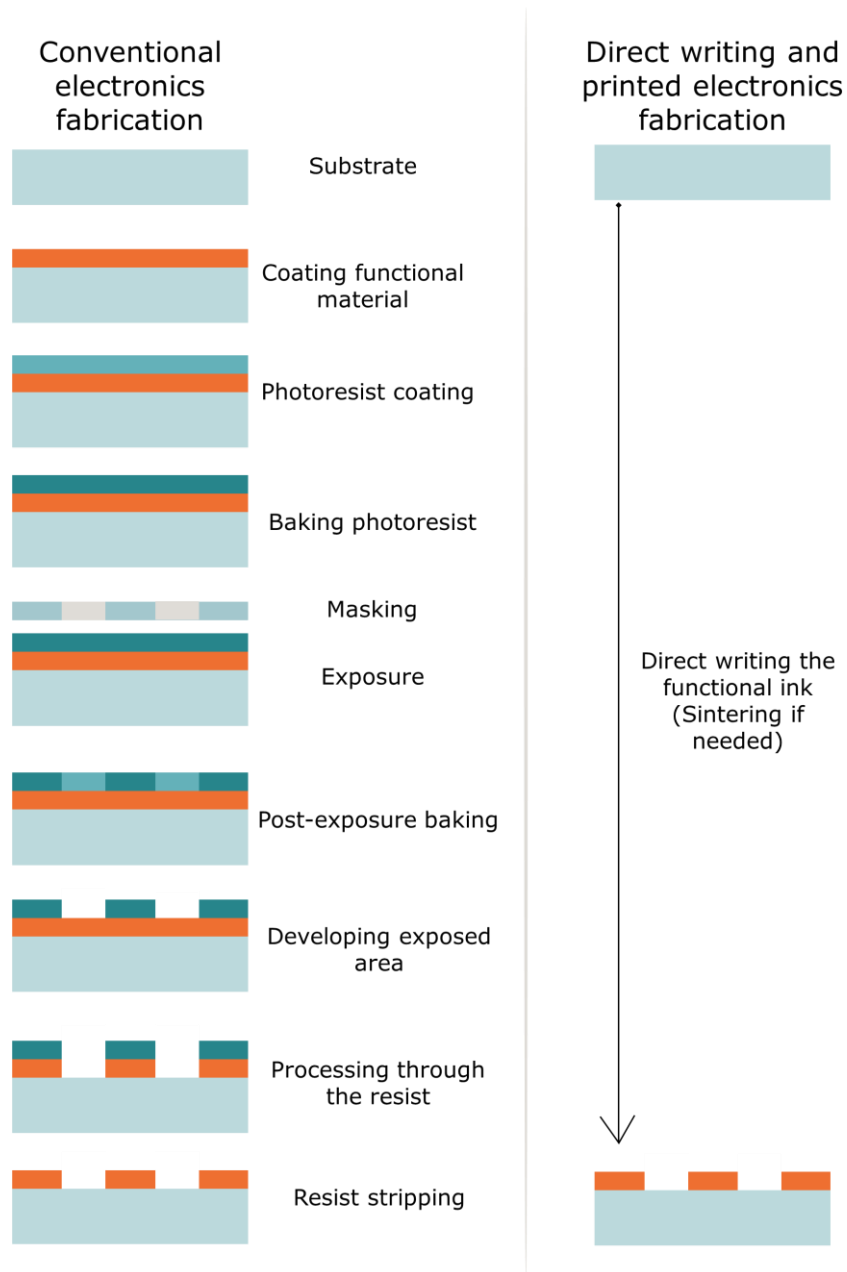


Figure 1. 2: Comparison of conventional electronic device manufacturing vs. printed electronics. Conventional electronics manufacturing involves a lot of complex steps, and it is based on subtractive methods; on the other hand, printed electronics is based on direct writing, thus can be (in comparison) simple and fast

The history of printing began with Johannes Gutenberg in the 1400s [11], who introduced the mechanical movable type printing press, the first printing revolution in Europe, and it was the origins of the printing process. A century ago, printing consisted primarily of text and graphics. Today, high-quality electronic devices are manufactured using printing technology. The history of printed electronics begins with organic electronics in 1977 when Alan Heeger, together with Alan G. MacDiarmid and Hideki Shirakawa (who were awarded the Nobel Prize in chemistry in 2000), discovered conductive polymers [12], then organic semiconductor materials were developed in 1983 [13], and organic field-effect transistors (OFETs) were first made in 1986 [14].

However, over the years, after the advances in PE with new materials and inorganic materials-based devices, especially semiconductors in transistors, it has been observed that organic materials suffer from low charge mobility, which is essential for a transistors' speed and driving ability [15]. Higher mobility offered by inorganic oxide semiconductors is preferred to increase the switching speed of FETs. Other than those, processing temperatures of functional inks are also an issue in PE. For conductors, the current significant challenges in directly writing metallic inks for PE can be summarized into three problems: electrical conductivity, processing temperatures, and cost of inks. The electrical conductivity of printed and annealed patterns using metal-based functional inks is typically around 10 times less than for the bulk form of the metal used in the respective ink [16]. In addition, metal-based inks require post-processing after printing through techniques such as drying and sintering to achieve electrical conductivity for the printed features. These post-processing steps are usually high-temperature steps and can limit the choice of substrates or other more sensitive components of a printed device. Furthermore, the NP metal inks often cost more than the same metal in bulk form, as it includes many complex steps and instrumental facilities to produce. This thesis address these issues in the upcoming chapters.

For printing microelectronic circuits, different printing technologies are available (discussed in detail in chapter 2), such as stencil lithography [17], [18], molding, embossing, screen printing, shadow mask printing [19]–[21], roll-to-roll printing, direct writing, or additive manufacturing, such as inkjet printing [18], [22]–[26], aerosol printing [27], laser printing (ablation, selective sintering, or reactive chemical processes) [28]–[30], electron beam and focused ion beam (FIB) based printing [31], microcontact printing and polymer pen lithography [32], [33], nano transfer printing, electrospray deposition [34], electrochemical printing [35], and scanning probe lithography techniques (with various different probe–surface interaction mechanisms such as mechanical, thermal, chemical, material transfer, oxidation, voltage and magnetic) [36]–[42].

PE is already being used for many different applications today such as RFID tag and antenna [43]–[50], temperature sensors [48], [51]–[54], humidity sensors [52], [54]–[57], strain sensors [54], [58]–[61], motion and tracking sensors [62]–[64],

pressure and capacitive sensors[27], [65]–[70], nanogenerator and energy harvesting [64], [65], [71], [72], solar cells [73]–[75], display [76], [77], electronic circuits and systems [78], transistors [79]–[81], shift registers [82], pulsed voltage multiplier [83], logic gates [84], flexible PMOS inverters and NOR gates [85], and amplifiers [86], [87]. On the bioelectronics side, PE is also an essential part of implantable, biodegradable, and flexible electronics-based applications [88]–[91]. IDTechEx, a market research firm reports that the market for printed, flexible, and organic electronics will grow to \$41.2 billion in 2020 and \$74 billion by 2030. [92].

1.2 Motivation and objectives of this thesis

1.2.1 Direct writing of liquid metals

As discussed in the previous section, the current metallic inks suffer from problems such as poor electrical conductivity, high processing temperatures, and high cost. As an alternative, low melting point metal alloys, also called liquid metals (further referred as LMs), have become a focus of attraction because they exhibit as high electrical and thermal conductivity as many conventional metals or alloys. Simultaneously LMs are ductile and fluid at or near room temperature (RT), rendering them processable by printing. Also, LMs do not require additional processing steps, such as chemical reduction or sintering, compared to metal precursors, metal powders, or metal nanoparticle-based approaches. These processes usually involve post-processing steps such as high temperatures, intense light, or vacuums and can be detrimental to many of the substrates used in PE. With this comprehensive and diverse range of applications, the issues of direct writing, patterning, and processing of LMs have received considerable attention and are an area of highly active research.

Despite its flexible and fluidic nature, favoring printability, LMs also suffer from a significant drawback: the combination of viscosity, surface tension, and density makes them hard to print with inkjet printing or any other standard direct writing methods resolving the low-micrometer range. While a diverse set of alternative lithography approaches can be employed and reach even sub-micron resolution, these approaches are usually based on stencils, masks, or templates and require sophisticated photolithography, electron beam lithography, or hybrid processes [93]–[95]. As these complicate fabrication and design changes and require much more complex and expensive infrastructure, the direct write additive methods still raise broad interest in the patterning of LM. Recently, some progress was achieved toward this challenge: Tabatabai et al. demonstrated microcontact printing of eutectic gallium-indium (EGaIn) and Galinstan (brand name for eutectic gallium-indium-tin) and successfully patterned dot arrays, lines, and pads and also presented a functioning elastic soft capacitor [96]. Similarly, Boley et al.

reported a direct writing method for gallium-indium-based inks in which the LM ink is printed on a substrate using a syringe pump and a computer-controlled stage, providing patterns with micron scales [97]. Nozzle-based LM deposition can even result in 3D structures: the oxide layer building up on Ga-In-Sn-based alloys under ambient conditions, though being only 1–3 nm thick [80], [98], provides sufficient stability to structures that would ordinarily be untenable due to the extremely high surface tension ($>500 \text{ mN}\cdot\text{m}^{-1}$) [99]. Free-standing mm-scale 3D structures were demonstrated by Ladd et al. at RT by pushing Ga–In alloy through a capillary and stacking droplets of LMs on top of each other forming filaments and other arbitrary 3D structures [100]. Recently, Park et al. demonstrated LM printing for microscale 3D interconnects for stretchable integration of electronics. Here, instead of depositing single droplets, low motion rates while printing allows printed features to be lifted off from the surface and remain stable while being placed at a different location to form 3D interconnects [101].

Here the research objective is also to develop the LM direct write method, which has the advantage of depositing material only where it is needed, thus using less material and generating less waste, as compared to subtractive methods, which must start with complete surface coverage and remove material to form the desired patterns.

1.2.2 Developing flexible and highly accessible on-demand printer

The techniques described in the last section can be divided into contact and non-contact printing methods or conventional and non-conventional printing systems based on the printing method. Other than that, printing systems can also be roughly divided into two groups according to technology: high-end technology and accessible technology. High-end technology and complex instrumentation-based printing setups, such as commercially available inkjet printing systems are expensive; these printing systems cost a hundred thousand euros for a printer and are afflicted by high maintenance. The center of attention to printing techniques has been mostly restricted to these commercially available high-technology inkjet printing systems. Recently, multiple partially accessible technology-based laboratory printing setups have been reported [97], [102]–[105]. As a complementary option, we need a low-cost, reliable, easy-to-use, tabletop-accessible technology that can be assembled and operated without additional training. Besides these features, accessible technology printing should also serve more reliability and excellent resolution competitive to high-end technology at best.

1.2.3 LM-based fully printed electronic devices

LM direct printing was never examined for its potential application in fully functional PE devices that utilize the inherent desirable attributes of LMs. The thesis aims to use the direct-write method for printing LMs and explore this potential for fully printed LM-enabled devices, such as resistors, p–n diodes, and field effect transistors (FETs).

1.2.4 LM-based microheater structures

It is possible to make microheaters out of LMs because they can be fabricated into the desired shape to generate Joule heat. Recently some LM-based microheaters have been reported [106], [107]. Unfortunately, these microheater structures were fabricated with microchannel-based systems, which might be complex in design and include multiple steps. Moreover, these microheaters based on liquid metal are susceptible to breakage caused by voids forming in the liquid metal as temperatures rise beyond 50 °C. Applying direct writing of LM microheaters can simplify the microheater fabrication, remove the multiple steps involved, and avoid the breakage of the LM microheater.

1.2.5 Interfaces studies between solid metal components and LMs

Most of the reported LM-based electronic devices also include interfaces between solid metal components and LMs, which might critically impact the device's overall functioning. Gallium and gallium alloys are very tainting with metals such as Al, Au, and Ag, even at room temperature, and they can diffuse into the grain boundaries of these solid metals. It is possible that this penetration can lead to a significant change in the mechanical or electrical properties, and current knowledge is limited here. In their study on capillary-printed eutectic gallium-indium (EGaIn), Park et al. found ohmic behavior for EGaIn forming electrical connections between pads of three metals Au, Cu, and Ag. They used two different modes of generating the LM lines: (I) direct-write, where the lines are written directly from one pad to the other, thus, the LM interfaces directly to the metal pads. And (II) reconfiguration, where a line is written on glass first and then lifted and laid over the metal pads, which leads to a formation of a thin oxide layer in between the LM and the metal pads. While the oxide layer is thin enough to cause a negligible rise in resistance, it changes the interaction between LM and solid metal pads. Resistance increased three times after 7 hours for the direct-write lines, while for the reconfigured, oxide-interfacing lines, no significant change was observed even after seven days [101]. Sato et al. also studied the contact resistance between Galinstan and a Cu film. A vacuum-induced reduction in

the oxide layer's effect has been demonstrated to reduce contact resistance up to 90% compared to the case where the Cu film was placed on a Galinstan surface with an interfacial oxide layer. Here, the formation of CuGa₂ alloy at the interface to the Cu film was monitored via energy-dispersive X-ray spectroscopy (EDS) and X-ray diffraction (XRD) over time [108].

Arguably gold is the most important industrial metal in the manufacture of electronics commonly used as electrodes and connectors, which is a highly efficient conductor and usually remains corrosion-free and stable (other than with LMs). Unfortunately, no comprehensive chemical study of the interaction of LMs with gold has been reported yet. The penetration of GaIn alloys into gold electrodes might affect the performance of electronic devices after a specific time. Thus, quantifying these processes is crucial for managing their impact on a device and a critical step in bringing devices from the lab to commercial and daily life.

1.3 Thesis outline

This dissertation work addresses the discussed challenges in PE and accomplishes the research objectives listed in the last section. Here the development of different printing methods to assist LM printing and low-cost, on-demand printing methods are reported. This dissertation work also discusses the fabrication of fully-printed electronic devices such as fully-printed resistors, microheaters, p-n diodes, and transistors. It also discusses the interaction of LM with metals, particularly with gold. The whole dissertation can be divided into several parts. The first part (the current chapter) provides an overall introduction to PE and the thesis outline. The second part discusses comprehensive printable materials, printing techniques in PE, and the basic understanding and functioning of p-n diodes, transistors, and microheaters. The second part also discusses the state-of-the-art for LM-based fully printed electronic devices. The third part describes the different experimental results obtained with the LM printing method, beginning with chapter 4.

The dissertation chapters are organized as listed below:

- **Chapter 1** offers a brief introduction to PE and the main objectives of the thesis.
- **Chapter 2** provides a general background of printable materials and basic printing methods available for PE. It also discusses some specific common printable materials and functional inks (insulator, semiconductor, conductor inks) used in PE, along with a brief introduction to LMs and the problem associated with writing these.
- **Chapter 3** offers an insight into device design, functioning, and typical characteristics of p-n diodes, FETs, and microheaters. It also discusses printed EGFET's (electrolyte-gated FETs) basic structure and functionality. Moreover,

it presents an introduction to state-of-the-art LM-based fully printed microelectronic devices.

- **Chapter 4** presents a high-resolution glass capillary-based direct-write method for printing LMs such as eutectic gallium alloys that overcomes the discussed challenges and describes the factors affecting printing.
- **Chapter 5** presents an affordable tabletop technique, which can deposit materials in substrate areas that are non-accessible with conventional printers. This setup can deposit materials in a controlled manner with microscale resolution, micrometer precision, and the highest flexibility in the pattern.
- **Chapter 6** shows the application of LM printing for the fabrication of LM interconnects and resistors, fully printed diodes, and fully printed transistor structures. It also probes the stability of printed LM structures and resistors for future uses with the help of encapsulation of LM lines in poly(methyl methacrylate) (PMMA).
- **Chapter 7** use direct writing of the LM technique described in Chapter 4 to fabricate LM-based microheaters on glass substrates. It also discusses the effects of power and voltage on the microstructural properties of Galinstan and different printed microheater designs. Additionally, the thermal characteristics of the microheater are evaluated.
- **Chapter 8** examines the interaction of Galinstan with solid gold surfaces by utilizing vertical scanning interferometry (VSI), EDX/EDS, X-ray photoelectron spectroscopy (XPS), XRD, atomic force microscopy (AFM), and X-ray nano computed tomography (nanoCT). Additionally, it explores the electrical properties of Galinstan resistors directly printed between gold pads. It also explores the oxide layer on Galinstan using time-of-flight secondary ion mass spectrometry (TOF-SIMS and thickness measurement using XPS).
- **Chapter 9** summarizes the whole thesis.
- **Chapter 10** gives an outlook for future works.

Part II. Theory and background

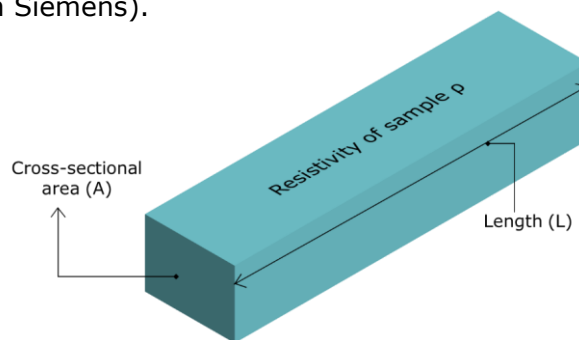
2. Printable materials and printing techniques

The main focus of this chapter is to discuss available printable materials and the printing technologies used in the fabrication of electronic devices. This present chapter briefly discusses different inks' formulation and their respective properties. Here we also try to understand the working principle of different techniques and their benefits, potential problems during the printing, and possible solutions available.

2.1 Printable materials

Functional inks are an important part of printed electronics, as ink is deposited on the substrate in different thin layers to fabricate printed electronics devices. Material selection, printing, and post-printing treatment are three complementary phases of this manufacturing process [109], [110].

Inks can be classified according to material and the property they carry, and the first classification of materials in electronics – conductor/semiconductor/insulator - can be easily understood by the resistance of material as described by Ohm's law. Which states that if a voltage (V) is applied to both ends of the sample and a current (I) is flowing through it, the resistance (R) is proportional to the voltage applied, the resistance (R) is $R = \frac{V}{I}$ (in Ohm). The reciprocal of resistance is conductance, denoted as $G = \frac{I}{V}$ (in Siemens).



The resistance of a material proportional to the length and is inversely proportional to the cross-sectional area: $R = \rho \frac{L}{A}$.

Where:

ρ : resistivity ($\Omega \cdot \text{cm}$)

σ : conductivity ($\Omega^{-1} \cdot \text{cm}^{-1}$ or $\text{S} \cdot \text{cm}^{-1}$)

L: length of sample

A: cross-sectional area of the sample

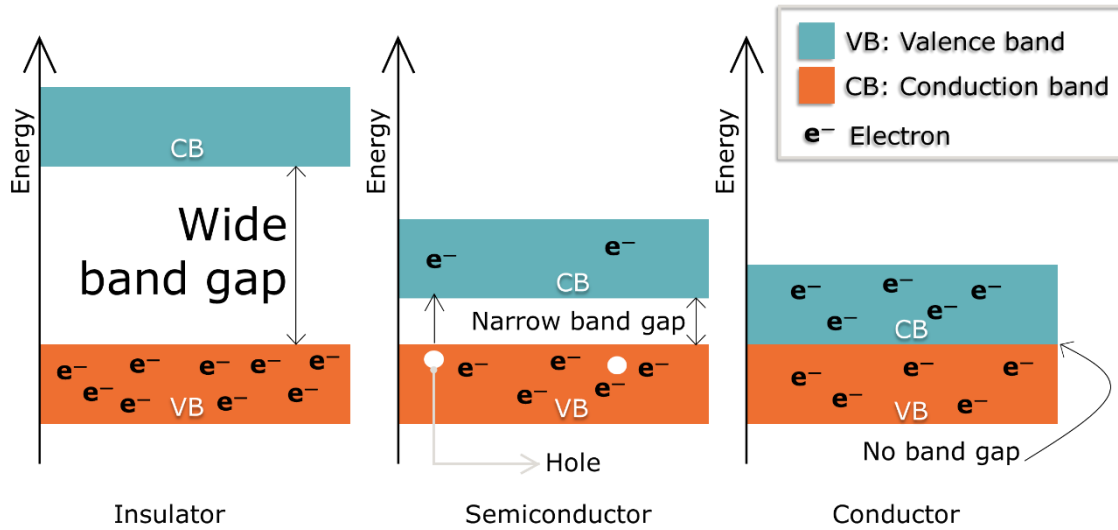


Figure 2. 1: Classification of materials based on the band gap.

Resistivity and conductivity are independent of actual sample geometry. These intrinsic properties are therefore convenient for characterizing conductive materials. The same classification can also be explained with the band gap, as shown in Figure 2. 1. The term insulator refers to a material that conducts electricity poorly; the reason is the wide band gap between VB (valence band) and CB (conduction band). A large amount of energy will be required to push electrons from VB to CB. Insulators include glass, wood, mica, and diamond. Semiconductors are materials that show the conductivity between a conductor and an insulator. Semiconductors have a narrow band gap. Common semiconductors include, e.g. silicon and germanium [111]. The conductors are usually metals (Au, Ag, Al, Cu, etc.) which allow the free flow of electrons.

When these conductive materials are applied to an actual device (e.g., a wire), the conductance and resistance are influenced by three main factors.

- **Material's cross-sectional area:** It determines how much current can pass through it. A bigger cross-section allows more current to flow through it; in the same way, current flow is restricted by thin cross-sections.
- **Conductor length:** As length will increase the conductance will decrease.
- **Temperature:** Increasing temperature increases particle vibration or movement, and when the molecules move more rapidly (increases in temperature), conductivity decreases since they get in the way of the current flow. Some materials can exhibit superconductivity at extremely low temperatures.

Also, when these materials are used to develop operational electronic devices, other important parameters also come along, such as the charge carrier's mobility. This

mobility can be defined as the drift velocity (v_d) of the charge carrier per unit electric field (E):

$$\mu = \frac{v_d}{E} \quad (2.1)$$

The carrier mobility can be either electron and hole mobility. μ unit is $\text{cm}^2 \cdot \text{V}^{-1} \cdot \text{s}^{-1}$ or $\text{m}^2 \cdot \text{V}^{-1} \cdot \text{s}^{-1}$ as SI unit.

A second important classification is to categorize these materials (conductor, semiconductor, and insulator) into organic and inorganic printable materials. A comparison of organic and inorganic materials is presented in Table 2.1 [112], [113].

Table 2.1: Comparison of general trends for different properties of organic and inorganic materials.

| Properties | Inorganic Materials | Organic Materials |
|--------------------------------|--|--|
| Charge Mobility | High Charge Mobility | Low charge mobility |
| Printability | Difficulty in ink formation, also surfactant affects other properties of ink | Easy for ink formulations, polymer material also supplements printability. |
| Post Processing Steps | steps such as high-temperature annealing and sintering are needed | With low annealing temperatures, also some inks do not require the annealing |
| Environmental Stability | Relatively stable with the environment | Poor environmental stability |

Several electronic materials, including dielectrics (polarizable insulators), conductors, and semiconductors, are briefly described in this present chapter in terms of their properties, the preparation of inks, and the formation of films by solution or printing [114], [115].

2.1.1 Insulators - dielectrics/electrolytes

The purpose of dielectric inks in printed electronics is to act as an insulation and capacitance layer at the same time. Printed field effect transistors or thin film transistors (TFT) require a thin dielectric layer for proper insulation to avoid current leakage and to operate at low voltages [116]. In addition to high capacitance, dielectric materials for printed electronics should be low-temperature processable and printable. Materials and inks used in insulator/dielectrics can be separated into polymers, organic materials, inorganic oxides, composites, and electrolytes. The most common traditional insulator and gate dielectric used in both academia and

the semiconductor industry are Si substrates with SiO₂ layers. The thickness of SiO₂ is typically 100–400 nm thick. Inorganic materials such as aluminum oxide (Al₂O₃) [117], tantalum oxide (Ta₂O₅)/SiO₂ [118], hafnium oxide (HfO₂) [119], yttrium oxide (Y₂O₃) [120], titanium oxide (TiO₂), etc. are also used as gate dielectric, and these can be usually deposited with a process such as evaporation, sputtering, plasma deposition and low vapor chemical vapor deposition (CVD) [121] and these are usually not printable [122].

On the other hand, organic materials have been developed in a number of solvent-processable dielectric materials inks, including polymers, inorganic oxides, ion gels, and solid-state electrolytes [123], [124]. Several popular organic dielectric materials are commonly used in printed electronics, such as poly(4-vinyl phenol) (PVP), poly(methyl methacrylate) (PMMA), polyethylene terephthalate (PET), polyimide (PI), polyvinyl alcohol, (PVAL) polystyrene (PS) and polydimethylsiloxane (PDMS). Compared to inorganic equivalents, these low-cost organic dielectric materials are widely available in large quantities, can be dissolved in various solvents, and can be printed easily. More details about high-k gate dielectrics can be found in this interesting review [124], [125].

Table 2. 2: Properties of various organic and inorganic gate dielectrics used in printed electronics.

| Materials | Method | T (°C) | k | d (nm) | C (nF·cm⁻²) | Source |
|--------------------------------|--------------------------|---------------|----------|---------------|-------------------------------|---------------|
| PEO/LiClO ₄ | Spin Coating | RT | - | 400 | 5×10 ³ | [126] |
| PVA | Spin-coating + UV | 60 | 6.2 | 250 | 22 | [127] |
| P(VDF-TrFE-CTFE) | Spin-coating + Annealing | 60 | 52 | 110 | 330 | [128] |
| GO/PVDF | Dip-coating + Annealing | 150 | 15.6 | 450 | 32 | [129] |
| ZrO ₂ | Inkjet Printing | 500 | 22 | 60 | 325 | [130] |
| HfO ₂ | Spray-pyrolysis | 450 | 18.8 | 104 | 151 | [131] |
| Al ₂ O ₃ | Spin-coating + Annealing | 350 | 9.7 | 115 | 75 | [117] |

Here T, is the deposition/annealing temperature, and k is the dielectric constant.

As the previous reports suggest, high permittivity and high-frequency stability can be achieved with solution-processable inorganic materials, but it is challenging to avoid pinholes and cracks in printed films, which can result in short circuits. Therefore, developing a new class of dielectric materials and composites is advised. High k inorganic nanoparticles (NPs) can be combined with a printable polymer to

achieve the best dielectric constant, high-frequency stability, and printability [132], [133].

Table 2. 2 summarizes the properties of various inorganic gate dielectrics inks fabricated by various processing methods. Figure 2. 2 also shows commonly used materials for gate dielectrics inks.

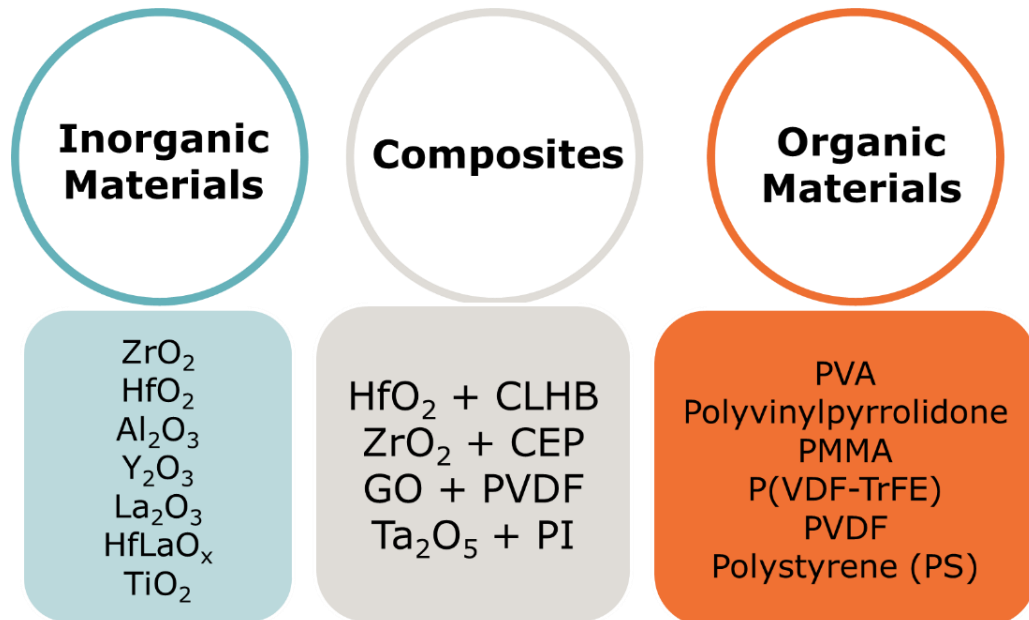


Figure 2. 2: Classification of some insulators/dielectrics materials.

Inorganic nanomaterial loading generally increases the dielectric constant of a composite dielectric material based on nanomaterials [134]–[136]. However, nanoparticle loading also increases leakage currents due to a lack of polymer filling between nanoparticles and metallic atoms electromigrating through gaps from electrode materials. Also, as nanoparticle concentrations increase, leakage current can also increase, which might be because of the agglomeration of nanoparticles [137]. It is possible to improve the solubility and dispensability of inorganic nanoparticles in both polymers and solutions by surface modification [138]. Many composites have been developed recently [135], [139].

Besides ink formulation, a number of parameters (such as thickness and homogeneity/roughness of printed pattern) must be studied to achieve high reliability and performance of printed electronic devices. For example, a very rough/thin printed/sintered insulating gate layer may increase current tunneling or leakage, which may result in higher power consumption [109], [140]. As a possible solution, printing a thick dielectric layer (usually a few micrometers or hundreds of nanometres) might help in order to prevent electrical leakage[114]. In order for carrier transport to be stable in printed electronic devices, the interface properties of the insulating layer and other layers must also be considered so that a possible solution can be designed.

2.1.2 Electrolyte dielectrics

Electrolytes at electrode/electrolyte interfaces in TFTs have opposite charges (anions and cations) that shift in response to electric fields. And at the interface, there is formation of two thin ion layers called as electric double layers (also referred to as EDLs). EDL is around 1 nm thick.

Based on the Helmholtz model, an equation can be used to estimate the specific capacitance of each double layer:

$$C_{sp} = \frac{k\epsilon_0}{\lambda} \quad (2.2)$$

Where:

λ : Debye screening length (usually around 1 nm),

ϵ_0 : permittivity of free space,

$k \approx 10$,

Typically, a C_{sp} between 1 and 10 $\mu\text{F}\cdot\text{cm}^{-2}$ is attainable with electrolytes. E.g., PEO/LiClO₄: 5 $\mu\text{F}\cdot\text{cm}^{-2}$ with a layer thickness of 400 nm [126], ionic gel: $\approx 10 \mu\text{F}\cdot\text{cm}^{-2}$ for a thickness of around 1 μm [141] has been reported

Thus, electrolyte gates can create exceptionally large charge carrier densities at semiconductor–dielectric interfaces, which is one of the primary advantages of TFTs made with electrolyte gates. Among electrolytes, ionic liquids, ion gels, polyelectrolytes, and polymer electrolytes are the most common. Table 2. 3 represents some of the common electrolytes.

A difference between polymer and inorganic dielectrics is that a electrolyte's capacitance is determined by the presence of the electric double layer (EDL) rather than by its physical thickness [142]. Still, in order to prevent unacceptable large leakage currents, thick electrolyte films ($\approx 1\text{-}10 \mu\text{m}$) are necessary [143].

When an electric field is applied to PEO/LiClO₄, lone oxygen pairs on the PEO chains coordinate the Li⁺ cation, resulting in coupled ionic motion and polymer backbone reorganization. PEO chains are flexible, and their flexibility depends on the operating temperature as well as the glass transition temperature (T_g) of the polymer. Hence, ions can move in solids [142].

In ion gels other copolymers are also used such as poly-(styrene-*b*-methyl methacrylate-*b*-styrene) (PS-PMMA-PS), poly(vinylidene-*co*-hexafluoropropylene) (P(VDFHFP)), and photoinitiated cross-linkable such as: poly(ethylene glycol) diacrylate (PEG-DA), poly[(styrene-*r*-vinylbenzylazide)-*b*-ethylene oxide-*b*-(styrene-*r*-vinylbenzylazide)] (SOS-N3) [144].

Table 2. 3: Common electrolytes used in printed electronics.

| Class | Description | Examples | Reference |
|---------------------------------|--|---|--------------|
| Polymer Electrolytes Composites | They consist of mobile ions and ion-coordinating polymers | PEO + LiClO ₄ , PEO + CsClO ₄ , PVA + H ₂ O + KF | [145] |
| Polyelectrolytes | Only small ions are mobile in these compounds with charged or ionizable groups | Poly(acrylic acid) (PAA), poly(styrenesulfonic acid) (PSS), poly(ionic liquid)s (PILs) | [146], [147] |
| Ionic Liquids | In most cases, these are binary salts composed of organic cations and inorganic anions. | EMIM-TFSI, Anion (TCB, FAP) Cation (DEME) Most used DEME-TFSI (up to 120 $\mu\text{F}\cdot\text{cm}^{-2}$) | [148] |
| Ion Gels | Typically, they are prepared by chemical crosslinking of monomers in an ionic liquid or by physical crosslinking of block copolymers | PS-PEO-PS (as copolymer) + BMIM-PF ₆ or EMIM-TFSI or EMIM-OctOSO ₃ | [123] |

Where:

PEO: poly(ethylene oxide)

EMIM: 1-ethyl-3-methylimidazolium

TFSI: trifluoromethylsulfonylimide

TCB: tetracyanoborate

FAP: trifluorotris(pentafluoroethyl)phosphate

DEME: diethyl-N-methyl-N-(2-methoxyethyl)ammonium

PS-PEO-PS: poly(styrene-block-ethylene oxide-block-styrene)

2.1.3 Semiconductors - n-type/p-type

In order to develop active printed electronics and transistors, semiconductor materials are critical to the process. Generally speaking, semiconductors can be divided into two categories based on their doping arrangements: n-type semiconductors (in which an intrinsic semiconductor is doped with an electron donor) and p-type semiconductors (in which an intrinsic semiconductor is doped with an electron acceptor). As shown in Figure 2. 3a, E_c represents the lowest energy state for a free electron [electrons in the conduction band (CB) means current can flow], E_v represents the highest energy state for filled outer shells in the valence

band (VB), E_f represents the fermi level, which represents the likely distribution of electrons. For an n-type material, as shown in Figure 2. 3b, there is a high probability of free electrons in CB and which moves E_f closer to E_c and increases the number of majority carriers (electrons). For a p-type material, as shown in Figure 2. 3c, there is a low probability of free electrons in CB and a high probability of holes in VB, which moves E_f closer to E_v , and VB has the number of majority carriers (holes) [149]. It is also possible to divide semiconductor materials and inks into three types: organic, inorganic, and hybrid composites.

As far as performance and stability are concerned, inorganic materials such as silicon, oxides of transition metals, and chalcogenides are superior to organic materials. Due to their high mobility, carbon nanotubes, graphene, and semiconductor quantum dots are also being studied due to their exceptional properties. On the other hand, processability, environmental stability, printability, and flexibility are some of the characteristics that make solution-processable organic semiconductors attractive.

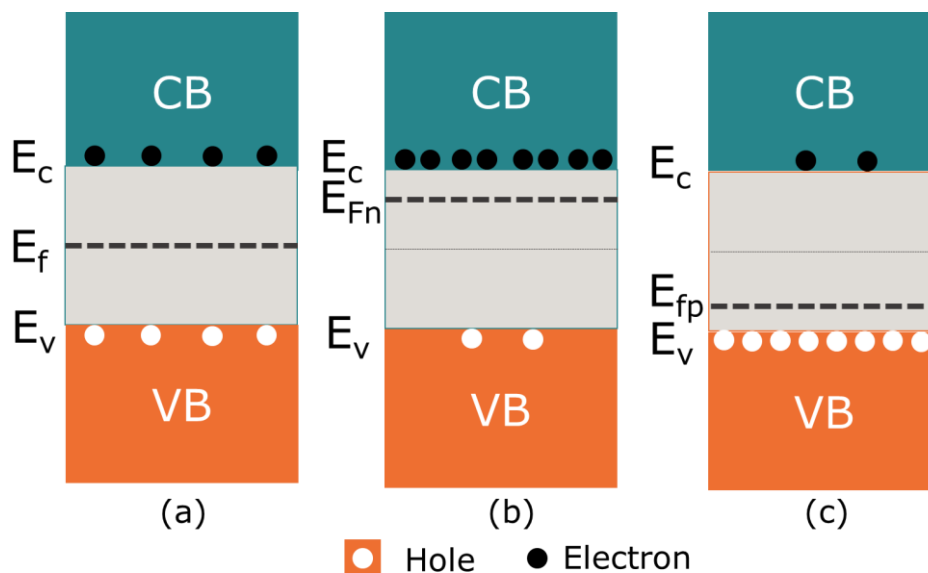


Figure 2. 3: Semiconductor energy band diagrams for (a) intrinsic, (b) n-type, and (c) p-type semiconductors.

Silicon (Si) and germanium (Ge) have dominated the history of microelectronics for over a half-century. In most cases, Si films are deposited through CVD [150]. Si films can also be solution-processed using precursors or nanoparticles, although it is usually necessary to anneal them at high temperatures (usually > 500 °C) in an inert atmosphere in order to achieve high-quality surfaces [151], [152]. "Silicon ink" also exists, which is made by polymerizing cyclopentasilane (CPS) under UV light, completing a pattern by spin-coating and inkjet printing [153], [154].

Another class of inorganic semiconductors is metal oxide semiconductors (MOS) [155], [156]. Compared to conventional covalent semiconductors such as silicon

(Si), metal oxide semiconductors offer unique electronic charge transport properties. It is the metal ions that are responsible for the excellent properties of transparent oxide semiconductors (TOS). Additionally, to these metal cations, oxygen also plays an important role in the electronic properties of oxide films since oxygen vacancies are one of the most important sources of free electrons [156]. There is a predominance of n-type conductivity for metal oxide semiconductors, such as In_2O_3 , ZnO , and SnO_2 , and their solid solutions [109].

There are several families of metal oxides that have been discovered as promising candidates for p-type semiconductors, such as Nickel oxide (NiO) and Cu(I)-based oxides (such as Cu_2O and CuMO_2 ($M = \text{Al, Ga, or In}$), attracting a lot of attention [157], [158]. In these metal oxides, the Cu 3d state is close to the VBM and helps to reduce the effective hole mass. Over the past few years, SnO has also been extensively studied for its p-type semiconductor properties [159].

Table 2. 4: The intrinsic mobility of commonly inorganic semiconductors in printed electronics.

| Material | Method | Type | Field-Effect Mobility (μ) ($\text{cm}^2\cdot\text{V}^{-1}\cdot\text{s}^{-1}$) | Referenc |
|--|-------------------|-------------|--|-----------------|
| In_2O_3 | Inkjet Printing | n | 120 | [165] |
| Indium Gallium Zinc Oxide (IGZO) | Inkjet Printing | n | 10.2 | [166] |
| Zn_2GeO_4 and $\text{In}_2\text{Ge}_2\text{O}_7$ Nanowires | Transfer Printing | n | 25.01 and 11.67 | [167] |
| Zn_3As_2 Nanowires | Transfer Printing | p | 305 | [168] |
| Cu_xO | Spin Coating | p | 0.29 | [169] |
| $\text{Cu}_{5\%}\text{NiO}$ | Spin Coating | p | 1.5 | [170] |
| NiO_x | Spin Coating | p | 1.5 | [171] |

Although all of these materials are capable of being made printable, they do have some challenges associated with their properties. There are two main challenges associated with printable TOS, which are the high annealing temperature and low charge mobility. In order to achieve optimum mobility after the printing of these inks (such as metal nitrate aqueous solutions), a sintering temperature of 300–500 °C is needed. There are also other methods available in metal-oxide and semiconductor ink systems other than high-temperature annealings, such as deep ultraviolet (DUV) and photo-annealings, that are used to achieve higher condensation rates and film densifications [160]–[162].

A recent progress report on solution-processed inorganic field-effect transistors can be found here [15], [163], [164]. Table 2. 4 compares the intrinsic motilities of some inorganic semiconductors.

Other than metal oxides, metal chalcogenides (sulphides, selenides, and tellurides) semiconductors combine direct bandgap with very high mobility and other characteristics. It is possible to print and then anneal metal chalcogenide semiconductors such as binary M-X (M = Cd, Zn, Pb, Sn, and X = S, Se, or Te) or ternary or quaternary compounds, such as CdZnTe, HgCdTe, HgZnSe, Cu(In, Ga)Se₂ [15], [172]–[174]. It is also interesting to note that this annealing/vacuum treatment of printed/evaporated metal chalcogenides also contributes to the switching of the films. When hydrazine-activated PbSe films are heated (up to 100 °C), their conductivity changes from n-type to ambipolar to p-type [175].

Semiconductor quantum dots such as CdX, PbX, and ZnX (X = S, Se, Te) have also been successful [176]. Due to their monodispersity, low cost, and small size, they are also suitable for printed electronics. As QD films are annealed and sintered, the distance between the particles is reduced, which improves their performance and is used for FET applications [177].

Carbon nanotube (CNT) and graphene are the two most studied carbon nanomaterials so far [178], [179]. Depending on their properties, they can be used as semiconductors or conductors. CNTs can either be metallic or semiconducting, depending on their diameter and twist. CNTs are semiconducting when the energy level of the conduction band exceeds the energy level of the valence band, thereby creating a gap between them [180]. When graphene is used as a semiconductor, its zero bandgap restricts its use in graphene-based electronics. The graphene bandgap has been opened by the use of several methods, including nanoribbon patterning, deposition on special substrates, use of graphene bilayers under dual gates, and chemical modification [181].

There are many advantages to using inorganic semiconductors, together which provide high field-effect mobilities and long-term stability under mechanical, electrical, and environmental conditions. Still, high temperature processing steps continue to be the main challenge when it comes to using inorganic semiconductors and associated printing methods [15].

Organic semiconductors (OSC) are receiving more and more attention these days. In printed electronics, as opposed to their inorganic counterparts, these organic semiconductors possess many characteristics that make them more appealing for some applications. OSCs are lightweight, low-cost, low-temperature processed, mechanically flexible, and readily available. It is possible to process them using existing semiconductor and printed electronics techniques [182].

There are two categories of organic semiconductor materials according to their molecular weights: small organic molecules and polymers. Both of these can also be divided into p-type materials, mainly with hole carriers, and n-type materials, mainly with electron carriers.

In the case of p-OFETs, the energy level structures of p-type organic semiconductors have HOMOs (Highest Occupied Molecular Orbitals) closer to the work function of the source and drain electrode contacts, and it allows holes to move from the source Fermi level to move into the organic HOMO level. On the other hand, in the case of n-OFETs, the n-type organic semiconductors have LUMO (Lowest Unoccupied Molecular Orbital) closer to the work function of the source and drain electrodes which facilitates electron injection from the source Fermi level into the organic LUMO level [109], [183]. Among organic semiconductor conductors, tunneling, hopping between localized states, mobility gaps, and phonon-assisted hopping are the most commonly observed ways of conductivity [184], [185]. The LUMO energy can also be approximated to an electron affinity (EA) [the energy released by adding an electron from infinite (vacuum energy) to the innermost unfilled electron shell], and HOMO energy can be approximated to ionization potential (IP) [the energy required to remove an electron from an atom to infinity] [186].

Molecular band structures, molecule energy levels, and stacking order influence the charge transport mobility of organic semiconductor materials. There are also composite semiconductors in which polymers are blended with small molecules. E.g. there are several types of p-type semiconductors that are widely investigated for organic field effect transistors (OFET)s and other organic devices, including aromatic hydrocarbons (primarily oligoacene/arene derivatives), chalcogen-containing heterocyclic derivatives, and nitrogen-containing heterocyclic materials [187], [188].

Organic semiconductors with n-type properties are difficult to develop due to their poor endurance in ambient conditions. It is common for n-type semiconductors to have high LUMO energies (> -4 eV [189]), which makes them highly susceptible to oxygen and compromises stability [190]. As a solution, a conjugated structure containing electron-withdrawing groups such as halogen, cyano, and carbonyl can improve an n-type semiconductor's air stability [187].

Charge carrier mobility in organic semiconductors are usually lower than in inorganic semiconductors [185]. Because of this limitation, organic semiconductors are not suitable for electronics requiring extremely high switching speeds. Nevertheless, with the view of printed electronic devices, organic semiconductors can compete in electronic applications that do not require fast switching speeds due to their performance and ease of processing.

Recent progress in printable organic field-effect transistors can be read here [182], [187], [191]. Although it shows reports with printable organic field-effect transistors, field-effect mobilities in most printed FET are less than $1 \text{ cm}^2 \cdot \text{V}^{-1} \cdot \text{s}^{-1}$. The following Table 2. 5 compares intrinsic mobilities larger than $10 \text{ cm}^2 \cdot \text{V}^{-1} \cdot \text{s}^{-1}$ offered by some organic semiconductors.

2. Printable materials and printing techniques

Table 2. 5: The intrinsic motilities of commonly organic semiconductors in printed electronics.

| Material | Method | Type | Field-Effect Mobility (μ) ($\text{cm}^2 \cdot \text{V}^{-1} \cdot \text{s}^{-1}$) | Reference |
|---|--|------|---|-----------|
| Hydrocarbons with thiophene groups C8-BTBT | Inkjet Printing | p | Max: 31.3 | [192] |
| DPP-DTT-based polymer | Spin coating, blade coating, and inkjet printing | p | 3.5-10.5 | [193] |
| PCDTPT based polymer | Drop Casting | p | Max: 23.7 | [194] |
| Halogenated tetraazapentacenes 4Cl-TAP | Drop Casting | n | Max: 27.8 Average: 14.9 ± 4.9 | [195] |
| Halogenated F4-BDOPV | Spin-coating | n | Max: 12.6 Average: 7.58 | [196] |

Where

μ : Field Effect Mobility

DPP: N-alkyl diketopyrrolo-pyrrole

DTT: dithienylthieno[3,2-b]thiophene

PCDTPT: poly[4-(4,4-dihexadecyl-4H-cyclopenta[1,2-b:5,4-b']dithiophen-2-yl)-alt[1,2,5]thiadiazolo[3,4-c]pyridine]

BTBT: 2,7-dioctyl[1]benzothieno[3,2-b][1]benzothiophene

BDOPV: benzodifurandione-based oligo(p-phenylenevinylene)

2.1.4 Conductors

There are two types of conductive materials inks: Organic (organic molecules and polymers) and Inorganic (inorganic materials, primarily metals). Additionally, polymer composites can be prepared using carbon black or metal powder as filler materials [197], [198].

On the inorganic side, metals are the main part of ink formulation (as can be seen in Table 2. 6) because of their high conductivity. In addition to conductivity, the selection of a particular metal for printing conductors depends on its cost, processing temperature, volume production, and its long-term reliability. In terms of resistivity, silver (Ag), copper (Cu), gold (Au), and aluminium (Al) rank the top four with 1.59, 1.72, 2.44, and 2.65 $\mu\Omega \cdot \text{cm}$, respectively. The differences in conductivity are so

small, that other factors, such as chemical inertness and cost, become more important [181]. Among printable metals, silver is the most successful and popular due to its relatively low price, high conductivity, and chemical inertness. When it comes to thermal stability and conductivity, Ag and Au inks are similar, but in terms of cost, silver is clearly superior to Au [199]. Conductive materials such as copper are also promising. Compared to Ag, it is 100 times cheaper. It is, however, difficult to prepare copper ink due to its high tendency to oxidize. Additionally, Cu particles require high temperatures for sintering and are easily oxidized in the atmosphere [200], [201]. Aluminum has the same problem; it is more chemically active than copper.

Table 2. 6: Common conductive inks used in printed electronics with their respective reported conductivity.

| Material | Method | T (in °C) | Conductivity (S.m⁻¹) Max reported in report | Reference |
|------------------------------|--------------------|----------------------|---|------------------|
| Copper aqueous ink | Desktop printing | 60 | 1.8×10^6 | [202] |
| Nickel aqueous ink | Desktop printing | - | 2.2×10^4 | |
| Copper MOD Ink | Inkjet printing | 300 | 8.1×10^6 | [203] |
| Au NP ink in PVP | Desktop printing | 500 | 8.0×10^4 | [204] |
| Ag Nanoflakes Ink | Screen printing | RT | 6.02×10^6 | [205] |
| Graphene Ink in Cyrene | Screen printing | 100 | 7.13×10^4 | [206] |
| CNT in Gellan gum | Extrusion printing | 21 | 5.03×10^3 | [207] |
| PEDOT/PSS in ethylene glycol | Drop casting | 160 | 1.75×10^4 | [208] |
| PEDOT:PSS | Spin cast | 120* | 4.38×10^5 | [209] |

Where:

MOD: Metal-Organic Decomposition

PVP: poly(N-vinylpyrrolidone)

*: additional treatment with H₂SO₄.

The commonly used aqueous and organic solvents cannot dissolve solid metals. So to fabricate metallic inks traditionally, either metal particles are mixed with polymer solutions to make them printable, or metal salts are used to make ink. In addition,

the recent development in nanomaterials and surface modification techniques allows metallic micro/nanoparticles and nanowires to be blended in organic solvents or water with little need for surfactants or lubricants [197], [210], [211].

Another important type of conductive ink is carbon-based material which offers excellent conductive properties. So to make conductive inks, carbon-based materials such as carbon black, graphene, graphene oxide, carbon nanotubes, and carbon nanofibers have been added to polymeric materials to form conductive inks [212]–[216]. However, graphene oxide is more commonly used as a precursor for conductive ink formulations than pristine graphene because it offers dispersibility in water along with high electrical conductivity even after it has been reduced by chemical or thermal treatment after printing.

Ink formulations based on carbon materials (graphene and CNT) are challenging because it is difficult to disperse non-aggregated materials in a proper vehicle at low viscosities [217]. A variety of stabilizing agents is used to obtain stable dispersions, including polycyclic aromatic hydrocarbons, sodium dodecyl sulfate (SDS), sodium dodecyl benzene sulfonate (NaDDBS), sodium deoxycholate, sodium cholate, and polymers such as poly(*N*-vinylpyrrolidone) (PVP), polyvinyl alcohol (PVA), and ethyl cellulose. Despite all this, low graphene loading remains one of the significant disadvantages of such dispersions for graphene ink [214].

Other than those, transparent conducting oxides (TCOs) are another class, TCOs exhibit conductivity as well as transparency. A number of different binary-doped TCOs can be produced, of which ITO (indium tin oxide) is the most preferred [213], [218].

Detailed reports about metal nanoparticles and carbon materials-based inks can be studied here [115], [181], [213], [219], [220]. Among the conductive organic molecule and polymers studied, such as polyacetylene, polyaniline, polypyrrole, and polythiophene, doped polyacetylene [115], [221]. There are two forms of conduction mechanisms: electronic conduction and ionic conduction [222]. Chemical structure and doping state determine the conductivity of these polymers [223], [224].

The most widely used conductive polymer is poly(3,4-ethylenedioxythiophene) or commonly referred to as PEDOT [225]. It is composed of the monomer 3,4-ethylenedioxythiophene. Other than being a conducting polymer, this material is optically transparent, highly stable, has a moderate bandgap, and has a low redox potential. Its main disadvantage is its poor solubility, which can partly be overcome by doping it with PSS (poly(styrene sulfonic acid)), here the PSS serve as the dopant which stabilizes the charge balance and referred as PEDOT:PSS composite (polyethylenedioxythiophene:polystyrene sulfonate), it consists of two ionomers, Figure 2. 4 shows its structure. One of its components is sodium polystyrene sulfonate. There is a negative charge associated with sulfonyl groups that have been

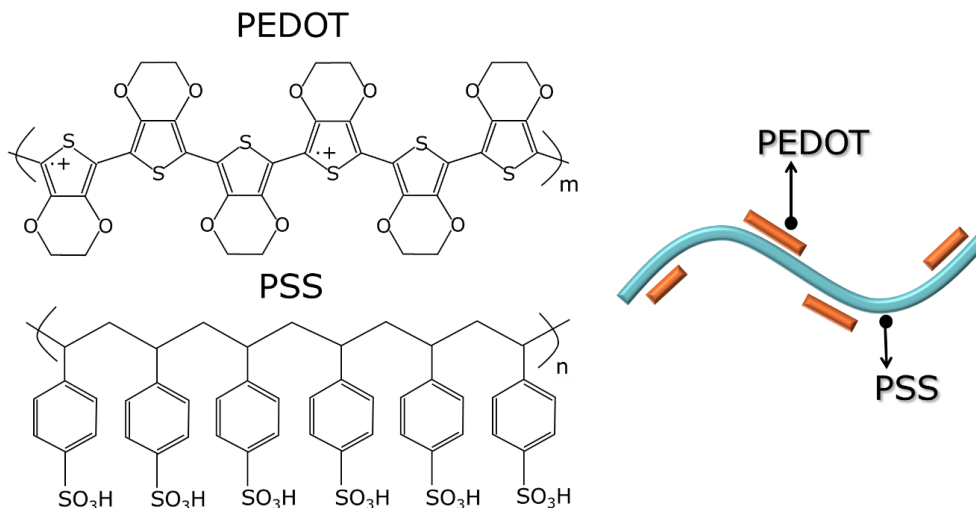


Figure 2. 4: Structure of PEDOT:PSS.

deprotonated. The other component is PEDOT, a conjugated polymer carrying a positive charge. This conductive polymer has a high degree of ductility and transparency [222], [226].

Several other conductive polymers have also been used in inkjet and aerosol jet printing, such as polypyrrole, and polyaniline. Typically, these polymers are less conductive than metallic inks and usually require an inert atmosphere due to their high sensitivity to ambient humidity and their reactivity with oxygen [222].

It is possible to considerably increase the conductivity of PEDOT:PSS by adding organic compounds, including solvents such as dimethylformamide (DMF), dimethyl sulfoxide (DMSO), ethylene glycol (EG), sorbitol, N-methyl-2-pyrrolidone (NMP), ionic liquids, and surfactants [227], [228]. Moreover, stabilizers for PEDOT, such as PSS, can also help overcome problems such as conductivity issues, degradation from ultraviolet light, high temperatures, and humidity [229].

A recent study found that PEDOT:PSS treated with sulfuric acid exhibited a conductivity of more than 3000 S, which is as good as that of ITO [228].

Printing usually involves spin coating or direct writing to obtain a conductive layer. Different PEDOT:PSS inks and formulations have also been developed for printing processes. Additionally, there are several commercially available aqueous PEDOT:PSS inks [Sigma Aldrich 655201-25G (used in experiments in this thesis, see Annex A.1)].

The conductivity of conductive polymers can degrade over time if they are exposed to air. Other than stability, costs, toxicity, poor solubility/inhomogeneity in solvents, and problems during ink formulations also exist. Nevertheless, standard structural conductive polymers have made substantial progress in recent years, offering better properties and lower costs.

Composite conductive inks are another important type of ink. A composite conductive polymer is one in which the polymer product itself serves as an adhesive, regardless of whether it is conductive or not [198], [214], [230]. Typically, virtually all polymer materials can be used as a matrix for composite conductive polymers. Among the most commonly used polymers are polypropylene (PP), polyvinyl chloride (PVC), polyethylene (PE), polystyrene (PS), acrylonitrile butadiene styrene (ABS), polyurethane, polyimide (PI), epoxy resin, acrylic resin, phenolic resin, and unsaturated polyester. Moreover, matrices of conductive rubbers are also made using styrene-butadiene rubber, butyl rubber, and acrylonitrile-butadiene rubber. For the inorganic part of composites, the most common conductive fillers include gold, silver, copper, nickel, aluminium, cobalt, carbon black, graphite, tungsten carbide, etc., in powder, micro/nanoparticles, or other forms [115], [181], [198], [230]–[232].

During the current section of this chapter, we examined some common formulations of ink for use in the fabrication of printed electronic devices, but before printing these inks, it is important to pay attention to the rheological properties and wettability of ink, surface tension, and viscosity, which are also very important to get good quality and repeatable pattern. These ink properties and substrate wettability parameters may determine the need to take certain steps to prepare the substrate according to the ink demand. This process is referred to as the pre-printing process, and it is done in order to make the substrates ready for printing.

2.2 Pre-printing processes

The usual pre-process procedure includes surface treatment to increase substrate surface energy, making the surface (more) hydrophilic [115]. This can be a critical step while printing aqueous ink (such as metal nitrate dissolved in water) because the substrate's surface energy directly affects the uniformity and adhesion of printed patterns to the substrate, which in the end, affects the print size and resolution [115]. The most common methods for creating hydrophilic surfaces are oxygen plasma and ultraviolet irradiation. As an alternative, hydrophilic treatment can also be achieved with stronger oxidizing solutions, such as potassium dichromate solution and peroxymonosulfuric acid (Piranha Solution). The use of these methods poses a high risk of corrosiveness and also meets problems with waste disposal and safety, so they should be used with caution. The surface energy of a substrate can also be modified using molecular self-assembly. The Self-assembled Monolayers (SAMs) of silanes (such as octadecyl trichlorosilane) on a silicon surface, and thiol SAMs on metal surfaces, are typical examples [115], [233].

Surface modification can also be achieved by coating. The term coating refers to the process of depositing materials on a substrate without any pattern. The spin coating method, widely used in laboratories, is a simple and probably most important general applicable coating technique [234]. There are also other types of coatings

methods that are less used but crucial in specific applications such as doctor blading, sprays, plating, and slot dies. Even some printing technologies can also be used for plain coatings, such as gravure, screen printing, inkjet printing, or flexography [109], [114], [235].

Similarly, it is critically important to ensure that pattern and mask fabrication is carefully designed so that ink does not leak or spread on the patterned surface, resulting in disfigurement.

2.3 Post-printing processes

Regardless of the type of ink used (composite or nanoparticle type), it is crucial that the printed ink pattern is converted into a fully functional pattern. Often, this requires an additional process, usually heat treatment for drying and sintering the ink. In the case of conductors, the conductivity is improved through improving interparticle connectivity. Usually, two kinds of post-processing steps exist, which can be referred to as curing and sintering [109], [236].

Ink curing is the process of crosslinking polymer chains to become harder and more durable by applying heat, radiation (such as an electron beam or UV), plasma, or chemical modifications. Also, when the crosslinking /additives are activated by ultraviolet radiation, the process is called UV curing [181], [205], [237]. An organic layer covering the conductive part or the solvent in inks may prevent electrons from moving between them. During the drying process, first, the solvent dries, which forces the metal particles to move closer together; after that, in higher temperatures, sintering occurs when organic materials are burned off, which reduces the distance between particles even further. An additional increase in temperature results in a further decrease in the inter-particle distance, and finally, a metallic crystal structure is formed with a low number of grain boundaries. In the case of NP-based inks, by increasing the temperature, metal nanoparticles melt easily as they have a low melting temperature; after melting, they merge, which makes the printed film denser and solid [161], [181].

Ostwald ripening is one of the modes of particle growth in which larger particles take over smaller ones [115]. Surface energy reduction drives Ostwald ripening because smaller particles have a higher chemical potential than larger particles. Ostwald ripening occurs at the surface (interface) of NPs and at grain boundary rather than in bulk (fully merged large structures of NPs), causing neck growth (the interface of two merging NPs) and increasing neck radius, but still resulting in lower conductivity than the bulk [161], [238]. In traditional thermal annealing, conductive films are annealed in ovens, hot air flow, or hotplates. It is also crucial to consider the thermal stability of printed metal tracks during high-temperature sintering, which might be burnt off due to very high temperatures, or the interface between the metal part and another functional part can be compromised.

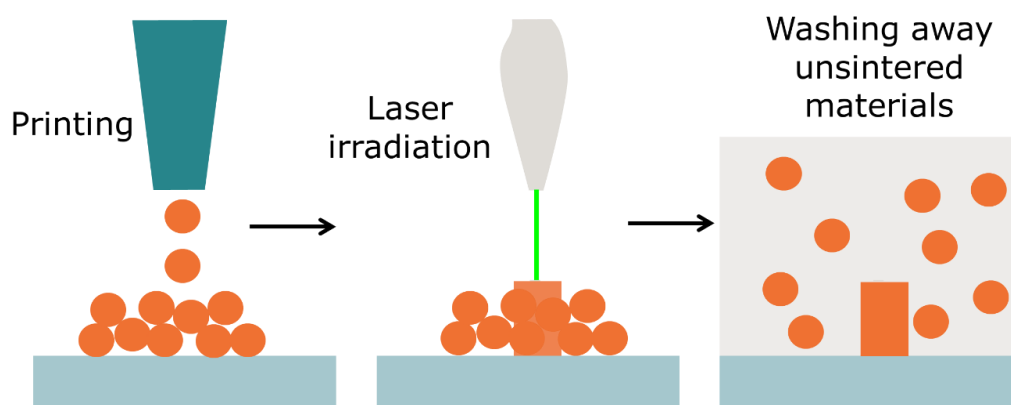


Figure 2. 5: Laser-based selective sintering technologies.

To process substrates or functional ink layers that cannot tolerate high temperatures, selective heating methods such as scanned laser irradiation (shown in Figure 2. 5) can be used. The downside of this approach is that it is relatively slow, and removing any unsintered materials requires subsequent steps such as washing. Other techniques, such as plasma sintering with low pressure, UV radiation, and electrical current sintering, are also used for selective sintering [161], [181], [215], [239], [240].

In addition to the general considerations discussed in the last sections, many additional problems, such as device swelling, thermal hardening, or large thermal expansion, continue to exist, which may lead to poor performance of printed, electronic devices. It is necessary to address these problems and issues in order to print multiple layers and fabricate fully printed electronic devices [109].

2.4 3D printing of conductors

3D printing or additive manufacturing is the fabrication of three-dimensional parts using layer-by-layer material deposition on a surface. In this case, the terms can be used interchangeably. Also, in additive manufacturing or additive processes, the material is placed only where it is needed, resulting in less waste. Although 3D printing processes can be accomplished with inkjet and aerosol jets, the main challenge for these is getting the printed pattern to adhere quickly to the substrate despite using low-viscosity inks. Usually, conductive inks for printing 3D structures are produced by dispersing/blending metal nanoparticles in solvents or UV-curable liquids. Two approaches are most generally used: In the first approach, the process starts with printing dispersions of nanoparticles on heated substrates; as the solvent evaporates upon contact with the substrate, the metal load and viscosity increase considerably, and each drop is fixed simultaneously with obvious shrinkage of the droplets [198], [211], [219].

The second approach also allows actual layer-by-layer printing in the exact location; UV-curable inks contain monomers or oligomers (such as acrylate derivatives) and photoinitiators which are capable of rapid polymerization when exposed to UV light. The fabrication of conductive 3D patterns can be achieved using UV-curable compositions combined with conductive NPS [241]. In addition to these, a modified electrode plating process has been found to be effective for 2D and 3D printing with electrochemical deposition using reactive silver, copper, and nickel inks [242]. Electroless copper plating baths usually contain copper salts, complexing agents, reducing agents, and pH adjusters. During plating, metal nanoparticles on the substrate catalyze copper ion reduction to metal when they are in contact with the plating solution [243], [244].

Recent advances in multi-material 3D and 4D printing (stimuli-influenced shape-morphing systems) are summarized in [198], [245]–[250].

2.5 Liquid Metals (LMs)

New conductive ink classes, such as liquid metals (LMs), exhibit characteristics that are similar to traditional rigid metals and alloys, including high electrical and thermal conductivity (as shown in Table 2.7). LMs, however, are inherently soft and can be dispensed and stretched more easily than solid metals. In general, "liquid metal" is used to refer to metals or metal alloys with melting points close to room temperature. LMs are generally liquid Ga and Ga alloys [251].

Mercury – though being probably the first LM known to humans – is excluded from widespread use in printed electronics due to its toxicity and is only used for very specialized applications, usually in lab settings [252].

The melting temperature of gallium-based liquid metal is around $<20\text{ }^{\circ}\text{C}$ or RT, and it also exhibits low toxicity and negligible vapor pressure [253]. The low melting temperatures and excellent conductivity of LMs ensure they are an ideal material for a variety of applications, such as stretchable circuits, flexible/wearable electronics, and soft robotics, where they need to withstand varying degrees of stress [254], [255]. Thus, LMs are being investigated for additive manufacturing of microscales, and patterning and processing of LMs are highly active research areas. In a liquid metal, patterns and processing can be achieved in a way impossible in solid metals. The technique of additive manufacturing, commonly known as "3D printing," is also among the most effective ways of patterning liquid metals.

Table 2. 7: Physical properties of common liquid metals. Reproduced from [99], [253] with permission from © 2012 IEEE and the Royal Society of Chemistry.

| Property | Mercury | Gallium | EGaIn | Galinstan | DI water @ 25 °C |
|--|------------------------|------------------------------|-----------------------|---------------------------------|---------------------|
| Density (kg·m ⁻³) | 13533 | 6093 | 6280 | 6440 | 998 |
| Viscosity (Pa·s) | 1.526×10^{-3} | 1.37×10^{-3} | 1.99×10^{-3} | 2.4×10^{-3} | 1×10^{-3} |
| Surface tension (N·m ⁻¹) | 487×10^{-3} | 707×10^{-3} | 624×10^{-3} | 534×10^{-3} [256] | 72×10^{-3} |
| Specific heat (J kg ⁻¹ ·K ⁻¹) | 140 | 410 | 404 | 295 | 4183 |
| Thermal conductivity (W·m ⁻¹ ·K ⁻¹) | 8.5 | 29.3 | 26.6 | 16.5 | 0.6 |
| Electrical conductivity (S·m ⁻¹) | 1.04×10^6 | 6.73×10^6 | 3.4×10^6 | 3.46×10^6 | $<5 \times 10^5$ |
| Melting point (°C) | -38.8 | 29.8 | 15.5 | -19 | 0 |
| Boiling point (°C) | 356 | 2205 | 2000 | >1300 | 100 |
| Vapour pressure (Pa) | 1 @ 42 °C | $\approx 10^{-35}$ @ 29.9 °C | N/A | $<1.33 \times 10^{-6}$ @ 500 °C | 3169 @ 25 °C |

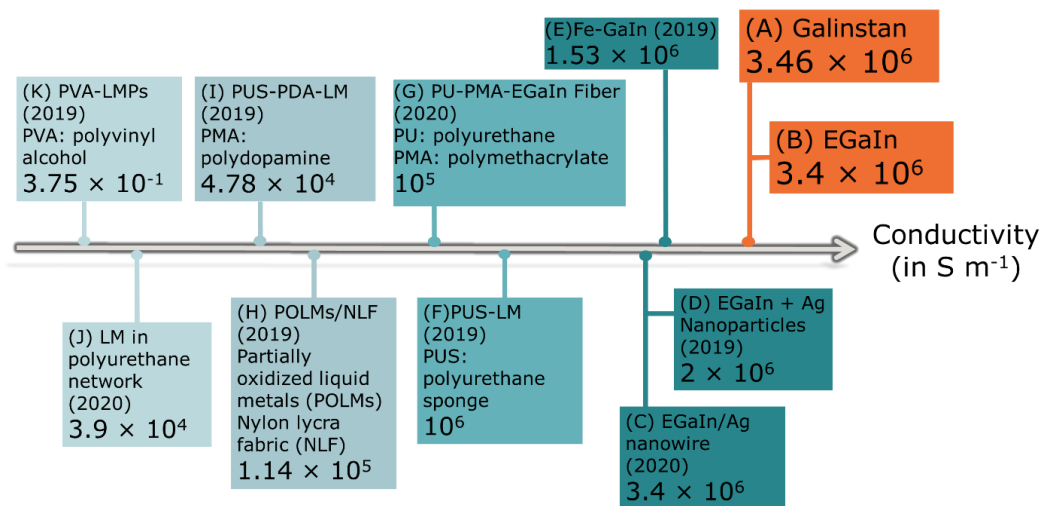


Figure 2. 6: Conductivity comparison of different liquid metal composites. A:[99], [253], B:[253], C:[257], D:[258], E:[259], F:[260], G:[261], H:[262], I:[263], J:[264], and K:[265].

Direct writing and inkjet printing are used to pattern LM instead of subtractive methods, later work by covering a surface and then removing material, which in the end results in material waste if the surface coverage of the desired material pattern is low.

There are three groups of LM inks based on their forms. (1) Bulk LM ink, (2) LM particle-based inks, (3) Composite inks. As the name suggests, bulk LM ink consists of a single, continuous stream of ink containing only the LM itself. Another way is to use inks containing LM particles; LM particles are low in viscosity and are easily broken up into colloidal droplets. As long as the native oxide reforms on the particles, particles will not readily merge back together once they have formed. There is a great deal of interest in particles that can be used to catalyze or initiate reactions because they provide a high surface area and, at very small length scales, have plasmonic optical properties. Additionally, these LM nanoparticle-based inks maintain soft mechanical properties while replacing conventional nanoparticle-based polymeric or oxide inks. Particles of liquid metal can be produced by probe sonication, shearing, or nebulization with piezoelectric transducers. Depending on the different operating parameters, such as power and duration of the energy input, these methods yield micro/nano LM particles with different diameters and morphology. As a result of the stochastic breakup of the metal, the particles are typically polydisperse in size [266], [267].

Composite materials can also improve LM's printability. Figure 2. 6 shows a comparison of liquid metal composites based on conductivity. It is possible for LMs to be ideal fillers for conductive polymer composites for at least two reasons. First, the LMs may change a number of properties of elastomers, including dielectric constants, electrical conductivities, and thermal conductivities, while maintaining the soft, stretchable, and self-healing mechanical properties of elastomers [254], [268], [269]. Second, because of their shape-changing properties, LM fillers also show unique strain-dependent properties when the composite is deformed. Further, LM composites can be separated into three categories: LM composites (I) with a core-shell structure, (II) polymer composites, and (III) micro/nanoparticles composites. Printed conductors can be created with all of these materials [270].

2.6 Challenges printing liquid metal

The rheological properties of liquid metals make the direct writing of LMs more complex than the usual extruding of viscoelastic inks. Inherently, Ga is a reactive material since it readily gives up electrons quickly and oxidizes to produce Ga^{3+} , which is the most stable state of oxidation for Ga. Therefore, LMs are capable of forming a self-passivating oxide layer on top of it and covering itself [271]. As shown in Figure 2. 8, at the interface of this process, a native oxide is formed nearly instantly, typically as an amorphous or poorly crystallized film ranging from 1 to 5 nm in thickness [80], [98]. While bulk Gallium-based LM is a water-like low,

viscosity Newtonian fluid, it obtains non-Newtonian rheology because of this native oxide layer on its surface.

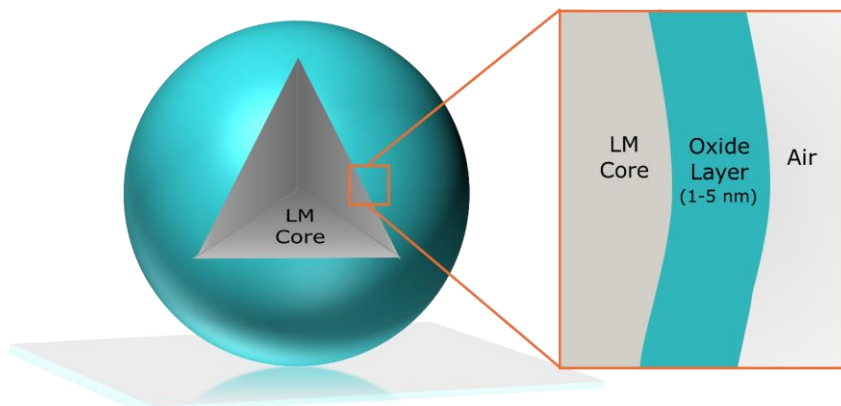


Figure 2. 8: Scheme outlining the oxide layer surrounding the LM core.

Additional to the rheology, the oxide layer also affects the LM's high surface tension. As a result of the surface oxide layer, LM has surface tension $>500 \text{ mN}\cdot\text{m}^{-1}$ at room temperature [99], [272]. However, the oxide shell helps to maintain the shape of printed structures, even allowing for 3D freestanding arcs (discussed in Chapter 4).

As a result of the oxide, LM also has different rheology. When there is sufficiently high pressure at the back to rupture the oxide layer, the metal will flow easily due to its low viscosity. The pressure necessary to break native oxide in ambient conditions is $0.2\text{--}0.6 \text{ N}\cdot\text{m}^{-1}$ multiplied by the interfacial curvature; water has an interfacial tension of $0.072 \text{ N}\cdot\text{m}^{-1}$. As a result, oxide-coated LMs exhibit yield stress behavior, the stress that must be applied to the sample before it starts to flow. A pressure greater than this permits injecting, spraying, smearing, and extruding of the metal [271], [273], [274].

The oxide layer can also efficiently separate LM droplets from each other, enabling even stacks of droplets. Without an oxide layer, these droplets quickly combine into larger spheres. However, when the oxide is exposed only below the critical stress, the LM can maintain shape, thus enabling complex printed structures.

As shown in Figure 2. 9, as a result of the oxide layer, wetting is also more complex. Surfaces are not wetted by bare LMs (since they have large contact angles) except when interacting with metals, in which case the wetting is reactive [275]. On the other hand, oxide-coated LMs adhere to nearly any flat surface [272], [276]. The oxide layer can react and be removed by bringing acid or base vapor around, as it is amphoteric (a compound, molecule, or ion that can react both as an acid and as a base) [274], [277] While comparing HCl and NaOH, with NaOH, the etching of the oxide layer seems to be faster [277]. Aside from the oxide layer as the main influence, other factors such as interfacial behavior, segregation of LM components,

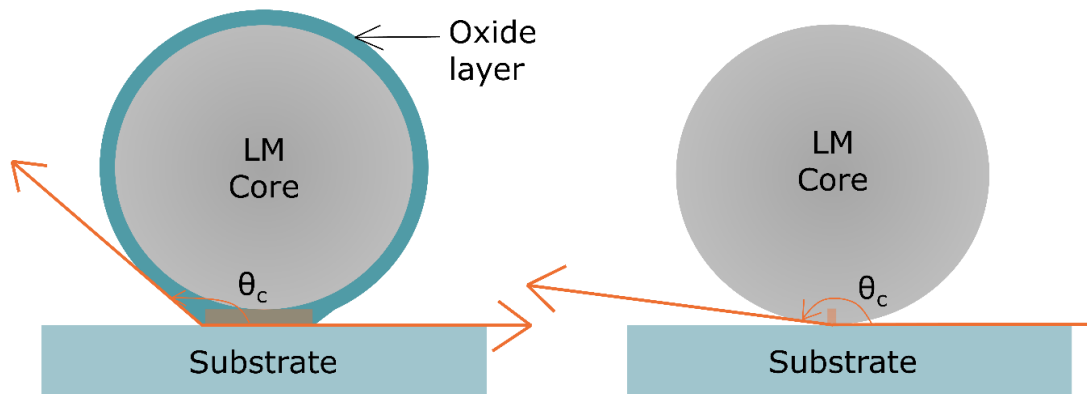


Figure 2. 9: Effect of oxide layer on wetting and contact angle.

and temperature gradients can complicate the printing of LM and fabrication of electronic devices [80], [278].

2.7 Printing techniques

To achieve specific electronic properties, not only the inks and their composition but also the printing processes are crucial. Printing can be divided into different categories based on contact or non-contact printing methods, conventional or non-conventional techniques, and template-based or non-template-based printing methods [109], [114], [279].

There are different ink properties required for different printing methods. Therefore, a particular ink must be matched to a suitable printing method according to ink properties. Some laboratory-made inks, for instance, have a viscosity of less than 5 cP (centipoises), and increasing the viscosity leads to a loss of the desired electrical properties. Inkjet printers and gravure printers can easily print this type of ink, but screen printers have difficulty printing it.

On the other hand, there are some inorganic materials that can only be made into inks using microparticles or nanoparticles. It is common for these types of inks to have a high viscosity, like dielectric and conductive pastes, which are suitable only for screen-printing mask-based techniques to obtain thick and uniform patterns. These ink pastes might not be ideal for other printing methods. Other key parameters to consider when choosing a printing method are resolution and speed.

Different printing methods exist and are commonly used in printed electronics, including screen printing, gravure printing, letterpress printing, offset printing, flexography printing, and inkjet printing [109], [114], [279]. In addition, techniques less commonly used in printed electronics, like microcontact printing or scanning probe lithography techniques such as dip-pen nanolithography (DPN) and fluidic force microscopy (FluidFM), gain rising interest as of their capabilities to deal with certain inks not processable by standard methods and offering higher resolution.

The purpose of this section is to briefly discuss some commonly used printing techniques.

2.7.1 Inkjet printing

The most widely used printing technique is inkjet printing (IJ), which is a non-contact technique. The IJ printing process involves a computer controlling a nozzle to spray ink droplets, creating a digital pattern by combining them. A typical inkjet printer produces droplets of ink with diameters ranging from 10 to 150 μm , which roughly correspond to a nozzle's diameter.

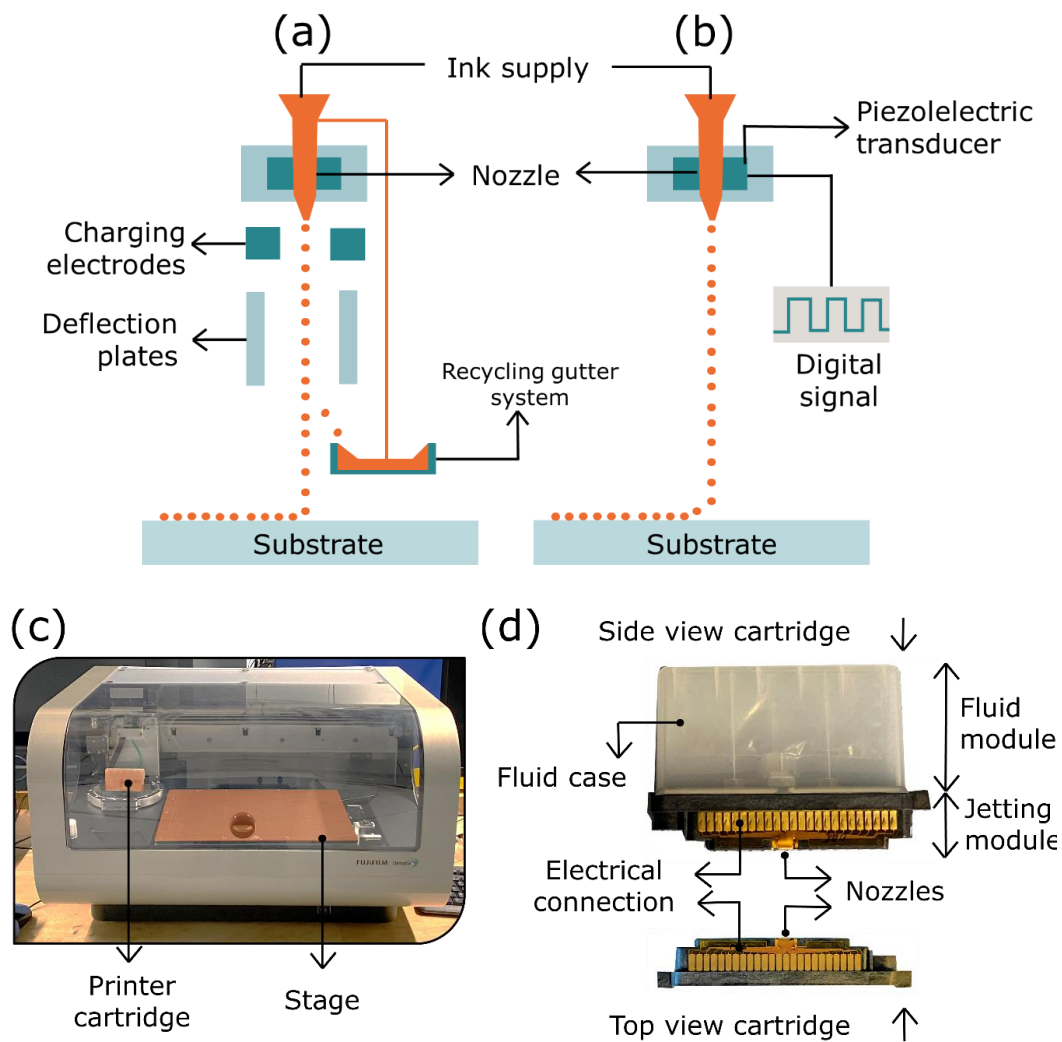


Figure 2. 10: Schematic diagram of inkjet printing. (a) Continuous mode; (b) DOD mode (c) Dimatix Materials Printer DMP-2850 at INT (d) components of cartridge.

IJ printing serves the following advantages over other techniques:

- In terms of volume, the droplets are picoliters in size. In accordance with its non-contact nature, it enables a wide range of materials to be selectively deposited on a variety of substrates in a drop-by-drop manner without being limited by substrate properties such as roughness, brittleness, and flexibility, thus minimizing damage and contamination.
- It is also suitable for prototyping for large-scale industrial production because it does not require a master plate.
- Most importantly, since inkjet printing deposits ink only where it is necessary, it consumes little ink and wastes little material.

There are two modes of operation for inkjet printing in principle, continuous inkjet (CIJ) and drop-on-demand (DOD) [280]. The types of DOD printing include thermal inkjet, piezo inkjet, and electrostatic inkjet. A CIJ printer continuously produces and ejects charged ink droplets. During printing, an electrostatic field controls the ink droplets. Due to the electrostatic field, only in desired position droplets are deposited on the substrate, while in other places, the droplets are deflected into an ink catcher. In contrast, the DOD printer ejects ink droplets by a voltage pulse only when at desired positions, without the need for charging and deflecting droplets [115]. Thus, DOD printers have more straightforward inkjet heads, but CIJ printers have higher jetting frequencies. The working principles of these devices are depicted schematically in Figure 2. 10.

The most common inkjet printer heads propel ink drops using one of two primary mechanisms: piezoelectric and thermal bubble propelling. Piezo inkjet systems work by actuating piezoelectric transducers (PZT) via voltage pulses. A phenomenon that is known as inverse piezoelectricity. A piezoelectric pressure transducer bends or changes shape when a voltage is applied; this piezo actuation generates acoustic waves, which propagate through the ink channel, producing droplets and forcing these ink droplets out of the nozzle. Commercial printing systems usually operate at a voltage pulse frequency of 1 to 20 kHz. On the other hand, in thermal bubble propelling, heat is applied by a heating element in the thermal bubble inkjet head, causing the ink to vaporize rapidly. As a result, a bubble forms in the chamber, causing pressure to increase, which propels an ink droplet out of the nozzle. In printed electronics, piezoelectric DOD inkjet heads are the most popular inkjet heads, as, during thermal inkjet printing, cyclic thermal loading can damage functional materials present in the ink. In contrast, piezo inkjet is an isothermal process. Compared to thermal inkjet, piezo inkjet uses a much more comprehensive range of ink solvents.

Alternatively, but much less used, there are some other types of jet printing, such as electrohydrodynamic jet printing and aerosol jet printing. The aerosol jet printing

process involves spraying an aerosol stream onto a substrate at high velocity. Electrohydrodynamic Jet Printing creates a flow of ink through a fine nozzle onto a surface using an electric field.

Printing with inkjet is digital printing, as it is not necessary to use a mask, master, or template plate. An image for printing is stored digitally on a computer. A digital image can be created and edited using software provided by manufacturers of inkjet equipment. Inkjet printers commonly use monochrome bitmap images. Bitmap files consist of black pixels corresponding to the print matrix and white pixels corresponding to non-printed areas. The software provided with an inkjet printer can convert any pattern file into a monochrome bitmap digital file and further monochrome bitmap image into electrical pulses that propel drops of ink. It is also possible to manually create a pattern by setting parameters directly in the manufacturer's software, such as dot spacing, number of dots, line spacing, arrays, matrix, and layers, which may be convenient for printing simple patterns.

It is important to take into account a number of factors when manufacturing ink for inkjet printing, including dynamic viscosity, surface tension, stability of the ink, and particle size of the components of the ink, which should be well below the nozzle orifice. Different printing systems and cartridges may require different parameters. Similarly, particle loading plays an important role in determining printing process stability. The following articles provide further detailed information on inkjet printing [280]–[287].

It has been mentioned in the previous section that liquid metals with IJ printing suffer from one considerable drawback: their viscosity, surface tension, and density make them difficult to print using inkjet printing or any other standard direct writing method reaching resolutions below 10 micrometers. Hydrochloric acid (HCl)-impregnated paper was used as orifice plate material in some attempts to print LM with inkjet printing [288]. In another effort, a polydimethylsiloxane (PDMS) based microfluidic channel filled with HCl was used as a printing head, where HCl removes the oxide layer of Galinstan, and continuous Galinstan droplets are ejected from the nozzle [289].

2.7.2 Stencil and contact printing

There are several types of contact printing systems, including screen printing, offset printing, gravure printing, flexographic printing, micro-contact printing, nanoimprinting, and dry transfer printing, where the patterns originate from master plates.

In particular, stencil-based printing is one of the most commonly used, low-cost, high-resolution printing techniques available [290], [291]. It contains a master plate that consists of patterned and unpatterned areas on a mesh. Usually, the screen-printing ink is a paste; this allows for the produce thick film patterns. During

printing, the screen is prepared by covering it with paste, and a substrate is placed underneath it. The blade applies pressure to the paste-covered screen, forcing the paste to pass through and deposit on the substrate. Due to its viscous nature, the paste does not leak onto the substrate. Traditionally, screen printers use a flat screen and flat substrate holder.

Stencil lithography, as shown in Figure 2. 11, uses stencils (shadow masks) with nanometer-sized apertures and also fabricates nanometer-scale patterns. Unlike conventional lithography techniques, which use resists, stencils in lithography are mechanically stable and self-supporting, enabling them to be moved during processing and reused multiple times. It involves no heat or chemical treatment of the substrates. For micropatterning and nanopatterning, stencils/masks are usually made from Si, Al, or SiN membranes, but polymer stencils/masks are also being developed [292], [293]. For material deposition, stencils are placed between substrates and sources to mask the deposition. It reproduces the aperture patterns on the substrate in the same manner as they appear on the stencil. Stencil membranes generally do not have intimate contact with substrates due to stress, curvature, or topography. This may be advantageous to preserving fragile substrates in some cases.

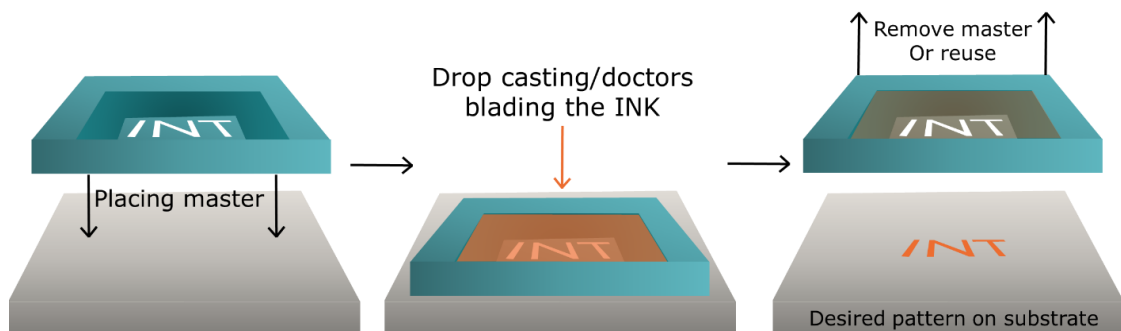


Figure 2. 11: Resistless lithography, such as screen printing and stencil (shadow mask) lithography workflow.

Another printing technique is gravure printing, which replicates patterns by engraving patterns onto a gravure plate. Typical gravure printer components include a gravure plate or roller, a doctor blading system, an ink supply unit, and an impression roller. First, the gravure plate is immersed in ink before printing; then, any excess ink is removed with the help of a doctor blading. Further printing can be finished by applying pressure to the gravure and ink at the same time; the ink in the engraving area is deposited on the substrate. A detailed description of stencil printing can be found here [294], [295].

2.7.3 Microcontact printing & Polymer Pen Lithography

Microcontact printing is an advanced version of stamping; it involves replicating a microlithographic master through replica molding to make the stamp [296]. As

shown in Figure 2. 12a, the microcontact printing (μ CP) process involves ink, a substrate, and a stamp, just like conventional contact printing. After the stamp has been soaked with ink, it comes into contact with the substrate. Ideally, the transfer of ink from stamp to substrate would take place only in the area of contact, which

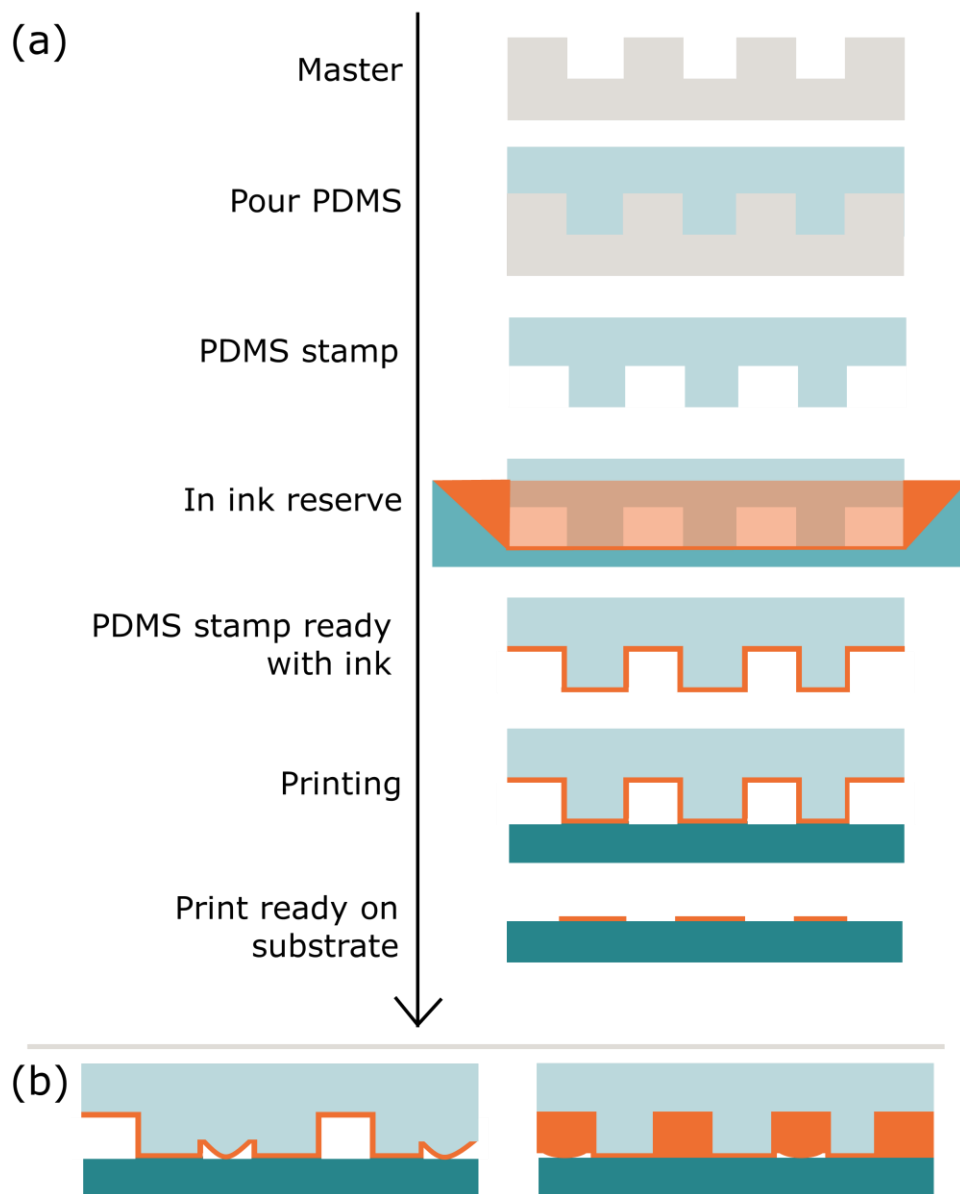


Figure 2. 12: (a) Microcontact printing process and (b) problems during printing such as stamp collapse and ink filling up the trenches.

helps to create high-resolution patterns and structures with specified characteristics. However, this needs careful tuning of the aspect ratio of the patterned stamp and ink load, as shown in Figure 2. 12b; it can be subject to stamp collapse (large "empty" areas of the stamp getting in touch with the surface) or trenches in the stamp being completely filled with ink (thus also transferring some amount of ink to the substrate). The most widely used stamp material is poly(dimethylsiloxane) (PDMS) because it is flexible enough to make contact even on inhomogeneous or

rough surfaces and is still stiff enough to achieve patterns down to micrometers [297]–[299]. Sylgard 184 is a widely used commercially available PDMS that is cheap and easy to obtain. Also, PDMS is transparent, making it suitable for optical applications and for controlling processes through the eye or microscope. It is possible to produce PDMS stamps with pattern features with a sub-micrometer length.

There are also many improvements in microcontact printing, such as Magnetic field-assisted microcontact printing, in which the iron powder is injected into PDMS, and a magnetic field is applied so that homogeneous pressure is applied during the printing [300]. Multiplexing is another development; it is used to print different inks in one step, where the stamp is composed of dots or lines. This led, in particular, to the development of polymer pen lithography (PPL) [297], [301], which combines aspects of μ CP and scanning probe lithography techniques. Here, a PDMS stamp carrying tens of thousands of individual pyramidal features is used in a μ CP-like stamping process, but by virtue of high precision control over the stamp via the scanning probe lithography (SPL) printing setup, multiple controlled substrate contacts are enabled, allowing for a digital pattern generation and multiplexing [302], [303].

To overcome some drawbacks of PDMS for μ CP – in particular low mechanical stability, stamps are being prepared from other polymers such as thermoplastic polymer blends (poly(ether-block-ester) (PEE) [304], poly(styrene-block-butadiene-block-styrene) (commercially available as Kraton D1102 [305]) and poly(styrene-block-ethylene-co-butylene-block styrene) (commercially available as Kraton G1652 [306]) and Polyolefin elastomers (POP). Some photocurable polymers are also used for the stamp by mixing poly(ethylene glycol) (PEG), poly(ethylene glycol) diacrylate (PEGDA), hydrogels, and agarose gel, with respective photoinitiators [307].

Detailed descriptions of microcontact printing or soft lithography can be studied here [307]–[310]. μ CP has also been used to print LMs [311].

2.7.4 Scanning probe lithography

A scanning probe lithography (SPL) method uses scanning probes to pattern materials on the nanoscale. Several SPL methods (as shown in Figure 2. 13) have been developed to modify a material at the probe/surface interface. It is possible to categorize SPL methods by the chemical nature of the process versus the physical nature, such as thermal, electrical, mechanical, and diffusion-based processes, or by considering if SPL involves removing or adding material [41].

A mechanical scanning probe lithography (m-SPL) is a top-down approach to nano machining or nano scratching. However, thermo-mechanical SPL (tm-SPL) works by combining heat and mechanical force. In comparison, in thermal scanning probe

lithography (t-SPL), the material is efficiently removed from the surface without requiring significant mechanical force. High-resolution 3D structures can also be created by controlling patterning depth in these techniques. With thermochemical scanning probe lithography (tc-SPL) or thermochemical nanolithography (TCNL) [312], thermally activated chemical reactions are used on the scanning probe tips to alter the chemistry and phase of materials on the surface. The most common method of heating is using lasers that emit pulses every microsecond or silicon cantilevers that have integrated heaters.

Dip-pen nanolithography (DPN) is based on diffusion, in which ink is first deposited on a pyramidal tip of an AFM (Atomic Force Microscopy) to further form patterns on a number of substrates [40], [313], [314]. When the tip comes into contact with the substrate, a water meniscus between the tip apex and the surface allows the molecules and nano-objects to diffuse from the tip to the surface. By using unique AFM probes with built-in heaters, thermal dip-pen lithography (t-DPN) can easily deposit melted solid inks into the liquid form, extending the useable range of inks to solids [39], [315], [316].

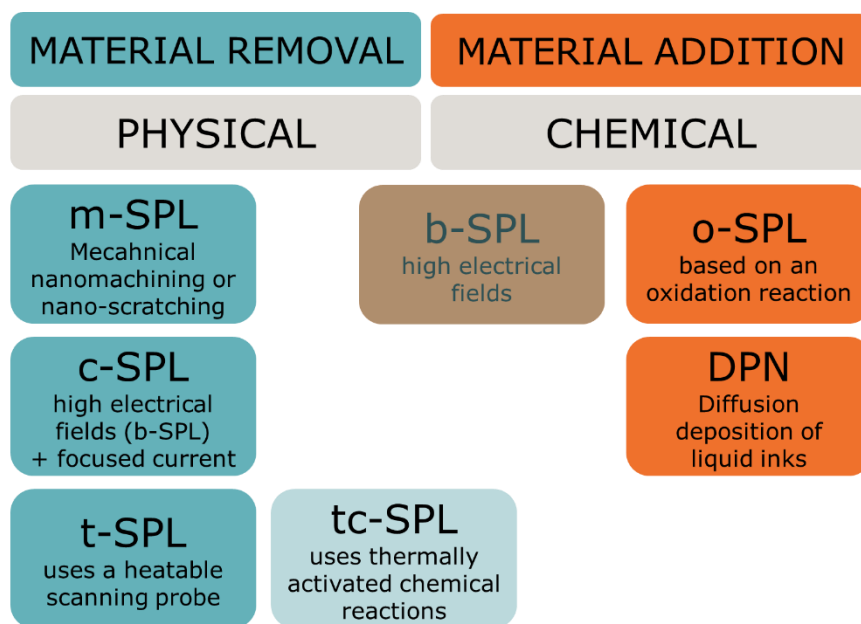


Figure 2. 13: Classification of SPL methods. Adapted from [41] with permission from Springer Nature, copyright 2014.

In oxidation-based SPL (o-SPL), the oxidation reaction is spatially contained, and the scanning probe is used as the source of oxidation [317], [318]. Other names for o-SPL include local oxidation nanolithography, nano-oxidation, and AFM oxidation lithography. By applying voltages between the tip and sample apex, bias-induced scanning probe lithography (b-SPL) is able to confine and facilitate chemical reactions to deposit and grow materials on surfaces locally. In current-induced scanning probe lithography (c-SPL) and the high electrical fields of b-SPL, a focused electron current that emanates from the SPM tip is also used to create nanopatterns

[41], [319]. Another technique is nano-xerography process, which involves generating charge patterns on substrates with conductive AFMs and then immersing the substrates in a suspension of nanoparticles that bind to the patterns [320].

Most of these SPL techniques are capable of patterning lines with a line width of 15 nm and a spatial resolution of 5 nm with a high level of accuracy. One of the most significant advantages of SPL over other techniques, such as electron-beam lithography [321], is that it is a single-step process with a resolution reaching below 10nm in particular cases [316], [319]. Other than that, SPL writing processes operate on 'direct write' principles, creating structures without subsequent development steps. It is possible to pattern a variety of materials with SPL techniques, including biomaterials and polymers. Detailed descriptions of scanning probe lithography can be studied here [39], [41], [297].

2.7.5 Microchannel cantilever spotting (μ CS)

Another commonly used technique for printing electronic materials is microcantilevers-based microchannel cantilever spotting (μ CS), also referred to as surface patterning tool (SPT) techniques. A device named the surface patterning tool (SPT) was initially developed by Eric Henderson et al. and used to deposit biological inks such as Cy3-streptavidin [322]. A standard SPT printing setup available now is the NanoeNabler system (BioForce Nanosciences, Ames, IA, USA, founded by Eric Henderson) [323]. As shown in Figure 2. 14, an SPT tip is composed of a cantilever (ink cartridge) with a split gap at the end, a reservoir on the handling chip, and a 1 μ m deep open transportation microchannel. A sample is loaded into the reservoir by pouring sample solutions and dipping the cantilever end into the sample fluid. SPT cantilevers range 200/300 μ m in length, from 10/30/60 μ m in width, and height is 2 μ m [324]. The cantilevers are also available according to the spot size required starting as low as 1 μ m. A rectangular reservoir is located at the fixed end of the cantilever, which is usually 10 μ m deep. A microchannel measure 1 μ m in depth and 1-15 μ m in width. SPT cantilevers are mounted inclined so that an angle (around 12 $^\circ$) is formed between the SPT cantilevers and the substrates, so only the tip end is in contact with them. Once the cantilever touches the substrate, the ink is transferred onto the substrate. The cantilever/stage is moved according to the desired pattern in a controlled manner. Once the pattern is finished, the tip can be retracted easily.

SPT cantilevers have also been demonstrated multiplexing; Belaubre et al. fabricated arrays (4 cantilevers) of 2-mm-long, 210- μ m-wide, and 5- μ m-thick cantilevers, spaced 450 μ m apart for micro-spotting arrays of cyanine3-labeled oligonucleotides and Anti-goat IgG (rabbit) [325].

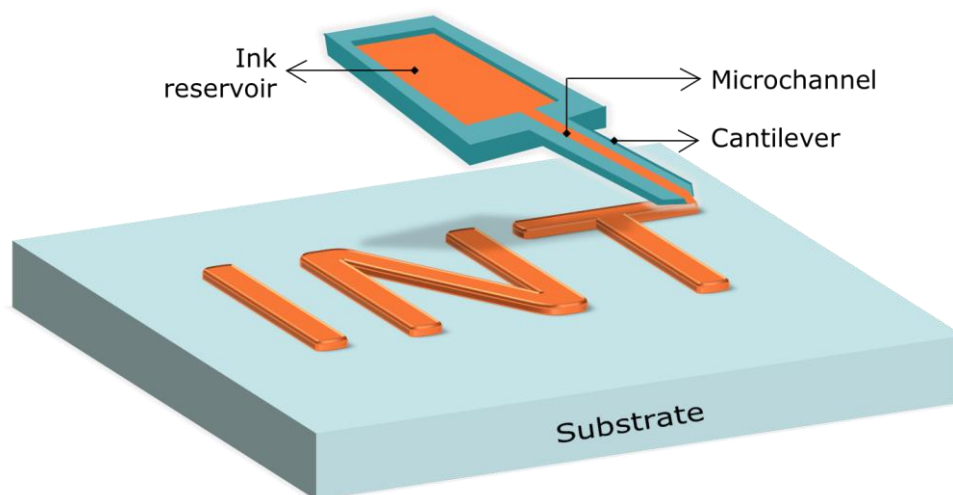


Figure 2. 14: Schematics of microchannel cantilever spotting (μ CS) technique.

Microchannel cantilever spotting (μ CS) can be used to pattern lines and dots and has been used to pattern a lot of biological inks such as fluorescent/nonfluorescent labeled amino acid, protein, and antigen/antibody inks [326]–[332].

The μ CS (SPT-based) printing has also been used to deposit electronic materials such as ZnO SNW-based Schottky diodes [333], gas sensors [334], microresistors of AgNP ink [335], [336], and polyaniline emeraldine salt (PANI-ES) semiconductor ink arrays [336].

2.7.6 Fluidic force microscopy lithography

The fluid force microscopy (FluidFM) lithography method is also a form of scanning probe lithography combining it with aspects of liquid spotting techniques [337].

The base setup comprises an inverted light microscope equipped with hollow AFM cantilevers having nanofluidic channels with apertures of less than 300 nm to some micrometers, which allow direct printing of liquids with submicrometer sizes [338]–[340]. As part of a FluidFM system, microchannel AFM probes are directly coupled with a closed fluid circuit, acting as an "infinite reservoir." It is possible to use the system in liquid, and soluble molecules can be ejected from the internal solution through the pyramid aperture by applying pressure; meanwhile, the force feedback regulates the contact with the substrate. When a tip approaches a substrate, it can be controlled to a very localized modification of surfaces with the sensitive force feedback of AFM. In experiments measuring single-cell adhesion (where the cell is fixed to the cantilever by applying negative pressure), a larger diameter is helpful, while a smaller diameter offers better opportunities for nanolithography and handling sub-micron objects. With pN and nm precision, the tip is able to approach the substrate more precisely and handle volumes more consistently [337].

Applications of FluidFM include injecting liquids into or sampling them from cells, dispensing proteins on a surface in a liquid environment, manipulating mammalian

cells [341] or single-cell manipulations [342], nanolithography, and spotting [339], [343].

Relevant to my thesis, FluidFM has been used to enable localized electroplating in 3D printing using nanochannel cantilevers. Figure 2. 14 illustrates the electrochemical deposition setup, consisting of an electrochemical cell containing a silver quasi-reference electrode and a platinum counter electrode, as well as a FluidFM cantilever (inset). FluidFM probes are filled with a metal salt solution and the flow of this solution is controlled by a pressure controller from the reservoir in the probe to the aperture of the cantilever. The FluidFM probe tip works as a local source of metal ions. A potentiostat polarizes the substrate, reducing the metal ions locally under the probe. The metal ions exiting the aperture of the FluidFM tip are reduced by a sufficient cathodic potential, resulting in localized electroplating, and

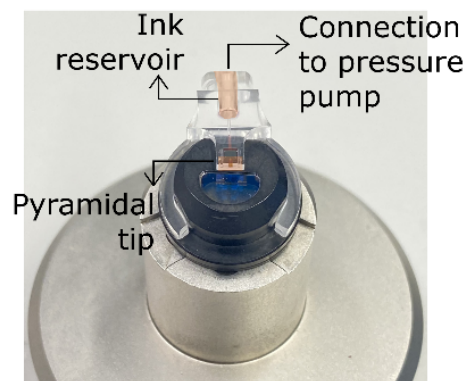
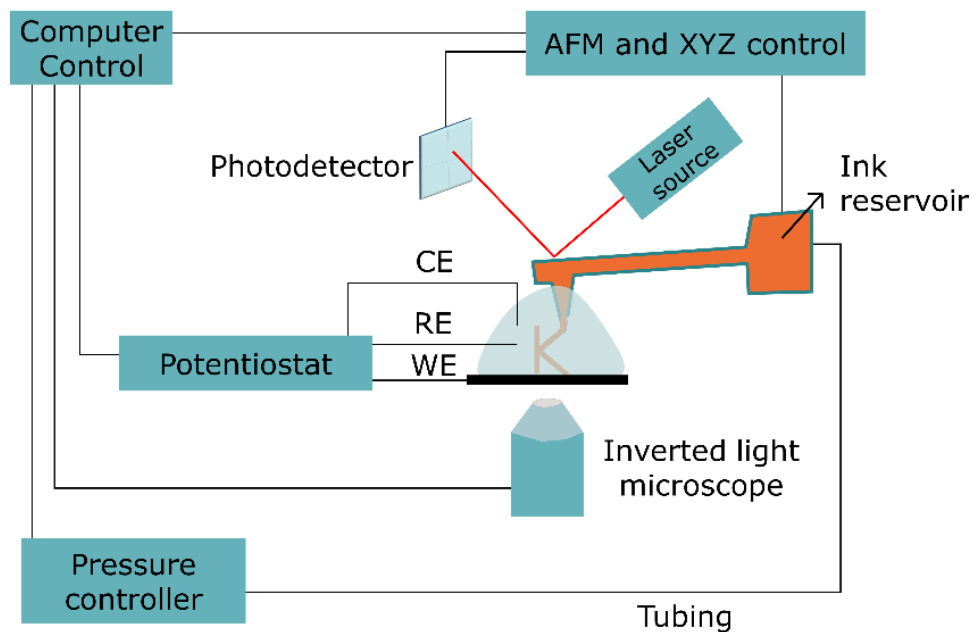


Figure 2. 15: FluidFM-based additive manufacturing (3D metal printing) that does not need post-processing steps. FluidFM cantilever (inset). Here CE: Counter Electrode, RE: Reference Electrode, and WE: Working Electrode.

metal ion diffusion defines the deposit size. All of these components are automated and synchronized with each other and offer 3D metal printing on the nanoscale [244]. Detailed descriptions and applications of fluidic force microscopy-based lithography can be studied here [244], [338].

2.7.7 Summary and comparison of printing methods

Table 2. 8 and Figure 2. 16 represent key properties and parameters of different printing methods. In general, compared to other printing techniques, inkjet or direct writing methods have good resolution and offer less material wastage. However, the printing setup can be used according to the demand of structure and feature sizes required.

Table 2. 8: Comparison of different printing methods [114], [233], [344].

| Printing technique | Inkjet | Screen | Gravure | Offset | Flexography |
|---|--------------------------------------|----------------------------------|-------------------|---------------|--------------------------|
| Image Carrier | Digital | Stencil | Engraved Cylinder | Flat | Polymer Plates |
| Printing Speed (in $m \cdot min^{-1}$) | 15-500 | 10-15 | 100-1000 | 100-900 | 100-700 |
| Resolution (lines per cm) | 60-250 | 50 | 20-400 | 100-200 | 60 |
| Layer Thickness (in μm) | 0.05-20 | 0.015-100 | 0.1-8 | 0.5-2 | 0.04-2.5 |
| Feature Size (in μm) | 20-50 | 20-100 | 70-80 | 10-50 | 80 |
| Maximum particle size | up to 1/100th of the nozzle diameter | up to 1/10th of the mesh opening | <15 μm , | <10 μm , | <15 μm , preferably |
| Preferable Particle Size | <50 nm | <100 nm | <3 μm | <1 μm | <3 μm |
| Solids loading (wt%) | <20 | <90 | <30 | <90 | <40 |
| Surface tension ($mN \cdot m^{-1}$) | 25-50 | 30-50 | 41-44 | 30-37 | 28-38 |
| Ink viscosity (Pa·s) | 0.001-0.05 | 0.1-1000 | 0.01-2 | 20-100 | 0.01-2 |

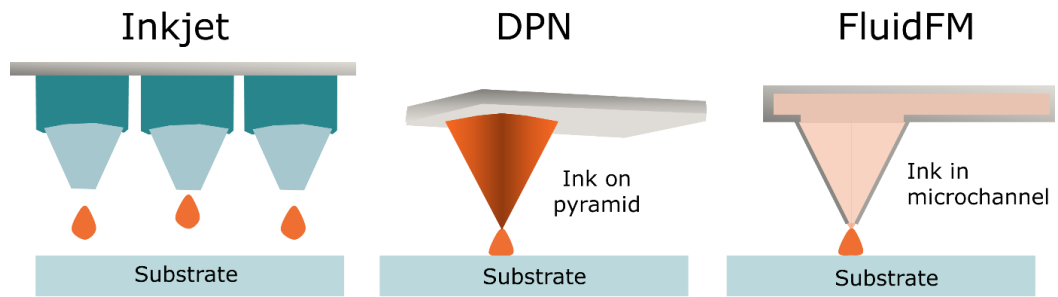


Figure 2. 16: Comparison of different printing methods.

Other direct-write methods of printing liquid metals can be studied here [345].

3. Printed devices

Various inorganic and organic structures of various dimensions and materials have been printed with the different printing techniques described in the previous chapter to create fully functional electronic devices. Due to their potential for high throughput and cost-effective production, fully printed devices have received increasing attention in recent years. This chapter discusses device structure, working, and characteristics of p-n diodes, transistors, and microheaters.

3.1 p-n diode

For understanding other semiconductor devices and designing modern electronic applications, study of p-n diodes are of great significance. A p-n junction diode is a two-terminal semiconductor device that allows the electric current in only one direction while blocking the electric current in the opposite or reverse direction. These p-n junctions are essential for semiconductor electronic devices and building blocks of diodes, transistors, and integrated circuits. Figure 3. 1 represents the circuit symbol of the p-n junction diode.

(a) Schematic symbol



(b) Component



Figure 3. 1: (a) The circuit symbol, where the triangle corresponds to the p side. (b) Physical diode orientation indicating the cathode.

3.1.1 Device structure of p-n diodes

A diode with a p-n junction is an interface between p-type and n-type semiconductor materials (also shown in Figure 3. 2). It depends on the relative voltages of the two semiconductor regions whether a junction between two semiconductors (p-doped and n-doped) is relatively conductive or depleted of charge carriers, resulting in a non-conductive channel.



Figure 3. 2: A p-n junction.

These non-conductive layers can be manipulated to form diodes, allowing current to flow in one direction but not the opposite.

3.1.2 Working of p-n junction diode

A diode with its p- and n-terminals connected would exhibit zero voltage across the diode, and there would be no current flowing. This state with no external voltage applied is called a zero-bias state. However, adding an external potential to the p-n

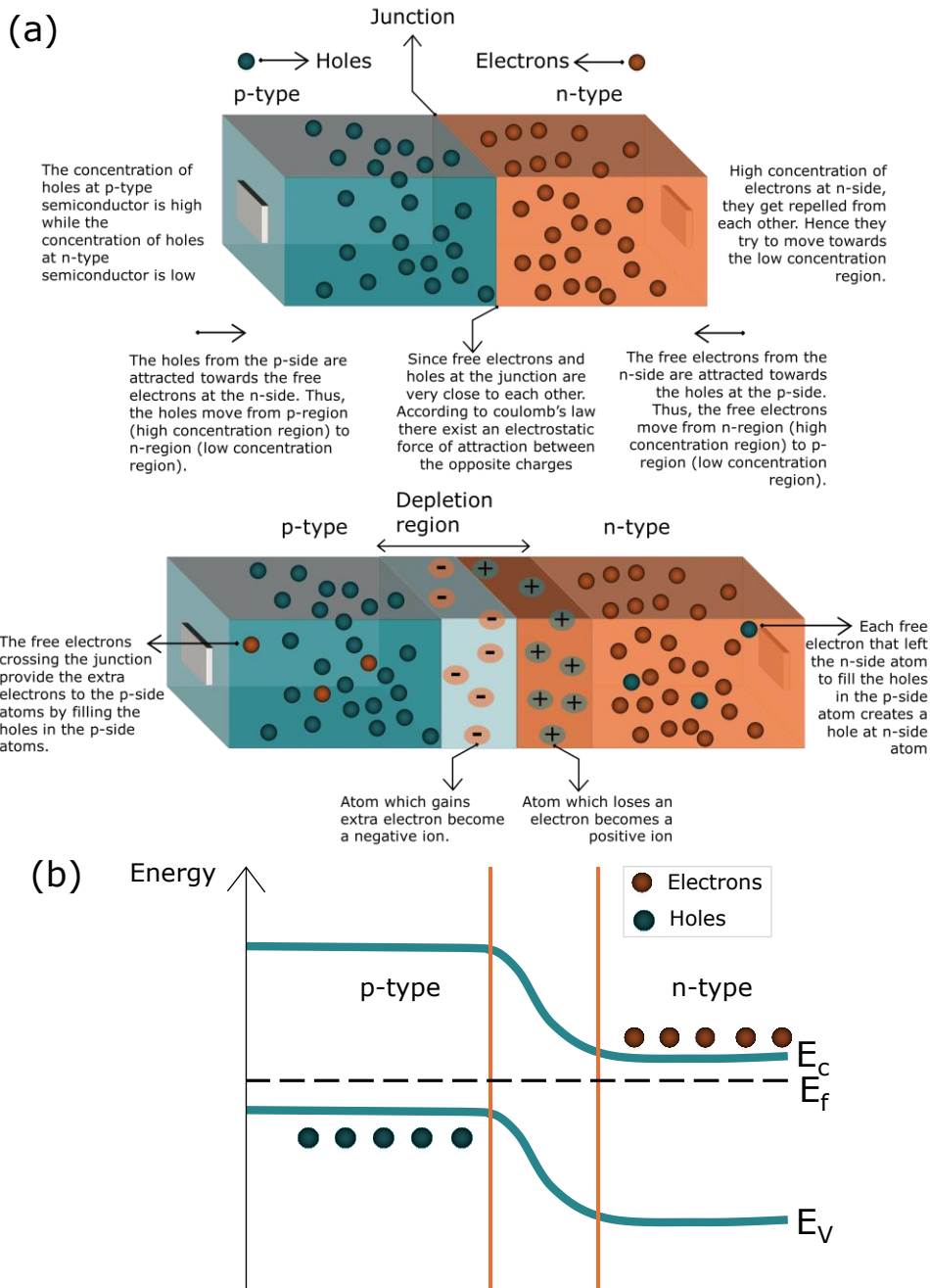


Figure 3. 3: (a) A p-n junction at zero bias and formation of the depletion region. (b) Energy band diagram of a p-n junction in zero bias state under thermal equilibrium.

junction terminals will alter the potential between the p- and n-regions. If an external voltage is applied to a p-n junction semiconductor diode, it is called biasing. A p-n junction can use this potential difference as an opportunity for electrons and holes to diffuse, resulting in a one-directional current flow, which is the defining characteristic of a diode. A p-n junction diode can be biased with an external voltage in one of two ways: forward biasing or reverse biasing.

Zero bias

It is called a zero (unbiased) bias p-n junction when no external voltage is applied.

Depletion region

Overall, there are three layers in the p-n junction: a neutral n-layer, a neutral p-layer, and a depletion layer in the middle. On the n-side, which is rich in free electrons, electrons constitute the majority carriers, and holes are the minority carriers. On the p-side, holes constitute the dominant and are the majority carriers. Nevertheless, it also has a few electrons generated by thermal processes, which are referred to as minority carriers. While approaching the junction, a region without free charge carriers exists, this region is known as the depletion layer, and it acts as an insulator. As shown in Figure 3. 3, the energy band diagram, in the depletion layer, E_F is neither close to E_V nor E_C . Any material interface containing two dissimilar materials (in our case, p-n junction) has a built-in potential; this voltage differential is referred to as the built-in potential, which is difficult to detect directly. Under zero bias conditions, there is no change in the depletion layer.

Forward bias

Forward-biased p-n junction diodes allow electric current when voltage is applied to them. As shown in Figure 3. 4, in a forward-biased p-n junction diode, the positive terminal of the battery (or voltage/current source) is connected to the p-type semiconductor material, while its negative terminal is connected to the n-type semiconductor material.

P-n junctions contain anodes (positive terminal), positively charged electrodes, or conductors that supply holes to the p-n junction. These positive charge carriers (holes) are generated at the anode terminal and travel to the cathode terminal via the diode. At the other end, the cathode is the negatively charged electrode or conductor that supplies the junction with free electrons. Alternatively, the cathode or negative terminal is the source of free electrons; they start at the cathode and travel through the diode to the anode terminal. The anode or positive terminals attract free electrons, whereas the cathode or negative terminals attract holes. By applying an external forward voltage to a p-n junction diode or gradually increasing its voltage (e.g., from zero to 0.1 volts), the depletion region is reduced slightly. This allows for a minimal (usually regarded as negligible) current without practical use. Further increasing the voltage applied to the p-n junction diode generates more electrons

and holes for the diode to function. Consequently, the depletion region (positive and negative ions) is further reduced by a large number of free electrons and holes. Now, the p-n junction diode thus produces a higher electric current. In other words, the depletion region of a p-n junction diode shrinks as voltage increases. Therefore, as voltage increases, the p-n junction diode generates more current. This current is primarily because of recombination, a mechanism of bringing together oppositely charged carriers (electrons and holes) and annihilation.

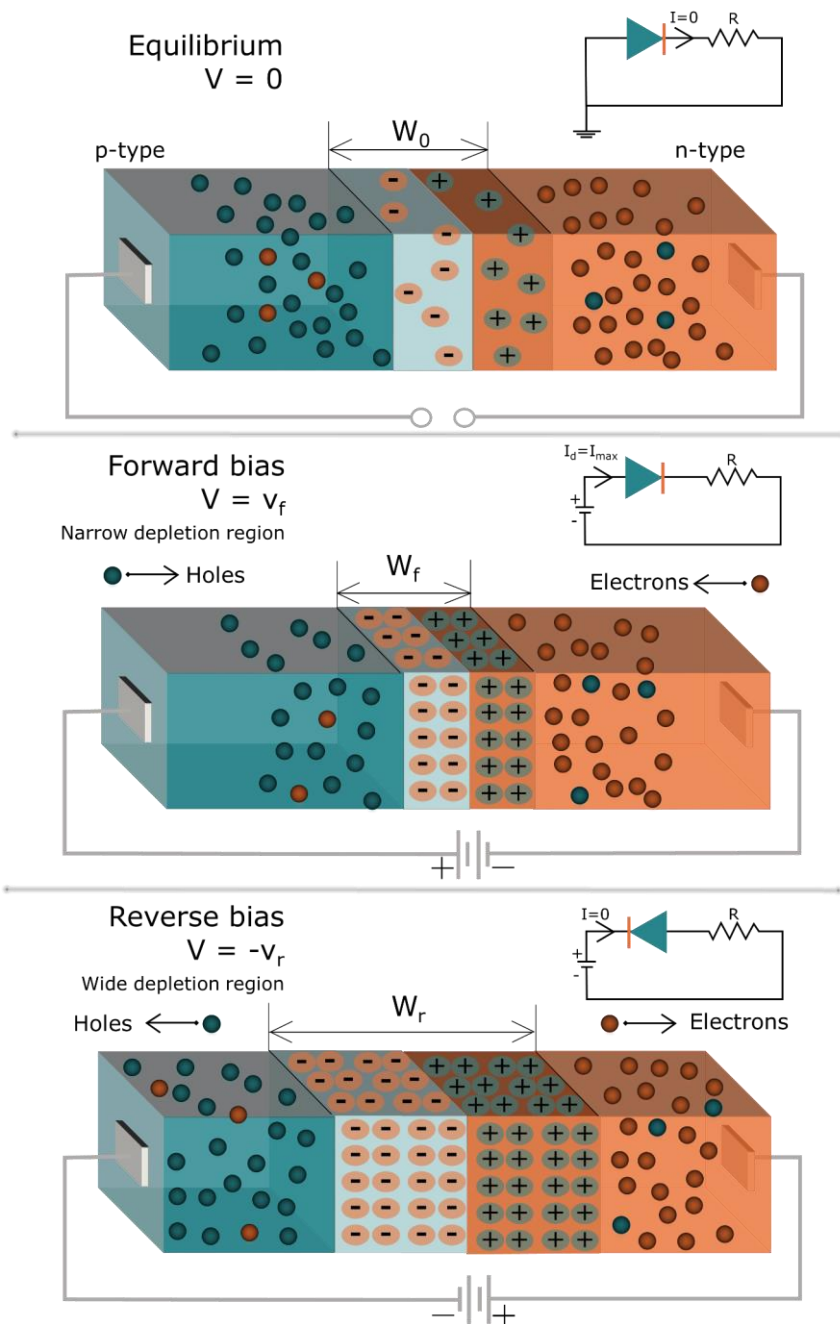


Figure 3. 4: A p-n junction at zero bias, forward bias, and reverse bias. W_0 , W_f , and W_r represent the width of the depletion region, respectively. I is current. V , V_f , and V_r represent the applied voltage, respectively.



Reverse Bias

As shown in Figure 3. 4, during reverse-biased p-n junction diodes, the electric current is blocked when a voltage is applied. Here, the battery (or voltage/current source) positive terminals are connected to the semiconductor n-type materials side, while battery negative terminals are connected to the semiconductor p-type materials side. In this case, when an external voltage is applied, holes from the p-side are attracted towards the negative terminal, whereas free electrons from the n-side are attracted toward the positive terminal.

When a reverse-biased voltage is applied to the p-n junction diode, it further pulls away more electrons and holes from the diode. As a result, the width of the depletion region increases with an increase in voltage. These reverse-biased p-n junction diodes have a broad depletion region that completely blocks most charge carriers, thus, electric current. Despite this, the p-n junction diode allows minority charge carriers to flow. Positive terminals of batteries push holes toward p-type semiconductors, and negative terminals push electrons toward n-type semiconductors. In this situation, both holes and electrons are minority carriers.

As positive charge carriers (holes) cross the p-n junction, they are attracted to the battery's negative terminal. Conversely, negatively charged carriers (free electrons) are attracted to the battery's positive terminal. So reverse-biased p-n junction diodes

Table 3. 1: Comparison of forward and reverse biased p-n diode.

| Parameter | Forward bias | Reverse bias |
|--|---|---|
| Connection | Positive terminal of battery is connected to p-type and negative terminal to n-type semiconductor | Positive terminal of battery is connected to n-type and negative terminal to p-type semiconductor |
| Symbol |  |  |
| Barrier Potential | Reduces | Strengthen |
| Resistance | Low | High |
| The ideal diode behaves as a device with | Zero resistance | Infinite resistance |
| Depletion layer | Narrows | Widen |

can still carry a minimal (usually considered negligible) electric current through these minority charge carriers. Table 3. 1 shows the differences between forward and reverse biased p-n diode.

3.1.3 V-I characteristics of p-n junction diode

Sah, Noyce, Shockley, and Moll extended Shockley's basic theory of the current-voltage characteristics of p-n junctions [346]. In the forward direction, p-n junctions can conduct considerable current because of their reduced resistance, but almost no current in reverse.

The current through the p-n junction is expressed as:

$$I = I_s \left(e^{\frac{qV}{NkT}} - 1 \right) \quad (3.1)$$

Where:

I: total current flows through the p-n junction,

I_s : reverse saturation current (typically around 10^{-12} A),

q: charge of an electron,

V: voltage applied across the p-n junction,

N: Nonideality or emission coefficient,

k: Boltzmann constant, and

T: temperature (in Kelvin).

The value $\frac{kT}{q}$ is usually also noted as V_T , which is thermal voltage (within the p-n diode junction) usually generated by the action of temperature. Reverse saturation current (I_s) is generated due to the diffusive flow of minority electrons from the p-side to the n-side and the minority holes from the n-side to the p-side). In the case of positive V, the junction is forward-biased, while in the case of negative V, the junction is reverse-biased. There is minimal current when V is negative and $V < V_{th}$. When V exceeds V_{th} , the current becomes extremely high; this voltage V_{th} is called cut-in voltage, threshold voltage, or knee voltage. V_{th} for silicon diodes is 0.6 V. Also, a sudden increase in reverse current occurs in the reverse voltage region; this area is called the breakdown region. Figure 3. 5a and b show the I-V characteristics of an ideal and real p-n diode, respectively.

The characteristic I-V curve consists of three distinct regions:

1. Forward-bias region ($V > 0$),
2. Reverse-bias region ($V < 0$),
3. Breakdown region ($V < -V_b$).

The following sections describe each of these regions.

Forward I-V characteristics of the p-n diode

To overcome the depletion region, a minimum voltage threshold is needed; this voltage is known as the forward voltage. During the operation of a p-n diode, only a small electric current can pass through with a small external voltage, which is considered negligible. Whenever a p-n junction diode reaches a certain voltage, a large electric current can flow through it. Upon reaching this point, the electrical

current increases rapidly with a small increase in voltage. This is called cut-in voltage, which indicates a point where a diode begins to allow large currents.

Reverse I-V characteristics of the p-n diode

An increase in reverse voltage applied to the p-n junction diode will result in electrons leaving the n-type semiconductor and holes leaving the p-type semiconductor far from the p-n junction. As a result, the depletion region becomes wider. Due to the wide depletion region, the majority of charge carrier current cannot flow through the reverse-biased p-n junction diode. Minority carriers, however, can pass through it. A current is carried by electrons (minority carriers) in p-type semiconductor and holes (also minority carriers) in n-type semiconductors. This current generated from these minority carriers is called reverse current.

A very small number of minority charge carriers exist in n-type and p-type semiconductors. Therefore, a small voltage applied to the diode will induce all the minority carriers to approach the junction. As a result, the electric current does not increase with an increase in external voltage. It is known as reverse saturation current. The reverse saturation current is produced when the electric current reaches its maximum level at a voltage, and further increases in voltage do not increase the current. Temperature affects the reverse saturation current. Increasing temperatures result in more minority charge carriers being generated; as a result, the reverse current also increases with temperature.

In contrast, reverse saturation currents are independent of reverse voltages. With an increase in voltage, the reverse saturation current remains constant. However, a continuous increase in voltage (even after saturation) will result in a breakdown of the junction and lead to a rapid increase in reverse current, as shown in Figure 3. 5b.

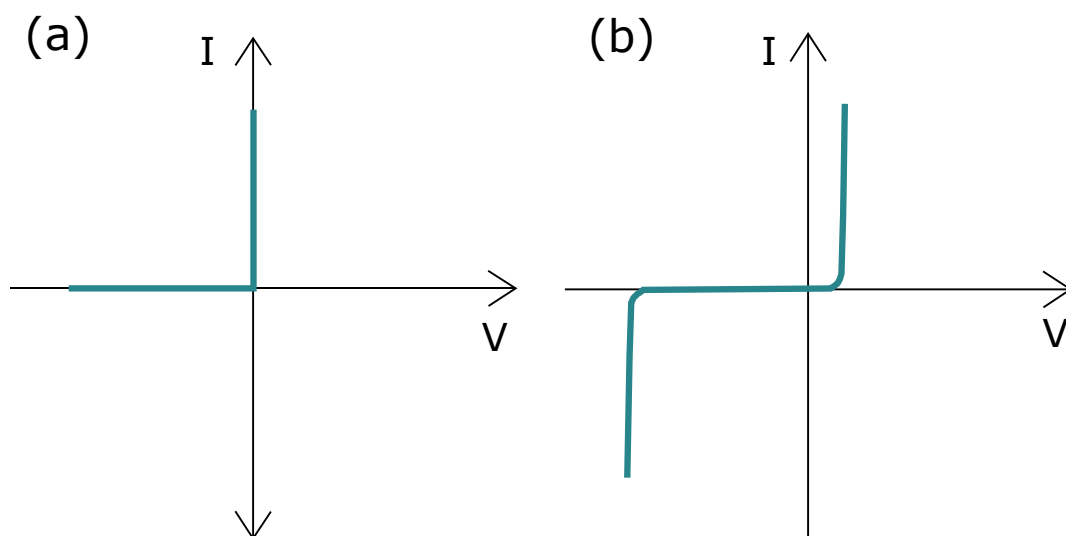


Figure 3. 5: I-V characteristic of the p-n diode. (a) Shows the ideal I-V characteristics. (b) I-V characteristics of the real p-n junction diode.

3.1.4 Depletion region breakdown

Depletion region breakdown occurs when a depletion region at the p-n junction is destroyed, and a large reverse current starts flowing. The breakdown voltage is defined as the voltage or point at which a junction breaks down, which depends on the width of the depletion region. In other words, p-n junction diodes with wide depletion regions have high breakdown voltages, and p-n junction diodes with narrow depletion regions have low breakdown voltages. Depletion regions or junctions can break down in two different ways: Avalanche breakdown (because of the collision of free electrons with atoms) and Zener breakdown (because of the high electric field generated) [347].

For device architecture, working, and I-V characteristics of p-n diodes, the following books can be referred to [348], [349]. The next section describes the classification of transistors, in particular, the design, working, and characteristics of field-effect transistors (FETs).

3.2 Field-Effect Transistors

A transistor is an electronic device that controls electrons' movement (or, more generally, controls charge carriers) and amplifies or switches the flow of current or electrical signals and power. John Bardeen, William Shockley, and Walter Brattain are credited with the invention of the transistor, which was first successfully demonstrated at Bell Laboratories in New Jersey on December 23, 1947 [350], [351]. Compared with vacuum tubes, which were used to amplify electronic signals before, transistors consume less power, are less expensive, smaller, lighter, more efficient, require less voltage to operate, produce less heat and have a higher physical resilience than vacuum tubes.

3.2.1 Classification of transistors

According to the type of charge transport carrier, transistors can be classified as unipolar, bipolar, or ambipolar. FETs, or unipolar transistors, use either electrons (in an n-channel FET) or holes (in a p-channel FET) to conduct electric current, whereas bipolar junction transistors (BJTs) use both electrons and holes. Compared to BJTs, FETs have much higher current gains. FETs are voltage-controlled devices, while BJTs are current-controlled devices. In general, FETs are divided into two categories: (I) Junction-gate devices and (II) insulated-gate devices (IGFETs), in which metal oxide semiconductor FETs (MOSFETs) are the most commonly used for logic circuits.

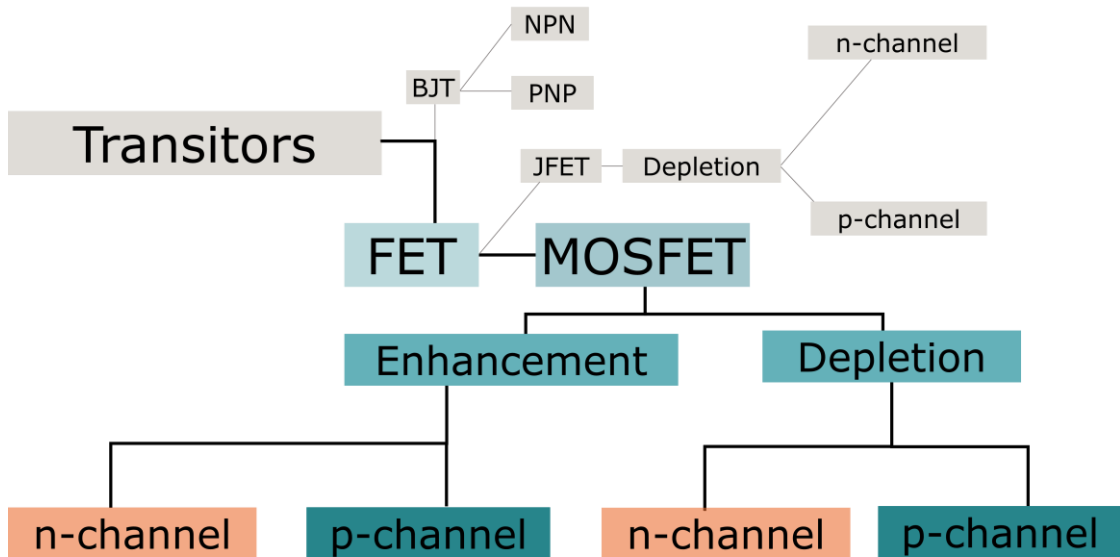


Figure 3. 6: Classification of transistors.

Devices with insulated gates or MOSFETs can be further subdivided based on their channel configuration: n-type or p-type channel. Whether the transistor is ON or OFF state at zero gate voltage depends on the channel type, with n-channel and p-channel MOSFETs operating in enhancement and depletion modes, respectively. Depletion-mode MOSFETs (discussed intensively in the next section) are in OFF-state with zero gate voltage, while enhancement-mode MOSFETs are in ON-state with zero gate voltage. Figure 3. 6 summarizes all types and working modes of transistors. A representative transfer characteristic curve for p-type, n-type, and ambipolar transistors is shown in Figure 3. 7.

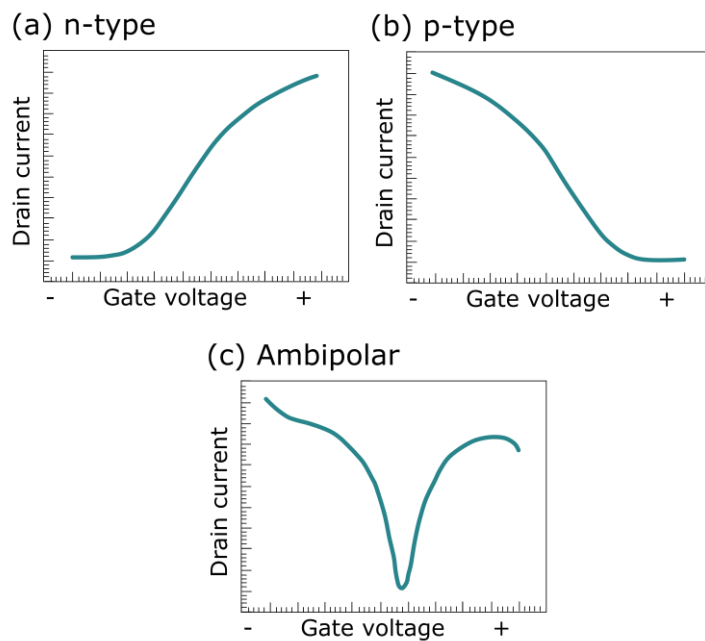


Figure 3. 7: Typical transfer characteristics of (a) n-type, (b) p-type, and (c) ambipolar transistor.

3.2.2 Device structure of printed FETs

Printed FETs are similar to conventional transistors, which consist of a source electrode, a drain electrode, a gate electrode, as well as an active semiconductor channel layer, and a dielectric layer. There are three types of terminals in the channel: source (S), drain (D), and gate (G).

Carriers enter through the source and exit at the drain; the gate is where conductivity in the channel is modulated. Gate electrodes can be either metal or a conducting polymer, whereas source/drain electrodes are mostly metal contacts. The semiconductor channel is connected to the source and drain terminals through ohmic contacts.

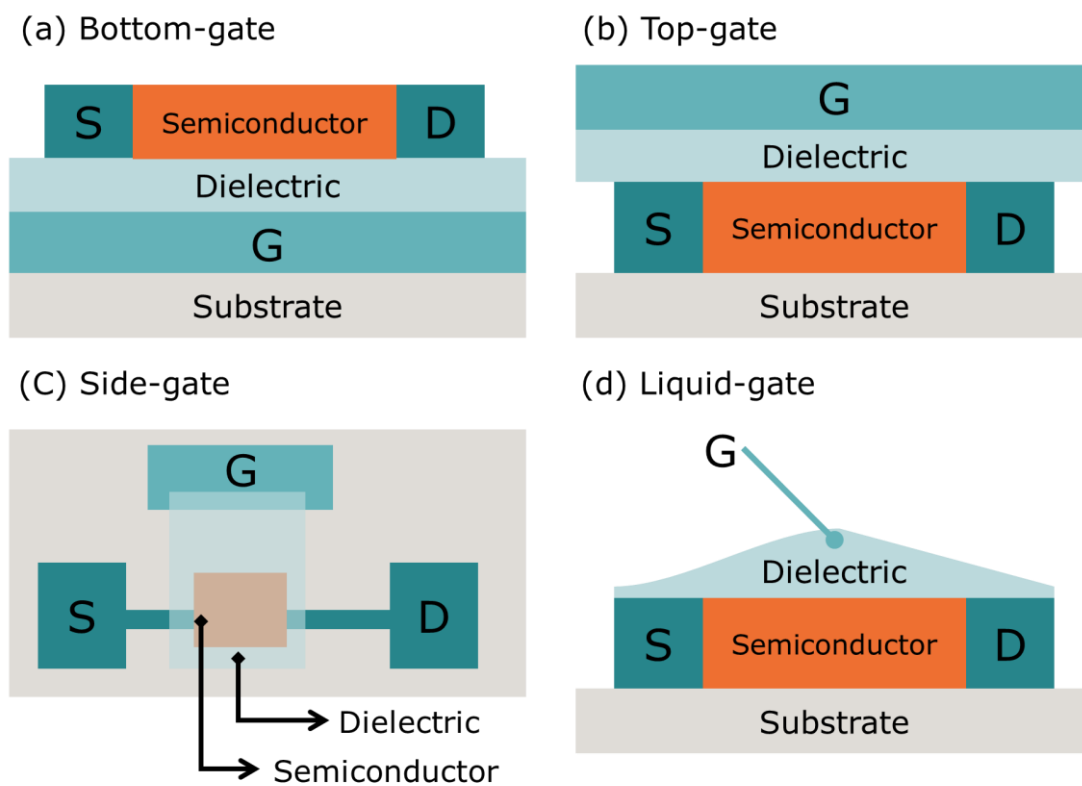


Figure 3. 8: Basic layer structures of printed FET: (a) bottom-gate; (b) top-gate; (c) side-gate; (d) liquid-gate.

The name of each terminal corresponds to its function. In this context, the gate terminal is similar to a physical gate that opens and controls some flow, allowing electrons to pass through or blocking them out by creating or eliminating a conductive channel between the source and drain. As an important part of FET, the active channel semiconductor transports charge carriers (electrons or holes) from the source to the drain, and this process can be controlled by applying a voltage to the

gate. As shown in Figure 3. 8, four different types of transistor structures can be distinguished based on the location of the gate electrode.

It is also possible to divide FETs into organic and inorganic types or p-channel and n-channel types, depending on the semiconductor materials used. As discussed in chapter 2, the advantages of inorganic FETs compared to OFETs are high field-effect mobilities of more than $100 \text{ cm}^2 \cdot \text{V} \cdot \text{s}^{-1}$ [117], and high environmental stability such as thermal and long-term stability in air.

It is possible to deposit the layers of printed FETs with solution processes (spin coatings, drop castings, etc.) or with vacuum processes (thermal evaporation). Source/drain electrodes must be in contact with the semiconductor layer, and the dielectric layer (also called gate dielectric) must be in contact with the gate electrode.

3.2.3 Electrolyte-gated FETs

One of the major challenges with printed FETs is lowering their operating voltage. When efforts to decrease the voltage by printing traditional insulating materials inks such as silicon dioxide, polymeric insulators, and even high- κ dielectrics yielded limited success, electrolytic gating emerged as a useful alternative. An electrolyte-gated FET operates in a capacitive mode, taking advantage of the high capacitance of the electrical double layer at the electrolyte–semiconductor interface. The electrolyte layer (a solid or liquid layer) is situated between the semiconductor and the gate, which modulates the conductivity in the semiconducting channel.

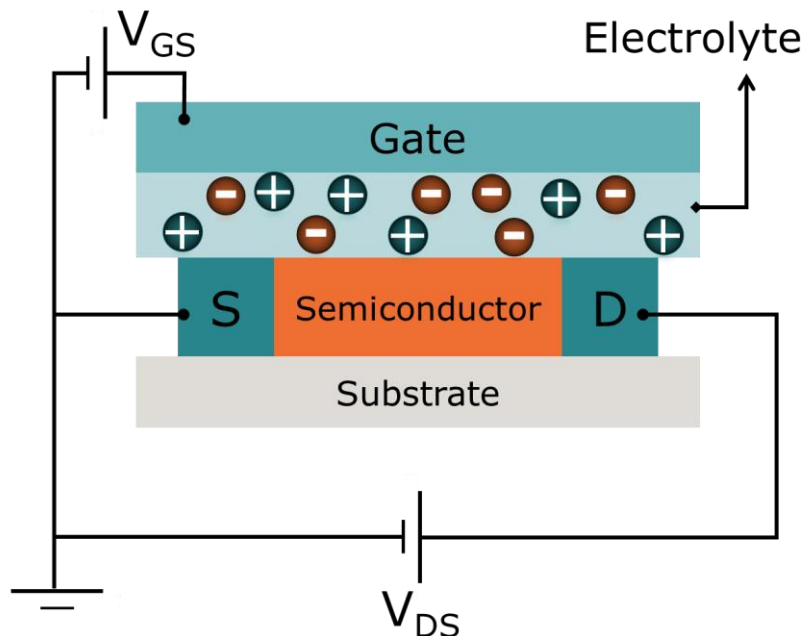


Figure 3. 9: An electrolyte-gated organic field-effect transistor.

There is a principal reason for using electrolyte gating in printed FETs since they have a large capacitance (C) in comparison to dielectrics with high- k values, and it improves the field-effect mobility and the drain current ($I_{DS} \propto C_i$, explained in the next section) due to the improved surface interface between the gate-dielectric material and the semiconductor, which offers high transconductance; as a result, same amplification can be achieved at comparatively smaller voltage, and also offers better switching. Besides offering low source and drain contact resistances, electrolyte gating also offers the high potential to enable new device architectures because electrolytes are easily solution processable and printable. Besides that, a disadvantage of electrolyte-gated FETs (EGFETs, sometimes also referred to as EGTs) is that they can also have high parasitic capacitances (also called overlap capacitances) as well as high leak currents between the gate and source, which reduces the switching speeds and increases power consumption [142], [352].

As shown in Figure 3. 9, in the EGFET, the gate dielectric is an electrolyte material (materials are further discussed in chapter 2), either liquid, solid, or semi-solid, e.g., a salt suspended in a polymeric matrix, an ionic liquid, or ionic gel [353]. The gate electrode is immersed in this electrolytic solution, the source and drain electrodes are in contact with the semiconductor, and the channel in the semiconductor forms between the two contacts [142].

As shown in Figure 3. 10, electrolyte-gated FETs (EGFETs) can be printed with top-gate geometry or in-plane (displaced-gate) geometry. In-plane gate architecture refers to a gate that is printed in the same plane as the channel, and the channel is modulated by an electric field laterally. Only electrolyte gating allows such displaced-gate geometry since the gate does not need not be vertically aligned with the channel. However, in-plane geometry also has a significant disadvantage during

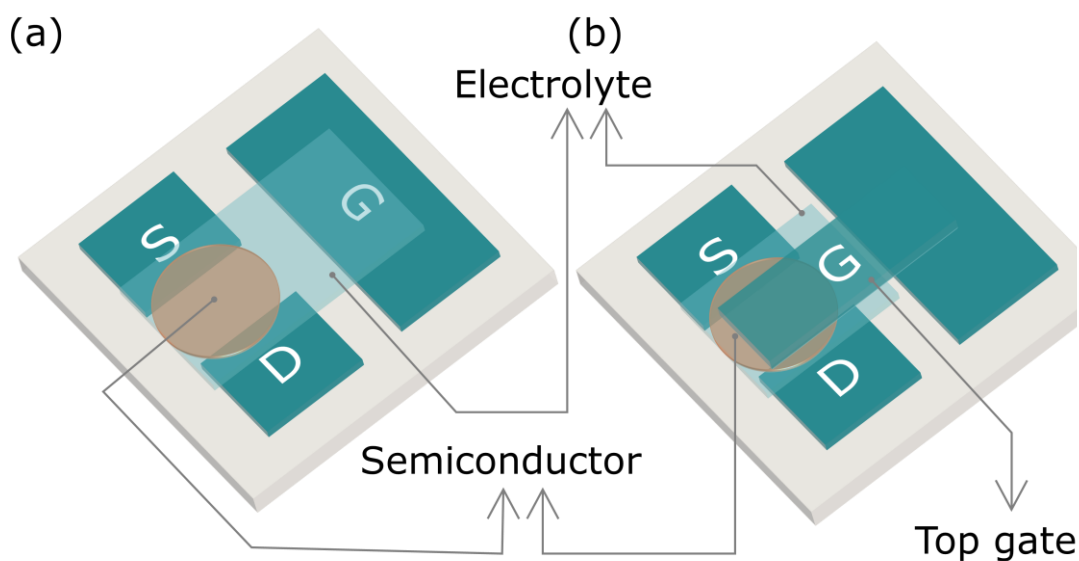


Figure 3. 10: Schematics of EGFETs (a) in-plane gate (also called displaced-gate) and (b) top gate configuration.

operation, as it will require long migration distances for ions to accumulate at the electrolyte–channel interface upon application of a gate voltage [142].

On the other hand, in top gate geometry, the gate is directly printed on top of the dielectric layer, which can be an electrolyte. Here, the top-gate structure eliminates the need for ions to migrate. EGFETs may also be faster and more efficient with this geometry because it improves the electrostatic coupling between the gate electrode and the channel.

3.2.4 Transistor operation and characteristics

A standard MOSFET model can describe the operation mode of both normal printed FETs and EGFETs. A schematic illustration of an enhancement-mode FET with an n-type channel can be seen in Figure 3. 11, where S, D, and G again represent the source, drain, and gate electrodes, respectively. Source and drain regions are formed with n-doping (N^+). In order to isolate the doping channel from the gate electrode, a thin layer of silicon dioxide is deposited on top of the channel.

During the operation of a FET, two potentials are applied at the gate electrode and the drain electrode, while the source electrode is grounded.

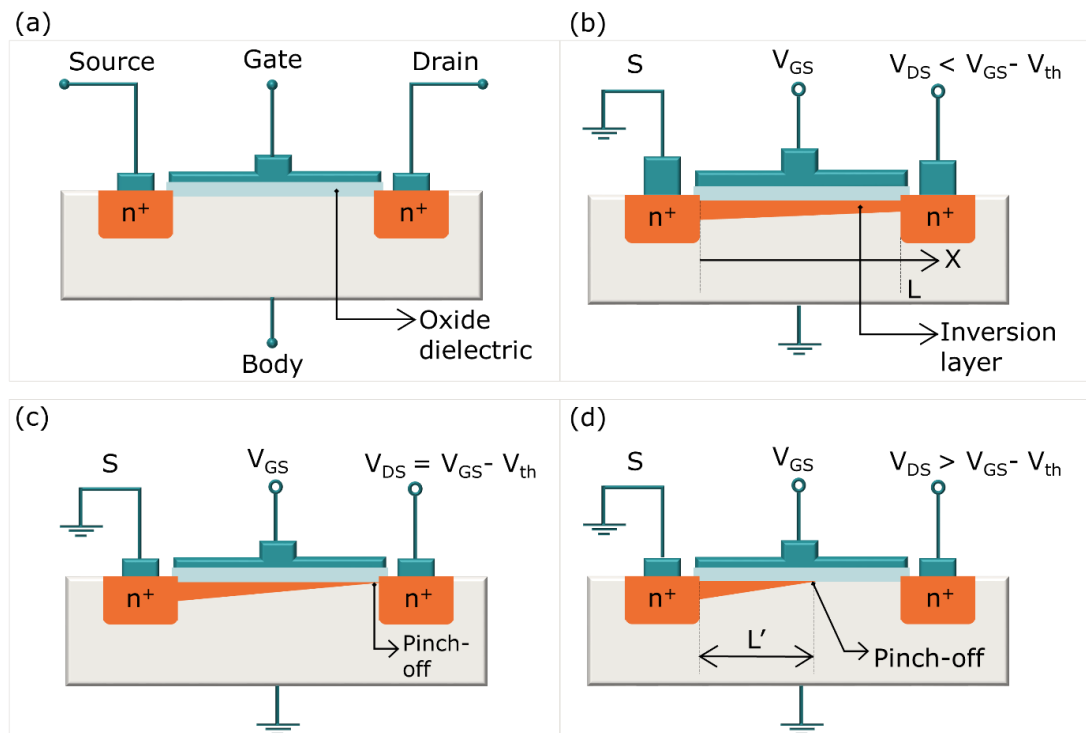


Figure 3. 11: Schematic diagram of the working principle of an n-type MOSFET in different bias conditions. (a) Cross-section view (without gate voltage). MOSFET is driven by gate voltage: (b) Triode region, (c) Channel pinch-off region, and (d) Saturation region.

When no voltage is applied to the gate of an n-channel enhancement mode transistor, no conductive channel exists, and a positive gate-to-source voltage bias will be needed to create a conductive channel. So, when a positive gate-source voltage (V_{GS}) is applied, an electron inversion layer is formed at the insulating oxide-semiconductor interface. At this point, it can be explained as two capacitors working in series: the gate oxide capacitor and the depletion-region capacitor. As the gate voltage increases, electrons are attracted by the positive voltage and accumulate near the gate to counteract the doping ions. A depletion region is formed when the gate voltage reaches a certain value; this voltage is known as the **threshold voltage**.

The greater the gate-source voltage, the more electrons are attracted to the gate, establishing a conductive channel between the source and the drain; this phenomenon is known as inversion. A threshold voltage (V_{th}) is required to form an inversion layer at the interface. At a lower gate-source voltage, even though the source and drain electrodes are connected by a voltage, no current flows from the source to the drain. Only upon exceeding the threshold voltage the gate voltage will cause an inversion layer to form beneath the dielectric layer, thus creating a conduction channel for electrons. In this case, electrons will flow from the source electrode to the drain electrode due to the voltage applied to the source/drain electrode. The gate voltage affects the channel thickness, which in turn determines the source/drain current. When the gate voltage is increased, the current increases. This phenomenon (source/drain current is amplified from the signal voltage input to the gate electrode) is called amplification, where even relatively small gate voltage changes can control comparably large currents between source/drain.

In some applications, such as FET amplifiers, an external resistor R_L (load) is connected, which causes voltage amplification, and transistors are often used as amplifiers. When the external load is a small resistor, transistor circuits can be used as current amplifiers, whereas when the external load is a large resistor, voltage amplification can be achieved.

Parameters

Charge carrier mobility

There are two charge carriers in a semiconductor: negatively charged electrons and positively charged holes, these are the majority carriers in n-type and p-type semiconductors, respectively, and their opposites are called minority carriers.

These carriers move as a result of two factors: the electric field and the concentration gradient. Electric-field-induced carrier movements are called drift, while concentration gradient-induced movements are called diffusion. Applied electric fields cause carriers to drift in semiconductor materials. The charge carrier mobility is usually represented as μ_p (hole mobility) and μ_n (electron mobility), and the unit is $\text{cm}^2 \cdot \text{V} \cdot \text{s}^{-1}$ (SI unit: $\text{m}^2 \cdot \text{V} \cdot \text{s}^{-1}$). It is crucial to consider these parameters when selecting

semiconductor materials for printed FETs. As mobility defines the ability of the carrier (electron or hole) to move into the channel, higher mobilities also provide high speed of carriers with minimal scattering (reducing the heat dissipation), and more currents flow if we have higher mobility, in the end, it provides high operating speeds.

Output characteristics

Primarily, MOSFET I-V characteristics are described by (I) output characteristics and (II) transfer characteristics. Each curve in Figure 3. 12a shows the drain-source current I_{DS} with respect to the drain-source voltage V_{DS} (each curve is measured at a fixed gate-source voltage V_{GS}); this type of measurement is known as an output curve. In a transfer curve (Figure 3. 12b), the drain-source current I_{DS} is plotted with respect to gate-source voltage V_{GS} for a fixed V_{DS} . Like standard FETs, the printed FETs also are described according to their operation in the cut-off, the linear or the saturation regions of their output curve.

When $V_{DS} < |V_{GS} - V_{th}|$, as shown in Figure 3. 12c, it is in the linear regime; here, the drain current increases linearly with the drain-source voltage. Under this regime, the device acts as a voltage-controlled variable resistor. When V_{GS} approaches V_{DS} , the shape of the conduction channel changes because of the two interacting potentials, and this transition depends on threshold voltage magnitude. This critical point is shown in Figure 3. 12d, where $V_{DS} = |V_{GS} - V_{th}|$, resulting in a depletion of free carriers near the drain electrode, resulting in a pinch-off of the channel. As V_{DS} increases, competing effects force charges from source to drain, and a growing depletion zone near the drain leads to I_D saturation, as shown in Figure 3. 12e. Reaching this saturation, the current cannot grow any further.

Drain current (I_{DS})

The drain-source current I_{DS} can be gives as [354]:

$$I_{DS} = \mu_{FET} C_{OX} \frac{W}{L} \left[(V_{GS} - V_{th}) V_{DS} - \frac{1}{2} V_{DS}^2 \right] \quad (3.2)$$

This equation, 3.2, holds true for a small $V_{DS} \leq V_{GS} - V_{th}$ (also called triode region). If in equation 3.2, $V_{DS} \ll (V_{GS} - V_{th})$, mathematically, it can be seen that $\frac{1}{2} V_{DS}^2$ is negligible, so we have I_{DS} for the linear region as:

$$I_{DS} = \mu_{FET} C_{OX} \frac{W}{L} (V_{GS} - V_{th}) V_{DS} \quad (3.3)$$

So for small V_{DS} , the drain current is a linear function of V_{DS} .

And the peak current can be given by:

$$I_{DS} = \frac{1}{2} \mu_{FET} C_{OX} \frac{W}{L} (V_{GS} - V_{TH})^2 \quad (3.4)$$

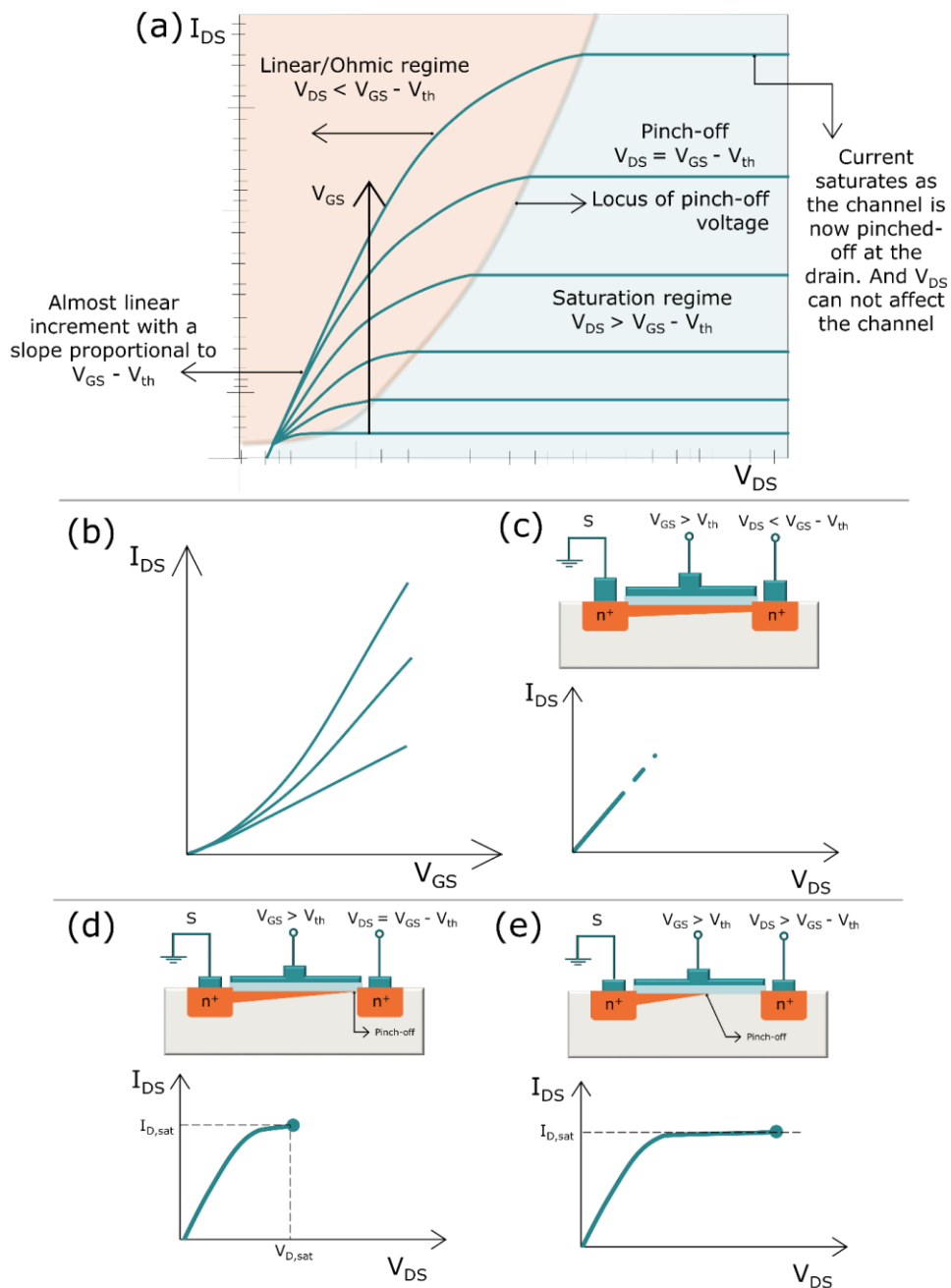


Figure 3. 12: Typical I-V characteristics of the n-type MOSFET. (a) Output curve. (b) Transfer curve. (c) triode, (d) pinch-off, (e) saturation regions of output characteristics curve.

The length of the channel gradually decreases as the potential difference between the gate and the drain decreases. In other words, in (3.2), L is, in fact, a function of V_{DS} . This effect is called "channel-length modulation" [354].

$$\Delta L = L - L'$$

assuming a first-order relationship as $\frac{\Delta L}{L} = \lambda \cdot V_{DS}$ (from [354]), the current I_{DS} in equations 3.2 and 3.4 can be represented as:

$$I_{DS} = \mu_{FET} C_{OX} \frac{W}{L} \left[(V_{GS} - V_{th}) V_{DS} - \frac{1}{2} V_{DS}^2 \right] \cdot (1 + \lambda V_{DS}) \quad (3.5)$$

And

$$I_{DS} = \frac{1}{2} \mu_{FET} C_{OX} \frac{W}{L} (V_{GS} - V_{TH})^2 \cdot (1 + \lambda V_{DS}) \quad (3.6)$$

In a p-channel MOSFET, applied voltage polarities and current directions will be reversed. For PMOS devices, equations 3.2 and 3.4 can be written with a negative sign.

If one knows the drain current, gate voltage, threshold voltage, channel width, channel length, and device capacitance of printed FETs, one can calculate the effective mobility from equations 3.2 and 3.4.

When a printed FET is operating in the saturation region, parasitic capacitance may appear, overestimating mobility. There is a difference in the mobility of a printed FET in a linear and saturation region, and effective mobility in saturation region is generally higher [109]. For this reason, in printed FETs, equation (3.3) is usually used in order to avoid overestimating mobility.

And field-effect mobility for the linear region is:

$$\mu_{FET} = \left(\frac{dI_{DS}}{dV_{GS}} \right) \frac{L}{WC_{OX}V_{DS}} \quad (3.7)$$

Which gives effective mobility according to the slope of the transfer curve $\left(\frac{dI_{DS}}{dV_{GS}} \right)$.

When the semiconductor layer is printed with solution-processed inks, the transfer curve may not reflect the true characteristics of the semiconductor layer inside the channel because the semiconductor layer is not confined inside the channel. In addition to movement inside the channel, carriers can move outside of it as well. To avoid these overestimations, the semiconductor material must be printed so that it is confined in the channel.

Threshold voltage (V_{th})

V_{th} stands for threshold voltage, or the voltage at which the conducting channel of the FET just begins to connect the transistor's source and drain. In other words, it is a voltage required to switch the device ON and function in linear and saturation regimes. V_{th} can be derived from the linear region of the I_{DS} vs. V_{GS} curve at small drain voltages ($V_{DS} \ll V_{GS} - V_{th}$), which is the voltage when extrapolating the curve to $I_{DS} = 0$. Alternatively, as shown in Figure 3. 13, the threshold voltage can be extracted from the graph $\sqrt{I_{DS}}$ vs. V_{GS} .

In semiconductor physics, the V_{th} of an NFET is usually defined as:

$$V_{th} = \frac{\sqrt{4q\epsilon_{Si}N_{Sub}\Phi_F}}{C_{OX}} + V_{FB} + 2\Phi_F \quad (3.8)$$

$$\text{Here } \Phi_F = \frac{kT}{q} \ln \left(\frac{N_{\text{Sub}}}{N_i} \right) \quad (3.9)$$

where

q : is the electron charge,

ϵ_{Si} : the dielectric constant of silicon,

k : Boltzmann's constant,

T : operating temperature (in K),

N_{Sub} : doping density of the substrate,

N_i : density of electrons in undoped silicon,

C_{OX} : gate-oxide capacitance per unit area, and

V_{FB} : Flat band voltage, which equals to the difference between the work functions of metal and semiconductor. ($V_{\text{FB}} = \Phi_{\text{MS}} = \Phi_{\text{M}} - \Phi_{\text{S}}$).

Also $\sqrt{4q\epsilon_{\text{Si}}N_{\text{Sub}}\Phi_F}$ is the charge in the depletion region, sometimes also represented as Q_{dep} . We can also observe that the work function difference at every interface (Φ_{MS}) plays a crucial role in increasing the threshold voltage.

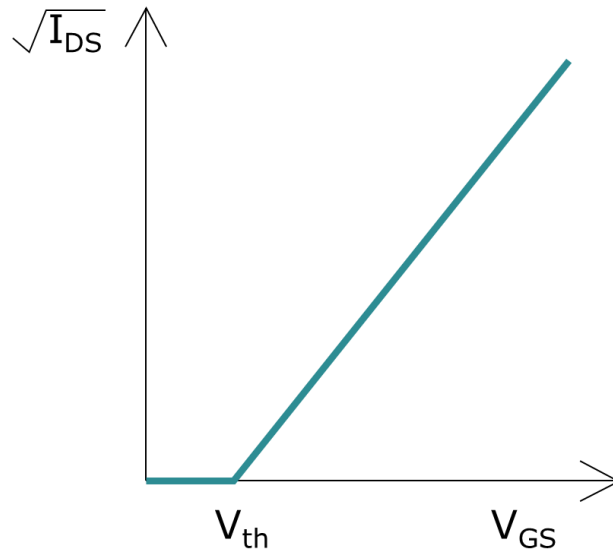


Figure 3. 13: The $\sqrt{I_{\text{DS}}}$ vs. V_{GS} curve for threshold voltage (V_{th}) value extraction.

It is also possible to reduce the V_{th} by using a high capacitance gate dielectric (see equation 3.8). In addition, electron or hole doping can be used to tune V_{th} , as well as alter the ratio between channel width and channel length. Because of the trapped charge in the thin semiconducting film, the threshold voltage of solution-processed printed FET is normally high. Adsorption or immobilization of chemicals or biological molecules on semiconducting materials will also change the threshold voltage of FETs, enabling printed FETs to be used as sensors [355]–[358].

Leakage current

The current flowing through the insulated path or the dielectric layer (the gate current) is the leakage current, usually a very small current. In other words, "leaks" between the drain and source (D/S) of a FET when the device is OFF (at $V_{GS} = 0$).

Subthreshold swing (SS)

Increasing the gate voltage increases the drain current exponentially in the subthreshold region; also, the logarithmic drain current (I_{DS}) and gate voltage exhibit a linear relation. The slope of this curve (as shown in Figure 3. 14) is known as the subthreshold slope. The OFF-to-ON inversion in FET is faster when the subthreshold slope is steeper. Generally, subthreshold swing (SS) represents the maximum subthreshold slope.

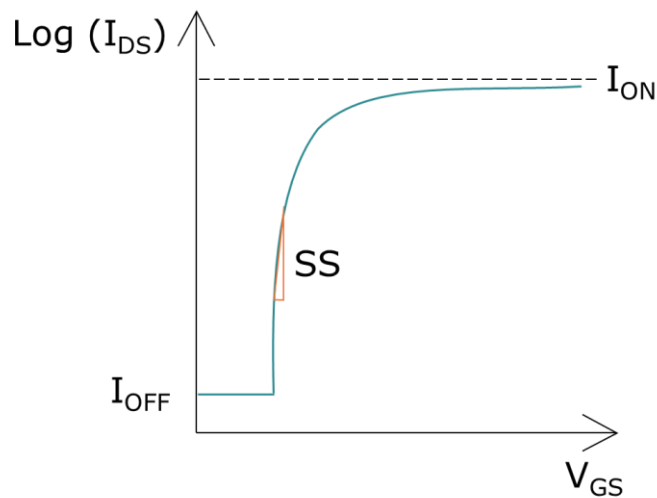


Figure 3. 14: Log I_{DS} vs. V_{GS} curve to estimate the SS, I_{ON} , and I_{OFF} .

ON/OFF current ratio (I_{ON}/I_{OFF})

This is defined as the ratio between drain currents in a saturation region (I_{ON}) and drain currents at zero gate voltages (I_{OFF}) with fixed source-drain voltages. At constant V_{DS} , I_{ON} is I_{DS} at the highest V_{GS} , and I_{OFF} is I_D at the lowest V_{GS} . In other words, the cut-off region can be considered as OFF (without any channel formation), and when a channel is formed between the source and drain (in the other two regions, linear and saturation), it can be called ON. Also, to understand with threshold voltage and gate voltage: I_{OFF} is when $V_{GS} < V_{th}$ and I_{ON} at $V_{GS} > V_{th}$.

As shown in Figure 3. 14, the graph I_{DS} (log scale) vs V_{GS} at the maximum V_{DS} gives the subthreshold slope, ON-current (I_{ON}) and OFF-current (I_{OFF}). The I_{OFF} is the minimum, and the I_{ON} is the maximum current value. In order to operate efficiently, transistors must have a high ON/OFF ratio and a low operating voltage.

Hysteresis

A typical hysteresis can be seen in transfer curves (also shown in Figure 3. 15) that do not exhibit the same characteristics as forward and backward switching of bias

voltage. Hysteresis behaviour increases with lower sweeping gate frequencies, indicating that slow-moving charge species cause hysteresis [109].

In printed transistors, hysteresis is mainly caused by absorbents like oxygen, water, and other impurities. Hence, impurities in the active layer and dielectric layer can be removed to eliminate or decrease hysteresis. Dielectric materials with high capacitance, such as ion gel and hybrid nanomaterials, can effectively eliminate or reduce hysteresis.

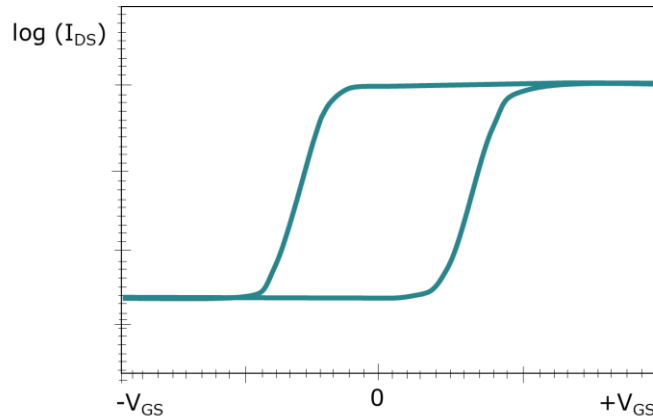


Figure 3. 15: Schematic transfer characteristics ($\log I_{DS}$ vs. V_{GS}) show hysteresis for n-type FET.

Transconductance (g_m)

For a MOSFET, transconductance g_m is defined as the ratio of change in drain current caused by a small gate voltage change with keeping the source-drain voltage (V_{DS}) constant; g_m is defined as:

$$g_m = \frac{\Delta I_{Output}}{\Delta V_{Input}} = \frac{\Delta I_{DS}}{\Delta V_{GS}} \quad (3.10)$$

Operating voltage

An operating voltage is a voltage necessary to make a printed FET switch ON from an OFF state. The operating voltage should be low to reduce power consumption. The operating voltage can be significantly reduced by using a gate dielectric with high capacitance.

Device capacitance

The following equation can calculate gate dielectric capacitance:

$$C_G = \frac{\epsilon_0 \epsilon_r}{d} \quad (3.11)$$

Dielectric materials with high-k values, such as aluminum oxide or hafnium oxide (also their composite materials) or thinner dielectric layers, can be used to increase the capacitance. It is also possible to achieve high capacitance with thick ion gel

dielectric layers (the high polarization is obtained due to the transference of ions in the dielectric layer as the voltage is applied). It also reduces the operating voltage significantly.

Stability

It represents FET sensitivity to oxygen, water, light, or other environmental and operational factors. Printed FETs with organic materials are not stable in their ambient state, whereas inorganic printed FETs based on metal oxides or all other components are more stable.

3.2.5 Effect of printed layers and their interface in FET

Other than the charge carrier mobility of the materials some other factors such as the interface between different layers play an important role in FET performance. It is necessary to consider/improve the following factors [359], [360]:

1. Thin dielectric layer: It provides high capacitance, which helps to achieve low power consumption.
2. Less defective sites: Defects such as dangling bonds and interstitial/substitutional defects must be avoided in films. These can impede effective polarization.
3. High film density: Its offers reduced/minimum leakage current.
4. Surface roughness at interfaces: Overall, surface roughness at the interface should be low (smooth layers). A roughness greater than the critical roughness threshold can result in a rapid drop in mobility.
5. Surface energy matching: It is also evident from equation 3.8 that work function differences at the metal and semiconductor interface play a crucial role in increasing threshold voltages. A good match between the surface energy of the semiconducting layer and the dielectric layer might encourage charge accumulation at the interface and minimizes charge trapping [361].

It is possible to achieve excellent printed FET performance as a result of these factors, which also are associated with charge carrier mobility. For device architecture, working, I-V characteristics field effect transistors following books can be referred to [348], [349], [354].

The next section describes the design, working, and characteristics of microheater structures.

3.3 Microheater

A microheater is a small, high-power heater with precision control that can generate heat by Joule heating, ultrasonic heating, or radiative heating.

3.3.1 Microheater structure and working

Joule heating is commonly used to generate heat in micro heaters, referred to as resistive micro heaters. Microheaters made from resistive filaments have a thickness from 100 nanometers up to more than 100 micrometers, which generate heat by joule heating. They generate heat by conducting electric current through these resistive filaments.

According to Joule's first law (also called just Joule's law), at voltage (V) applied, the power (P) of heating is equal to the product of resistance (R) and current (I) squared:

$$P = IV = I^2R = \frac{V^2}{R} \quad (3.12)$$

There are a variety of devices and industrial processes that use joule heating or resistive heating. Electricity is converted into heat by a heating element.

When microheaters are used in high-temperature applications, they must be supported or surrounded by materials that are highly thermally resistant, e.g., ceramics. Several applications of microheaters in microdevices exist, such as micro hotplates, gas sensors, biomedical testing devices, electron microscopes, anvil cells, and fiber heater enhancements. A microheater can also be used in micro propulsion systems for micro ignition, as well as explosion sensors for micro explosions. A wide range of 2D and 3D printing systems are also being used for the fabrication of microheater structures [362].

In order to integrate with ultrasensitive temperature-dependent devices and measurements, the heating area must have a uniform distribution of temperature and a short response time. Microheaters are ideal for applications where thermal response, heat confinement, power consumption, mechanical stability, and fabrication yield are also important considerations, and they will be discussed in later sections.

3.3.2 Material for microheater

As shown in Figure 3. 16, during the material selection process, it is necessary to take into account the operating temperature range for a specific application and select a heating element with good homogeneity on its active surface. Among the most common materials used for microheaters are Pt, Au, Ag, Ti, W, NiC, polysilicon, carbon nanotubes (CNT), Al, Cu, ITO, and Aluminum-doped Zinc Oxide (AZO). Additionally, liquid metal microheaters based on a eutectic alloy of gallium and indium (EGaIn) are available. In order to reduce the amount of undesirable heat in the contact pads, the heater resistor's electrical resistance should be higher than the contact pad's electrical resistance.

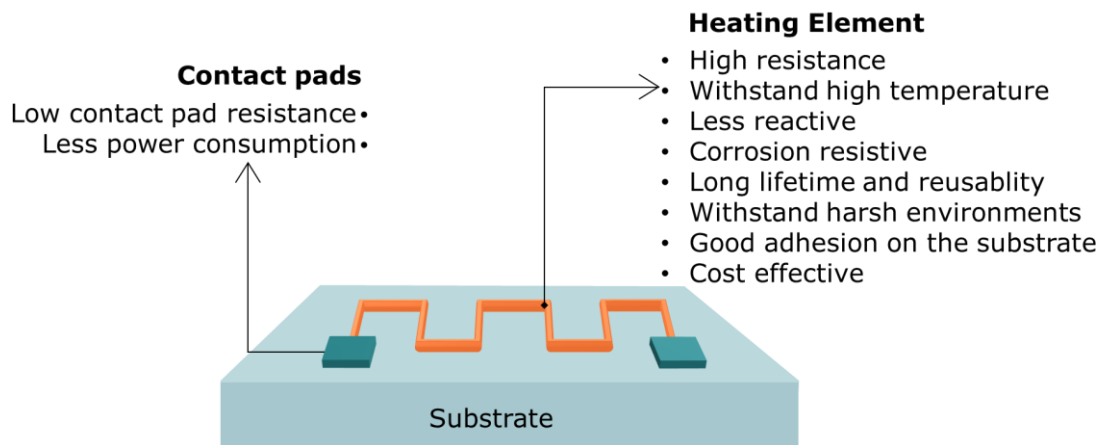


Figure 3. 16: A resistive microheater structure and material properties.

Substrate: The substrate is also selected according to the desired application and the analysis. The appropriate substrate material can be rigid, flexible, transparent, or non-transparent. These can be classified as flexible and rigid substrates.

- Rigid substrates such as borosilicate glass, soda lime glass, silicon wafers, sapphire, and quartz.
- Flexible substrates such as polymers: Kapton film, pyralux, Polyimide Film, PMMA, polydimethylsiloxane, polyethylene naphtalate, and polyethylene terephthalate.

3.3.3 Geometry of microheaters

The design/geometry, size (width, height, and length of heating elements), and their distribution is also very important to achieve the ideal characteristics of a microheater. As shown in Figure 3. 17, different designs and geometries of microheaters are available, ranging from simple line patterns to complex box, circular, and spherical patterns to provide uniform thermal distribution. The resistance of the heating elements is highly affected by the physical dimensions as the thinner heating elements offer high resistances, which as a result, can offer joule heating to achieve higher temperatures with less power consumption. The different design also helps to achieve uniform thermal distribution with the help of altering physical dimensions or changing the resistance of heating elements in the central region and outer region or vice versa. The resistance of the heating elements can also be varied; it also includes using a different material for designing the central part and outer edges. The design should also be simple to fabricate, and the pattern should have sufficient width and thickness to handle the heat generated.

The uniformity of temperature distribution in microheaters is also important while considering a design, as an example a study conducted by Joy et al. using simulations of five different patterns: single meander, double meander, fan shape, rectangle shape, and porous structure shows that, with a meander structure, the temperature

distribution is highly uniform at the same time, consuming a low amount of power [363].

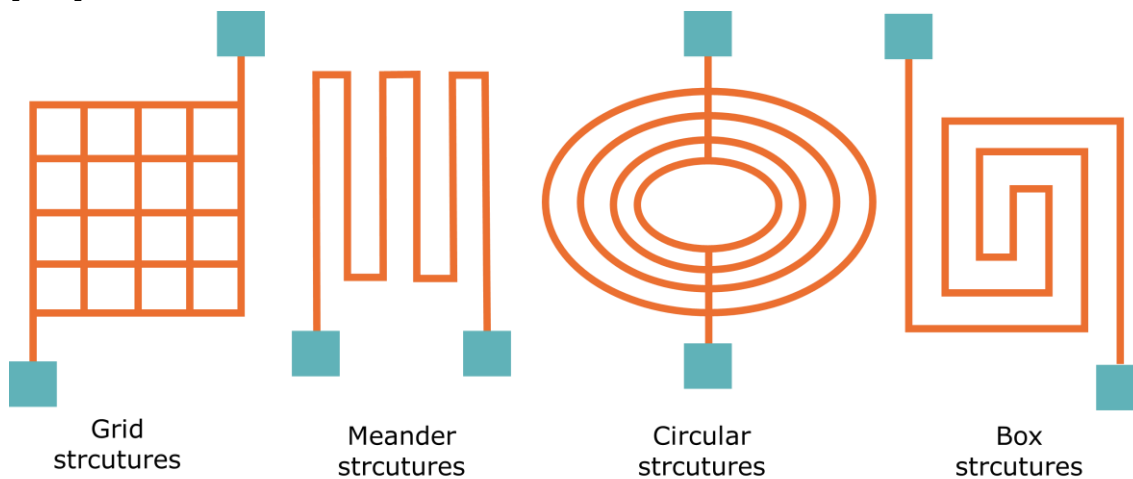


Figure 3. 17: Different microheater designs.

In addition to material properties and geometries, multiple physical principles influence the temperature of the microheater.

3.3.4 Characteristics of a microheater

In order to be an ideal microheater, it should have low power consumption, a quick thermal response, good heat confinement, good mechanical stability, and high fabrication yield. The physical, mechanical, and thermal characteristics of microheater can also be classified as following [362]:

- **Response time:** Structures should be characterized for response time, microheaters should have a short response time.
- **Mechanical stability:** The heating element, as well as the substrate, should be examined for thermal expansion and possible deformation with respect to temperature. The materials must withstand high temperatures according to the demand of the application.
- **Power consumption:** Overall, the power consumption of the microheater structures should be as low as possible. There are several factors that affect power consumption, such as the optimal design, thickness, substrate, and thermally conductive layer. Additionally, creating a cavity within an insulating substrate can be an effective method to reduce power consumption.
- **Uniform heating:** Managing the thermal distribution with variable resistance is crucial to the design. It is important that the heater produces uniform heating all over the area of activity and that there are no hotspots.

- **Lifetime and reusability:** To increase the device's long-term reliability and reusability, a protective layer of materials, like SiO₂, should be deposited above the heater in order to prevent oxidation of the heating element.

The following reviews describe detailed work, different microheater designs, materials, fabrication, and application [362].

3.4 Prior work/State of the art work on liquid metal printing and devices

As discussed in Chapters 1 and 2, the current metallic inks suffer from problems such as poor electrical conductivity performance, high processing temperatures, and high cost. As an alternative, low melting point metal alloys, also called liquid metals (LMs), have become a focus of attraction because they exhibit as high electrical and thermal conductivity as many conventional metals or alloys. Simultaneously LMs are ductile and fluid at or near room temperature (RT), being processable by printing. In contrast to the use of metal precursors, metal powders, or metal nanoparticles-based approaches, LMs do not require additional processing steps such as chemical reduction or sintering, which usually involve high temperature, intense light, or vacuum processing and can be detrimental to many substrates used in PE. With this comprehensive and diverse range of applications, the issues of direct writing, patterning, and processing of LMs have received considerable critical attention and are an area of highly active research.

There have a lot of reports about patterning the gallium based LM alloys as well as diverse applications using LMs as conductors for flexible capacitors, pressure and, proximity sensors [364]–[367], strain sensors [97], [290], [368], [369], temperature sensors [370]–[372], acceleration sensors [371] and other flexible sensors [373]–[375], flexible antennas [369], [375]–[378], self-healing interconnects wires and sensors [259], [379]–[381], stretchable wireless power transfer [382], stretchable electromagnetic actuators [383], [384], stretchable loudspeaker [385], stretchable interconnects, wires and electronic components [100], [386]–[391], devices to integrate chip light emitting diodes (LEDs) [101], [371], [392], [393], printed diodes and transistors [80], [394], [395], flexible display devices [396], [397], flexible solar cells [398], heat dissipation and liquid metal coolant [399], stretchable thermoelectric generators [400], e-skin [401], [402], wearable electronics and biological prosthetic devices [370], [372], [403]–[405], wireless monitoring [406], health monitoring [366], [389], eye movement tracking [407], neural microelectrode array [408], and implantable and epidermal electronics [408], [409]. Table 4. 1 summarizes a few of the reports according to the ink used, method of LM deposition, application reported, and year of publication of the report.

All of these reports are either partly printed or partly fabricated. LM direct printing capability was never examined for its potential application in LM-based, fully

3. Printed devices

functional, fully printed electronic devices that utilize the inherent desirable attributes of LMs.

Table 4. 1: Summary of a few scientific reports based on LM use for application. According to the ink used method of LM deposition, application reported, and year of publication of the report.

| LM ink type | Method | Application | Year | Reference |
|--------------------|--|---|-------------|------------------|
| Galinstan | Selective deposition LM over plated Cu | Stretchable conductors | 2021 | [388] |
| Ni-EGaIn | Stencil-based printing | Strain sensors and implantable electronics | 2021 | [368] |
| Galinstan | Flexography (stamp) printing | Interconnects for led illumination | 2019 | [393] |
| Fe-EGaIn | Magnetic field-based printing | Self-healing, stretchable interconnects circuit for led | 2019 | [259] |
| Ni-EGaIn | Magnetic field-based printing | Flexible antennas, strain sensors, led array circuit | 2019 | [369] |
| EGaIn | LM 3D direct writing | Interconnects for LED illumination | 2019 | [101] |
| EGaIn | Laser patterning (ablation) | Stretchable conductors | 2018 | [367] |
| Galinstan | Microfluidic channels injection for LM interconnects | Temperature sensors and wearable electronics | 2017 | [370] |
| Galinstan | Stencil-based printing | Capacitors and resistive strain sensors | 2017 | [290] |
| Galinstan | Microfluidic channels injection for LM interconnects formation | Heater and temperature sensor for wearable applications | 2016 | [372] |
| Galinstan | Inkjet printing with LM channel surrounded by HCl | Interconnects for LED illumination | 2016 | [289] |

3.4 Prior work/State of the art work on liquid metal printing and devices

| | | | | |
|----------------------|----------------------------------|---|------|-------|
| Ga 75.5 %, In 24.5 % | Desktop LM printer | Interconnects for LED illumination | 2015 | [392] |
| EGaIn | Imprinting and transfer-printing | Stretchable circuit wires or capacitor electrodes | 2014 | [391] |
| EGaIn | Direct writing | Strain gauge device | 2014 | [97] |
| Ga 75.5 %, In 24.5 % | Atomized spraying | Interconnects for LED illumination | 2014 | [410] |
| Galinstan | Microchannels injection | Capacitors and inductors | 2013 | [411] |
| EGaIn | Direct writing | Stretchable interconnects for led illumination | 2013 | [100] |

Part III. Results

4. Capillary printing of LM alloys

As previously discussed in Chapters 1 and 2, Liquid metals (LMs) are becoming a consistent element of printed electronics (PE) due to their favorable characteristics, such as their high electrical and thermal conductivity, on par with that found in conventional rigid metals and alloys. Liquid metals or LM are referred to Gallium based alloys throughout this thesis. The difference between liquid metals and solid metals is their inherent softness and ease of dispensing, deforming, and stretching. In spite of their soft, ductile, and fluidic properties, LMs have a significant drawback: their viscosity, surface tension, and density make them challenging to print with inkjet printing or any other standard direct writing methods achieving low-micrometer resolution.

The goal of this chapter is to depict the newly developed versatile LM printing setup, method of patterning and challenges that have arisen during printing liquid metals, and possible solution to address those challenges. Most of the work presented in this chapter is published in Hussain et al. [80]

4.1 LM printing setup

As shown schematically in Figure 4. 1, a unique printing setup was designed to pattern LMs. All of the LM direct writing experiments reported in chapters 6 and 7 were carried out using this printing setup.

A modified NLP 2000 nanolithography system (NanoInk, USA) was used to print Galinstan lines directly. Different parts of this system are shown in cutaway Figure 4. 2a. This custom-designed commercial nanolithography system provides a five-axis stage with automatic movement in the XY plane, a tilting axis in the XY plane, and automatic movement in the Z-axis. As part of this system, a glass capillary is mounted on a static holder, a syringe acts as the ink reservoir, and a pump push ink from the syringe to the substrate via glass capillary and LDPE (Low-density polyethylene) tubing. The custom glass capillary holder was designed and constructed in-house (Figure 4. 2). Figure 4. 1 shows the connection between the glass capillary and the syringe pump, which use LDPE tubing (from RCT Reichelt Chemietechnik GmbH Co) of 1 mm and 3 mm inner diameter (ID) and outer diameter (OD), respectively. As part of each experiment, the syringe was filled with Galinstan, which served as an ink reservoir, with LDPE tubing pushing ink to the glass capillary at a constant flow rate.

Depending on the size of the tip, the distance between the glass capillary tip and the substrate should vary between 0 (touching the surface) and 5 μm . When dispensing LM from the tip, the surface area of the LM increases, so the oxide layer must first be ruptured and then reformed after printing. Syringe pumps parameters should be optimized for each capillary to ensure proper extrusion of LM and avoid droplets

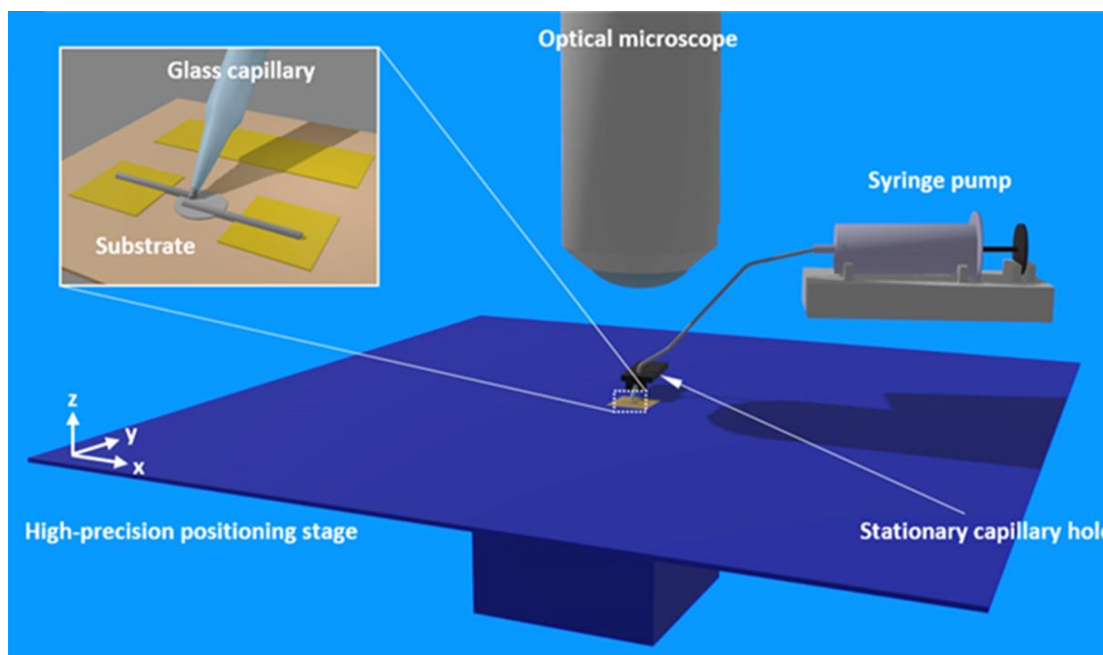


Figure 4. 1: Schematic depicting the printing setup, which consists of a high-precision positioning stage, an optical microscope for monitoring the process, and a stationary holder for a glass capillary, which is further attached to a syringe pump. As illustrated in the inset, the positioning stage can be moved appropriately in the x, y, and z directions in order to write an LM line onto the substrate. Reproduced from [80] with permission from Wiley.

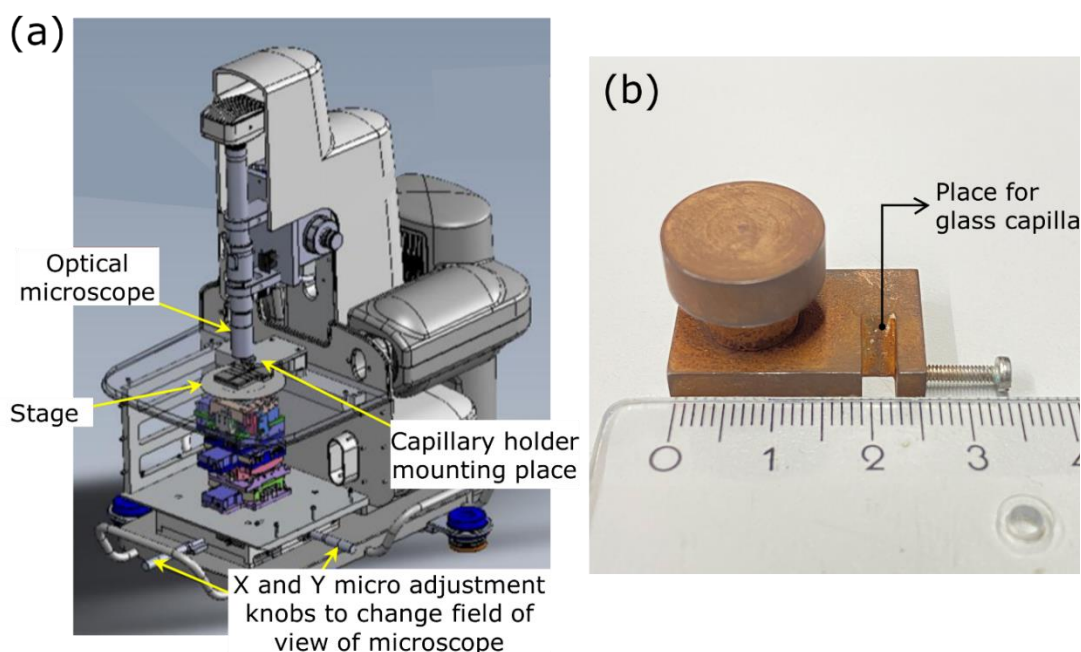


Figure 4. 2: Setup components (a) Cutaway figure showing different parts of the NLP-2000 system. (Adapted from NLP-2000 getting started guide received with the system) (b) Customized glass capillary static holder.

forming on the capillary tip. First, the Galinstan was brought to the glass capillary tip by varying the parameters between 5 and 100 $\mu\text{L}\cdot\text{min}^{-1}$. A low flow rate was maintained after initial conditioning, allowing the LM to stay at the capillary tip and patterns to be formed by bringing the tip in close contact with the substrate.

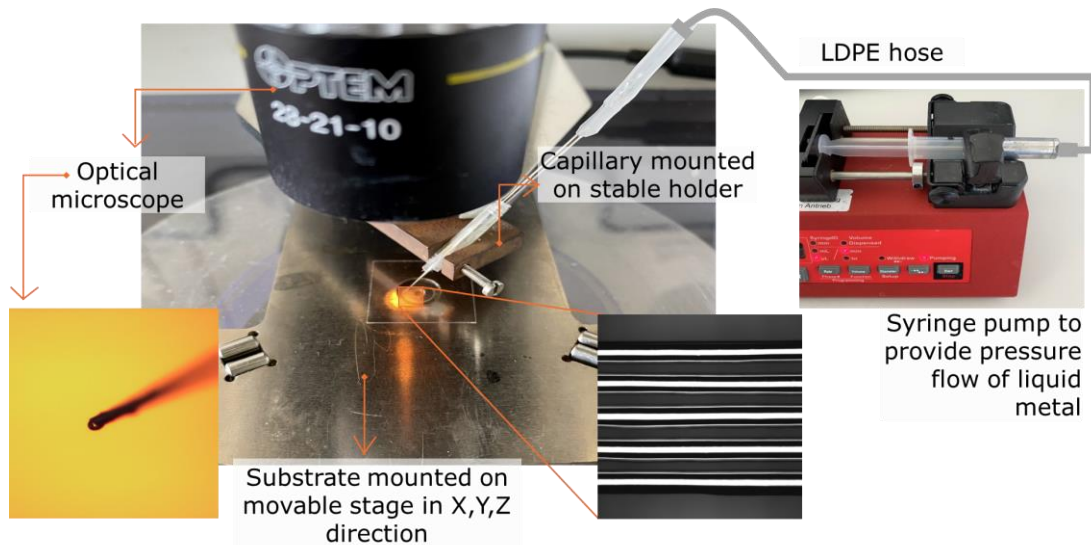


Figure 4. 3: Actual image of the printing process: glass capillary mounted in the fixed holder, positioned over a glass sample used as substrate. The glass capillary is connected to the pump via LDPE tubing. The microscope image on the left shows a glass capillary tip while printing. Adapted from [80] with permission from Wiley.

Throughout the experiments, the height between the tip of the glass capillary and the substrate was kept constant. To visually monitor tip interaction with the glass substrate, an optical microscope was used (Figure 4. 2a and and 4.4).

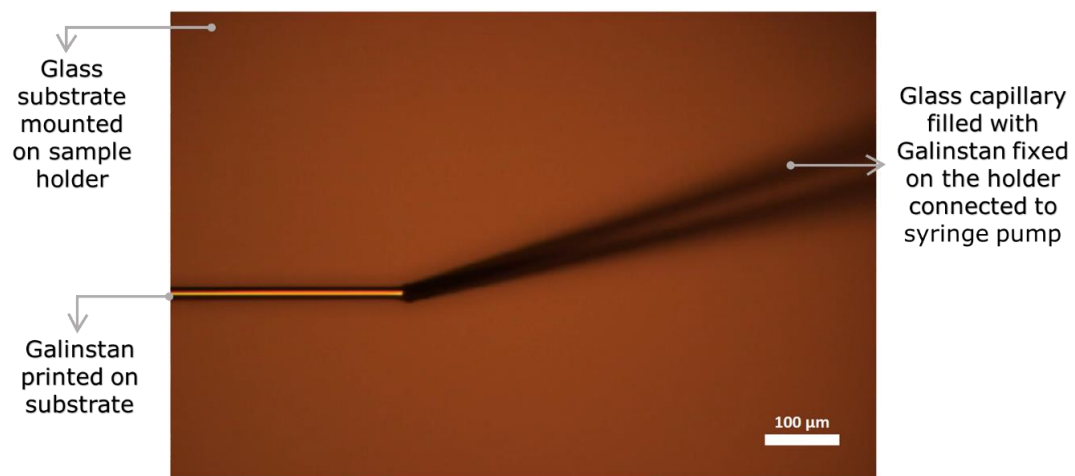


Figure 4. 4: View from the optical microscope while printing.

4. Capillary printing of LM alloys

After printing, the samples can be used straight away for the next process step because LM structures do not need sintering steps, which are typically required for particle/powder-based printed structures. These need high temperatures, heat, and/or chemical reactions to make them conductive. In contrast, LM structures are inherently conductors and can be used immediately after printing.

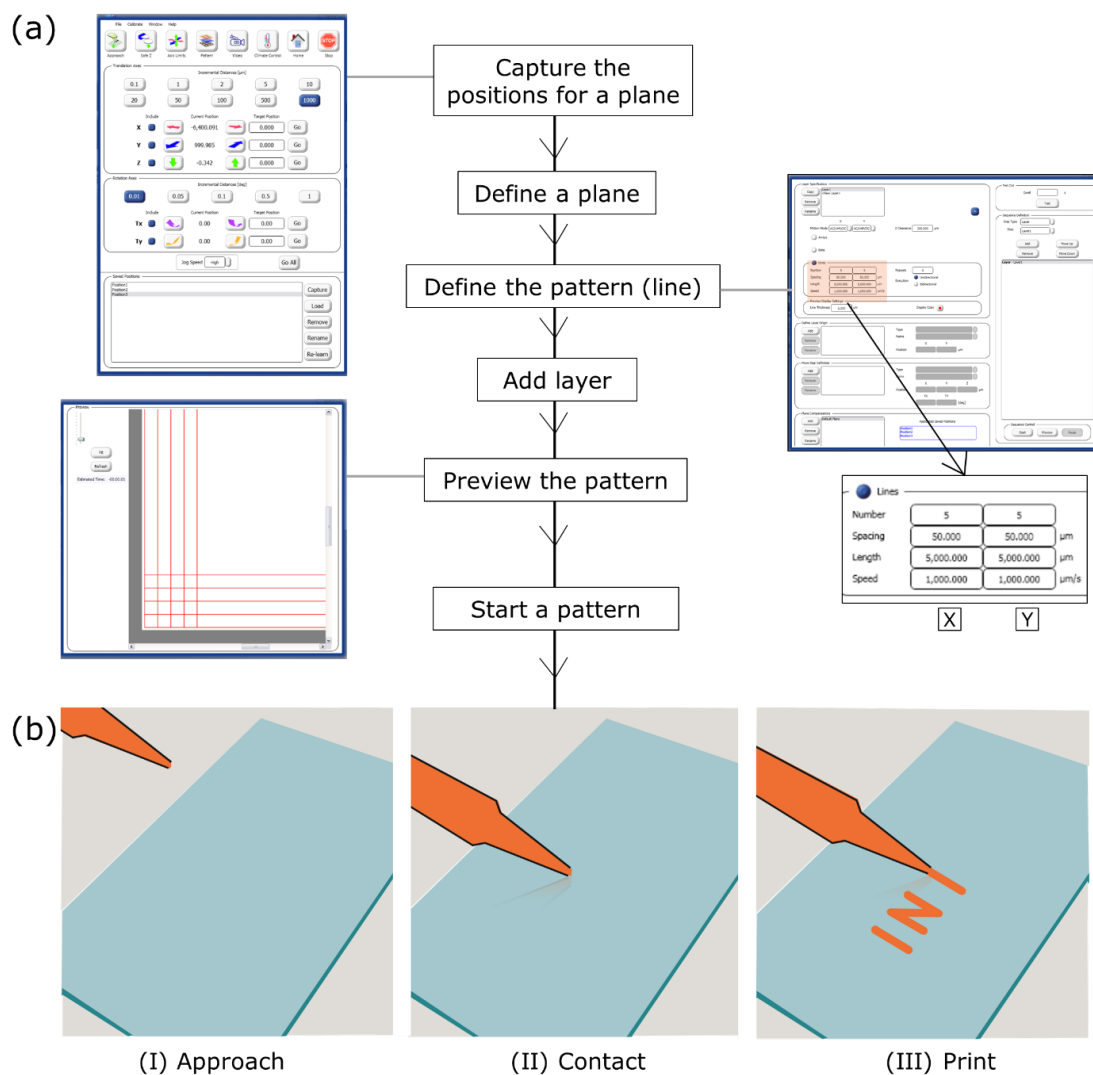


Figure 4. 5: Galinstan printing steps. (a) User interface and steps for the writing of LM with NLP 2000. (b) Steps after the "print" command is executed from the user interface. (I) Approach the starting point of the pattern. (II) Contact with the substrate. (III) Start the pre-programmed stage movements to form the desired pattern.

Galinstan printing steps

After mounting the glass capillary and placing the substrate, as shown in Figure 4. 6a, first, the positions are captured according to the touch of the tip, and the position is used to define a place for printing. After defining a plane, the pattern is designed in the NLP-200 CAD (Computer Aided Design) system with the number of lines, the

distance between the lines, the length of lines, and the speed of writing. Additional layers are added accordingly.

To start printing, as shown in Figure 4. 7b, the stage is first moved to the pattern's starting point. When the tip of the glass capillary reaches the starting position, it is brought in contact with the substrate or kept at a certain height from the substrate, depending on its size. After contacting the surface with the capillary, pre-programmed stage movements are initiated to form the desired pattern. Immediately following the completion of the desired pattern, the stage automatically moves down to a safe "Z clearance" position (usually given 200 μm throughout the experiment in the thesis). The glass capillary and pattern are successfully separated.

4.2 Printing of LM structures

The LM ink used throughout the experiments is Galinstan alloy, which is a commercially available alloy of Gallium, Indium, and Tin. At room temperature, Galinstan is ductile and fluid (since it melts between 10 and 19°C), so it can easily be dispensed, deformed, and stretched, which makes it printable. The last section explains the design in brief, and Figure 4. 1 shows a schematic illustration of a direct printing system using glass capillaries. Glass capillaries with long tapers around 9–15 mm and small tips around 1–3 μm (as shown in Figure 4. 6) were prepared with the use of a pipette puller at appropriate operating parameters. In order to obtain bigger tip openings (20–100 μm), the glass capillary was scored at a position that did match the desired width. The glass capillary was then moved above the score location and pushed with a smooth and continuous motion to break it.

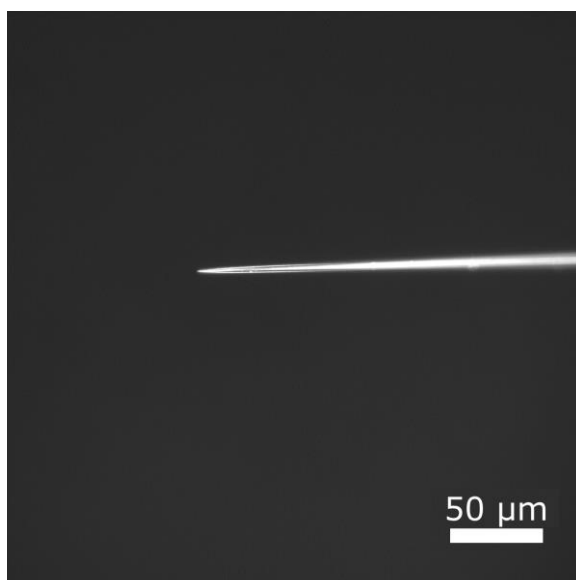


Figure 4. 8: Microscopy image of a freshly prepared glass capillary prior to opening up the tip aperture. Reproduced from [80] with permission from Wiley.

When the glass capillary has been mounted and filled with the Galinstan, its proximity to the target substrate is closely monitored to deposit the Galinstan on the target. The syringe pump controls the Galinstan flow rate so that there is always Galinstan at the tip sufficient to make a contact and keep the printing process active. The stationary glass capillary sits above the nanolithography stage. For printing the Galinstan lines, the glass substrate is moved in a pre-programmed movement at a controlled speed under the stationary capillary.

A variety of writing speeds were used to complete the patterns, from 200 to 1000 $\mu\text{m}\cdot\text{s}^{-1}$. All experiments were conducted with freshly cleaned glass substrates. Standard glass coverslips (size: 18mm X 18mm, from VWR Germany) were cleaned with chloroform, 2-propanol, and finally with deionized water, and later dried by blowing with nitrogen. In some cases, an ATTO B plasma cleaner (Diener electronic GmbH, Germany) was used for cleaning substrates for hydroxyl functionalization with O_2 flow at 10 sccm (Standard cubic centimeters per minute), 0.2 mbar, and 100 W power for 2 minutes. The interconnects were characterized by optical microscopy and AFM after printing.

4.3 Influence of writing parameters

Several factors affect the dimensions of written patterns, such as the inner diameter (ID) of the glass capillary, the opening size of the capillary tip, and the distance between the substrate and the glass capillary tip.

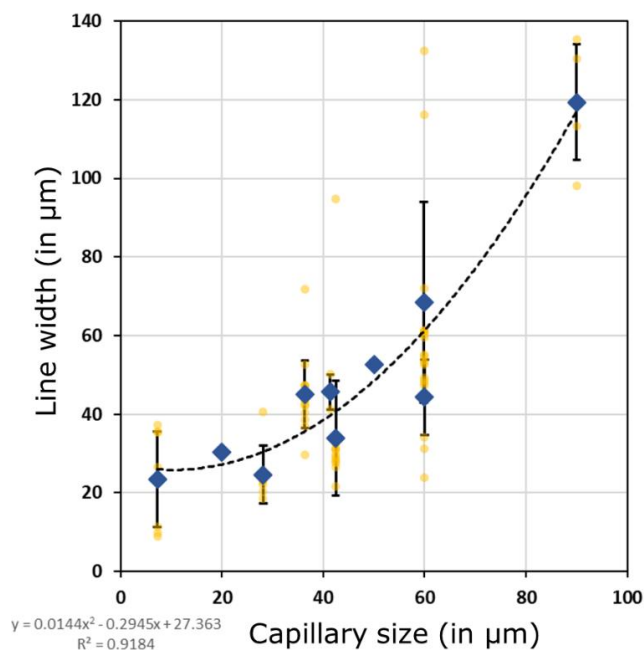


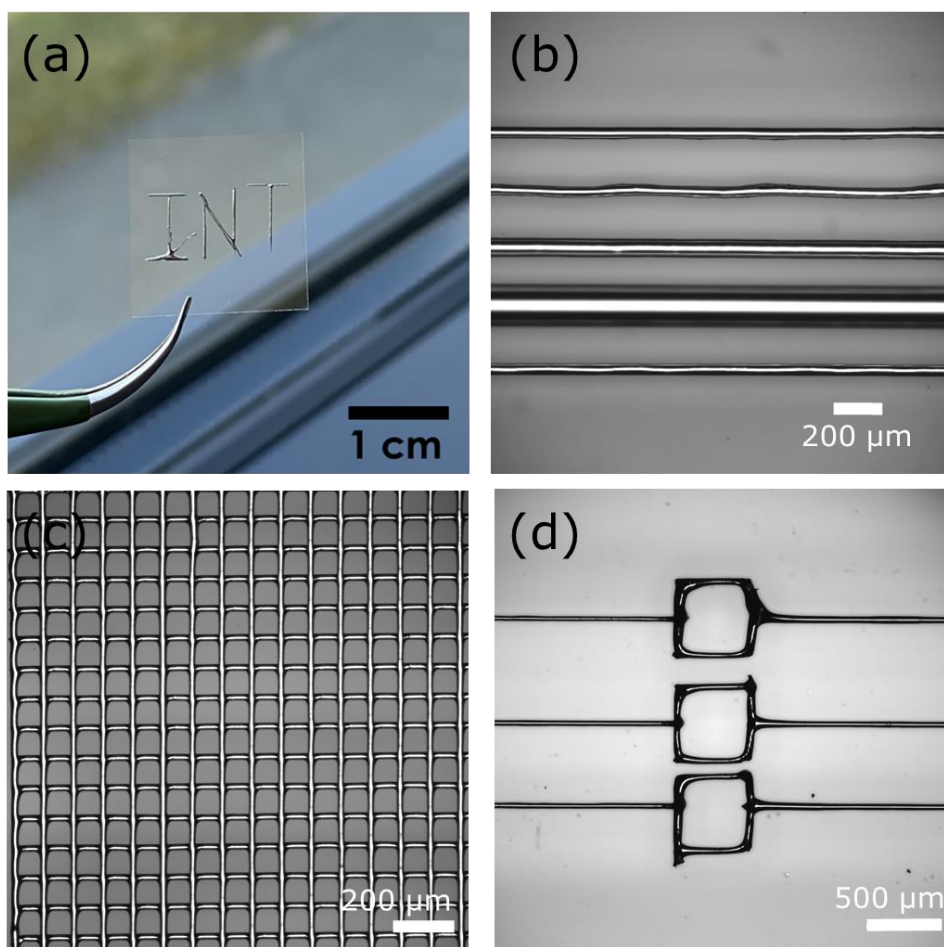
Figure 4. 9: Resulting line widths versus tip opening size. The blue diamonds show average line widths obtained from 10 different capillaries. The yellow circles show the distribution of obtained lines, and the error bars represent the standard deviation (SD). The dashed line is a polynomial fit for guiding the eye ($y = 0.0144x^2 - 0.2945x + 27.363$, $R^2 = 0.9184$). Reproduced from [80] with permission from Wiley.

It is also possible to control the printing resolution by using different nozzle diameters and to increase the line width by increasing the tip opening size (Figure 4. 10). Additionally, line width can be controlled by printing at different speeds. When using the same aperture size of the tip, faster writing speeds generally lead to narrower line widths, but they can also result in discontinued lines as the Galinstan is dispensed slowly or not a stable flow of LM at the tip of the glass capillary. On the other hand, a slow writing speed with the same aperture size can show a slight increase in the line width.

Other than glass, capillary size and speed of printing surface properties of substrates also affect the printing. Freshly clean and plasma-cleaned substrates are easier to wet while setting up contact between tip and substrate.

4.4 Characterization of LM structures

Figure 4. 8 illustrates some typical line pattern outcomes. Glass slides of 18 mm × 18 mm were used as substrates in these experiments. The results show the possibility of high-resolution printing of complex interconnects patterns or electric circuits using complex designs. There is a high degree of uniformity in line width across these patterns, which can span over 1 cm (Figure 4. 8e).



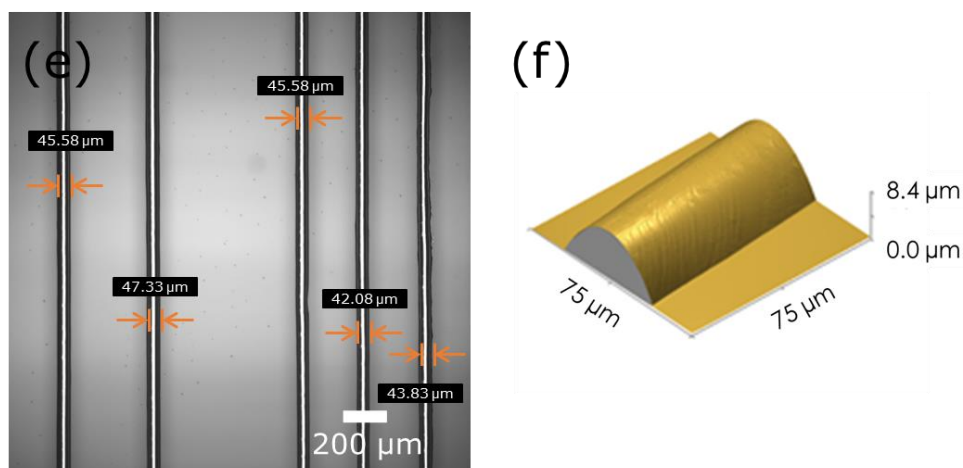


Figure 4. 11: Line printing with Galinstan. (a) The letters INT are patterned in macroscale on a glass substrate. (b) Different widths of Galinstan lines are achieved by tuning writing velocity. (c) Printed Galinstan grid structures. (d) Microwell structures. (e) The parallel Galinstan lines demonstrate conformity and reproducibility in writing. (f) AFM image of a printed Galinstan line. Adapted from [80] with permission from Wiley.

By using this printing setup, homogeneous, well-defined lines can be produced with minimum width $(1.3 \pm 0.1) \mu\text{m}$ (Figure 4. 9), slightly smaller than in previous reports [97], [101]. This high-resolution LM deposition was achieved using a tip of $2 \mu\text{m}$ opening and a writing speed of $1000 \mu\text{m}\cdot\text{s}^{-1}$. Interspacing resolution among lines can be achieved in the sub- $10 \mu\text{m}$ range without merging of lines (Figure 4. 10).

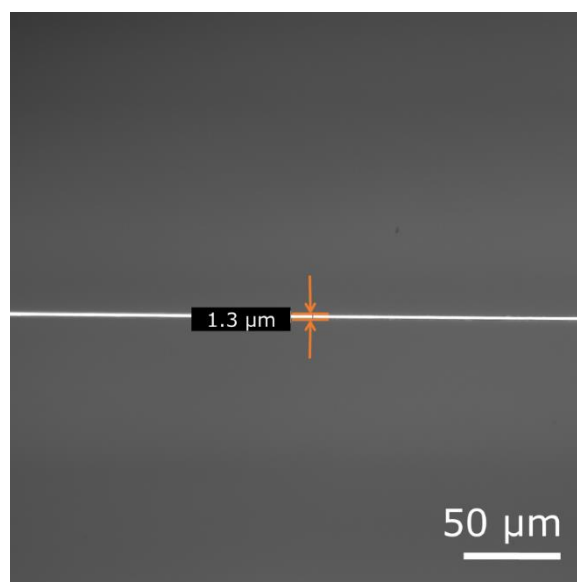


Figure 4. 12: Optical micrograph of a single printed Galinstan line with a width of $(1.3 \pm 0.1) \mu\text{m}$. For analysis, the greyscale image was thresholded at an intensity of 150, and then the diameter of the wire was measured at 10 randomly selected sites along the line. The orange overlay has a thickness of $1.3 \mu\text{m}$ for direct scale. Reproduced from [80] with permission from Wiley.

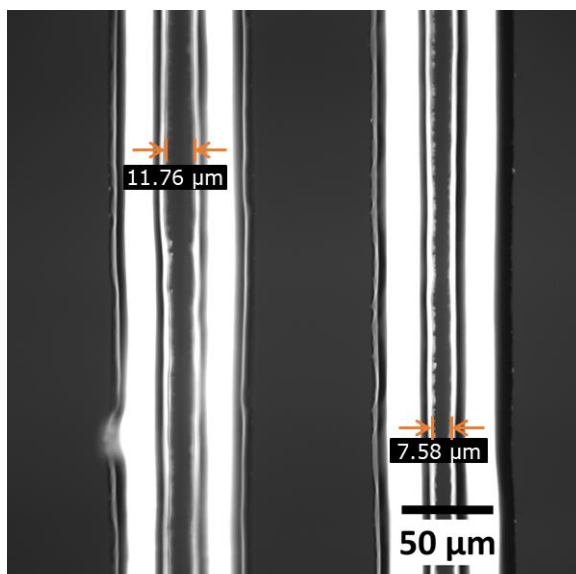


Figure 4. 13: Optical micrograph of parallel lines with different interspacing in between. The minimal line distances achievable with the setup in experiments is about $6.3 \mu\text{m}$ spacing; overall, the minimal line distance is well below the $10\text{-}\mu\text{m}$ threshold. Reproduced from [80] with permission from Wiley.

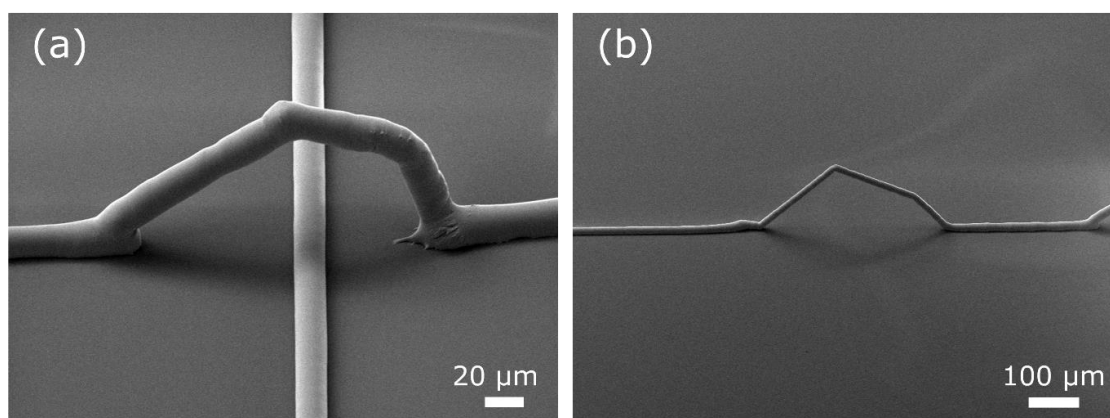


Figure 4. 14: SEM images of 3D prints. (a) Galinstan line arching over another previously printed line. (b) Interconnect arching over the substrate. Adapted from [80] with permission from Wiley.

Other than co-planar Galinstan lines, free-standing 3D structures can also be produced using this method of direct printing. Based on the fact that an oxide layer "skin" forms immediately on contact with oxygen from the environment, Galinstan-based LM structures can also support 3D free-standing arcs (Figure 4. 11). In order to fabricate 3D structures, the glass capillary tip was moved very slowly, step by step, in the direction of the standing pattern in a careful manner to prevent falling off of the LM. It is possible to break the 3D structures or the arc when moving too fast.

With this method, intricate designs spanning a wide range from low microscales to centimeter scales can be achieved without the use of micromachining, masks, or molding techniques. As a result, waste material can also be reduced.

4.5 Challenges during the writing

It is possible for the LM to flow readily within its oxide layer due to its low viscosity. However, during printing, the LM requires dispensing from a nozzle. During this process, the surface area increases, and the oxide layer ruptures and rapidly reforms. Moreover, to achieve this, a pressure (in the form of continuous flow in our case) is applied from the syringe pump. Any applied pressure in the LDPE tubing will cause uniform expansion throughout the channel. So, the pressure felt throughout the LM volume, as well as at the tip, is similar to what is applied in the tubing. It is true that the oxide layer breaks or fractures above a critical value of pressure applied; however, a new oxide layer reforms immediately over the exposed metal. This capillary pressure above the critical value will push LM out of the capillary and help to maintain a continuous flow of LM for printing.

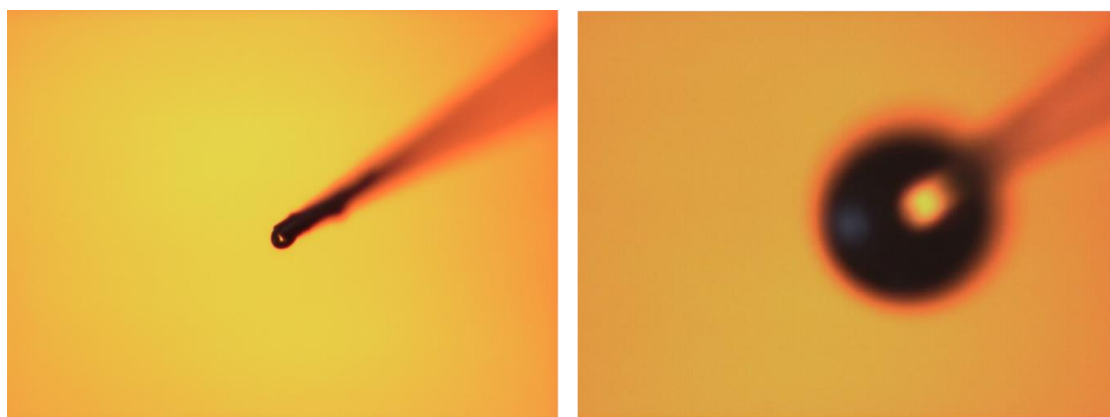


Figure 4. 15: Droplet formation on the glass capillary tip.

Figure 4. 12 shows microscope images (taken in-situ on the NLP 2000 system) as the result of applying pressure to extrude LM from a glass capillary. It is sometimes possible for LM droplets to form on the glass capillary tip when pressure is applied. The droplet can also continue expanding radially at much higher pressures. However, if the pressure inside the metal is not greater than the stress necessary to rupture the oxide layer and to keep LM moving, then the oxide layer will mechanically stabilize the surface. In this case, there is a dilemma, as there must be enough pressure in the capillary to get the LM out of the tip without forming a droplet at the tip. Depending on the capillary aperture size and the presence of LM at the end of the tip seen under the microscope, it is possible to adjust the flow rate in the pump so that sufficient LM for printing is available at the tip.

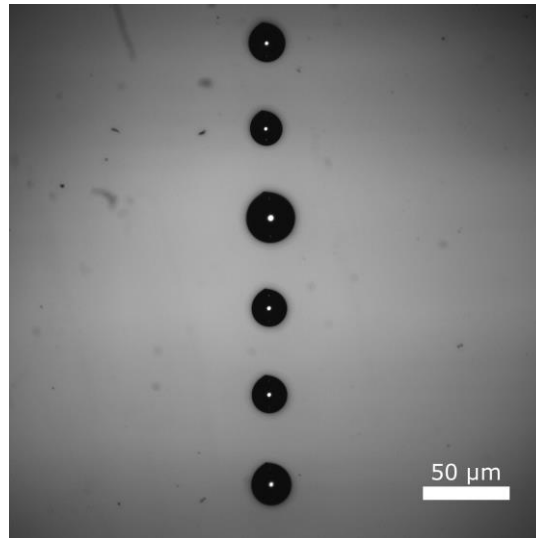


Figure 4. 16: Droplet printing at the place of line formation.

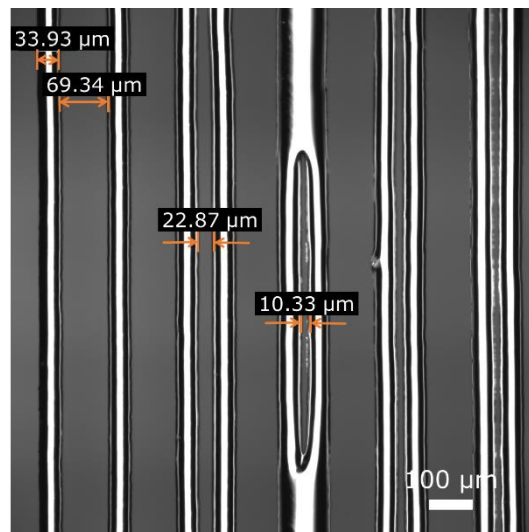


Figure 4. 17: Printing lines with different interspacing. Printing lines next to each other in close proximity (around 10 μm) might merge. Reproduced from [80] with permission from Wiley.

Another problem might be the adhesion of printed Galinstan with the surface. If the adhesion is not proper or if the tip is far away from the substrate, only droplets can be seen (as shown in Figure 4. 13) at the place of proper lines. To avoid adhesion issues, pre-processing of the substrates with a surface treatment might help, as while printing, the oxide layer ruptures, and a new oxide layer is immediately formed. These methods to achieve a high-energy surface can help better writing because of the oxide layer wetting. Oxygen plasma cleaning, UV irradiation, and oxidation reactions are usually used to improve hydrophilicity. Additionally, strong oxidizing liquids, such as potassium dichromate solution and peroxymonosulfuric acid (also called Piranha solution), can also be applied to obtain hydrophilic surfaces. It is crucial to handle these solutions carefully as they are corrosive and must be used/disposed of safely.

4. Capillary printing of LM alloys

Other than that, one more problem is commonly faced while printing LM lines next to each other; if they are printed very close together (Figure 4. 14, when the distance between the ending of lines is $<10\mu\text{m}$), they can merge spontaneously.

As compared to subtractive methods, this LM printing method uses less material and generates less waste. In addition, these printed structures can provide an unparalleled combination of conductivity and stretchability. Direct patterning allows LMs to be used side-by-side with other materials. Devices utilizing these materials are attractive because they can be rapidly designed and manufactured, making it straightforward to fabricate even complex designs and enabling the creation of a variety of new types of functional devices. Encapsulation of LM-based devices, as well as compatibility with materials like polymers (PMMA), formation of devices and application for structural purposes, will be discussed in chapter 6, 7 and 8.

5. Tabletop microplotter for enhanced access to printing areas

As discussed in chapter 2, there are several ways to pattern functional inks to a surface. These printing techniques can be classified into contact and non-contact printing or conventional and non-conventional printing. In addition, these printing systems are also roughly divided into two groups based on technology: high technology and accessible technology. Technology-based printing setups that rely on complex instrumentation, such as commercially available inkjet printing, or SPL-setup-based spotting systems, are costly; they cost hundreds of thousands of euros and require high maintenance. These printing systems have been the focus of attention for printing techniques, and as such, demand for more broadly accessible options is rising. In this regard, it's time to develop a tabletop-accessible technology that is low-cost, reliable, easy to use and can be assembled and operated without further training.

Aside from these benefits, an accessible printing technology should also provide the highest possible resolution (within the limits of staying reasonable expensive) and be more resilient compared to high-technology and complex machinery-based printers. Recently, several lab printing setups have been reported that use (at least partially) accessible technology [97], [102]–[105].

Most of the methods and results presented in this chapter are published in Hussain et al. [412]. The chapter will start with introducing a newly designed affordable tabletop technique, followed by some of the printing results. This chapter also shows gold lines and conductive microarrays printed on glass and polyimide films (aka commercially Kapton). These microdots and line structures can serve as microelectrodes and in soldering applications for printable and flexible electronic circuits. Furthermore, this chapter demonstrates printing with inks containing phospholipids (DOPC), proteins [bovine serum albumin (BSA)], and small bioactive molecules (biotin) as examples of compatibility with biomaterial inks.

5.1 Printing setup

This setup (as shown in Figure 5. 1) is designed to facilitate rapid and easy assembly and provide superior accessibility in the case of non-flat or otherwise hard-to-access surfaces. It was therefore decided to use a highly versatile micromanipulator mini-robot (miBot, Imina Technologies) as the core component of the scanning probe lithography (SPL) setup rather than relying on a micropositioning sample stage or a fixed spotting probe hovering above the sample as is the case with most present SPL setups. It is a non-tethered, highly precise, compact micromanipulator that can freely move in x–y on a metal plate and has an arm that can be raised and lowered. With these miBots, submicrometer positioning precision over several millimeters can be

achieved. These robots are frequently used in probe station setups for especially flexible contacting under challenging conditions [413] or for interactive micro- and nanomanipulation [414], [415] and nanomechanical studies [416], [417]. The platform for the micromanipulator is a steel frame that was built in-house. As shown in Figure 5. 1, this frame holds a universal serial bus (USB) camera (Webcam 1080P, Wansview) with a microlens (10X mobile objective, Mpow), which supplants a microscope and allows real-time monitoring of the printing process. With an adjustable height head, the camera can be adjusted for a wide range of sample/camera distances which, in principle, helps to achieve the best focus with the sample.

Moreover, this design provides ample headroom for accessing the sample from all sides. The design includes an inbuilt groove for leveling the substrate; when printing in-plane, this groove can be filled to provide a flat stage. Alternatively, while vertical printing, the 3D-printed substrate holder can be fixed in the groove for better accessibility.

By simply setting the micromanipulator to the desired starting position by hand, the platform allows very flexible rough positioning of the device. The miBot offers access

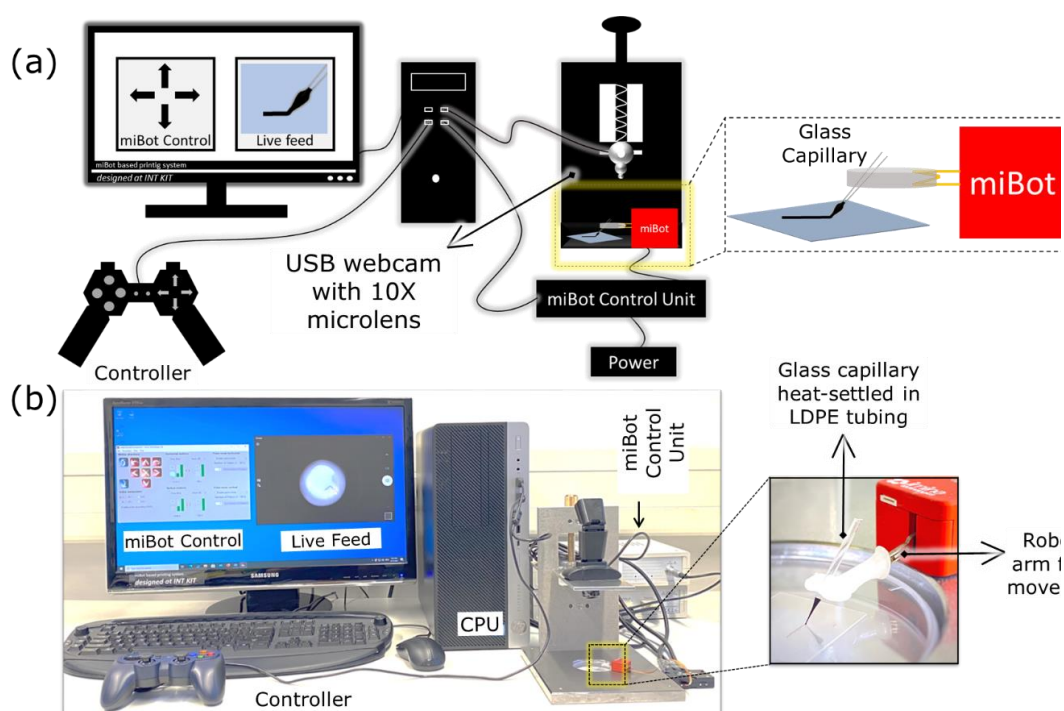


Figure 5. 1: An overview of the printing setup: (a) a schematic representation and (b) a photo of the actual setup. The setup comprises a printing stage with a USB webcam above the sample area and an arm-mounted micromanipulator carrying a glass capillary. The micromanipulator is connected to the computer via a control unit and can be controlled by handheld controllers, while a webcam displays the positioning of the capillary over the sample. Reproduced from [412] with permission from AIP.

to a high-precision workspace of 20 x 20 mm² in X and Y, as well as a 42° sector in the Z direction (with the movement of the arm). It is possible to achieve a maximum speed of 2.5 mm·s⁻¹ in X-Y and 150 mrad·s⁻¹ in Z movement, depending on the desired positioning precision [418], [419]. The micromanipulator was equipped with styluses that allowed the ink to be dispensed. First, various tip and taper sizes of glass capillaries were prepared using a micropipette puller system (Sutter Instruments, P-1000, described in Annex A.2.1). Following this, the capillary was cut to 3 cm length, heat-settled, and mounted into low-density polyethylene tubing (ID: 0.13 mm, OD: 3 mm diameter, Reichelt Chemietechnik). The micromanipulator's arm fits well with the 0.1 mm tubing and allows mounting the stylus easily on the arm. In addition, the LDPE (Low-Density Polyethylene) tubing dampens vibrations when

Table 5. 1: Components of the printing setup. Reproduced from [412] with permission from AIP.

| Component | Type, supplier |
|---|---|
| System frame | Aluminum/steel, built in-house, STL file, https://www.doi.org/10.5445/IR/1000134042 |
| Height adjustment for the webcam holder | Aluminum, built in-house, STL file, https://www.doi.org/10.5445/IR/1000134043 |
| Substrate holder plate | Steel, built in-house, STL file, https://www.doi.org/10.5445/IR/1000134044 |
| Webcam holder | Aluminum, built in-house, STL file, https://www.doi.org/10.5445/IR/1000134046 |
| Sample holder (vertical printing example) | Thermoplastic, 3D-printed in-house, STL file, https://www.doi.org/10.5445/IR/1000134047 |
| Scaffold structure (difficult access example) | Thermoplastic, 3D-printed in-house, STL file, https://www.doi.org/10.5445/IR/1000134048 |
| Metallic sample holder (<i>in situ</i> curing example) | Metal filament, 3D-printed in-house, STL file, https://www.doi.org/10.5445/IR/1000134049 |
| Camera | Webcam 1080P, Wansview |
| Lens | 10× mobile objective, Mpow |
| Micromanipulator | miBot, Imina Technologies |
| Controller software | miBot remote control 2.5.7/Precisio Software Suite, Imina Technologies |
| Joypad | Gamepad F310, Logitech |
| Printing stylus | Glass capillary in LDPE mount, built in-house |

contact is made between the glass capillary and the sample during printing. Table 5.1 lists all the components used in the microplotter setup reported in this chapter.

A miBot is usually operated in stepping mode, in which the frequency and amplitude of driving signals are used to adjust the speed and resolution. The frequency determines the movement speed of miBots, and the amplitude determines the size of their steps. To travel long distances around the sample, the manipulator can be set up to move at high speed while also utilizing larger step sizes by adjusting the frequency and amplitude in the user interface. If needed, this allows a wide range of movement speed and precision: for example, the manipulator can move at a maximum speed of $2.5 \text{ mm}\cdot\text{s}^{-1}$ in X and Y and $150 \text{ mrad}\cdot\text{s}^{-1}$ in Z (arm movement), which is suitable for rough positioning on a sample, but can be adjusted to 60 nm step size in X and Y and 120 nm step size in Z [420], [421] for highest precision (in principle), or even sub-nanometer step size in scanning mode. The miBot can be controlled manually by using either a monitor-based user interface or a handheld control pad that makes use particular intuitive.

5.2 Printing process

A typical printing process begins with loading a fresh capillary stylus onto the robotic arm of the micromanipulator (Figure 5.2). Once the stylus is loaded, the manipulator is moved to the ink reservoir. Upon contact between the stylus capillary and the ink reservoir, capillary forces pull the ink into the glass capillary nozzle tip. As soon as the capillary has been filled, it is retracted from the inkwell and moved/positioned at the pattern's starting point. The inkwell and sample can be positioned right next to each other by moving the micromanipulator through the software controls, or it is

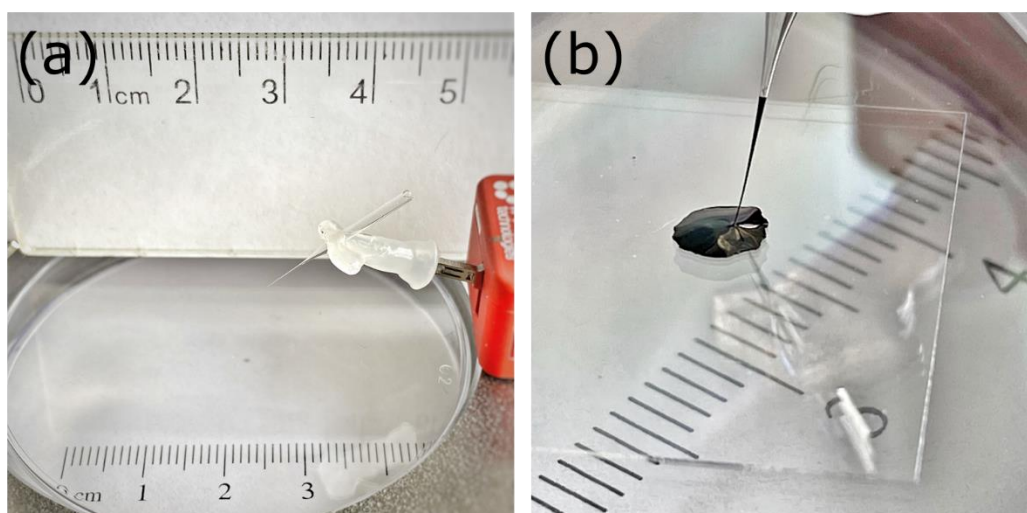


Figure 5.2: An illustration showing the capillary stylus and printing process. (a) Close-up photo of a glass capillary stylus mounted on a micromanipulator. (b) Photography of the capillary during the ink loading process in the ink reservoir. Reproduced from [412] with permission from AIP.

also possible to remove the inkwell and replace it with the sample. After the exchange, the micromanipulator can be roughly positioned by hand (around the pattern's starting point) since it can be freely picked up and repositioned on the stage.

In the next step, the glass capillary tip is brought close to the substrate (as shown in Figure 5. 3a) under software control in order to dispense liquid on a surface. It is possible to see the gentle physical contact between the stylus and the substrate using a USB camera in a microlens monitoring system with a 10x objective. Upon contact between the substrate and the glass capillary tip, ink is transferred (as shown in Figure 5. 3b). The speed of movement and the duration of touch (referred to as dwell time) influence the width of lines and the size of dots. As soon as the micromanipulator unit touches the substrate, it can also be moved in a straight line or an arbitrary curve (as shown in Figure 5. 3d,e,f) in accordance with the geometry demand, leaving behind the desired structure.

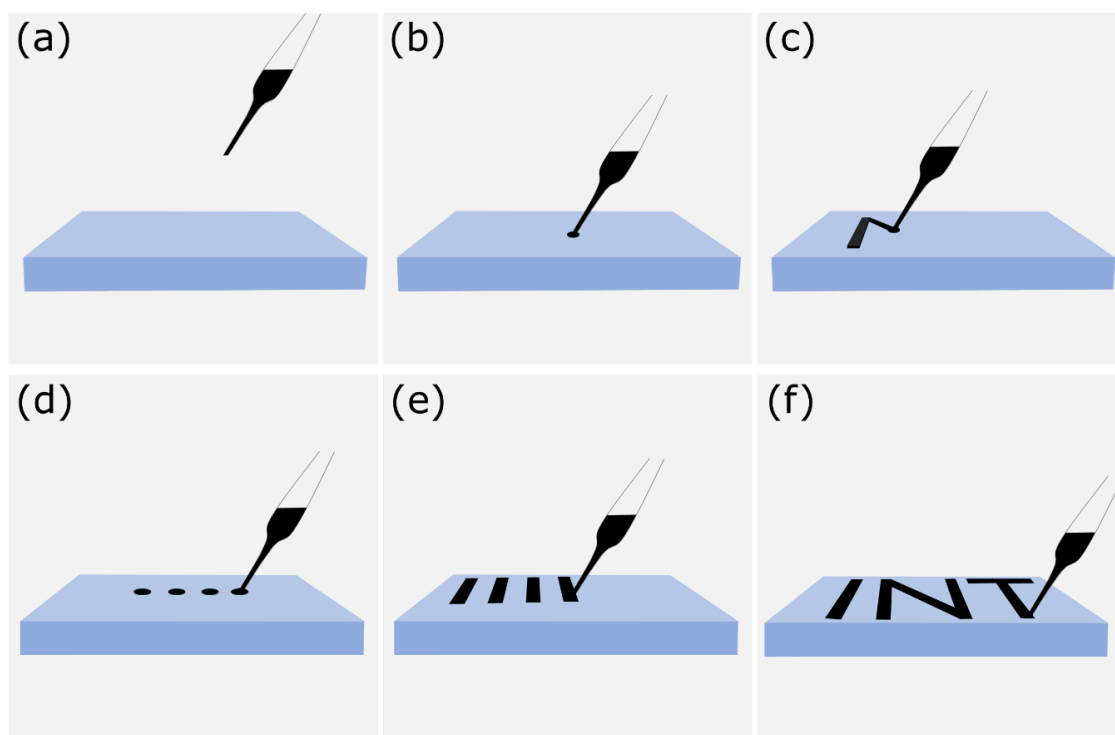


Figure 5. 3: Printing steps. (a) Glass capillary tip approaching the substrate under software control. (b) Upon contact with the substrate, the glass capillary nozzles transfer ink to the substrate. (c) Moving the tip mounted on the miBot according to the desired structure or pattern. (d), (e), (f) An illustration of writing dots, lines, and arbitrary curves, respectively. Figures (d), (e), and (f) are reproduced from [412] with permission from AIP.

Various shapes, such as microarrays, lines, curves, and other structures, can be printed on the fly. The glass capillary stylus is retracted from the substrate after completing the line or desired pattern, effectively separating the substrate and glass capillary tip. Implementing all of the steps shown in Figure 5. 3, a simple dot or line

pattern can be printed within five minutes from mounting the capillary to printing the pattern. For a short tutorial, printing tips, and safety concerns, see Annex A.2.8.

5.3 Challenges during printing

It was observed that the approaching angle between the tip and the substrate (θ_a shown in Figure 5. 4) plays an essential role in printing.

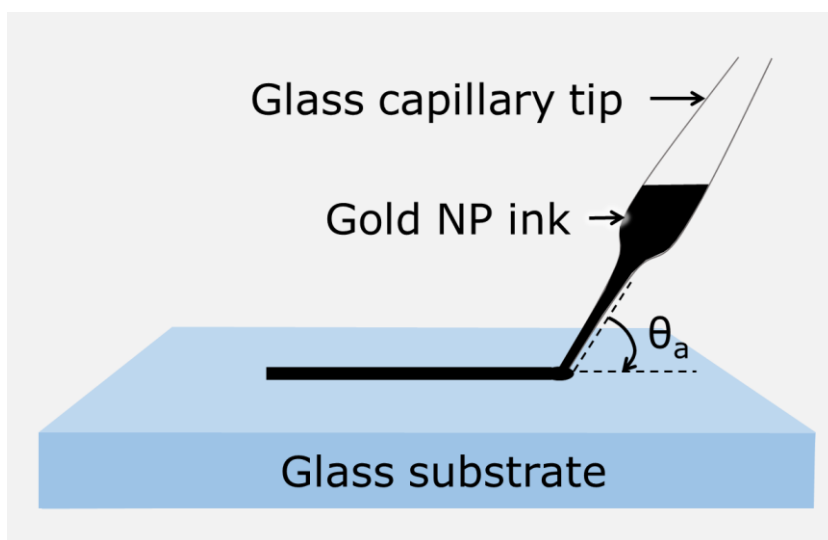


Figure 5. 4: Schematics of the interaction during the writing process. θ_a is the approaching angle between the glass capillary tip and substrate. Reproduced from [412] with permission from AIP.

Some challenges were experienced while printing lines, especially during vertical printing. While printing lines with a small tip size (around less than 50 μm), the gold polymer ink tends to hold onto the outside glass capillary, then moving along with the tip, as shown in Figure 5.5a. As a connected issue, lines breaking up into separate dots and non-homogeneous lines, as shown in Figure 5. 5b and Figure 5. 5c, respectively, were observed. The approaching angle (θ_a) around 30-80° seem to be working fine with the substrate, an approaching angle between this range might help the glass capillary tip to generate sufficient tip pressure on the surface, which might increase the roughness (by dragging tip on the surface can increase the surface area) as well as surface energy, finally favoring the printing. And the tip size can be varied from around 3 μm up to several hundred micrometers; these issues were solved by using bigger tip sizes (around more than 200 μm) as the spot size primarily depends on the tip's size. Alternatively, by using different tip sizes for better printing, the physico-chemical properties of ink and substrate can be tuned when possible (e.g., by adding additional components to ink or implementing surface treatments altering the substrate hydrophilicity). Once it is established that a given ink can be filled into the capillary by capillary force and it can be printed on the substrate, several factors

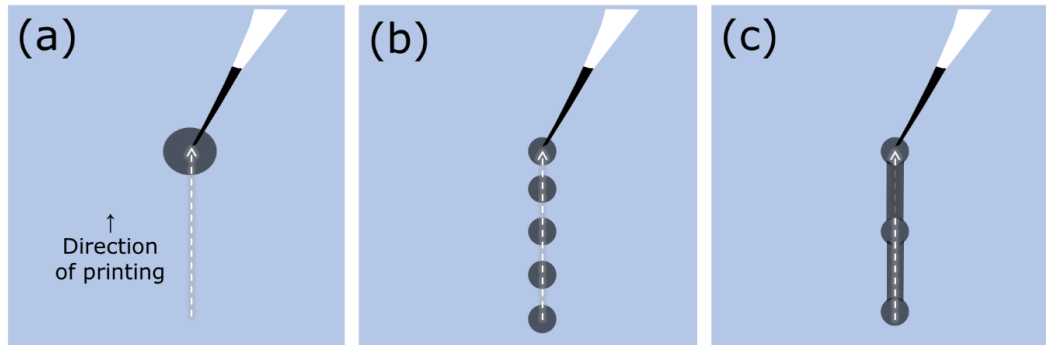


Figure 5. 5: Various issues while printing lines of a printed line on a substrate. (a) ink holding onto the glass capillary, moving along with the tip; (b) the line breaks up into microdots; (c) a non-homogeneous line.

must be noted and kept in mind to engineer for smooth printing, e.g., the viscosity of ink, contact angle, driving mode, wetting behavior, drying effects, line spreading, humidity and temperature conditions.

Further changes can also be made in these factors to achieve different widths of lines or size of microdots by changing substrate, varying ink composition, or substrate's wettability. As shown in microscope images, even printing with the same tip, deviations in the size of microdots or width of the line are possible due to the movement of miBots and some vibrations.

Another problem with the current setup is optical resolution, which is limited by the optical resolution of the camera used.

5.4 Enhanced access to printing areas

The open design and the use of the robotic micromanipulator make it possible to print on surfaces that would otherwise be unreachable. An example of this is shown in Figure 5. 6a, which shows a 3D-printed frame holding glass substrates. This setup is also suitable for printing on flat substrates with low laying areas, trenches, or troughs with high aspect ratios, which are generally unattainable to conventional SPL printers due to their respective geometry.

Due to its "on-the-fly" writing capability and enhanced access, the setup is especially suited for difficult lithography tasks or one-time processes not well addressed by conventional SPLs.

As part of demonstrating the capabilities of the printing setup, a variety of inks and substrate materials, as well as different substrate geometries, have been tested. The results are relevant to various research fields, including printable electronics and bioactive surface functionalization.

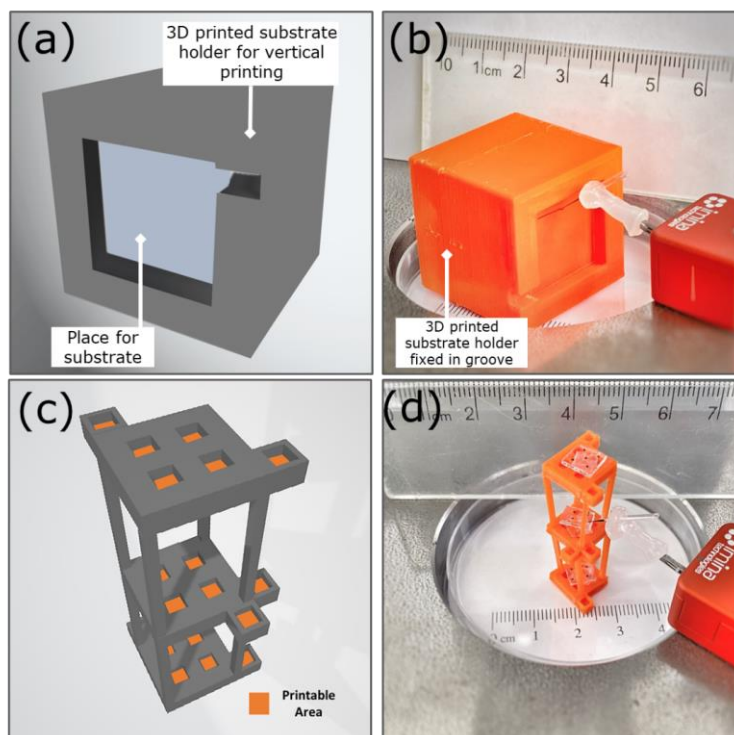


Figure 5. 6: "Hard-to-access" surfaces printability examples. (a) The design scheme for 3D-printed substrate holders for demonstration of vertical printing capabilities. (b) A photograph of the vertical printing setup with an ink-filled capillary and a micromanipulator in place. (c) The complex holder structure demonstrates the ability of this printing setup to reach places where regular printers cannot reach. (d) An actual photo of the multilevel printing, again with a micromanipulator and an ink-filled capillary. Reproduced from [412] with permission from AIP.

5.5 Gold structures on glass and Kapton film

Flexible substrates and conductive inks are important components of printable electronics. In our demonstration, a gold nanoparticle (NP) based ink (UTDAu25-IJ, UT Dots) was printed into dots and line structures in a printing process as described earlier. After printing, the substrates were annealed for 30 minutes at 250° C in a furnace (Nabertherm P330) to obtain high-quality and conductive printed gold patterns. The patterns were then examined using optical microscopy. A typical result of gold ink printing on glass (glass coverslips, VWR) and Kapton foil (Kapton-HN, Dupont) can be seen in Figure 5. 7. In addition to cleaning all substrates in chloroform, 2-propanol, and deionized water, oxygen plasma (10 sccm O₂, 0.2 mbar, 100 W, 2 min, in a Diener ATTO B plasma cleaner) was used when necessary to increase the hydrophilicity of glass substrates (experimental details in Annex A.2.2).

The micromanipulator's large working area and ease of operation allow it to be used for the free-hand writing of large structures, as shown in Figure 5. 7a. Through more precise control, small dots and lines can be printed. Figure 5. 7 shows conductive

printed gold patterns, both dots, and lines, on glass substrates and Kapton films. Various printing parameters, such as dwell times and tip sizes, were also studied in relation to dot diameter and linewidth.

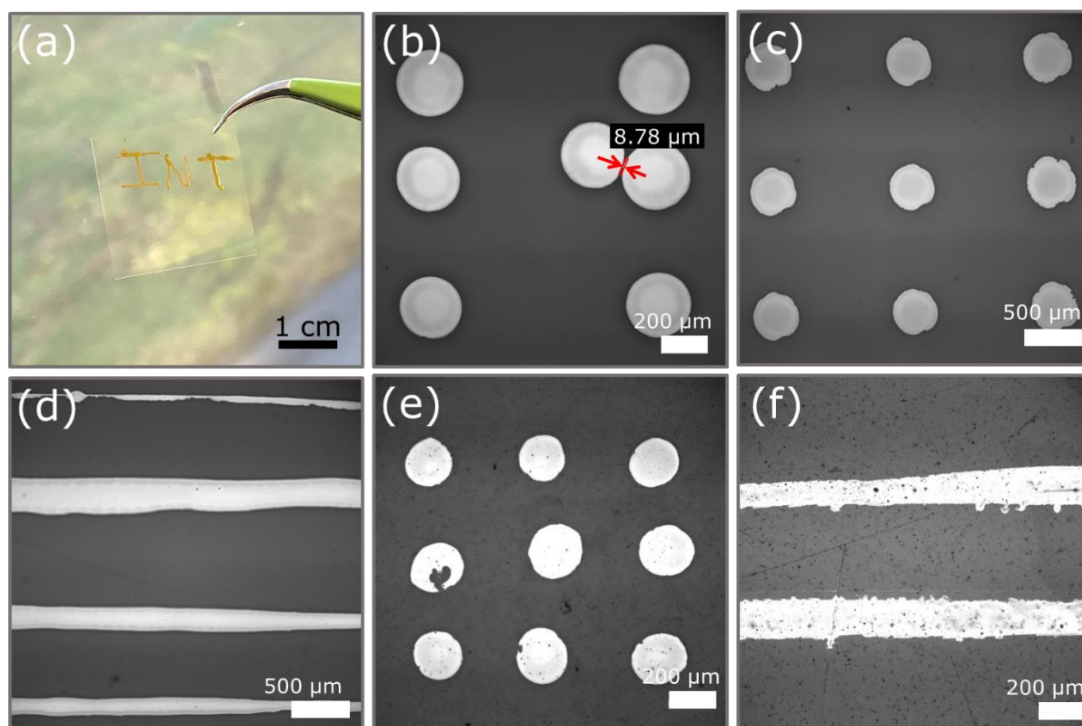


Figure 5. 7: Examples of gold patterns on glass and Kapton substrates. (a) Photography of macroscopic letters "INT" printed on a glass substrate. Bright-field microscopy images of (b) side-by-side printed dots on a glass substrate with a gap distance of sub-10 μm , (c) microdots on a glass substrate, (d) line structures of different widths on a glass substrate, (e) microdots on a Kapton substrate, and (f) line structures on a Kapton substrate. Reproduced from [412] with permission from AIP.

Varying tip sizes from 30 to 230 μm opening provide feature sizes in the range of (23.6 ± 2.6) to (458.0 ± 8.4) μm diameter for dots and (15.9 ± 3.7) to (389.4 ± 19.9) μm for linewidths. Despite the simplicity of the overall setup, gap sizes of less than 10 μm in-between features can still be achieved (as shown in Figure 5. 7b). Another parameter is dwell time, although dot size was not significantly affected by dwell time [probed for 2, 5, and 10 s, yielding an average of (458.0 ± 8.4) μm]. Dot thickness was measured using atomic force microscopy in tapping mode (Dimension Icon, Bruker) by scratching the middle of the dots features, yielding (118 ± 26) nm.

Gold NP ink was also printed on flexible substrate Kapton foil, which features sizes of 200–500 μm readily achieved (as shown in Figure 5. 7e and Figure 5. 7f). This underlines the general conclusion that pattern fidelity and resolution depend not only on capillary opening size but also on the wetting behavior of the ink/substrate combination. As discussed in section 5.2, a particularly noticeable effect was observed when using capillary tips of smaller sizes (<50 μm) or printing at low

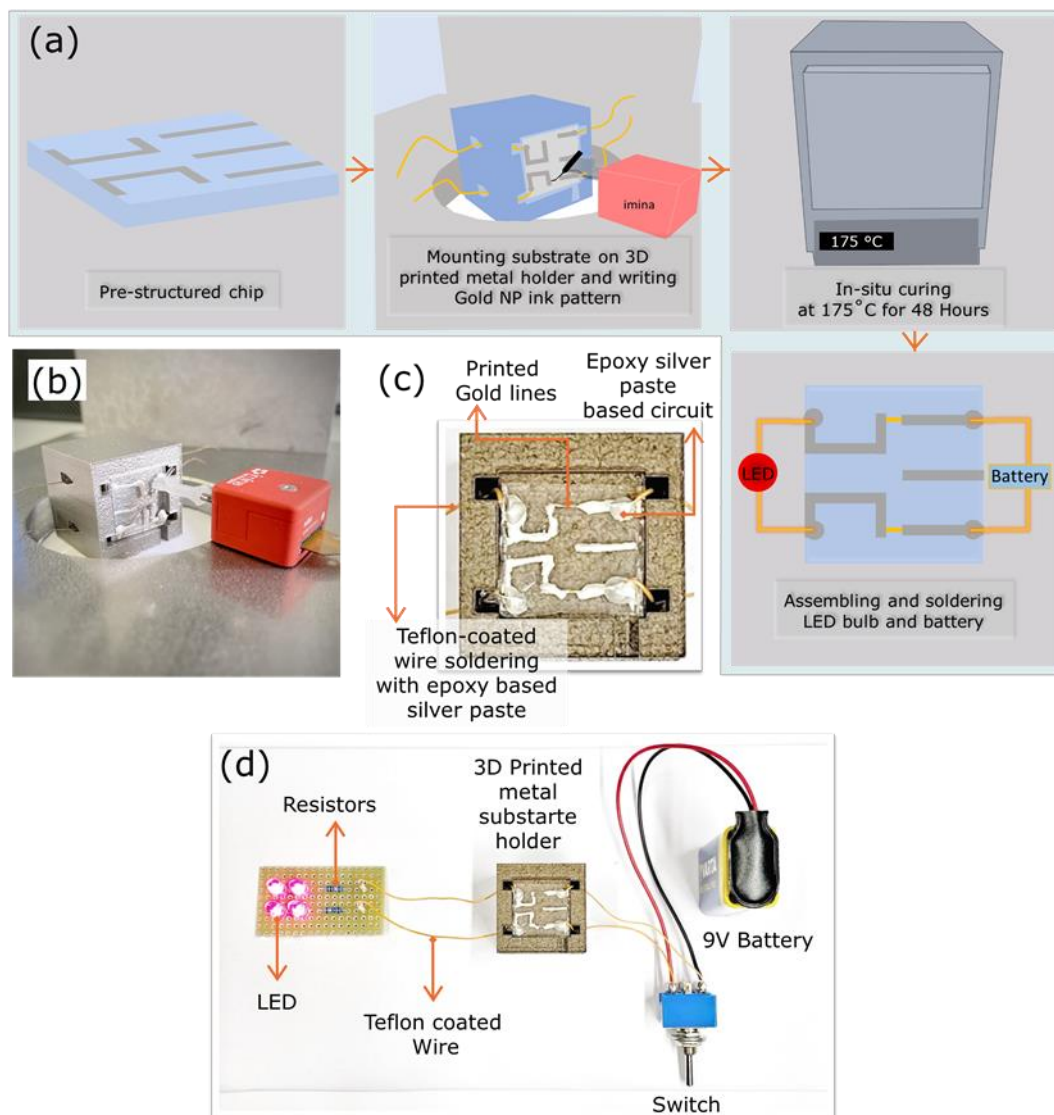


Figure 5. 8: In situ and on-demand connector writing. (a) The schematic workflow: The silver-epoxy paste electrodes are structured on a glass chip and recessed into a metal cube, which serves as a model device. After the wiring is done on the microplotter, Au-NP connector lines are written between the electrodes to close the circuit. The device is then cured in a furnace to make the printed pattern conductive. Finally, the LED and the power supply can be connected to demonstrate the function of the created circuit. (b) Actual photographs of the writing process. (c) An image of the fine gold connector lines printed by the microplotter. (d) The final photograph shows the circuit after curing and assembly of the LED and power supply. It demonstrates a fully functional circuit. Adapted from [412] with permission from AIP.

contact angles ($< 30^\circ$ between the glass-capillary tip and the substrate, θ_a in Figure 5. 4); the gold ink tends to adhere to the capillary tip rather than to the substrate, moving along with it rather than deposited on it. Also, Dewetting can cause already written lines to break up into droplets (as shown in Figure 5. 5b) if the surface energy of the substrate is not high enough. It is possible to resolve these problems by

increasing the writing speed, utilizing wider capillaries, and changing the substrate wetting by plasma cleaning. The printing process can be optimized based on and also by engineering the physico-chemical properties of the ink and substrate, for example, viscosity, driving mode, wetting behavior, contact angle, drying effects, line spreading, and temperature conditions similar to those of other spotting approaches and inkjet printing.

5.6 Flexible on-demand interconnects for printed electronics

The last section 5.5 demonstrated the printing capability of this setup to fabricate gold patterns; in this section, the microplotter was used to achieve functional electrical circuits. Due to its enhanced accessibility, this setup makes it possible to create flexible on-demand interconnects in-situ on complex structures. As part of this experiment, a scaffold was 3D-printed in metal and equipped with a recessed glass substrate that contained silver-epoxy electrodes connected to the outside of the scaffold by Teflon-coated copper wires. An LED and power supply were also connected to the electrodes via Teflon-coated copper wires. The scaffold holding the glass in a recessed cavity makes it arbitrarily unattainable to standard printing methods to demonstrate the flexibility of the micromanipulator approach for in situ and on-demand printing of interconnects (Figure 5. 8).

While this prestructure device would not be readily accessible for conventional SPL methods without prior disassembly, now all functionalization steps can take place in situ. The needed wiring to close pre-existing circuit can simply be applied to the device on-demand by direct writing the Au-NP ink in the desired layout between the pre-existing silver-epoxy-based electrodes. After curing of the device, the interconnects become conductive, and the circuit is rendered functional with an assembly of LEDs and a power supply (Figure 5. 8d).

5.7 Deposition of protein inks

Surface-immobilized biomaterials, often in the form of arrays, are used extensively in biomedical research and health care [422]–[426]. In this context, proteins are a particularly important class of biomaterial. For diagnostic purposes, these can act as antigens to detect the presence of antibodies or as antibodies themselves to detect antigens in body fluids like blood, or as external stimuli, such as modulating cell adhesion or activation in biomedical experiments [425], [426]. During the prototyping of lab-on-chip devices, researchers are seeking a flexible way to functionalize surfaces within larger structures, such as microfluidic channels or wells, which can be challenging to reach with conventional approaches due to geometrical limitations. Moreover, it may be desirable to deposit a small sample of analytes directly onto a particular position on a chip structure for testing purposes. In order

5. Tabletop microplotter for enhanced access to printing areas

to demonstrate that biomaterial inks may also be printed with this setup, inks containing fluorescence labels and biological materials such as lipids, proteins, and small bioactive molecules were also printed using this microplotter setup. Table 5. 2 shows the details of the applied ink formulations.

Table 5. 2: Ink formulations. Reproduced from [412] with permission from AIP.

| Ink description | Ink 1 | Ink 2 | Ink 3 |
|-----------------------------------|---|---|--|
| Component A (biomaterial) | 1,2-dioleoyl-sn-glycero-3-phosphocholine (DOPC) [supplied by Avanti Polar Lipids (USA)], concentration: 20 mg/ml in ethanol | Bovine serum albumin (BSA) (supplied by Invitrogen, Thermo Fisher Scientific), concentration: 50 mg/ml in water | Protein A–biotin from staphylococcus aureus (supplied by Sigma-Aldrich), concentration: 2 mg/ml in phosphate buffered saline (PBS) |
| Component B (avoiding ink drying) | Glycerol (supplied by Sigma-Aldrich) | | |
| Component C (fluorescent label) | Rhodamine 6G (supplied by Sigma-Aldrich), concentration: 1 mg/ml in water | Fluorescein isothiocyanate (FITC)-PEG (PG2-FCTH-1k, supplied by NANOCS), concentration: 1 mg/ml in water | Alexa fluor 647 azide, triethylammonium salt (A10277, Life Technologies, Thermo Fisher), concentration: 0.5 mg/ml in DMSO |
| Volumetric ratio (%) (A:B:C) | 60:35:5 | 60:35:5 | 60:30:10 |

After loading the inks into the capillary (as described in section 5.2), different spot patterns were written with the respective inks on glass surfaces. Figure 5. 9 shows fluorescence microscopy images (obtained on an Eclipse 80i, equipped with a DS-Qi2 camera and C-HGFIE Intensilight, Nikon) of the resulting bioink dot configurations. Dots with diameters of (357.9 ± 16.0) , (257.0 ± 13.6) , and (291.5 ± 13.6) μm were achieved for ink 1, ink 2, and ink 3, respectively.

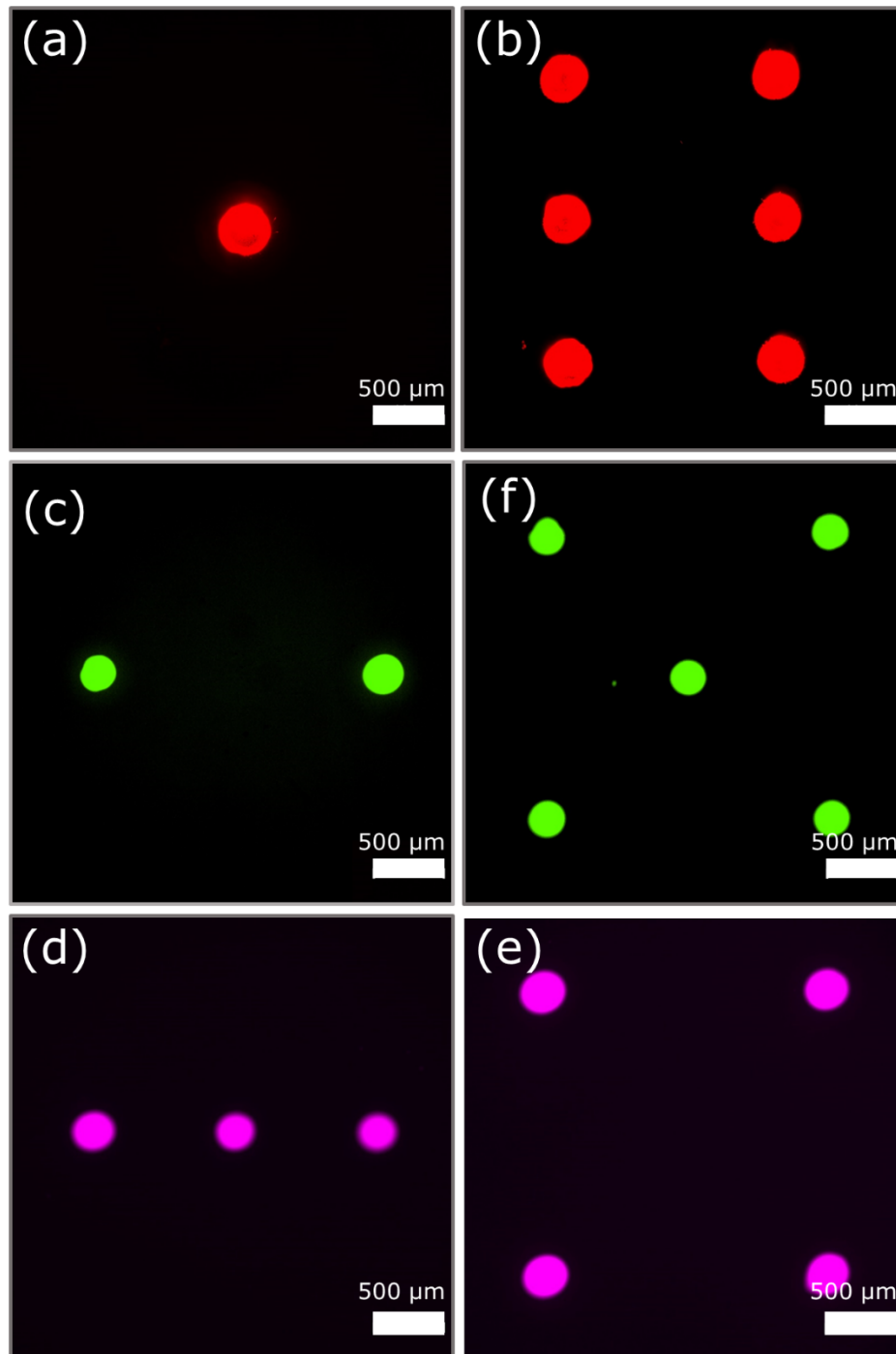


Figure 5. 9: Fluorescence microscopy images of the deposited bioink pattern. Different spot configurations were plotted with ink 1 (a) and (d), ink 2 (b) and (e), and ink 3 (c) and (f). Red channel: Texas Red filter set (Y-2E/C, Nikon, Ex.: 540–580 nm, Em.: 600–660 nm), green channel: FITC filter set (B-2E/C, Nikon, Ex.: 465–495 nm, Em.: 515–555 nm), and purple channel: Cy5 filter set (AHF F41-008, Nikon, Ex.: 590–650 nm, Em.: 662–738 nm). Reproduced from [412] with permission from AIP.

The microplotter setup described in this chapter is unique in its way because it can deposit materials in places that are unattainable with conventional printers. This setup deposits materials in a controlled manner with microscale resolution,

5. Tabletop microplotter for enhanced access to printing areas

micrometer precision, and the highest flexibility in the pattern. With this turnkey printing setup, users will be enabled to instantly start their work and printing according to the application without much training and assistance.

6. Fully printed electronic devices

Galinstan capillary printing, briefly described in chapter 4, is a versatile LM printing process that enables the fabrication of various fully printed devices. In this chapter, the following devices were fabricated and characterized for their electrical behavior:

- (I) LM interconnects and resistors,
- (II) Fully printed diodes, and
- (III) Fully printed transistor structures.

The devices also demonstrate that the LM capillary printing process is compatible with other digital printing methods and thin film structuring methods for integration. Most of the data presented in this chapter has already been published in Hussain et al. [80].

6.1 Fully printed LM interconnects and resistors

In order to test the use of the obtained LM structures in printable electronic applications as well as to probe the stability for future uses, electrical resistances of as-printed as well as encapsulated LM lines in poly(methyl methacrylate) (PMMA) were determined as the first test.

6.1.1 Galinstan interconnects fabrication

The fabrication steps for Galinstan interconnects are visualized in Figure 6. 1.

- I. The starting substrate was a glass substrate coated with 150 nm Au over a 7 nm Cr base layer; the Cr layer was deposited in order to improve adhesion between the substrate and the electrode.
- II. It was structured with a TRUMPF TruMicro 5000 laser ablation system for obtaining contact pads with varying distances between the pads (60–550 μm). After laser structuring, the substrates were rinsed with 2-propanol and deionized water, then dried by a stream of nitrogen. These Au structures will serve as the contact pads for the printed Galinstan interconnects during measurement steps.
- III. Subsequently, the Galinstan interconnects were printed by the customized nanolithography system described in Chapter 4. The capillary was filled with Galinstan by applying pressure through the syringe pump. For each experiment, freshly cleaned glasses were used. The patterns were completed at different writing speeds from 200 to 1000 $\mu\text{m}\cdot\text{s}^{-1}$.

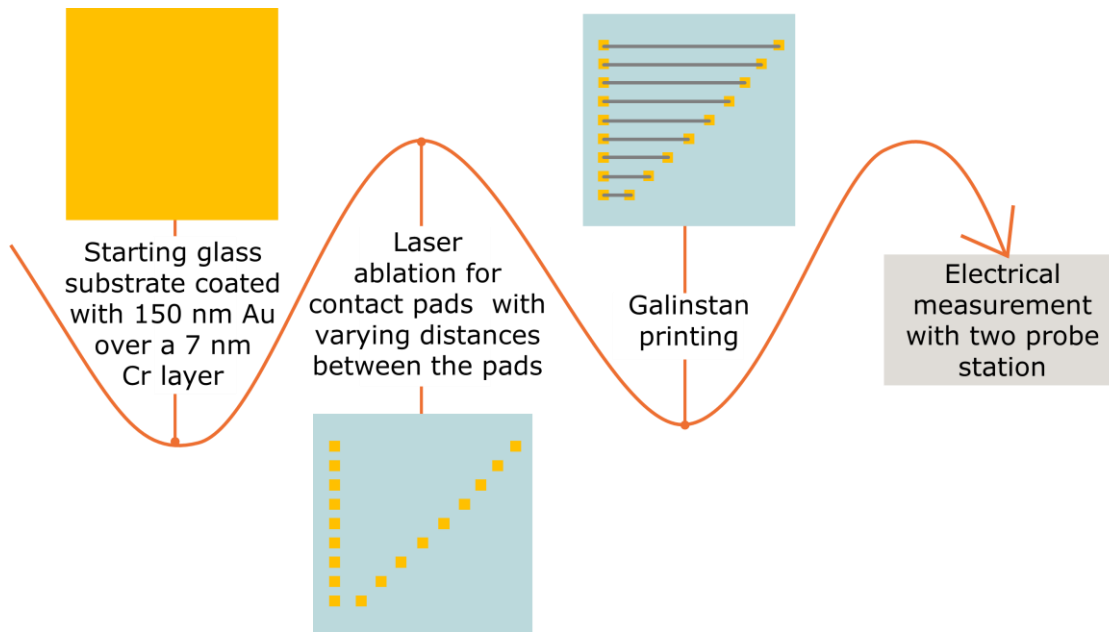


Figure 6. 1: Fabrication of interconnects.

6.1.2 Characterization of LM interconnects

Following the printing process, the interconnects were characterized using optical microscopy and resistance measurements. Measurement of the width, length, and height of the resistor structure are carried out by optical microscopy and profilometry.

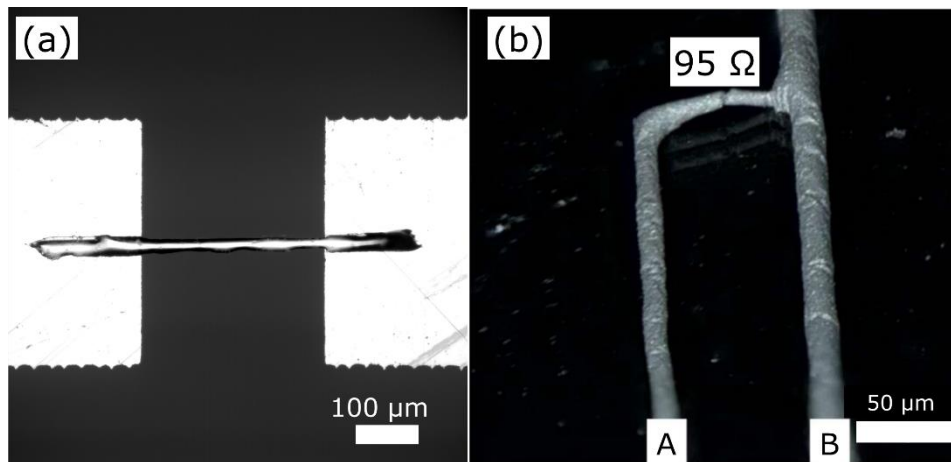


Figure 6. 2: Optical micrograph of a typical LM resistor structure. (a) Planar resistor structure (b) Stereo microscope image of freestanding interconnect. Reproduced from [80] with permission from Wiley.

Figure 6. 2a show an optical microscopy image of a typical printed resistor. Similar resistors with varying lengths l and width W (as shown in Figure 6. 3) were characterized. The height h of the obtained structures was measured with a profilometer.

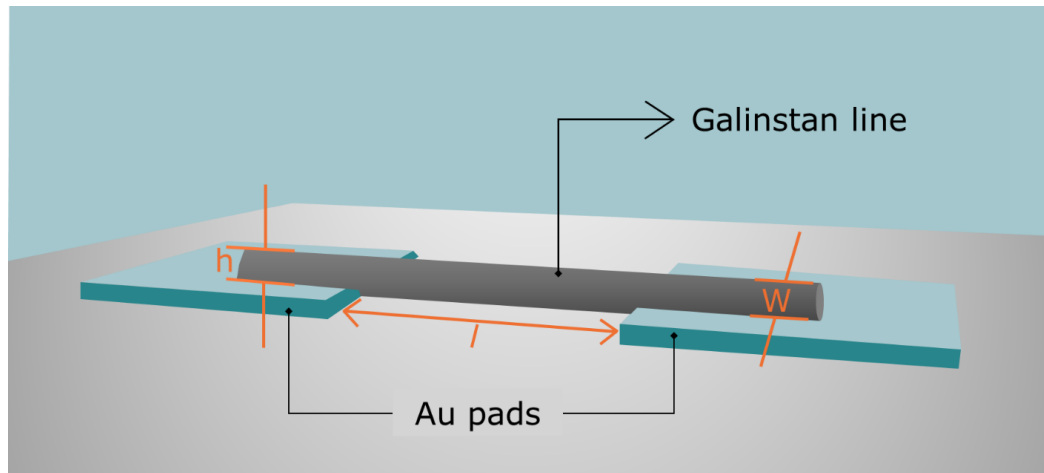


Figure 6. 3: A schematic of the Galinstan line printed over two gold pads shows the distance between the gold pads, which defines the length l of the resistor structure, the width of the LM line defines w , and the height h . Adapted from [80] with permission from Wiley.

Using two probe measurements, the absolute resistance (R) of the LM resistor structures was determined. All of the measurements were taken at room temperature

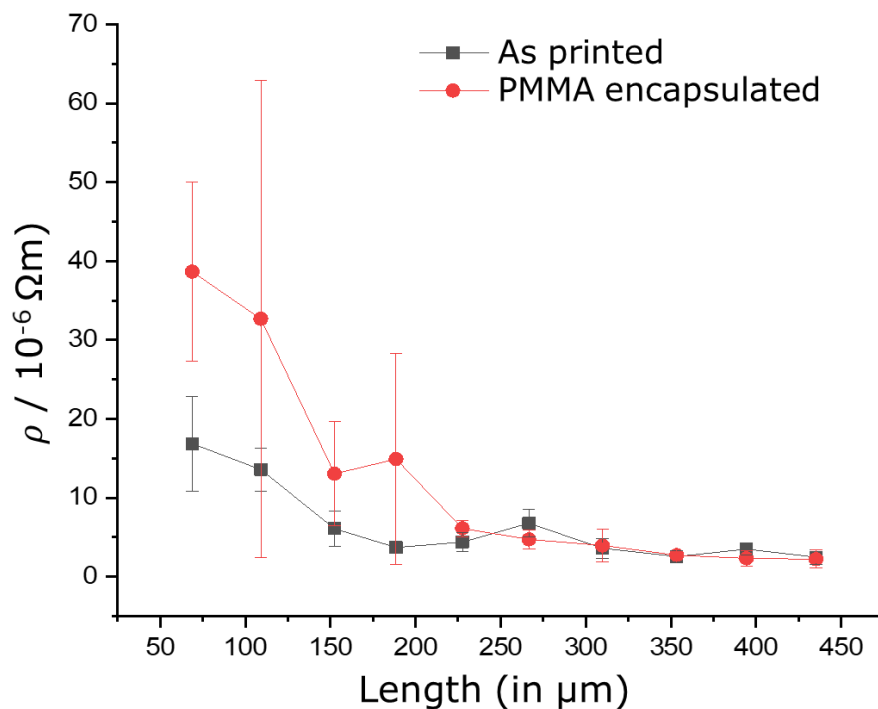


Figure 6. 4: Graph of specific resistance ρ for resistor structures of different lengths. The graph was plotted in Origin (OriginLab, USA). All error bars in graphs and error ranges reported represent one standard deviation (SD) of the reported mean. Reproduced from [80] with permission from Wiley.

and within eight hours after the LM printing. Measurements were done in triplicate from three different samples, and ρ was calculated from the measurements by:

$$\rho = R \frac{A}{l} \approx R \frac{wh}{l}$$

where

R : the measured absolute resistance

A : the area of the cross-section

w : width, l : length, and h : height of the printed interconnect/resistor.

The obtained data are plotted in Figure 6. 4, showing the calculated ρ for resistor structures of different lengths l . The area A can be approximated by $w \cdot h$ as the profilometer measurements reveal that for the relevant line widths, the curvature of

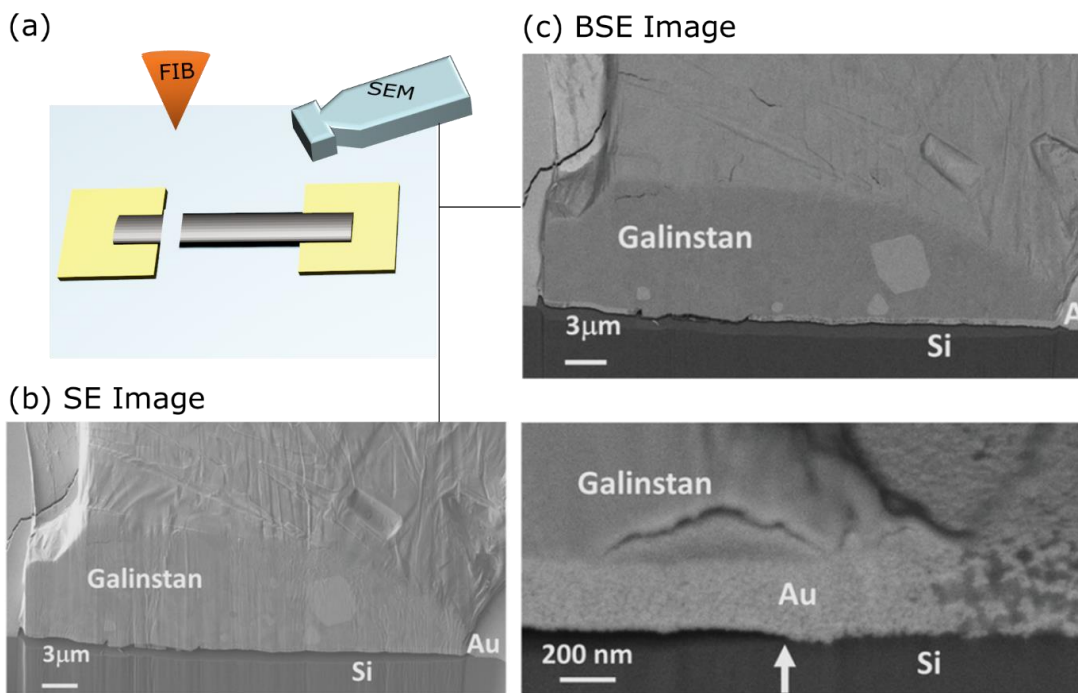


Figure 6. 5: Combination of focused Ion Beam for lithography and scanning electron microscope (FIB-SEM) analysis of a Galinstan line printed on a gold pad. (a) Sample description. (b) SEM secondary electron (SE, left) and (c) backscattered electron (BSE, right two) images of a cross-section through a Galinstan line show good contact between Galinstan and gold while the entire assembly lifted off the Si substrate during freezing (left of the arrow in BSE image) due to the larger thermal expansion coefficients of gold and Galinstan. Fabricated using a dual-focused ion beam (FIB)/scanning electron microscopy (SEM) (Crossbeam 540, Carl Zeiss Microscopy, Oberkochen, Germany) at Heidelberg University. Adapted from[80] with permission from Wiley.

the resistor lines is flattened to the extent that the cross-sectional area can be approximated as rectangular.

The material parameter ρ is expected to be constant. However, the plot (Figure 6.4) reveals that in the case of the resistor structures, ρ is significantly higher for short resistors, and it decreases as the length of the resistor increases. Above 150 to 225 μm in length, the change in ρ is insignificant and converges to a value that is just ten times lower than for bulk Galinstan [427], [428]. The raised ρ for small resistor lengths can be considered an artifact due to contact resistance at the Au/Galinstan interface dominating the overall resistance for shorter lines (as shown in Figure 6.5) and is discussed in chapter 8.

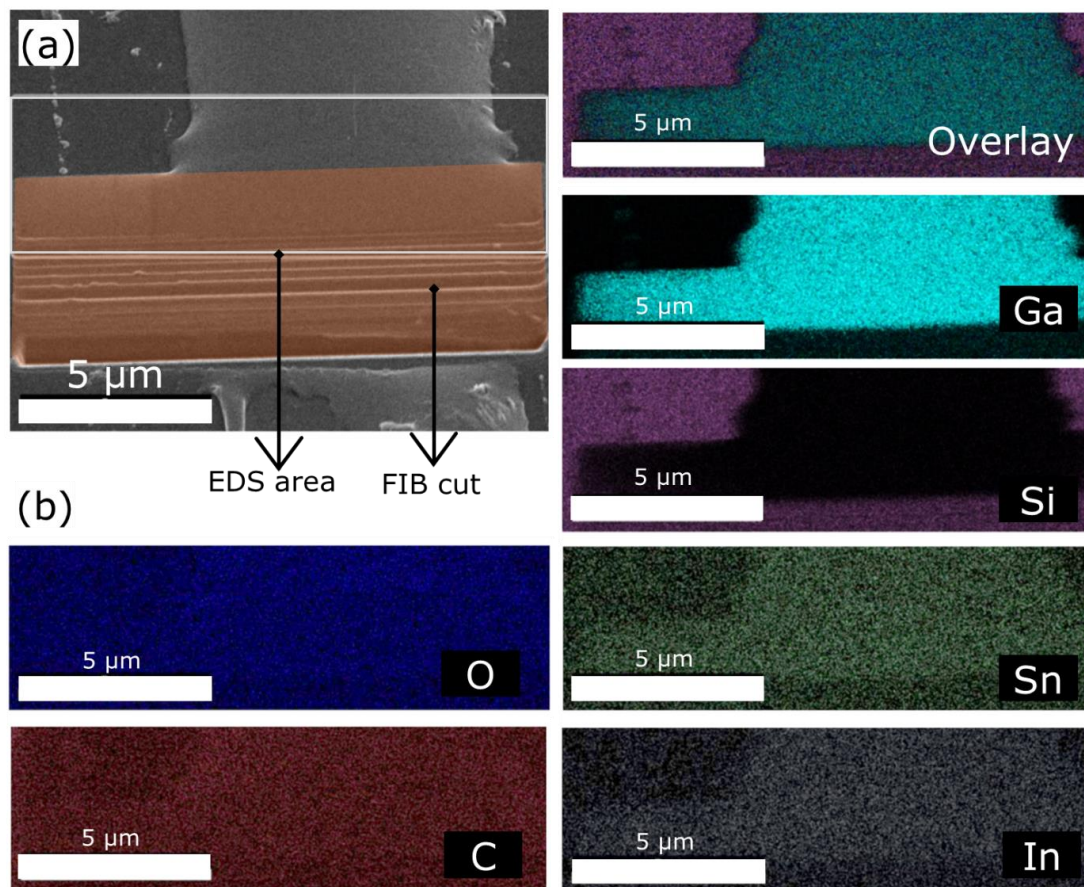


Figure 6. 6: EDS analysis of Galinstan line at room temperature. (a) Fresh cross-section of a printed Galinstan line shortly after milling with the FIB at room temperature. Multiple lines in the lower half of the image show drifting artifacts produced by the Ga-ion beam during milling, and image contrast reveal “wetting” of the complete cross-section with Galinstan (b) EDS-maps of detected elements, used energy lines in brackets. The displayed maps confirm the “wetting” process. Performed using a dual-beam Zeiss AURIGA 60 system (available at INT). Reproduced from [80] with permission from Wiley.

In this image, also a phase separation of the LM is visible as light and dark-shaded areas in the cross-sections. This separation is caused by the cooling of the LM for the cross-sectioning, as at room temperature, EDX shows a smooth and homogeneous chemical distribution (as shown in Figure 6. 6). It could also be caused by alloying and intermetallic structure formation, as discussed in chapter 8. As mentioned above, for smaller resistor lengths, the contact resistance dominates the overall resistance, while for longer resistor structures, it becomes negligible. Overall, the Galinstan retains a high electrical conductivity after processing with capillary printing, far exceeding other printable materials.

While being liquid is key for the processing of LMs and makes a big part of the appeal of such materials for applications, it also potentially is a source of concern in regard to stability, especially for structures built by additive manufacturing, as discussed here. Therefore, encapsulation of the structures after printing and its influence on electrical properties was probed for the resistor structures. Here, (PMMA) was chosen as it can act as a good barrier against oxygen and moisture and also provides mechanical protection. After completion of the first round of resistance measurements, PMMA was spin-coated on the substrates at 4000 rpm for 1 min, resulting in encapsulation of the LM resistor structures. After PMMA encapsulation, electrical resistance measurements were again conducted for the same resistor structures as before. All structures survived encapsulation, showing the relatively high mechanical stability of the LM due to the built-up oxide layer. Resistor structures of smaller length showed some minor increase in ρ and a higher variability (indicating that here the influence of encapsulation is most prominent), while for all structures longer than 150 μm , no significant change in ρ was observed due to encapsulation. These results show that encapsulation of printed LM structures is feasible and can be used to protect printed devices in applications if necessary.

6.2 Fully printed diode

Oxide semiconductors were studied widely in printed electronics due to their high electron mobility, transparency, and easy printability [15], [156]. Whereas oxides are usually n-type materials, also p-type semiconductors but with relatively lower mobility [15], [156]. Printed p–n diodes have shown excellent ON/OFF ratios in the range from 0 to 5 V with diode threshold voltages around 1 V [429]. However, these devices make use of ITO-sputtered electrodes, which were replaced in this work by LM-printed electrodes. Due to their elongated shape, these printed electrodes serve at the same time as intra-connecting wires in the fully printed diodes.

6.2.1 Fabrication of fully-printed p–n diode

Based on the printed Au pad structures, fully printed p–n diode devices were constructed with the help of oxide semiconductors (printed by an inkjet printer on a glass substrate) and capillary printed Galinstan lines with gold electrodes. The n-type

semiconductor film is based on an indium oxide precursor solution and was printed on top of the Galinstan line, which acts as the cathode of the diode. The device fabrication process (illustrated in Figure 6. 7) is as follows:

- I. Two pads for Anode and Cathode connection were printed with Gold nanoparticle-based ink. For the printing, the glass capillary was filled with Au polymer ink from UT Dots, Inc. (UTDAu25-IJ, see the materials in Table A.1) by dipping, utilizing the capillary force. Then, the ink was printed on the cleaned glass substrates (see substrate preparation) by contact spotting (bringing the capillary into direct contact with the substrate for a controlled time of 0.1 s). The substrates were then heated to 250 °C for 60 min for the Au nanoparticle-based ink to become conductive.
- II. The Galinstan bottom electrode was printed by glass capillary printing on the customized nanolithography system as described in chapter 4.
- III. Then, In_2O_3 ink was printed with a Dimatix 2831 inkjet printer on top of the Galinstan bottom electrode and dried for 10 min at 100 °C. The indium oxide precursor ink recipe is described in Annex A.2.3.

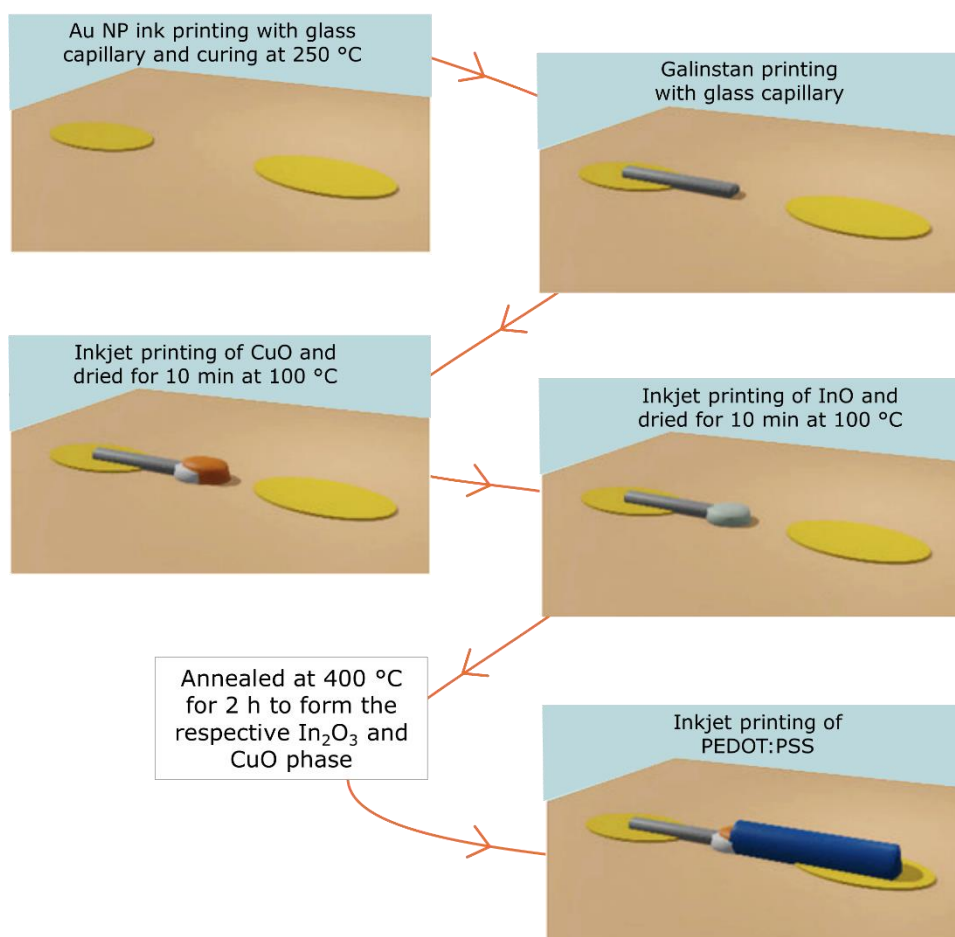


Figure 6. 7: Workflow for the construction of a fully printed diode by combining capillary and inkjet printing. Adapted from [80] with permission from Wiley.

- IV. After this, the p-type semiconductor ink was printed on top of the In_2O_3 pattern and dried as well for another 10 min at 100 °C. After drying, the substrate was annealed at 400 °C for 2 h to form the respective In_2O_3 and CuO phases. The precursor ink recipe is described in Annex A.2.3.
- V. Finally, the conductive polymer poly(3,4-ethylenedioxythiophene) polystyrene sulfonate (PEDOT:PSS) was printed on top of the CuO film and connected to the anode, which was based on printed gold NPs.

6.2.2 Characterization of fully-printed p–n diode

Figure 6. 8 shows an optical microscopy image of an optical micrograph of a typical printed diode (left) and the corresponding schematic.

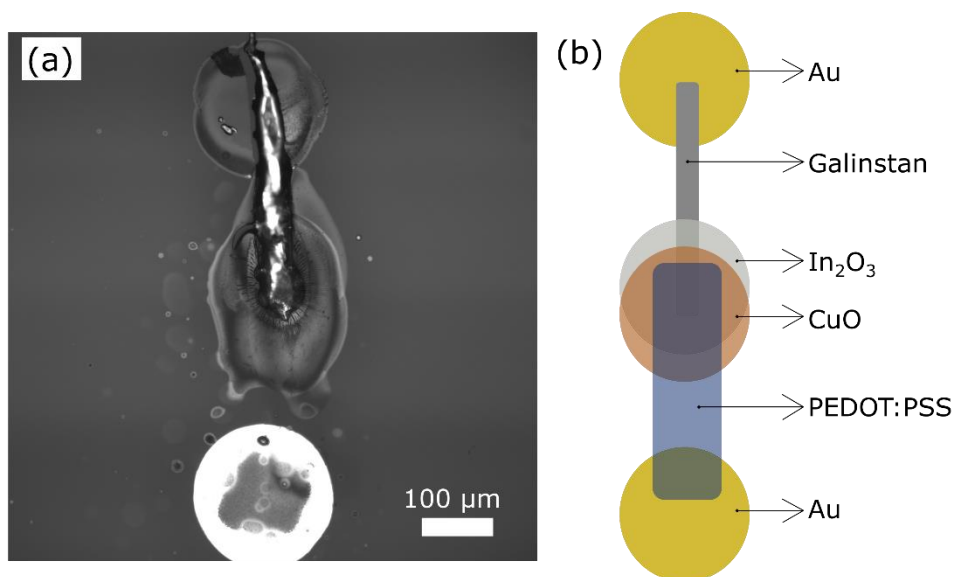


Figure 6. 8: Optical micrograph of a typical printed diode (left) and the corresponding schematic (right). Adapted from [80] with permission from Wiley.

The output characteristics of the diode were measured by sweeping the voltage from -10 to $+10$ V at the anode. The cathode of the diode is grounded. With the approximated p–n-diode area of $130 \times 60 \mu\text{m}^2$, the output in Figure 6. 9 shows that the current density of the Galinstan-connected diode is relatively high compared to previous work ($0.77 \text{ A}\cdot\text{cm}^{-2}$) [429].

Our results have shown currents in the order of $I_{\text{ON}} = 10^{-4}$ A and $I_{\text{OFF}} \approx 10^{-9}$ A, translating to a current density of $\approx 2.28 \text{ A}\cdot\text{cm}^{-2}$ at an area of $100 \times 100 \mu\text{m}^2$. This larger value in current density is the result of the improved performance related to the high conductivity of Galinstan combined with gold electrodes. Despite the satisfying I_{ON} , the current in the reverse region is quite high, which could be caused by pore formation during the annealing step of the oxide films. The PEDOT:PSS likely penetrated those pores and resulted in leakage currents. This might, however, be avoided by further engineering and printing process optimization.

A lot of solution-processed and inorganic materials are used in PE. Many of those can be used for developing fully printed electronic devices. In addition, these fully printed diodes have the potential to provide low-cost and flexible alternatives to traditional diodes through printed fabrication.

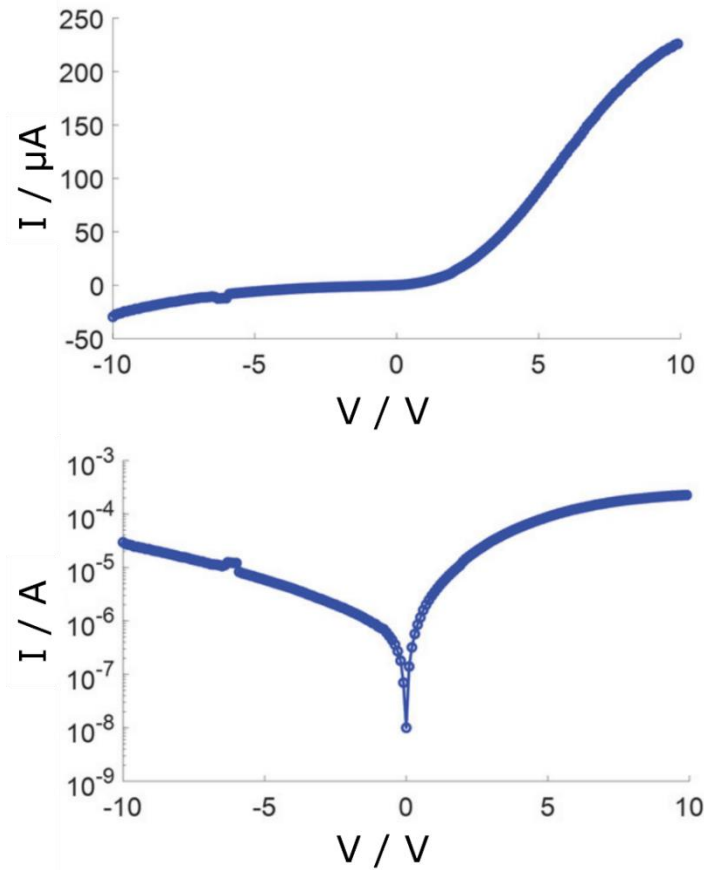


Figure 6. 9: Typical I–V characteristics of the printed diode in linear (top) and log-scale (bottom). Reproduced from [80] with permission from Wiley.

Table 6. 1: Comparison of fully printed p-n diodes.

| Electrodes | Method | n-type | Method | p-type | Method | Device architecture | Ref. |
|-------------------------|--|--------------------------------|--------------------------|--------|-----------------|---|---------------------------|
| Galinstan and PEDOT:PSS | Glass capillary printing and Inkjet printing | In ₂ O ₃ | Glass capillary printing | CuO | Inkjet printing | Glass/Galinstan/In ₂ O ₃ /CuO/PEDOT:PSS | Current work also in [80] |

| | | | | | | | |
|-------------------|--|--------------------------------|-----------------|-------------------|-----------------|---|-------|
| ITO and PEDOT:PSS | ITO structured using laser ablation and PEDOT:PSS with inkjet printing | In ₂ O ₃ | Inkjet printing | CuO or NiO | Inkjet printing | Glass/ITO/In ₂ O ₃ /CuO OR NiO/PEDOT:PS | [429] |
| Ag ink | - | InZnO | Spin coating | CNT network films | Drop casting | SiO ₂ -Si OR polyimide film/Ag/InZnO /CNT/Ag | [430] |

6.3 Fully printed transistor

Next, a fully printed transistor was fabricated based on prior work on partially printed electrolyte-gated field effect transistors (EGFETs). There all electrodes were not printed but were structured by lithography on sputtered ITO on glass [431], [432]. These EGTs showed higher gate capacitance compared to dielectrically gated, conventional ones due to the formation of a Helmholtz double layer. The high area-specific capacitance enables a low-voltage operated device with a high ON-current [433]. As in the case of the p–n diodes, an indium oxide (In₂O₃) precursor solution was used for printing, further annealed at 400 °C to form the functioning n-type channel material for EGT. These channel materials feature high field-effect mobility ($>30 \text{ cm}^2 \cdot \text{V}^{-1} \cdot \text{s}^{-1}$); therefore, high $I_{\text{ON}}/I_{\text{OFF}}$ ratios at low voltage levels are feasible.

6.3.1 Fabrication of fully-printed transistors

For the fully printed transistors following steps were completed for fabrication.

- I. All the drain, gate, and source electrodes were printed using a glass capillary system with gold nanoparticles ink. The pads were printed similarly to the pads printed in the last section.
- II. Galinstan conductive lines that are extended from the drain and the source gold electrode were printed by the glass capillary printing system described in chapter 4.
- III. Then, In₂O₃ as an n-type semiconductor channel was printed via glass capillary in between the extended Galinstan lines. Then, the substrate was annealed at 400 °C for 2 h.
- IV. Afterward, a composite solid polymer electrolyte (CSPE) was printed by inkjet printing on top of the indium oxide channel. This layer partially covers the Galinstan line that is attached to the channel.
- V. Subsequently, the conductive polymer (PEDOT:PSS) was inkjet printed on top of the CSPE layer and connected to the gate electrode pad.

The printing process of the transistor is illustrated in Figure 6. 10.

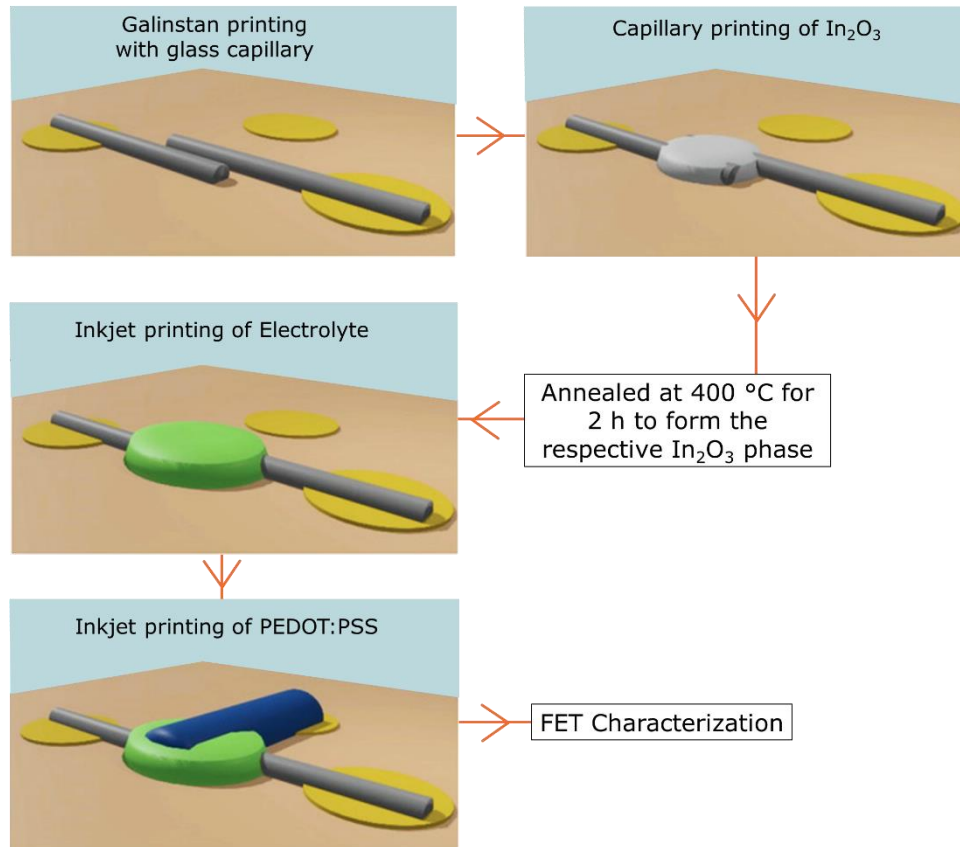


Figure 6. 10: Workflow for the construction of a fully printed FET by combining capillary printed Galinstan lines and inkjet printing for the materials In_2O_3 , PEDOT:PSS, and electrolyte. Adapted from [80] with permission from Wiley.

6.3.2 Characterization of fully-printed transistors

Figure 6. 11 shows an optical micrograph of a typical printed FET (left) and the corresponding schematic (right).

The transistor was characterized by a semiconductor parameter analyzer at RT with a 50% humidity level and a gate voltage (V_{GS}) sweeping from -1 to 1 V. As the transfer and output characteristic curves given in Figure 6. 12a,b show, the transistors display a negative threshold voltage (V_{th}) of -0.31 V and a current ON/OFF ratio of 1.84×10^3 . It was also observed that there is a leakage current in the order of 10^{-8} A. The thickness of the electrolyte layer on top of the Galinstan lines is thinner so that PEDOT:PSS might penetrate the electrolyte in these areas, causing this significant leakage current. This might be improved by future optimization of the printing process, also addressing the yield ($\approx 19\%$) of obtained transistors.

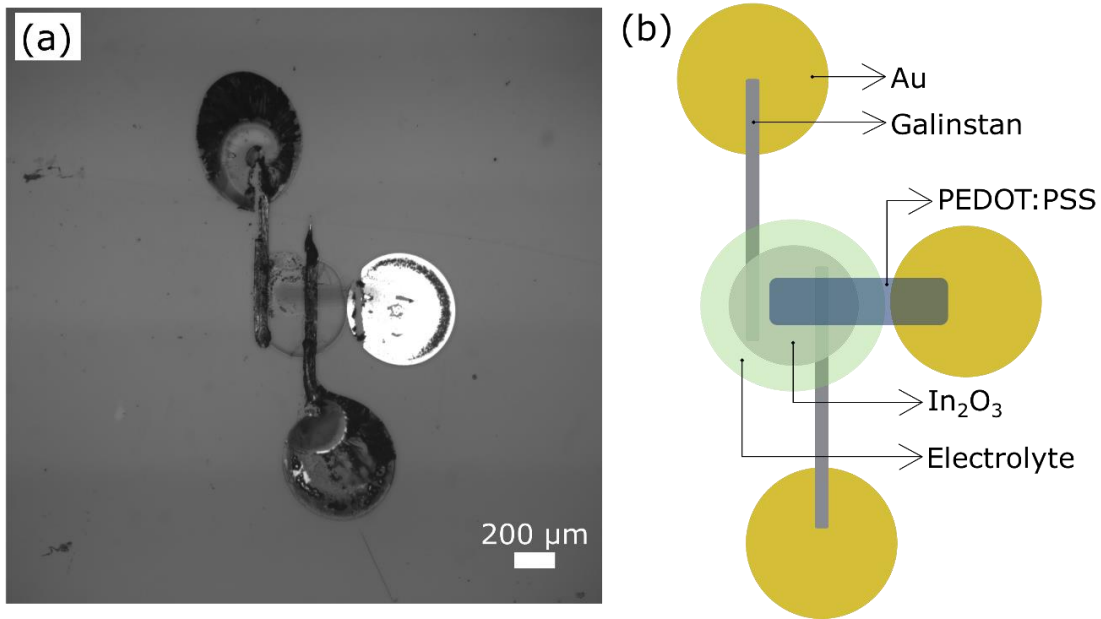


Figure 6. 11: Optical micrograph of a typical printed FET (left) and the corresponding schematic (right). Adapted from [80] with permission from Wiley.

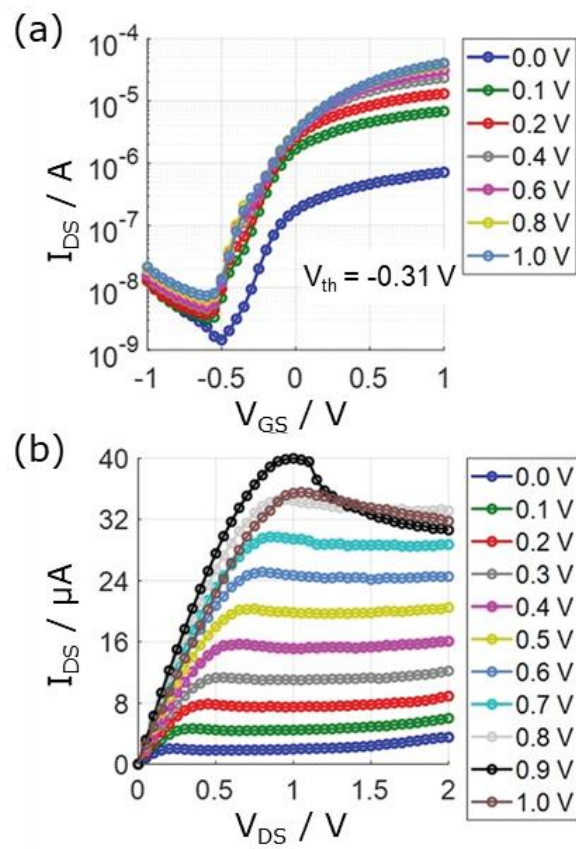


Figure 6. 12: I-V characteristics of the FET for the voltage applied to (a) ground/source (top) and (b) drain/source (bottom), respectively. Reproduced from [80] with permission from Wiley.

However, if a high yield and higher performance are required, the Galinstan can be replaced with gold. For a normally-OFF transistor with V_{th} of 0.206 V and a normally-ON transistor with a V_{th} of -0.211 V, the transfer curves are shown in Figure 6. 13a and b, respectively. For reliable circuit designs, both normally-ON and normally-OFF operation modes are essential. The subthreshold slope is comparable in both cases, ≈ 98 mV \cdot dec $^{-1}$ (normally OFF) and (≈ 109 mV \cdot dec $^{-1}$). Nevertheless, the fabricated all-gold printed devices demonstrated better reproducibility with a yield of $\approx 82\%$. A current leakage of $\approx 10^{-7}$ A was observed, which is higher compared to the Galinstan-based transistors; however, this is expected since the current driving capability in gold is higher than in Galinstan.

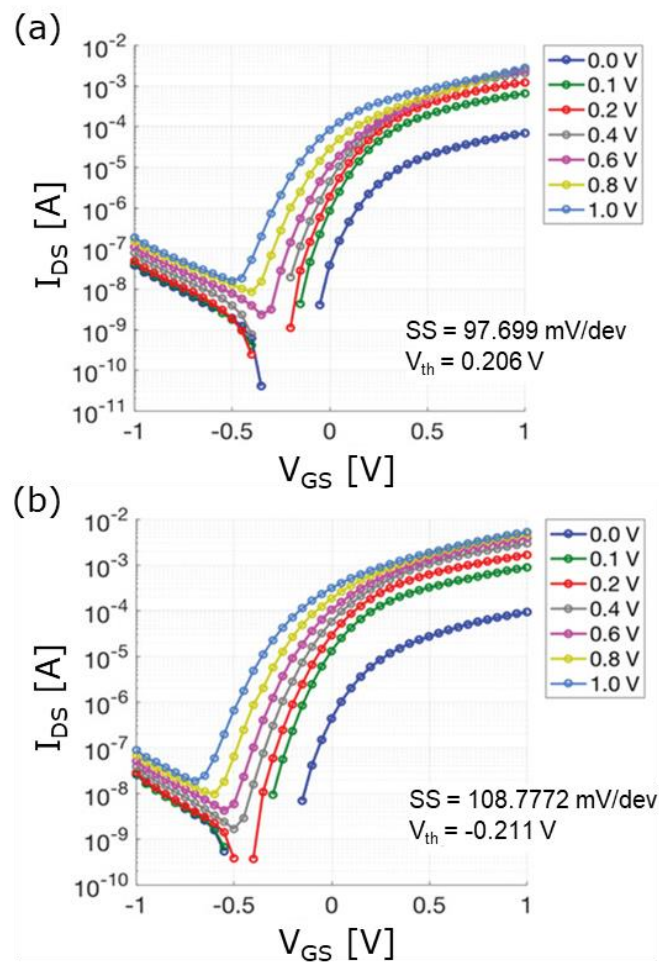


Figure 6. 13: Characterization of fully printed transistors with Au electrodes. Transfer characteristics of the transistor operating in (a) normally-OFF mode and (b) in normally-ON mode. Reproduced from [80] with permission from Wiley.

7. LM-based printed microheaters

The LM direct-write technique described in chapter 4 was used to fabricate LM-based microheaters on glass substrates. This chapter discusses the effects of power and voltage on the microstructural properties of Galinstan and different printed microheater designs. Additionally, the thermal characteristics of the microheater are evaluated.

7.1 Fabrication of the microheater structures

- I. First, macroscopic electrodes were hand-painted to the freshly cleaned glass substrate for a contact using Ag epoxy paste (Elecolit® 3653 10g).
- II. Galinstan microheater line structures were printed using glass capillaries of different apertures depending on different designs. The samples fabricated for the Resistance vs. Temperature studies, the Galinstan pads were hand-painted after the line printing.
- III. All of the samples were explored with optical microscopy, characterized via a resistance vs. temperature study and power vs. temperature study.
- IV. The digitally defined line width of the meander lines varies from a minimum of 20 to up to >1000 μm for various cross-sections and designs. Figure 7. 1 shows a summary of the different designs with varying lengths, widths, and cross-sections.

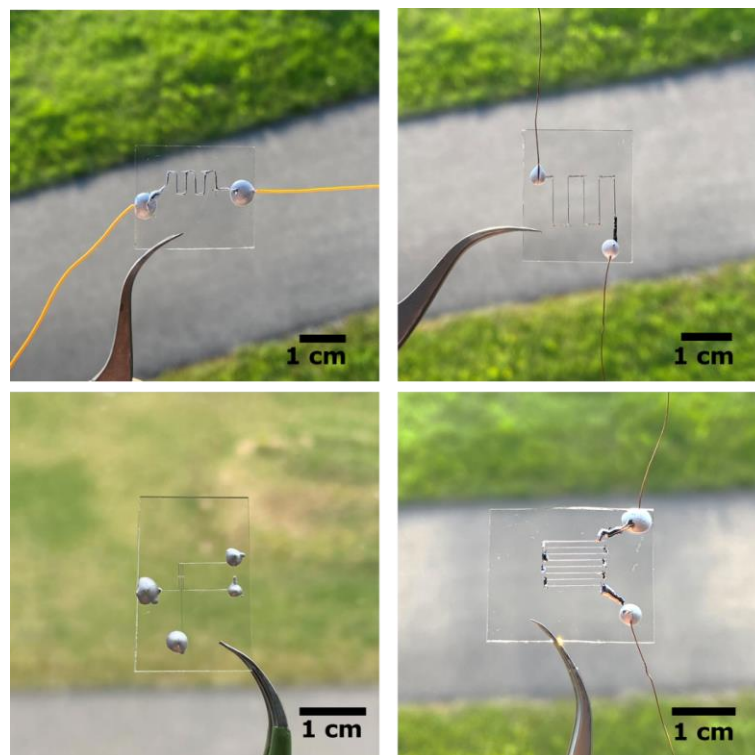


Figure 7. 1: Example of different LM microheaters with different designs and structure sizes (line width) obtained by tuning writing parameters.

7.2 Microheater characterization

All the printed microheater structures were characterized by an optical microscope. A Keithley 2000 multimeter was used to test the resistance. A Keysight B2902A source measure unit (SMU) was used to apply a voltage across the heater. The thermograms were captured with a Bosch professional GTC 400C, which was mechanically put near the microheater surface. Microheater structures were kept uncoated during all the experiments.

Optical microscope images of Galinstan microheaters onto a glass substrate were captured (Figure 7. 2). The minimum width of the LM-based microheater structures is around $20\ \mu\text{m}$, and the average width of the LM lines for microheaters tested in the experiments is about $100\ \mu\text{m}$, if not otherwise mentioned.

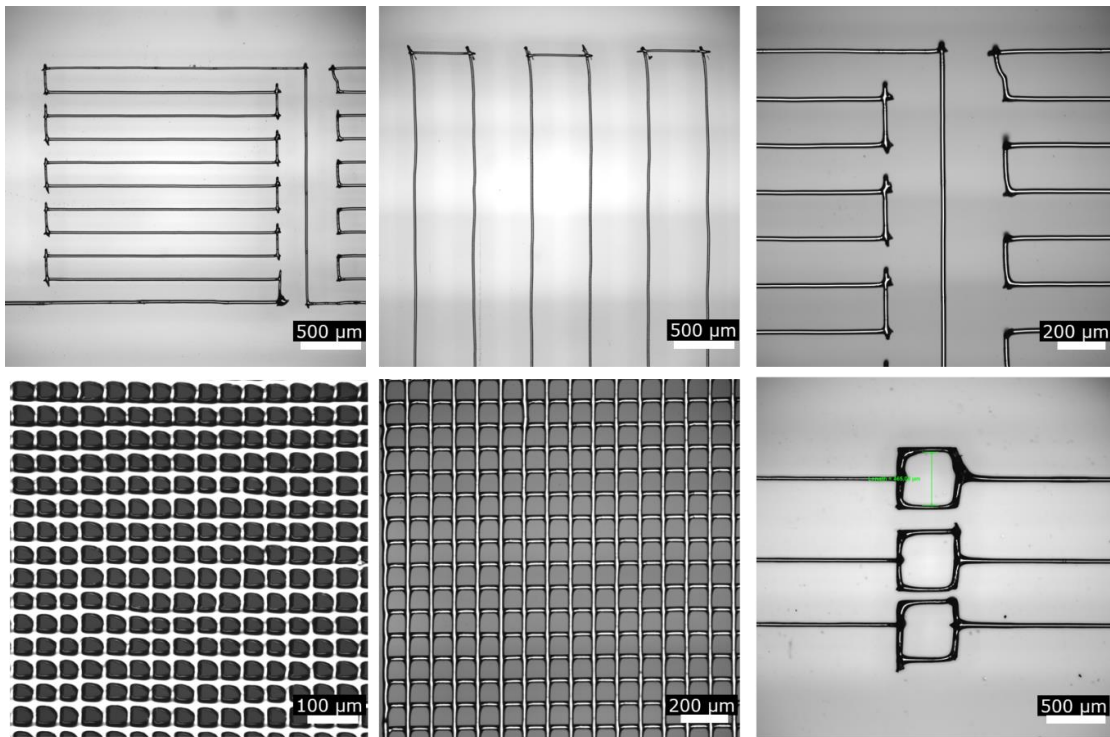


Figure 7. 2: Optical microscope images of different microheater structures on glass were used in this study.

7.2.1 Thermograms

The temperature distributions of the microheater were measured by an advanced thermography system, Bosch professional GTC 400C, which has a visual camera integrated with an infrared sensor with a thermal resolution of 160×120 pixels, providing detailed thermal images (Figure 7. 3 shows a typical thermogram capture).

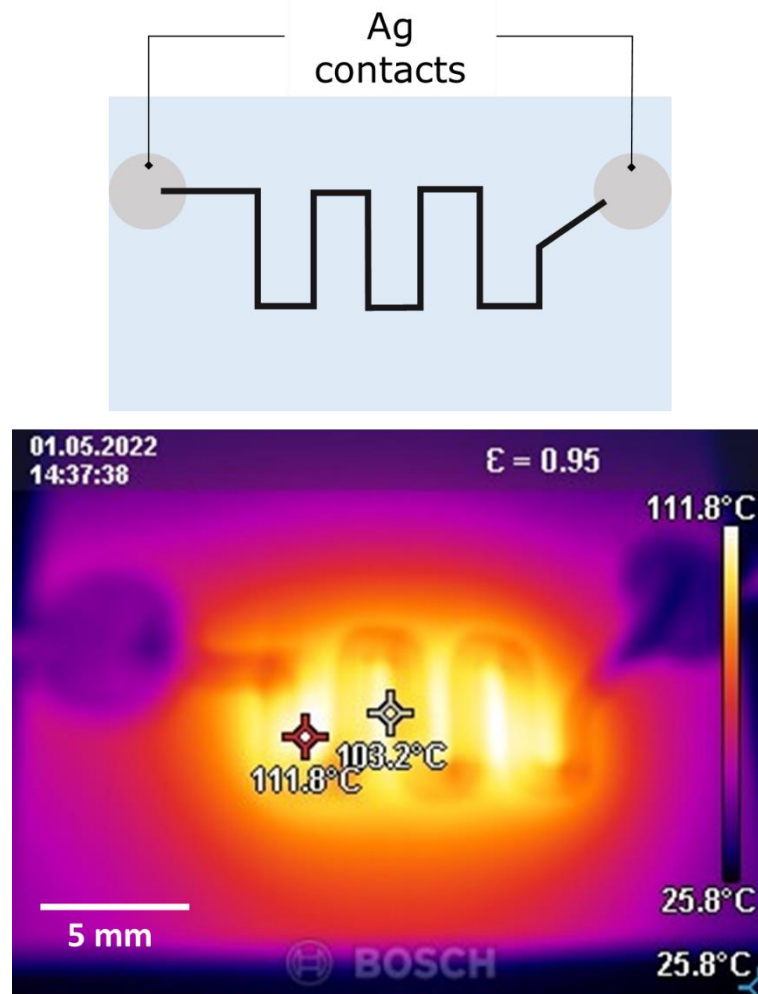


Figure 7. 3: A thermogram showing the temperature distribution for a typical microheater structure (bottom) and the corresponding design (top).

7.2.2 Temperature dependence of LM resistance

In order to acquire resistance vs. temperature data, each microheater was heated on a hotplate at different temperatures. When the microheater temperature was maintained at higher temperatures (around more than 60°C) for a longer duration, the resistance of the printed structures kept on increasing even after approximately 5 minutes, so to keep the data points comparable, at each temperature point, the micro heater was allowed to settle for 15 minutes after reaching thermal equilibrium. Figure 7. 4 shows the measurement setup, and Figure 7. 5 shows the measured electrical resistance of micro heaters with respect to temperature, which is similar to previous reports [434].

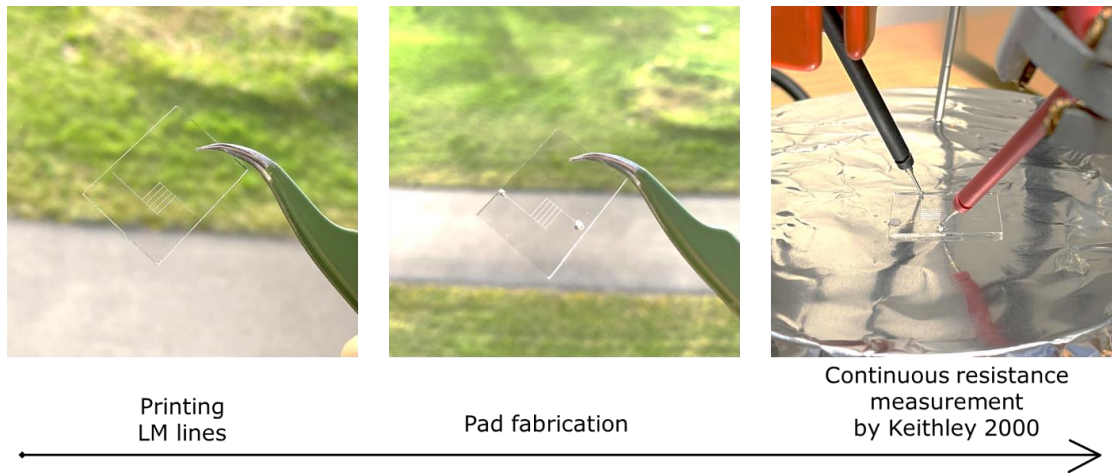


Figure 7. 4: Set up to measure resistance measurement at various temperatures.

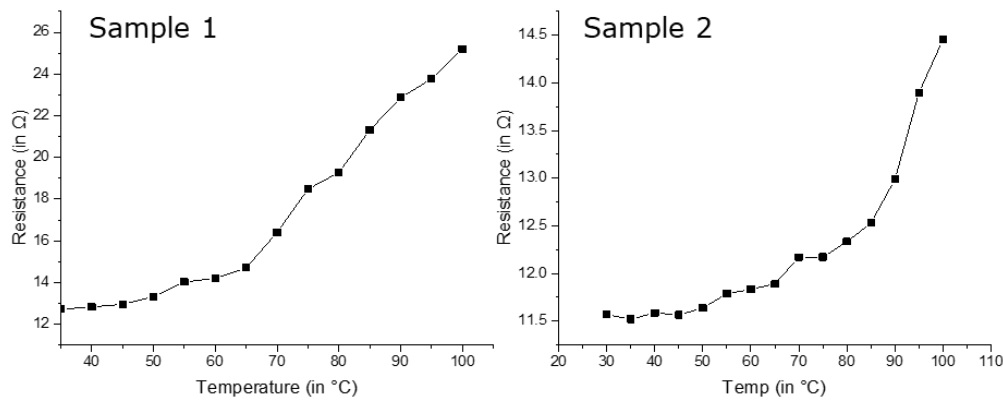


Figure 7. 5: Electrical resistance of LM microheaters of the design (devices shown in Figure 7. 4). This plot is in accordance with previously reported Resistivity vs. Temperature data from [434].

An interesting observation during measurement observed that upon heating beyond around 50 $^{\circ}\text{C}$, some LM line structures start showing high resistance in the range of $\text{k}\Omega$, or, at a certain point, the connection breaks completely.

When observed under the microscope (Figure 7. 6), these LM structures show shrinkage in the width of the LM line. It might be that LM displaces or voids are formed underneath the oxide layer as, during heating, the thermal gradient is formed. If LM-based patterns are subjected to high temperatures, these easily break. In previous reports, it has been suggested that this breakage occurs due to voids forming within the LM structures that expand while heating and finally break the circuit. There have been two hypotheses proposed in order to explain why voids can form in LM structures, which are either due to (I) metallic electromigration effects [107] or (II) a mismatch between temperature expansion coefficients (TEC) (the in case of LM filled in PDMS microchannels) [106].

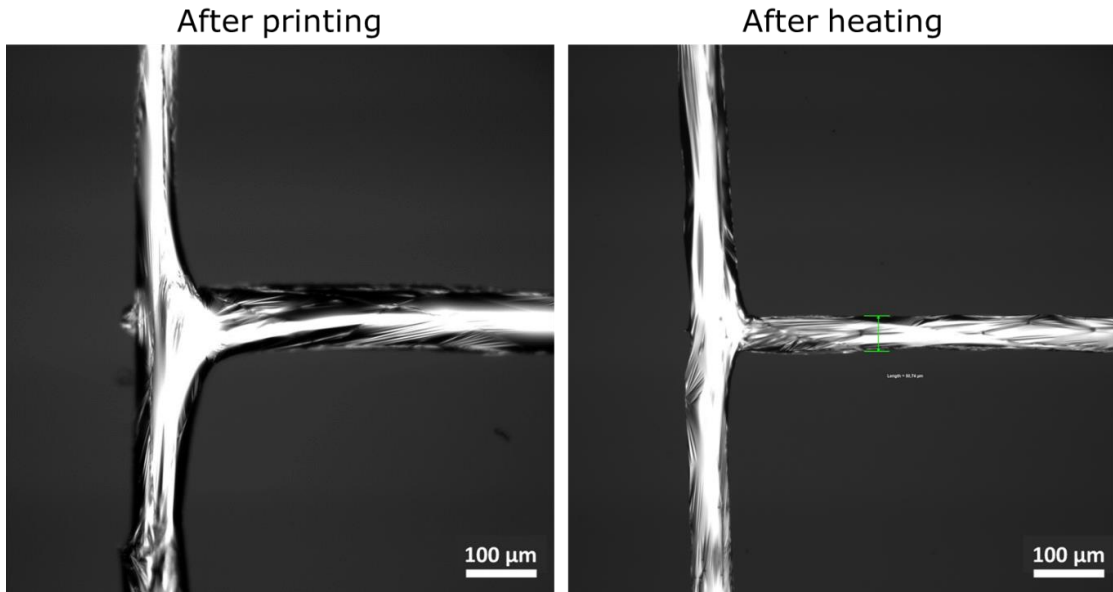


Figure 7. 6: Optical microscope images of a LM microheater structures part right after printing (left) and after heating (right).

The shrinking of the LM line, as shown in Figure 7. 6, and the breaking of LM lines can be explained by electromigration theory [435], [436]. According to this, it can be said that if a high current density is flowing through these LM lines, the momentum of these electrons, which are carrying current, can be transferred to the core metal ions, and these core metal ions can be drifted in the direction of electrons, and this drift from its original position can be referred to electromigration.

In our case, the LM ion cores might also feel opposing forces, as shown in Figure 7. 7a, the F_{Wind} is the wind force generated from the moment exchange between the electrons and the LM ion core, and it is in the opposite direction of the electric field and in the direction of electron wind flow. The second force is F_{Field} , the force in the direction of the electric field. Wind force can be higher than the Field force, and as a result, the LM ions may start drifting [435]. In the present case, the oxide layer (Ga_2O_3) stays with the glass substrate, but LM into the core moves, leaving behind only the oxide layer and the formation of the void at that place, as a result breaking the connection.

An alternative explanation is that a small amount of air may remain inside the heating LM line while printing. Aside from this, air can also leak through the oxide layer and enter the LM line. As the liquid metal is heated and voltage is applied to it, voids begin to form and expand in the LM line. When the temperature rises further, the volume of air inside the channel expands, causing the number and size of voids to increase, finally resulting in a circuit break. Figure 7. 7b shows the complete voiding, growth, and eventual breakdown of the liquid metal, which might be the reason behind the whole process of LM lines break-up and microheater failure [107].

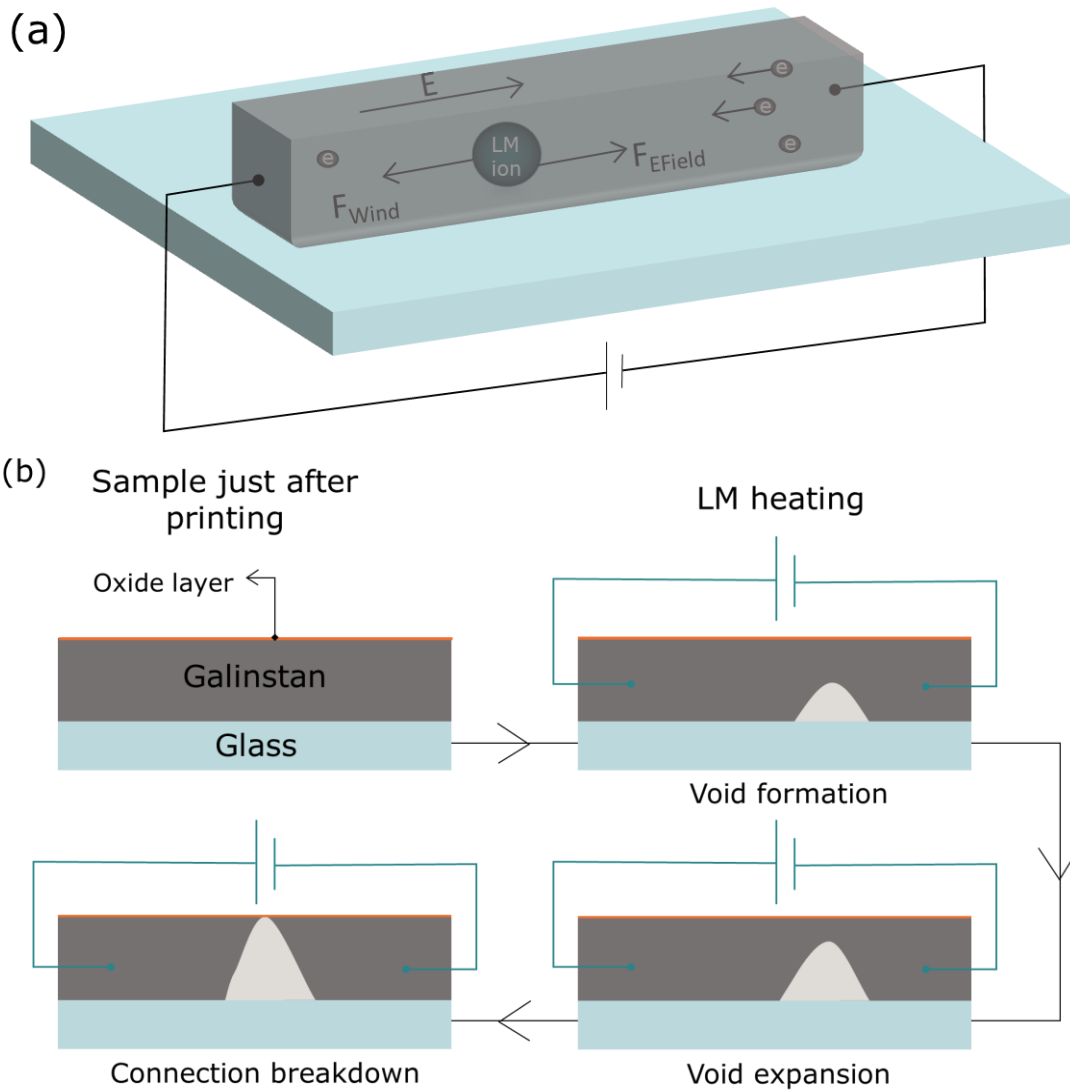


Figure 7. 7: (a) Schematics of electromigration in LM printed line. (b) Schematics of LM line break-up within the heating channel induced by voids. Adapted from [107] with permission from MDPI, © 2020, under the terms and conditions of the Creative Commons Attribution (CC BY) license (<http://creativecommons.org/licenses/by/4.0/>).

One possible solution to avoid the voids is – instead of using additive written wires of LM as heater elements – to continuously inject LM into a microfluidic device (as shown in Figure 7. 8) that is structured with encapsulated microchannels. However, this only partially solves the problem and generates another issue. Despite its effectiveness in filling voids and generating a uniform temperature field, this method needed an additional pump to supply LM, and also, the microchannel-substrate needs to be fabricated itself, which makes this approach inconvenient for use [106].

The temperature-dependent resistivity in LMs, microheater geometry, and air void expansion can affect these printed LM microheaters' electrical resistance and efficiency.

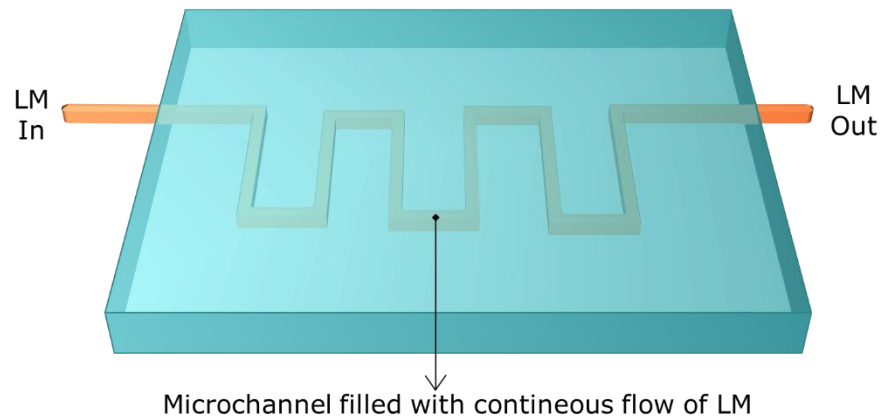


Figure 7. 8: Microheater based on continuous injection of LM in encapsulated microchannels.

For the direct-written LM microheaters, the problem of breaking connections can be partly solved by printing multiple layers on top of each other (Figure 7. 9) and thus increasing the height of the pattern. This approach enabled the fabrication of more stable microheater structures, which were then further characterized.

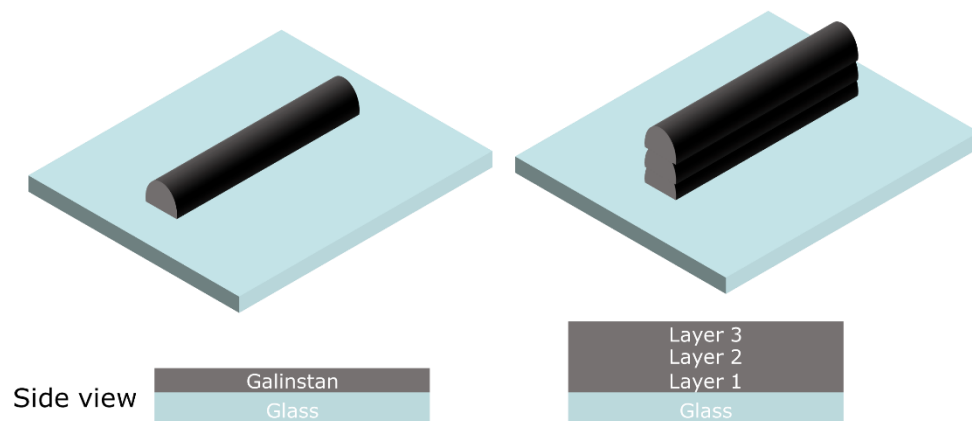


Figure 7. 9: Printing multiple layers on top of each other increases the pattern's height and provides more temperature-stable structures.

7.3 Thermal parameter characterization

Several thermal parameters should be considered when choosing a microheater, including its power consumption and response time [362], [437].

As shown in Figure 7. 10a, two samples (different from Sample 1 and 2 from the last section 7.2 and Figure 7. 5) named P-T_sample1 and 2, were printed with the help of the LM direct writing method. These structures were characterized for power consumption curves using a unit step voltage input, and local temperatures at the substrate's center and each microheater's resistances were measured before and after turning on the DC power supply. DC voltages ranging from 0.1 to 2 V were applied to characterize the microheater systematically. In order to ensure that the microheater achieves thermal equilibrium with its surroundings, the voltage was

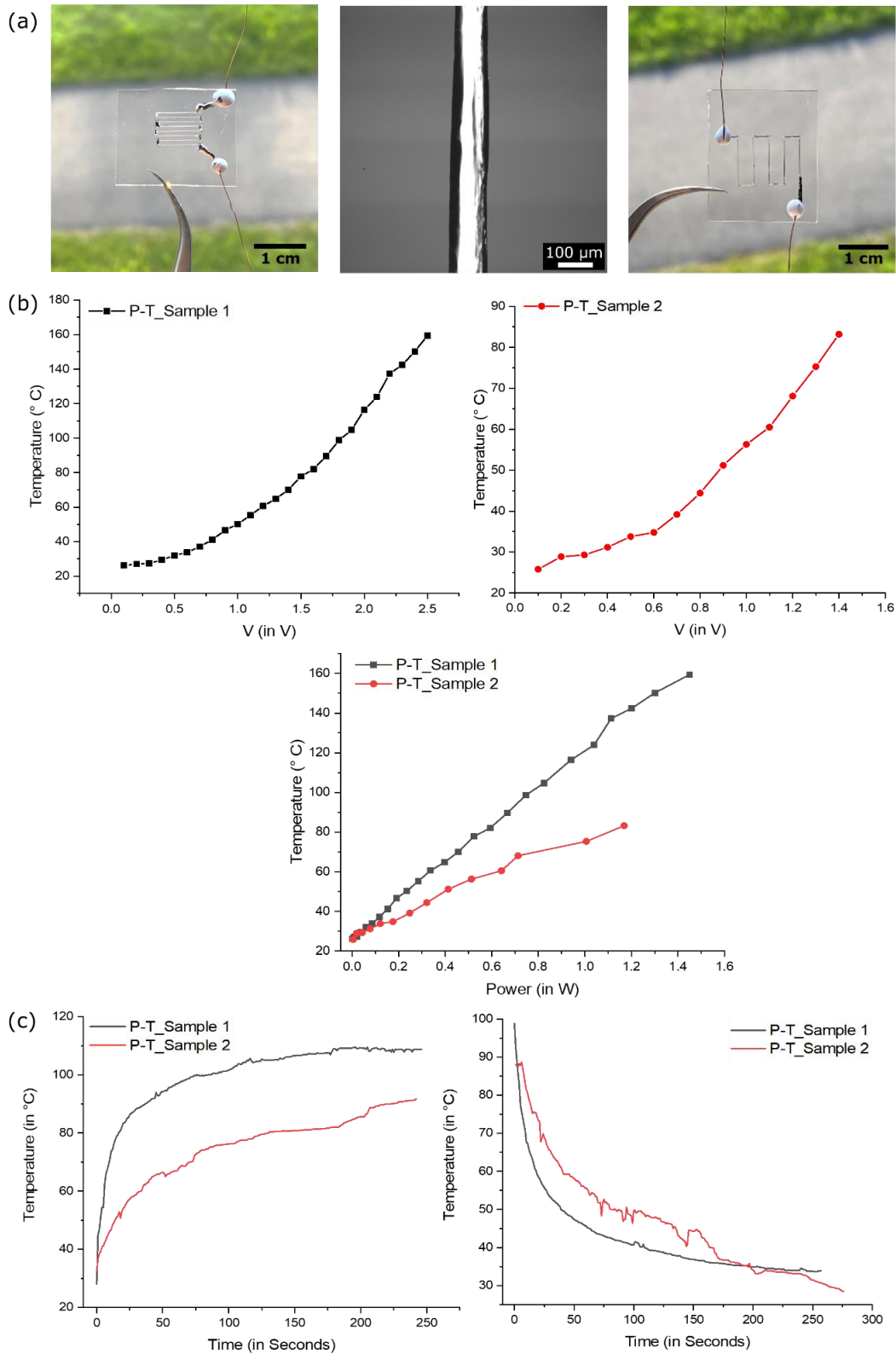


Figure 7. 10: (a) Photo and optical microscope image of P-T_sample1 and 2. Line width: $(108.49 \pm 4.54) \mu\text{m}$ (b) Recorded maximum surface temperature with respect to the power applied. (c) shows the heating and cooling cycles for both LM microheaters where a voltage of 1.5V and 2 V are applied, resulting in a 0.92 W and 1.54 W power consumption in LM microheaters P-T_Sample 1 and 2, respectively.

increased by 0.1 V, and the time interval between two consecutive runs was set to 15 minutes.

The Joule heat generated can be expressed as follows:

$$P = IV = I^2R = \frac{V^2}{R} \quad (7.1)$$

Where:

V: voltage is applied to the microheater,

R: is the resistance of microheater, and

I: current is flowing through it.

As shown in Figure 7. 10a, two samples were fabricated with an average line width of $108.49 \pm 4.54 \mu\text{m}$. The P-T_sample1 was fabricated by printing eight LM lines (each of 1cm in length) at a pitch of $1000 \mu\text{m}$, later connected to the Ag electrodes, so the total length of meander LM structures for P-T_sample1 is around 9.3 cm. On the other hand, the P-T_sample2 was fabricated by printing five LM lines (each of 1 cm in length) at a pitch of $3000 \mu\text{m}$ and later connected to Ag electrodes; the total length of meander LM structures for P-T_sample2 is around 6.9 cm. The resistance of each sample was monitored before and after the heating and temperature measurement; it remained at 3.5Ω and 1.4Ω for P-T_sample1 and 2, respectively.

Figure 7. 10b shows the thermal response curve of the LM microheater, and it shows the maximum temperature achieved on the microheater substrate (159.4 and 83.2 °C for P-T_Sample 1 and 2, respectively). In order to determine the response, the microheater was turned instantly onto the power of 0.92W and 1.54W for P-T_Sample 1 and 2, respectively, to study the heating cycle. After reaching the steady state, the power was turned off after the temperature stabilized, and the time it took to reach room temperature was also recorded to investigate the cooling cycle.

While heating, microheater P-T_Sample 1 reaches a steady state in around 175 s, and P-T_Sample 2 reaches a plateau after around 250 s. While cooling, both samples take around 250 s to reach near room temperature. The experiment shows that the layout can tune the obtainable temperature and general electronic/temperature characteristics. In general, higher-resistance heating resistors require a lower current to achieve the same temperature as a lower-resistance-heating resistor. So, in addition to tuning the layout - it is conceivable to construct a lower current LM microheater with higher resistance by mixing the LM intentionally with impurities and using these composite inks for the construction of the microheater.

Comparing the obtained microheater to existing demonstrations (Table 7 1) reveals the advantages and limitations of the LM-based heater structures.

7. LM-based printed microheaters

Table 7 1: Comparison of previously reported printed microheaters and LM-based microheaters with current work.

| Heating Material | Substrate | Method | Design | Line width | Max Temp (in °C) | Max Voltage | Power Consumption | Response Time | Application | Ref. |
|------------------|--------------------------------|--|--|------------|------------------------------|-------------|-------------------|-------------------------|---|-----------|
| Galinstan | Glass | Direct writing | Meander | 20 μm | 159.4 It can go up to 200 | 2.5 V | 1.45 W | ≈150 seconds | Microchannel and valve | This work |
| EGaIn | PDMS embedded | Injection | Meander | 200 μm | 223.4 | 2 V | 1.89 W | ≈ 03 hr 30 min | Flexible heater | [107] |
| EGaIn | PDMS or silicon | Liquid metal injection | C shaped | ≈350 μm | ≈100 | 2.42 V | ≈1W | ≈800 s for steady state | PCR, thermophoresis, and incubation | [106] |
| Galinstan | PDMS and other polymers | Laser ablated mask + LM droplet spraying | Circular, rectangle maze, and serpentine/meander | 20 μm | 30 as per the application | - | - | - | Epidermal patches on Drosophila abdomen | [438] |
| Pt | Alumina ceramic film | Aerosol jet printing | Meander | 40-60 μm | 450 | - | ≈80 mW | 3 seconds | Gas sensor | [439] |
| Pt | Al ₂ O ₃ | Micro-pen and laser sintering | Meander | 100-200 μm | 400 | - | 3.55 W | < 35 s | Microelectronic applications | [440] |

| | | | | | | | | | | |
|-------------------------------------|----------------------------------|-----------------|----------------------|----------------------------|---------------|-------|--------|-----------------|--|-------|
| Silver metal paste | ITO Glass | Screen printing | Plate | Thickness 10 μm | 42 | - | - | ≈ 60 s | Cell culture | [441] |
| Silver Ink (LOCTITE ECI 1010 E & C) | Polyethylene terephthalate (PET) | Screen printing | Meander | 500 μm | ≈ 100 | 2.7 V | | ≈ 200 s | Cell culture and PCR applications | [442] |
| Nanosilver Ink | Kapton | Inkjet printing | Meander (design 1_1) | 0.53 mm | ≈ 90 | 1V | 180 mW | - | E. coli and V. cholerae LAMP incubations | [443] |
| Nanoparticle silver ink | Polyethylene naphthalate (PEN) | Inkjet printing | Meander (Design 2) | Min 250 μm | ≈ 120 | 12 V | 4.8 W | ≈ 20 s | Flexible heater | [444] |

The main advantage of this direct writing of LM microheaters is that it offers freedom of design as no mask or microchannel design is needed. Also, in comparison to other microheaters based on Pt, Au, or Ag, these LM microheaters are more cost-effective. Direct writing also eases the fabrication process, and it is possible to fabricate a wide variety of designs on the substrate. These structures also have an extremely fast response time, able to reach beyond 100°C in 150 seconds, which is much shorter than previously observed microchannel microheaters [106], [445].

7.4 Microvalve application

This method of on-demand printing of LM structures for microheaters can be applied to produce microvalves to control fluid flow. For this purpose, a thermoresponsive poly(N-isopropylacrylamide) (PNIPAM) based hydrogel was used, which can work as material for stimuli-responsive release processes and microvalves. Hydrogels based on PNIPAM can be easily prepared in water [446]. A PNIPAM solution undergoes a reversible lower critical solution temperature (LCST) phase transition from its soluble hydrated state to its insoluble dehydrated state at temperatures higher than their cloud point. Generally, this transition occurs at 32 °C [447], [448]. For the demonstration as a microvalve, a commercially available microchannel was functionalized with the PNIPAM and microheater and used to gate a fluorescent liquid

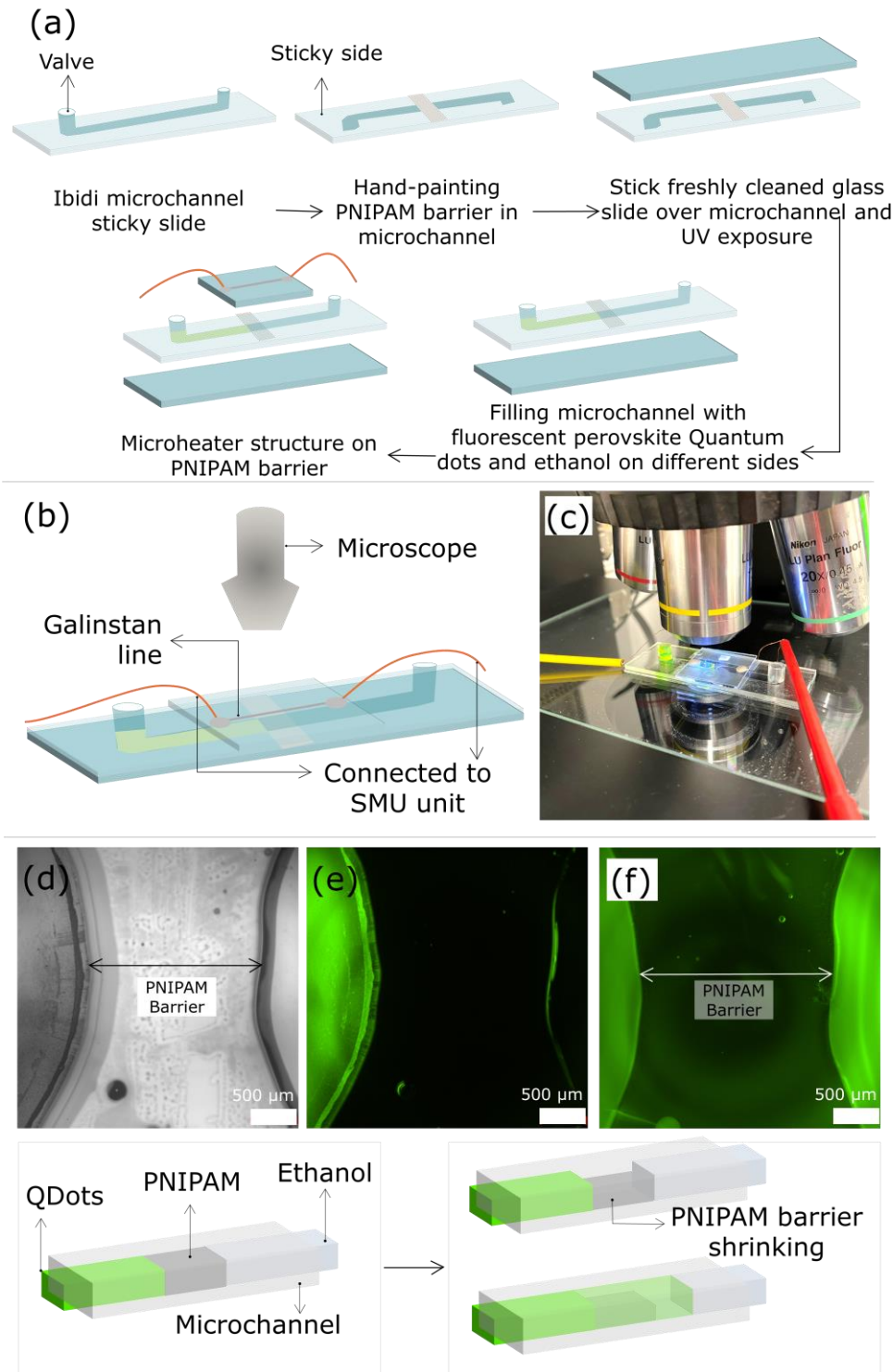


Figure 7. 11: Microheater for microvalve application. (a) Scheme of device fabrication. (b) Schematics of the complete setup. (c) Actual photograph of the setup. Microscope images of the PNIPAM barrier and adjacent QD liquid (d) in bright field and (e) in fluorescence with FITC filter (B-2E/C, Nikon, Ex.: 465–495 nm, Em.: 515–555 nm). (f) shows a fluorescent image of the microchannel after triggering the PNIPAM valve by heating, allowing the fluorescent QDs to diffuse into the other parts of the channel. Inset showing ON and OFF conditions.

(Perovskite QDs) and ethanol for visualization purposes. The preparation of the device and the observed gating activity are presented in Figure 7. 11.

Fabrication steps for the microvalve demonstrator:

- I. First, PNIPAM was hand painted in a microchannel (on the sticky side) of the ibidi microchannel slide.
- II. Freshly cleaned microscope glass slide (75 mm X 25 mm) was stuck on the microchannel side.
- III. The PNIPAM was exposed to UV light (torch with 365nm, 3 minutes) to cure.
- IV. One side of the microchannel was filled with Perovskite quantum dots solution in one side and another side with ethanol.
- V. Fabricated microheater structure was installed on the ibidi chip.

After the microvalve microchannel is completed, it is put under a fluorescence microscope for observation of the gating activity. When applying the voltage, the microheater heats up, and the PNIPAM barrier undergoes shrinkage, allowing the fluorescent perovskite QD solution to mix with the non-fluorescent ethanol. The shrinking process and mixing were monitored under a fluorescent microscope (Figure 7. 11 d-f). PNIPAM hydrogel barrier, acting as the microvalve gate, is shown in Figure 7. 11d between QD solution (left) and pure ethanol (right). An image of the same view is shown in Figure 7. 11e in fluorescence with a FITC filter (B-2E/C, Nikon, Ex: 465–495 nm, Em: 515–555 nm). In order to operate this microvalve gate, a microheater is turned on; the heat stimulates the PNIPAM barrier to shrink, causing the gate to open. The fluorescent QDs diffuse into the other parts of the channel after the gate is opened, as shown in Figure 7. 11f.

This simple demonstrator shows the feasibility of microheater/PNIPAM valve devices for liquid gating. In the future, these LM structures can also be modified to regulate the flow between two fluidic ports and more complicated microfluidic networks.

8. Gallium alloys and gold interfaces

As discussed in chapter 2, several methods can be used to deposit LM on substrates, one of these being to direct writing of LM, which simplifies the circuit production process and reduces cost. Gallium and gallium alloys show excellent wettability on most metallic surfaces. These LMs interact strongly with some metals, such as Al, Au, and Ag, even at room temperature, and they are capable of diffusing into the grain boundaries of these solid metals.

LM-based printed electronic devices also usually include connections between solid metal components and LMs, which might have a critical impact on the device's overall functioning. These contacts need to be studied, as current knowledge is limited here. Arguably gold is the most important industrial metal in the manufacture of electronics, commonly used as material for electrodes and connectors, is a highly efficient conductor, and can (without the involvement of LMs) usually remain corrosion-free and stable. The penetration of Ga-In into gold might affect the performance of the flexible electronic devices after a certain time. Thus, quantifying these processes might be crucial for managing their impact on a device and a critical step in bringing devices from the lab to commercial applications and daily life.

This chapter describes the interaction of Galinstan with solid gold surfaces by utilizing vertical scanning interferometry (VSI), energy-dispersive X-ray spectroscopy (EDX/EDS), X-ray photoelectron spectroscopy (XPS), X-ray diffraction (XRD), AFM, and X-ray nano computed tomography (nanoCT). Furthermore, the effect of this interaction on the electrical properties of Galinstan resistors directly printed between gold pads was also studied. Most of the work presented in this chapter is published in Hussain et al. [80], [449].

8.1 Sample preparation

A total of five different kinds of samples were prepared (Figure 8. 1) by capillary printing with the customized commercial nanolithography system described in chapter 4. The five sample kinds include two types of resistors, and two samples were printed on gold-coated glass substrates to measure gallium and indium spreading behavior on the gold surface. Multiple LM mixtures are available, generally based on gallium, indium, tin, and sometimes additional metallic parts. Galinstan (the LM used here) is a brand name also referred to as Ga-In-Sn, a mixture of 68.5% gallium and 21.5% indium, and 10% tin by weight (see Annex A.2.3). The printed resistors were characterized for resistance with respect to time on a probe station. One of these printed samples was encapsulated with PMMA to understand possible ways to slow gallium and indium penetration in gold surfaces.

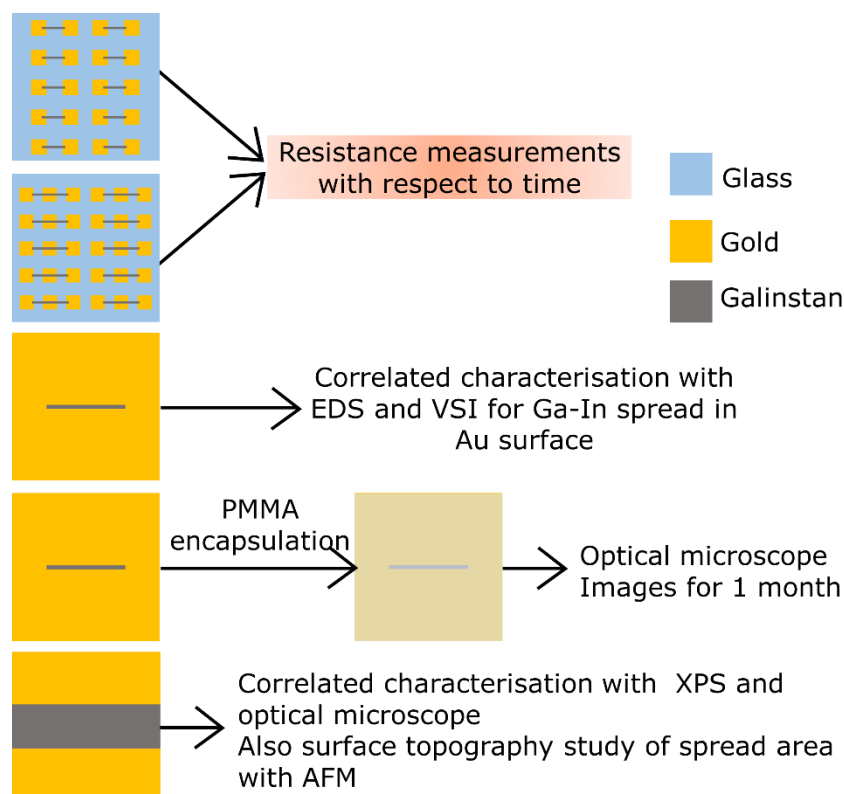


Figure 8. 1: Sample preparation and characterization description. Reproduced from [449] with permission from Wiley.

Optical microscope and scanning electron microscopy (SEM) images of these printed patterns were also collected. Two types of resistors (described in section 8.9) were fabricated with this technique, and their resistance over time was characterized.

8.2 Correlated characterization method

During the past decade, the use of LMs and other conductive materials for flexible electronics has significantly increased the number of electro-mechanical testing [450]; still, the importance of chemical interaction, degradation, and liquid metal embrittlement (LME) [451]–[453] studies (e.g., spread rate or grain growth) with gold and other metals is crucial to pre-analyze important factors in different processes and applications, e.g., soldering.

Ga and In can penetrate from LMs into solid gold along grain boundaries due to stress (then the process is called liquid metal embrittlement (LME)) and a thermodynamic driving force that reduces the interfacial energy (then referred to as grain boundary penetration (GBP)), detailed discussions on these models can be found in the literature [452]–[454]. The spread rate for the formation of intermetallic nanostructures can be challenging to measure with one method alone, so a correlated characterization approach is applied here that combines data from vertical scanning interferometry (VSI) with energy-dispersive X-ray spectroscopy (EDS) and scanning

electron microscopy (SEM) to assess the physical topography and chemical mapping (Figure 8. 2).

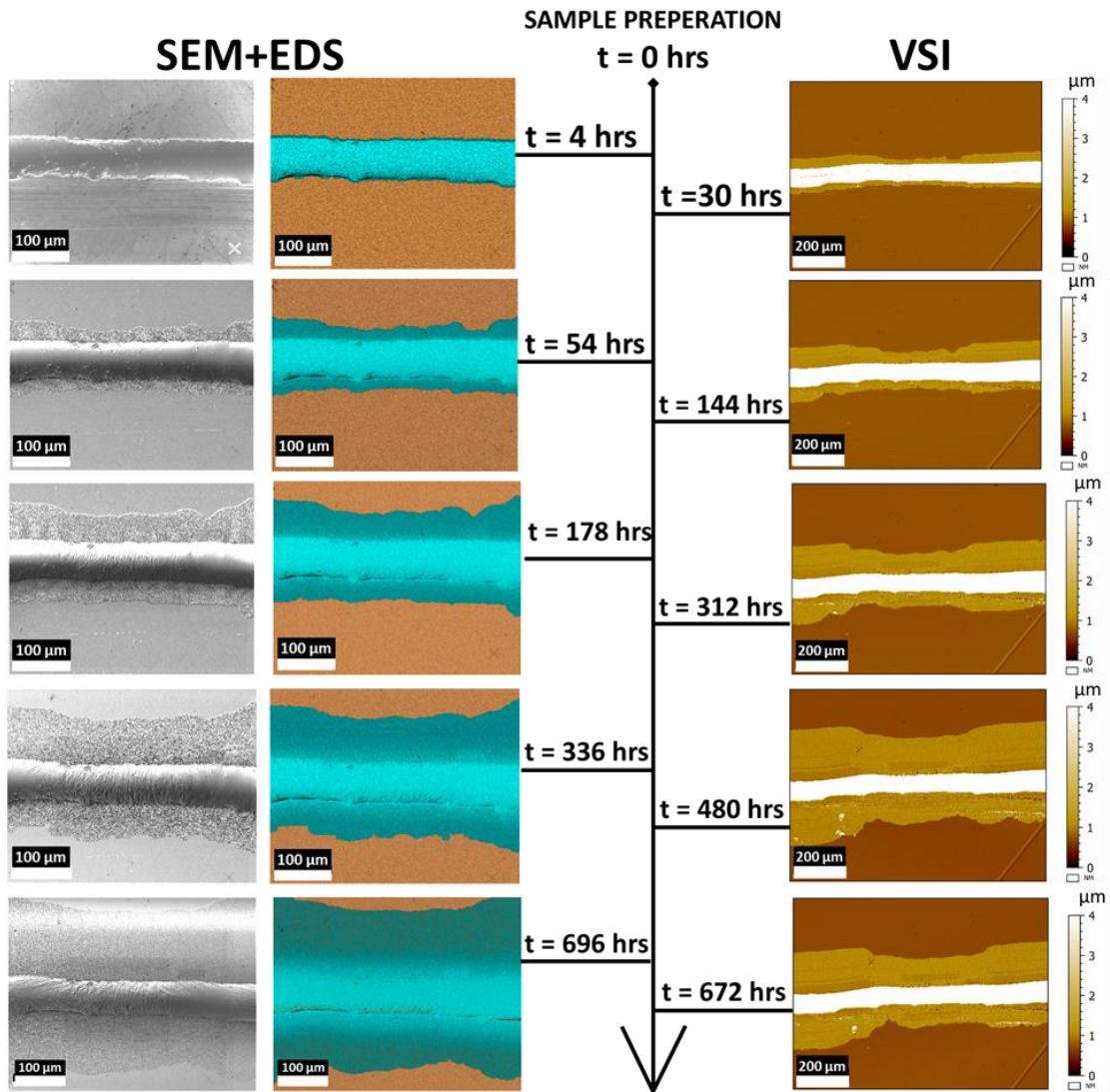


Figure 8. 2: Galinstan spread correlated study with Scanning Electron Microscopy (SEM), Energy-dispersive X-ray spectroscopy (EDS), and Vertical scanning interferometry (VSI) for the sample with respect to time. Reproduced from [449] with permission from Wiley.

SEM-VSI overlays were generated using the colocalization feature of the Mountain Map software, in which identical features in the SEM and VSI image were selected for proper alignment of images, in this case, FIB inscribed reference crosses. The correlated characterization method provides spatially resolved EDS maps and VSI maps that allow quantifying the Ga-In spread rate into the Au surfaces. Figure 8. 3 presents an SEM and VSI overlay of printed Galinstan; it also shows Ga and In widely spread out around the Galinstan line.

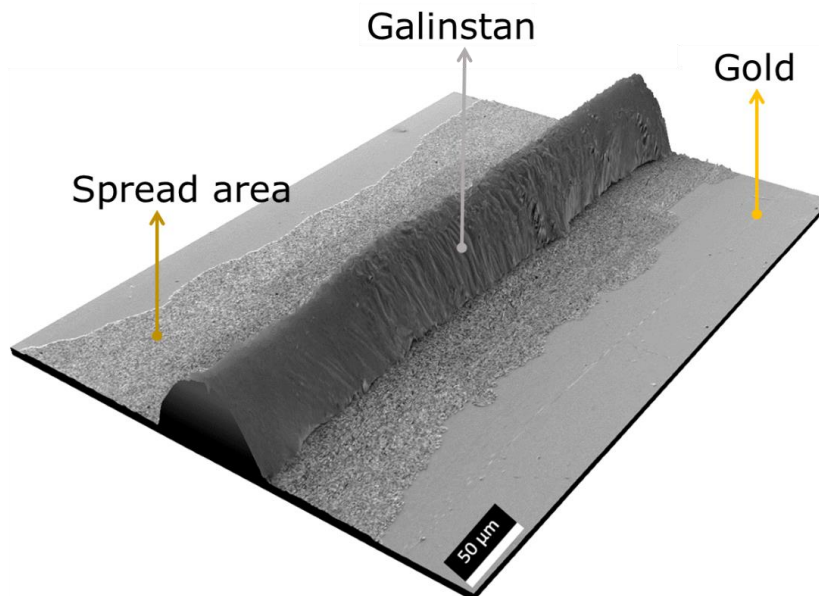


Figure 8. 3: SEM and VSI overlay of printed Galinstan line. The overlay was generated using the colocalization feature of MountainsMap (Digital Surf, France). Reproduced from [449] with permission from Wiley.

The quantification of these processes' results can help design longer-lasting devices. The correlated characterization approach employed here for the study of LM spread can also be applied to other systems. Other than describing important elemental details, in the future, this correlated characterization technique could also be added to tomographic studies, e.g., nanoCT, which might allow us to acquire a 3D grain map and might also allow us the quantification of the volume converted in intermetallic nanostructures [455]. These methods, integrated with other techniques, can also help predict a lifetime for LM-printed devices [456].

8.3 Intermetallic nanostructures formation rate

This correlated characterization approach provides a comprehensive quantitative description of Ga-In movement or dissolution and formation of intermetallic nanostructures on the surface and underneath. The approach can relate precise centimeters to nanometer-scale surface topographic measurements. Figure 8. 4 shows that using this system enables us to directly overlay EDS elemental analysis maps, SEM images, and VSI surface topography maps. In the vertical scanning interferometry method, product spread rates can be quantified at a nanometer-scale vertical resolution based on their topographical evolution. The EDS mapping provides additional information about the elemental/chemical spread. Over a time scale, multiple surface maps were obtained by measuring the development in Y and Z directions with VSI and EDS. With these maps available over the timeframes and subtracting them from each other, it is possible to obtain important information about the spread. These surface spread values can be converted into spread rates.

Moreover, finally, the spread distances from the Galinstan is analyzed in a graph, as shown in Figure 8. 4, and applying a statistical approach, the spread rate can be interpreted.

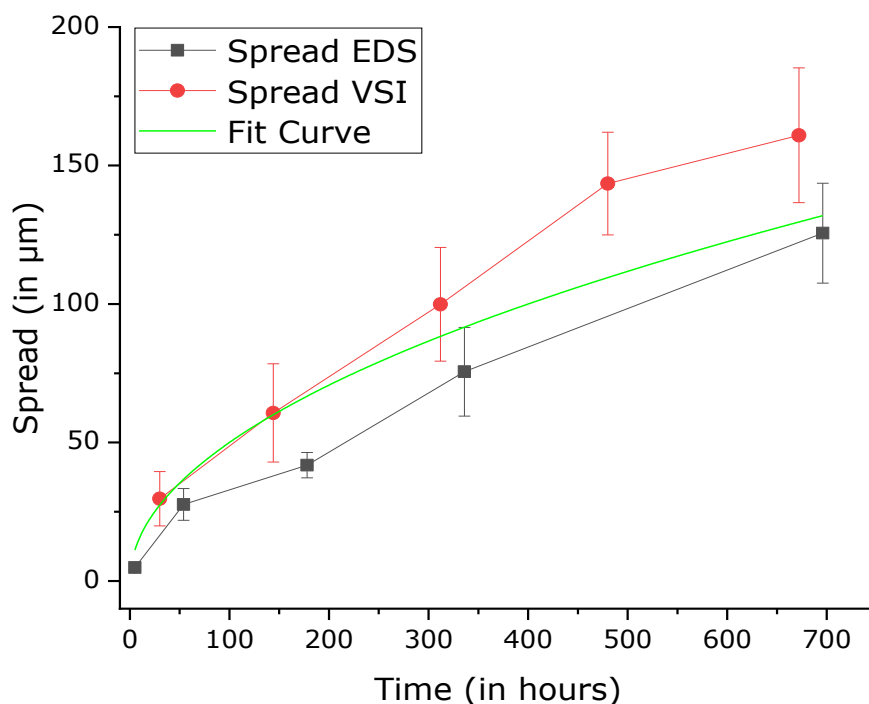


Figure 8. 4: Spread distances from the Galinstan line. Fitting the spread S dependence of time t , assuming the free-space diffusion process [457] results in $S(t) = (5 \pm 0.63) \sqrt{t}$. EDS/VSI images from the same sample positions were used to quantify the spread. In each image, the perpendicular distance of 15 random points at the spread front to the LM line was measured. The fit was done in Origin (OriginLab, USA). All error bars in graphs and error ranges reported represent one standard deviation (SD) of the reported mean. Reproduced from [449] with permission from Wiley.

For this correlated characterization, two Galinstan samples on gold surfaces were prepared. The first sample was explored with EDS four hours after the sample preparation. The sample was also studied by VSI subsequently, which shows the spread for the initial 30 hours was around $(32.97 \pm 3.59) \mu\text{m}$, translating into a spread rate of around $1.1 \mu\text{m}\cdot\text{h}^{-1}$. The same area of the sample was followed up for up to 28 days after printing. For the time period 30 hours to 144 hours (day 6), a spread of $(34.34 \pm 3.30) \mu\text{m}$, respectively, and a spread rate of $0.3 \mu\text{m}\cdot\text{h}^{-1}$ was observed. Assuming an underlying free-space diffusion process through the gold film bulk [457], the spread S dependence on the spreading time t can be fitted as $S(t) = (5 \pm 0.63) \sqrt{t}$, with an accompanying leveling-off spread rate over time.

While microscopic penetration as measured in similar systems can be substantially higher (e.g., Ga penetration into Al, where in-situ transmission electron microscopy (TEM) measurements revealed speeds varying between $0.01 \mu\text{m}\cdot\text{s}^{-1}$ to $12.2 \mu\text{m}\cdot\text{s}^{-1}$

along the grain boundaries) [458], it must be taken into account that the macroscopic process observed here is the result of penetration along the randomly oriented grain boundaries, thus expected to result in a much slower propagation. Compared to the few reports on the macroscopic spread (e.g., estimated by us from published optical microscopy images for EGaIn on Ag electrodes to $\approx 1.5 \mu\text{m}\cdot\text{h}^{-1}$) [101] the results seem in line with general expectations for such systems. Furthermore, the kinetics of GBP will be influenced by the way of preparation of the metal film, grain boundary type, and structure, grain size, mechanical stress, and temperature [459]. Interestingly, the penetration of Ga into grain boundaries can also influence the mobility of the grain boundaries itself, as reported for Ga/Al systems [460].

8.4 Characterization of intermetallic nanostructures

SEM imaging and EDS maps measurements were conducted after a time interval of 4h after printing LM. With good surface wetting, the penetration of Ga and In starts very fast as soon as it is in contact with the gold surface. Figure 8. 5 shows additional SEM imaging and corresponding EDS maps conducted 4h after the printing of the LM line. These clearly reveal the formation of intermetallic nanostructures in the spread area around the Galinstan line. Figure 8. 5a shows the grain-like texture of the resulting product at an angle, with the Galinstan line in the background. Figure 8. 5b

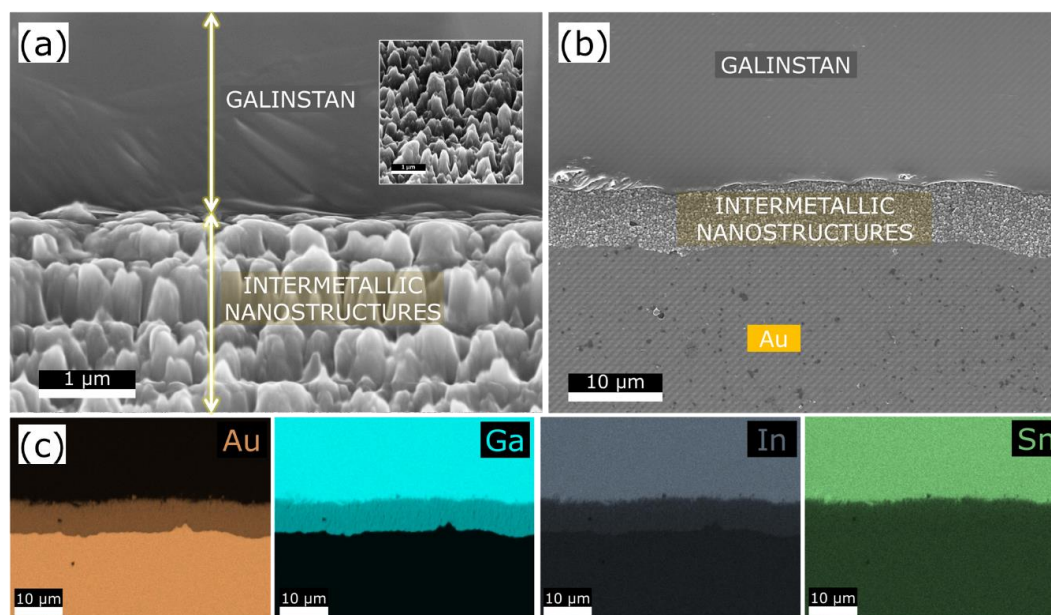


Figure 8. 5: Intermetallic nanostructures formation in Galinstan-Gold. (a) SEM image at a 60-degree angle (closed view in inset), scale bar: 100 μm . (b) SEM image shows an apparent border between the intermetallic nanostructures products and the bare gold surface just after 7 hours of printing Galinstan on the gold surface. (c) EDS map edge of Galinstan line printed on the gold surface, acquired at 10 kV, 120 pA, Working distance (WD) = 5mm. Reproduced from [449] with permission from Wiley.

shows the apparent band of intermetallic nanostructures in the spreading region in the top view.

Corresponding EDS maps (Figure 8. 5c) show that Ga and In start spreading into the gold surface immediately on contact. Sn penetration is not seen in initial EDS maps, and only later EDS maps after 1 week (Figure 8. 6) show slight signals of Sn appearing on the gold surface near the Galinstan line. The differential behavior in penetration speed for Ga, In, and Sn is similar to observations in LM/Zinc systems [461].

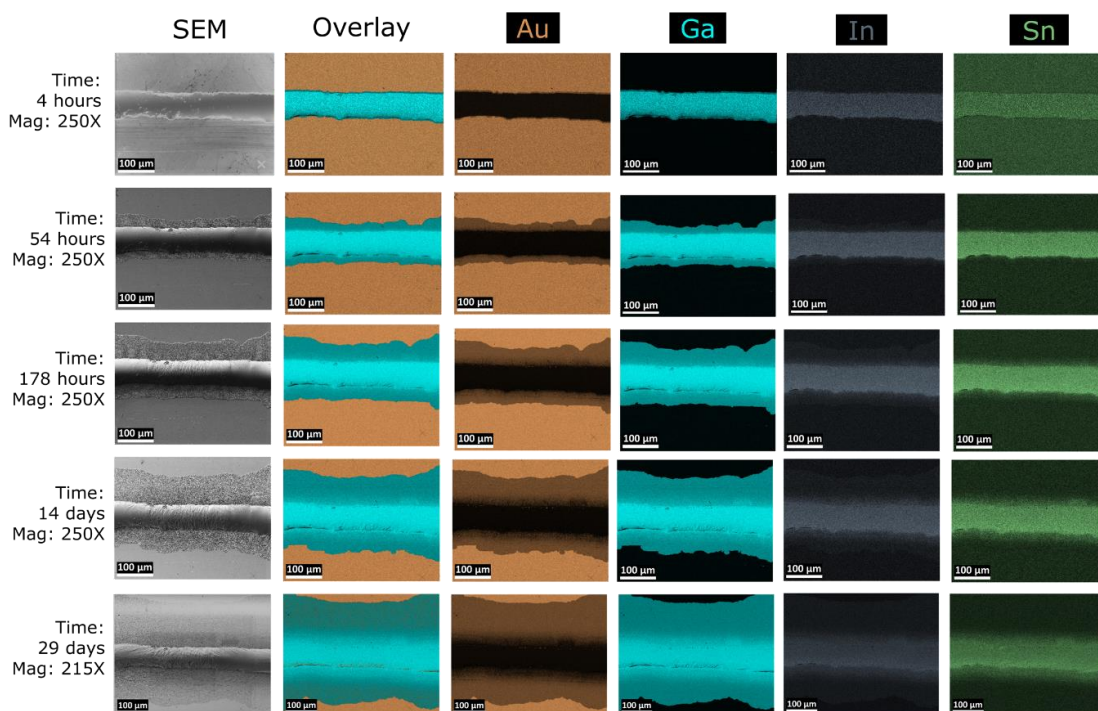


Figure 8. 6: EDS map for Galinstan, intermetallic nanostructure, and Au surface for freshly prepared sample for different time scales. 4 hours, 54 hours, 178 hours (1 week), 2 weeks, and 4 weeks. SEM image elemental overlay, Au signal, Ga signal, In signal, and Sn signal. Adapted from [449] with permission from Wiley.

The formation of the intermetallic nanostructures becomes visible even to the naked eye after enough time has passed. Here, a striking change in color from the grey/silver appearance of Galinstan to grey/blue color shades can be observed (Figure 8. 7). This indicates the formation of blue gold, an alloy of gold, and either Ga or In. The intermetallic compound AuIn_2 forms at 46wt% Au and AuGa_2 at 58.5wt% Au [462], [463]. Considering the Au-Ga and Au-In phase diagrams, multiple intermetallic phases can be witnessed, most of which are stable at and below room temperature [464], [465]; thus, the amount of gold will determine the stoichiometry and phase formation of the resulting nanostructures. Clarysse et al. have reported that regarding Au-Ga systems, small amounts of Ga-amide introduced in Au nanocrystals might result in fcc Ga-doped Au nanocrystals, while proportionally more

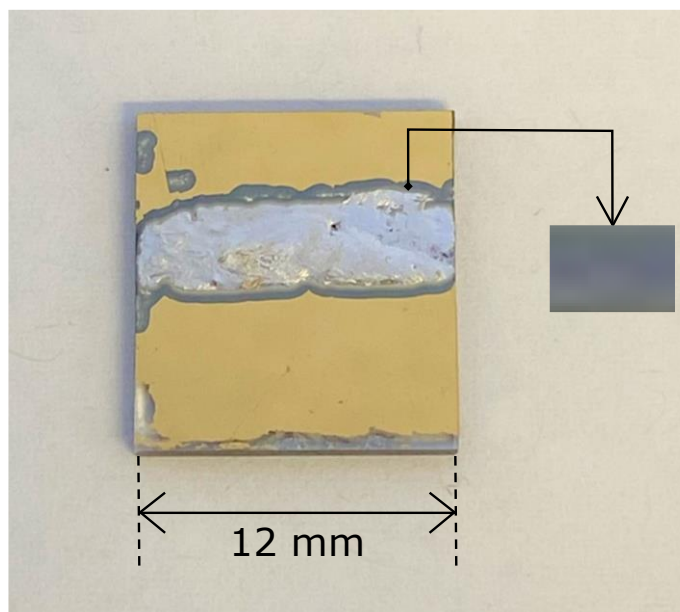


Figure 8. 7: Photo of LM sample on a gold-coated surface showing the light grey/blue color shades appearing on both sides due to Ga and In penetration into the gold film. The LM was applied to the film by the doctor blading without any contact or scratching of the gold film. The image is captured 190 days after the sample preparation. Reproduced from [449] with permission from Wiley.

significant quantities of Ga precursor lead to the conversion of Au seeds to various intermetallic phases including hexagonal Au_7Ga_2 , orthorhombic AuGa , and cubic AuGa_2 [466]. So, the nanostructures seen in the SEM image in Figure 8. 6 might chemically constitute a mix of all of those different phases.

8.4.1 X-Ray diffraction (XRD) study

To clarify the composition of the intermetallic structures, XRD was performed on the sample seen in Figure 8. 7. The results were taken together with EDS, and the notion of the formation of energetically favorable intermetallic phases in similar systems [467], [468] suggests predominantly AuGa_2 in the intermetallic region (Figure 8. 8).

8.4.2 X-ray photoelectron spectroscopy (XPS) study

As a complement to the EDS measurements, the more surface-sensitive method of XPS was performed on a sample with an LM line on a homogeneously Au-coated

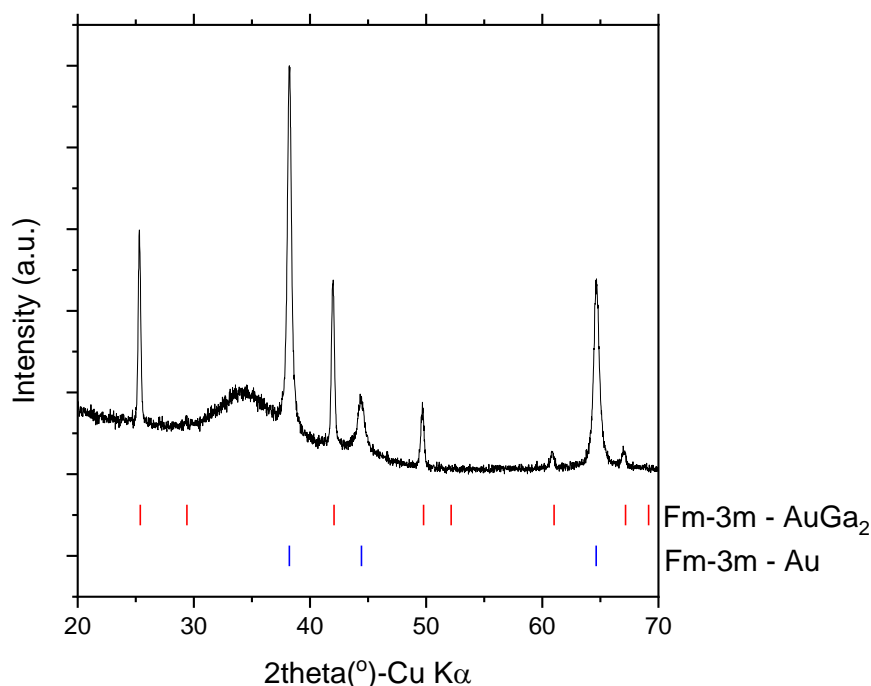


Figure 8. 8: XRD analysis of LM sample. Potential peak positions corresponding to metallic Au (in blue) and Au-Ga alloys (AuGa_2 in red) are marked in the graph. Overall the pattern of peaks clearly indicates the presence of intermetallic AuGa_2 , but AuIn_2 and AuSn_2 might be masked by peak overlaps. Keeping in mind additionally the (relative to Ga) low concentration of In and Sn indicated in the EDS measurements (Figure 8. 6), the intermetallic phase is expected to be predominantly AuGa_2 . Reproduced from [449] with permission from Wiley.

substrate. The spreading of Galinstan on the Au surface was studied by XPS over a period of 120 days (Figure 8. 9).

The spectral mapping of spin-orbit splitted $\text{Au}4f$, $\text{Ga}2p$, $\text{In}3d$, and $\text{Sn}3d$ core level spectra collected across the LM line on the Au substrate is shown in Figure 8. 9a. The color code blue to red in the map shows the change in intensity of the spectra from lower to higher in the Y-axis. While in the X-axis, the highest intensity represents the binding energy of the core level spectra. The core-level binding energy of $\text{Au}4f_{7/2}$ is 84.2 eV [469], while for $\text{Ga}2p_{3/2}$, $\text{In}3d_{5/2}$, and $\text{Sn}3d_{5/2}$, it is at 1118.66, 484.90, and 443.90 eV, respectively, corresponding to the metallic gold and the LM components Ga, In, and Sn [98]. However, the binding energy of $\text{Ga}2p$ shows the Galinstan is already oxidized after eight days of film deposition [80]. The $\text{Au}4f$ map on the 8th day shows the intensity of spectra has the lowest intensity at around measurement point 4, which is the point when the line scan reaches the edge of the LM line. Around this position, the $\text{Ga}2p$, $\text{In}3d$, and $\text{Sn}3d$ peak intensities start to increase, showing steps between Au and the LM. Comparing the Au map from the 8th, 14th, and 120th day, it can be seen that the position of the lowest intensity moved from 4 to 2.

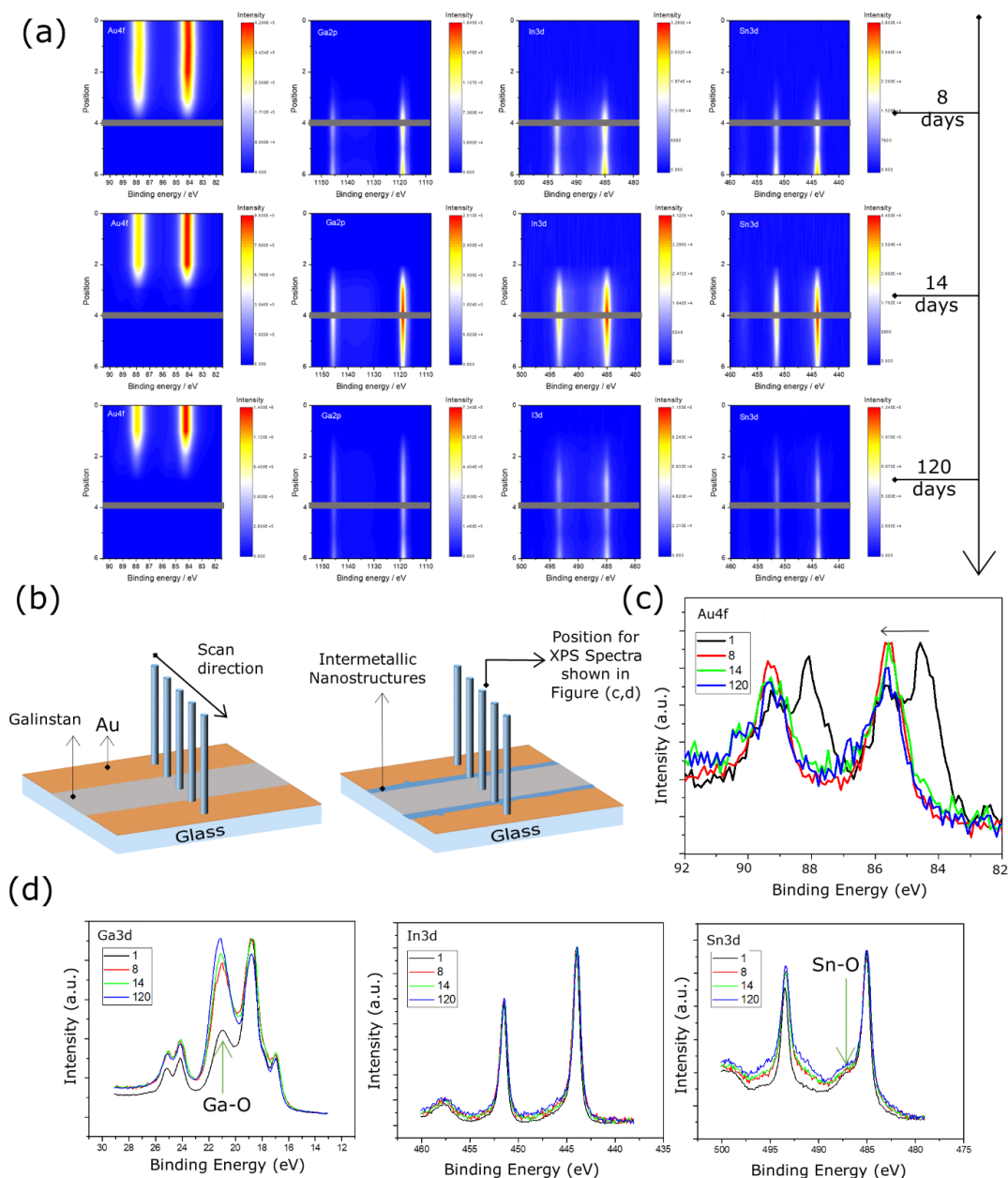


Figure 8. 9: Line scan on a LM line on a homogeneously Au-coated substrate at 8, 14, and 120 days after printing. (a) Core level maps of Au4f, Ga2p, In3d, and Sn3d. The map's color code from blue to red is the lowest to highest intensity of the peak along the Y-axis. Point 4 (dark grey line), shows the starting point of the LM line. (b) Scheme on the sample and scan positions. (c), (d) High-resolution core-level spectra of Au4f, Ga3d, In3d, and Sn3d orbitals for a LM line (at the position marked in (b)) on Au for fresh, 8 days, 14 days, and 120 days after deposition. Reproduced from [449] with permission from Wiley.

Similarly, the Ga2p, In3d, and Sn3d intensities move towards position 2 and beyond that point over the time from the 8th day to the 120th day. The movement of the spectral intensity of Au and LM opposite to each other on the map shows the

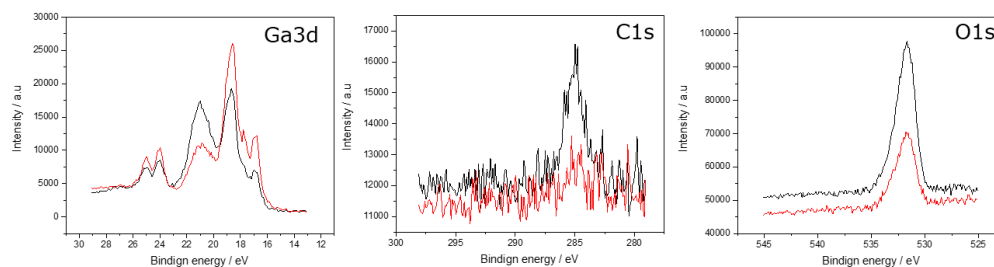
movement of Ga and In in the Gold surface and intermetallic nanostructure formation, which confirms the observations by the other methods.

Figure 8. 9c shows the Au4f spectra for a point in the center of the LM line on Au (as depicted in Figure 8. 9b) for the 1st, 8th, 14th, and 120th days after sample preparation. On the first day, the Au4f_{7/2} has two peaks at 84.5 and 85.7 eV corresponding to the In-Au and Au-Ga eutectic [470], [471]. From the first-day spectra, it is evident that some Au migrated to the surface of the LM film, forming a eutectic alloy with the LM. With the increase of time, the Au4f_{7/2} has only one peak at 85.7, indicating the Au mixes completely with the LM to form an eutectic. The combined observation of Figures 8.9a and Figure 8. 9c shows that the LM spreads into the Au film over time, but also some Au migrated into the LM, forming an eutectic. Figure 8. 9d shows the Ga3d, In3d, and Sn3d core level spectra collected on the 1st, 8th, 4th and 120th day. In Ga3d core-level spectra, the peak at around 20.8 eV and in Sn3d core-level spectra, the shoulder at around 487.0 eV show that the surface is oxidized with the formation of Ga₂O₃ and SnO₂ on the surface of the ML, while the In3d position does not change over time. This is in agreement with our previous work, where the thickness of the Ga₂O₃ layer on Galinstan was reported, along with the change in thickness over time [80].

The oxide layer can be removed by HCl vapor treatment (Figure 8. 10), but stable GaCl₃ hindered further XPS characterization of the intermetallic structures [272].

The Ga3d core level of the air-stored Galinstan sample shows the surface is oxidized to Ga₂O₃, while on the HCl etched sample, there is a single main peak at 22.0 eV, indicating the absence (or only negligible presence) of Ga₂O₃. Upon sputtering the air-stored sample with monoatomic Ar⁺, the Ga3d peak intensity at 21.0 eV decreased, and the peak at 18.6 eV increased, showing the removal of Ga₂O₃ with sputtering. Also, the decrease in O1s intensity and removal of C1s shows the general effectiveness of sputtering. In the case of the HCl-treated sample, a Cl2p signal appears on the sample, indicating the build-up of GaCl₃ during the vapor treatment [272]. On sputtering, the Ga3d peak shifts to 21.6 eV, which is not from metallic Ga or oxidized Ga. This peak shift, therefore, could be indicative of the relative enrichment of GaCl₃ during sputtering. Moreover, it can be seen that the Cl2p intensity does not change significantly upon sputtering, suggesting the removal of GaCl₃ is slower compared to other components (e.g., residual oxides), as the carbon removal is also efficient, showing again the general effectiveness of sputtering. In summary, the sputtering depth profile shows the air stored Galinstan is oxidized, while on HCl etching, the Ga₂O₃ is removed but forms an even more stable GaCl₃ layer.

(a) Air aged Galinstan



(b) HCl etched and stored in Ar

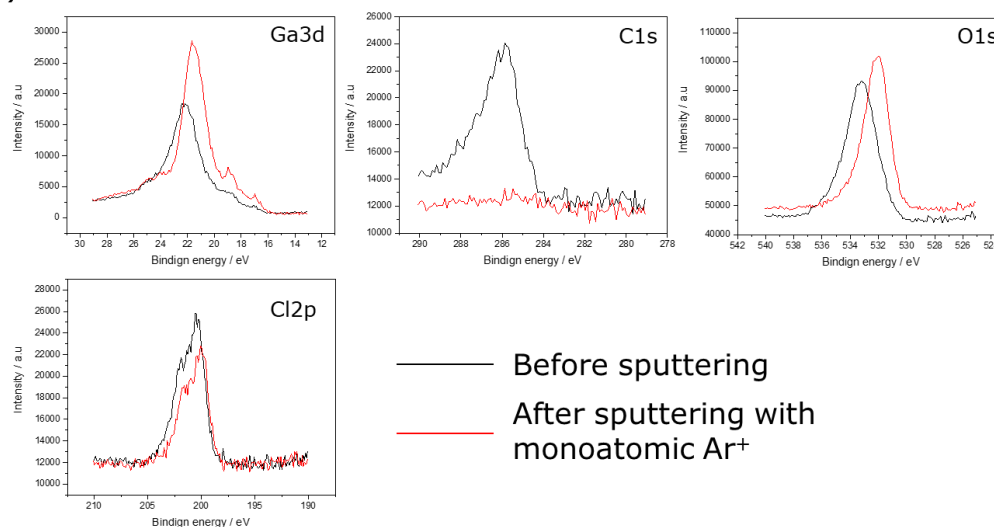


Figure 8. 10: High-resolution XPS spectra of Ga3d, C1s, O1s, and Cl2p orbitals for fresh/before sputtering and after sputtering with Ar+ Galinstan samples (a) air aged and (b) HCl etched and stored in Ar. The black line represents the first spectra (recorded before sputtering), and the red line represents the final spectra (after the sputtering experiment). Reproduced from [449] with permission from Wiley.

8.4.3 Topographic study with Atomic Force Microscopy (AFM)

Revisiting the sample in optical microscopy after several cycles of correlative measurements revealed another interesting phenomenon (Figure 8. 11).

Here, the intermetallic nanostructures show up in bands of slightly different reflectivity, as can be seen in the optical microscopy image of the spread area (Figure

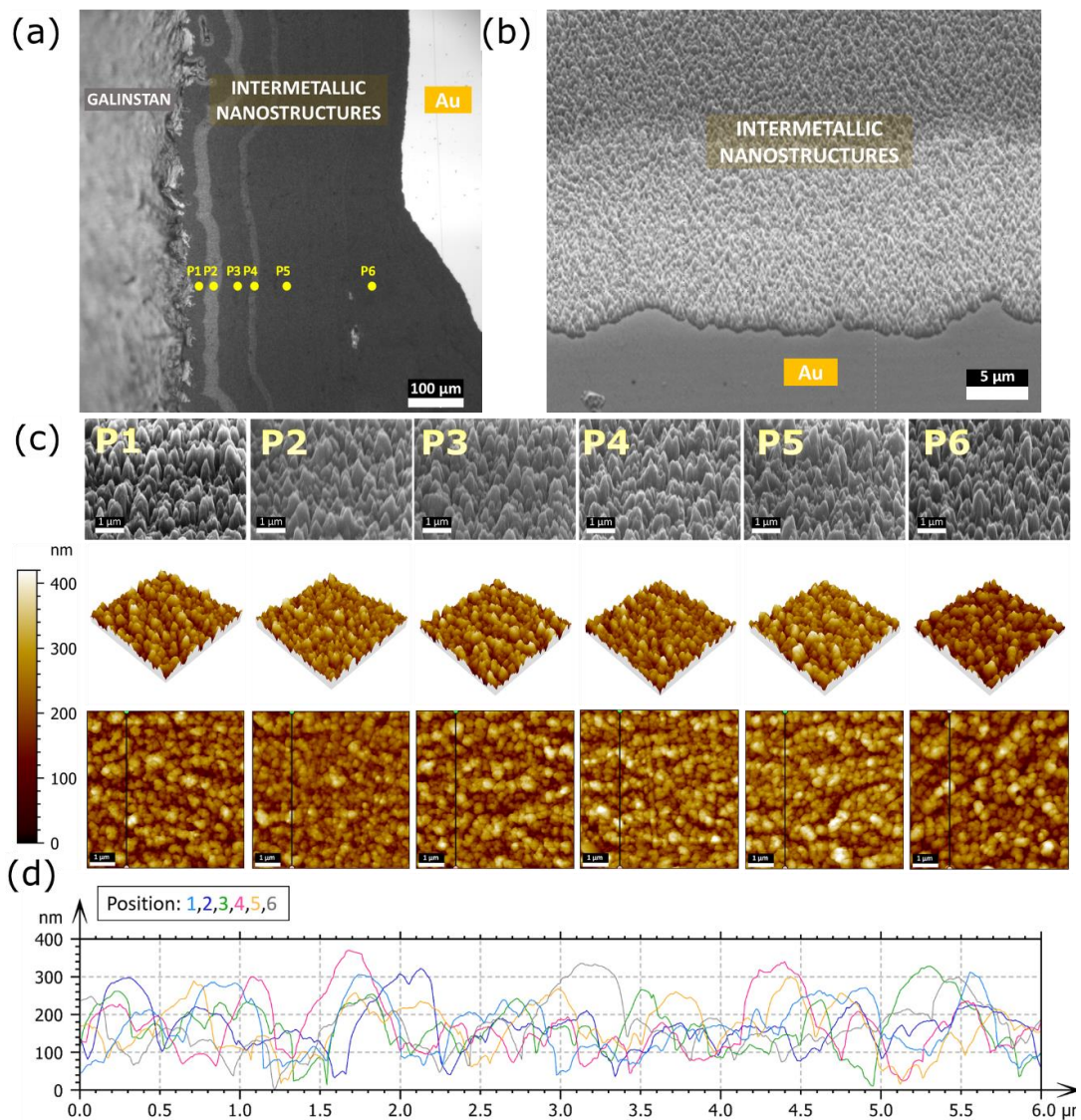


Figure 8. 11: Correlated SEM and AFM measurements on LM spread. (a) Optical microscopy image showing different shades of intermetallic nanostructure products. (b) SEM image of the edge of the intermetallic nanostructures band with the adjacent bare gold surface. (c) SEM imaging at a 60° angle (scale bar 1 μm) and corresponding AFM images for different positions. (d) Profile extraction from AFM images of positions. Reproduced from [449] with permission from Wiley.

8. 11a). The contrast change does not indicate a chemical difference of the bands in regard to Ga, In, Au, and Sn contents, as EDS shows a homogeneous chemical signal for the spread area at all aging stages (Figures 8.5 and 8.6). Therefore, it can be suspected that there are different morphologies of the spread areas in the different bands, and a more detailed microstructural analysis with high magnification SEM and roughness measurement with AFM was implemented. SEM imaging at a 60° angle and AFM at the different bands (P1 to P6) show the general topography in AFM and corresponding SEM images (Figure 8. 11c). Both show pit and heightened hill

structures in close vicinity uniformly dispersed throughout the surface. Scans of the complete areas reveal that the Au surface is fully covered with the intermetallic nanostructures, with no sign of any bare Au surface in between. All of the positions in the sample show similar hill structures in regard to size and height, which can be clearly observed in profile line extractions from the AFM images (Figure 8. 11d).

In addition to the topography, a roughness analysis was performed to provide additional information about the texture. Both the arithmetical mean deviation roughness (Sa) and the root mean square roughness (Sq) as measured by AFM present a low overall roughness varying from 42 to 55 nm (Sa) and 52 to 68 nm (Sq), respectively, with maximum heights of the intermetallic structures varying from 400 to 500 nm for the different bands (Table 8. 1).

Table 8. 1: Surface roughness for the positions in shades where the roughness average (Sa) represents the mean height on the surface, and the root mean square (Sq) indicates the standard deviation from the mean height. All reported values were calculated from the whole area of the recorded AFM images in MountainsMap (Digital Surf, France). Reproduced from [449] with permission from Wiley.

| Position | Mean Height Sa (nm) | Root Mean Square Height Sq (nm) | Maximum Height Sz (nm) |
|-----------------|----------------------------|--|-------------------------------|
| 1 | 53.2 | 65.1 | 429.1 |
| 2 | 41.7 | 52.2 | 401.8 |
| 3 | 54.7 | 67.0 | 432.6 |
| 4 | 50.7 | 63.4 | 464.6 |
| 5 | 52.4 | 64.6 | 443.5 |
| 6 | 54.7 | 67.8 | 486.1 |

These shades were examined with EDS (Figure 8. 12), which shows Ga-In spreading into the Au surface; no Sn spread was found with that. Similar shades were observed in the XPS sample and EDS mapping sample.

As even small changes in surface roughness and morphology can introduce substantial changes in the reflectance of surfaces [472], the differences between the bands seem sufficient for explaining the observed contrast. Furthermore, the bands can be correlated with cycles of vacuum (during XPS / EDS) and in air spreading, with the width of bands increasing with longer measuring or aging times (Figure 8. 13), indicating that the source of the different roughness could be different mechanical stresses during vacuum exposure and storage at ambient pressure.

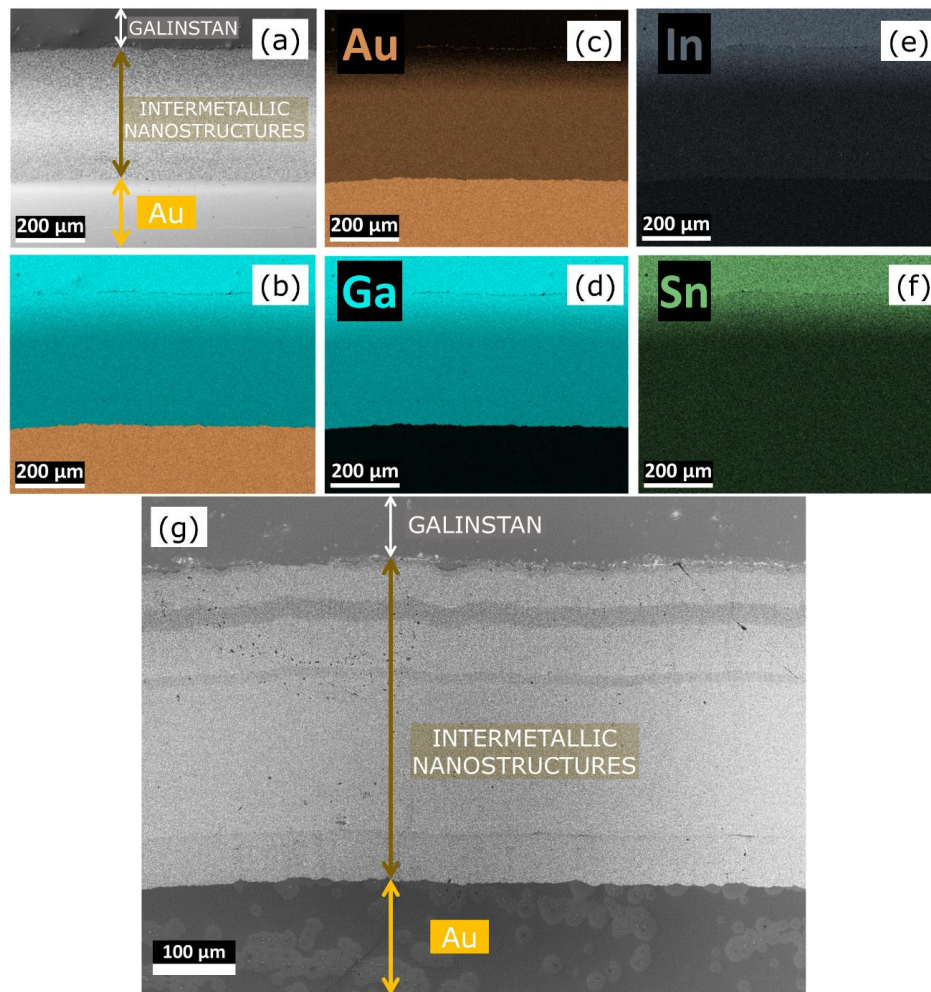


Figure 8. 12: EDS map for Galinstan, Galinstan-Au products, and Au surface, which constitutes different shades; these shades were seen in the optical microscope as well as InLens signal in SEM, not seen in the SESI (Secondary electron secondary ion) signal. (a) SEM image (SESI signal). (b) Elemental Overlay. (c) Au signal. (d) Ga signal. (e) In signal. (f) Sn signal. (g) SEM InLens signal image for the same spot as (a). (SESI: Secondary electron secondary ion) Reproduced from [449] with permission from Wiley.

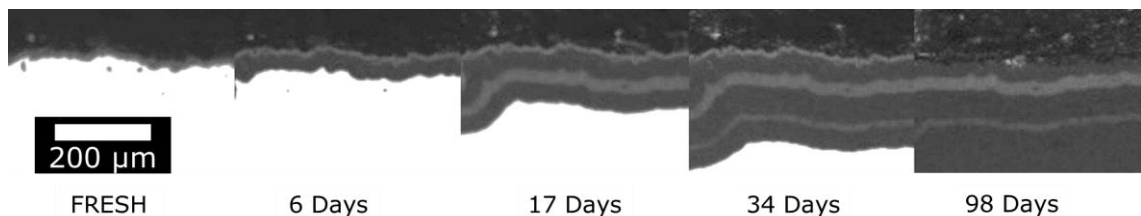


Figure 8. 13: A time-lapse optical microscope image shows bands, which can be correlated to vacuum cycles (when performing XPS) and air spread, where the corresponding width of the band increases in width with longer measuring and aging times. The grey spread area was influenced by high vacuum, and the black spread area is normal air aging. Reproduced from [449] with permission from Wiley.

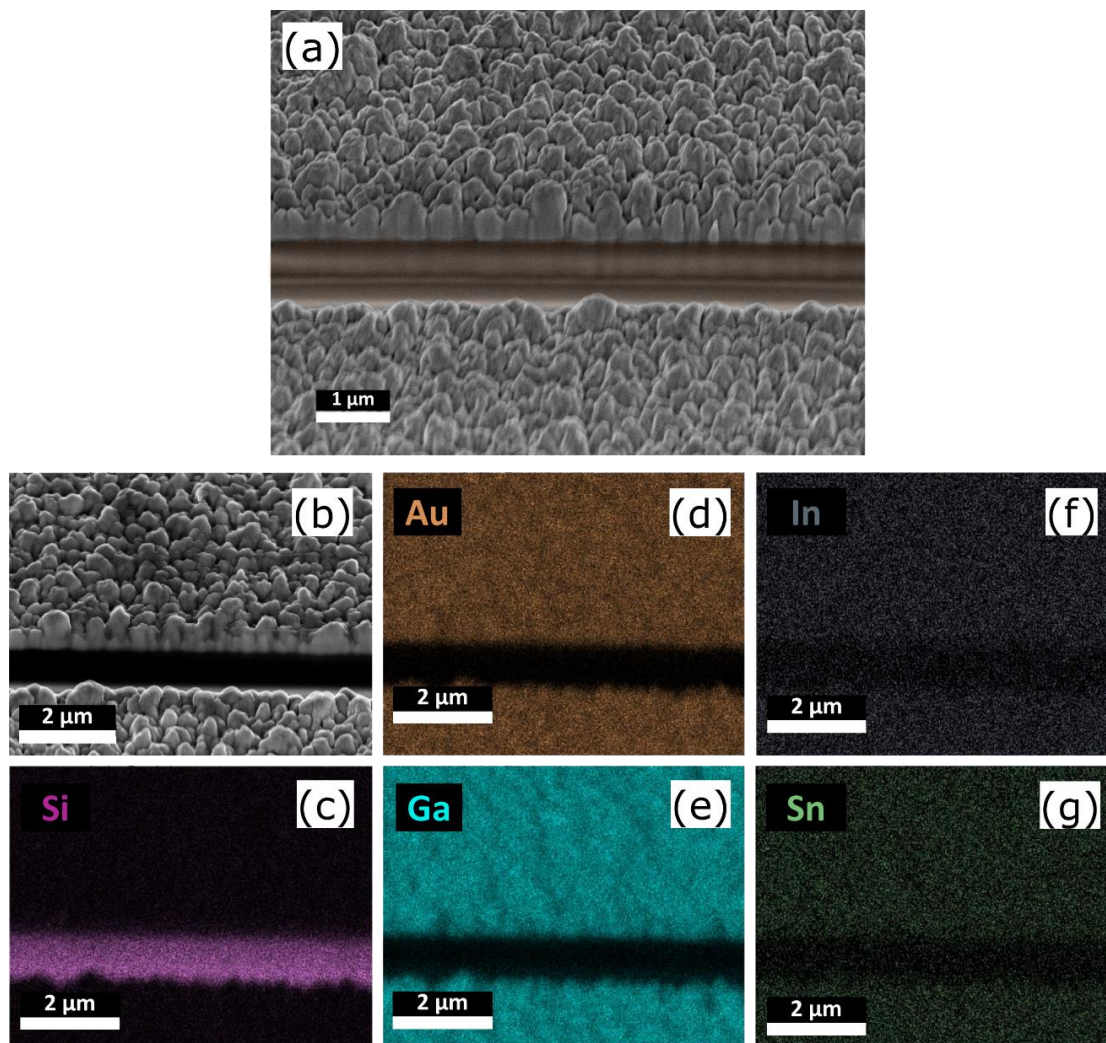


Figure 8. 14: FIB cross-section at 54 degrees showing nanostructures around 500 nm high (FIB cross-section depth 1 μm , width: 4 μm , milling current is 30kV:600pA) and EDS map at 54 degrees of FIB cross-section into the intermetallic nanostructures. For the fresh sample, the thickness of the gold layer was around 100 nm, with 7nm of Cr as the adhesion layer. (a), (b) SEM image. (c) Si Signal. (d) Au signal. (e) Ga signal. (f) In signal. (g) Sn signal. Reproduced from [449] with permission from Wiley.

8.4.4 3D propagation of atoms and X-ray nanotomography study

To inspect whether the Au-film gets only alloyed on the surface or also in deeper layers, a FIB section was prepared in an area of the intermetallic nanostructures (Figure 8. 14). Gold and Ga signals fully correlate in the section down to the silicon substrate, thus showing that the complete gold film got consumed by the LM spread.

EDS at a 60° angle shows gold signals within the Galinstan (Figure 8. 15), which also explains the growth of the granular nanostructures.

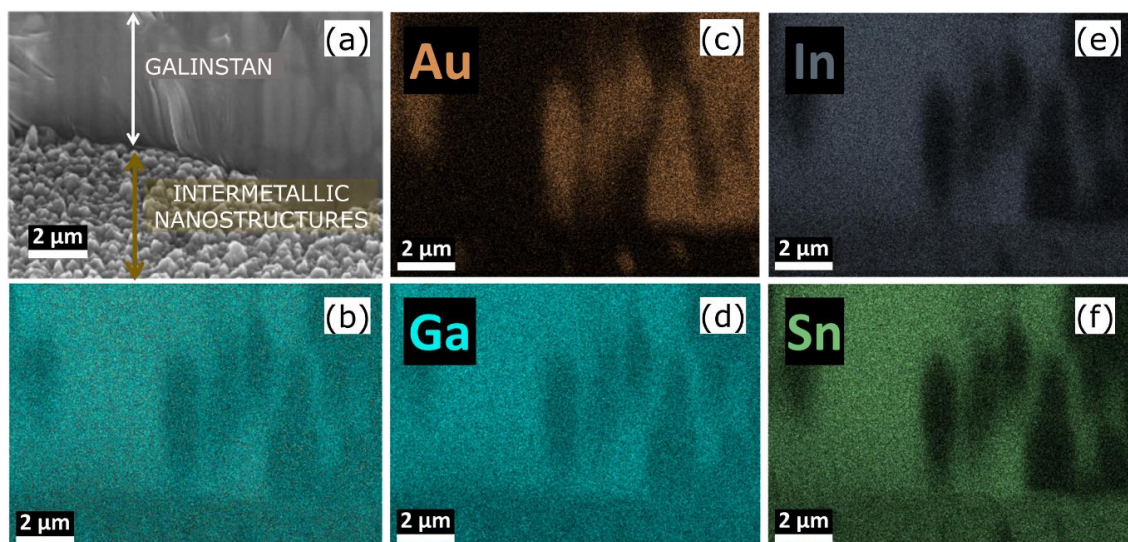


Figure 8. 15: EDS map for LM line and adjacent intermetallic nanostructures at 60° view angle. (a) SEM image. (b) Elemental Overlay. (c) Au signal. (d) Ga signal. (e) In signal. (f) Sn signal. The Au-signal in the LM line indicates a back-propagation of Au from the substrate into the LM itself. Reproduced from [449] with permission from Wiley.

Additionally, the X-ray nanotomography provided the 3D distribution of the Galinstan, gold, and intermetallic phases after 53 days of dipping a gold wire into Galinstan. Figure 8. 16c shows a 3D view of the sample in grayscale and color-mapped. The composition distribution is retrieved through the differences in the grayscale, with lighter gray corresponding to denser material. The scanned tip of 31 μm^3 has a distribution of ca. 48% of intermetallic phases, 35% of Galinstan, 12% of gold, and 5% of oxygen. While the inner structure is mostly intermetallic phases and gold, Galinstan is distributed in the more external layers, and oxygen forms a thin layer on the sample surface (Figure 8. 16c).

8.5 Intermetallic nanostructures formation and growing mechanism

Taking together the results so far, a growing mechanism for the intermetallic nanostructures can be proposed based on the penetration of Ga and In from the LM into the gold surface (Figure 8. 17).

In this model, the intermetallic structures are products of Ga and In alloying with Au after diffusion along intergranular cracks produced at grain boundaries of the underlying gold film. Multiple theories exist for crack initiation and LME/GBP based on adsorption or diffusion-penetration of LM

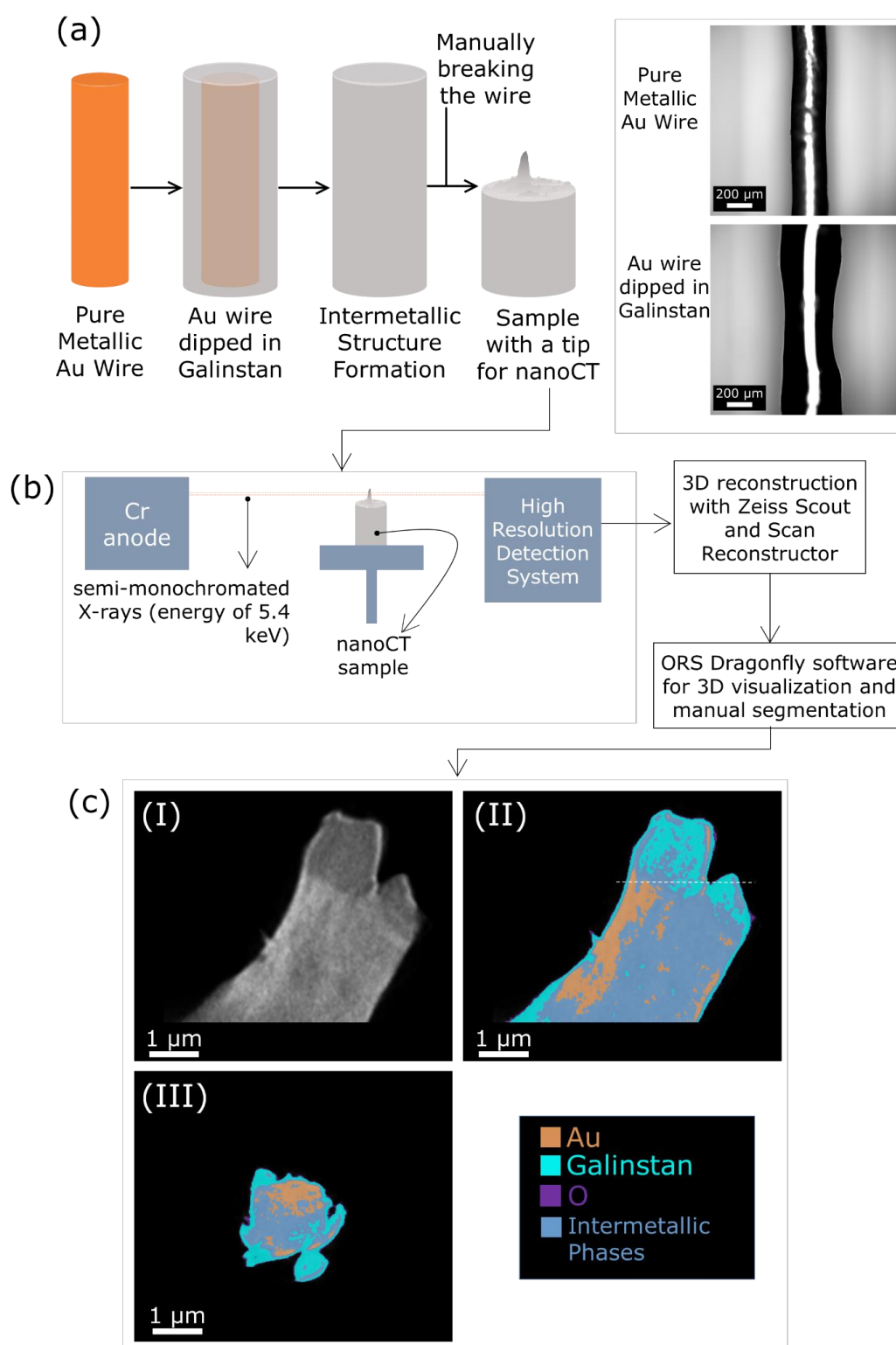


Figure 8. 16: (a) NanoCT sample preparation. (b) NanoCT scan process. (c) NanoCT 2D slices and volumetric reconstruction of a nanoCT scan were performed 53 days after dipping a gold wire into the Galinstan. (as shown in (a)) of a gold, wire dipped into Galinstan. Side view slice of the sample in (I) grayscale (lighter gray indicates denser material) and (II) color map. The white dashed line in (II) indicates the cut for the top view (III). Reproduced from [449] with permission from Wiley.

atoms on solid metal surfaces and weakening of inter-atomic bonds [451], [452]. Micro-void coalescence (MVC) and the dissolutions-condensation mechanism (DCM) are expected to be the reason for intergranular cracking. As the details of cracking, volume changes, and the vertical growth of the nanostructures itself will depend on mechanical stresses in the gold and interactions at the surfaces, in this model, it also becomes conceivable why slightly different morphologies for the intermetallic structures leading to the band structures in the spread area are formed. They reflect the different pressure regimes under which XPS and EDS, and the aging under ambient conditions at atmospheric pressure take place.

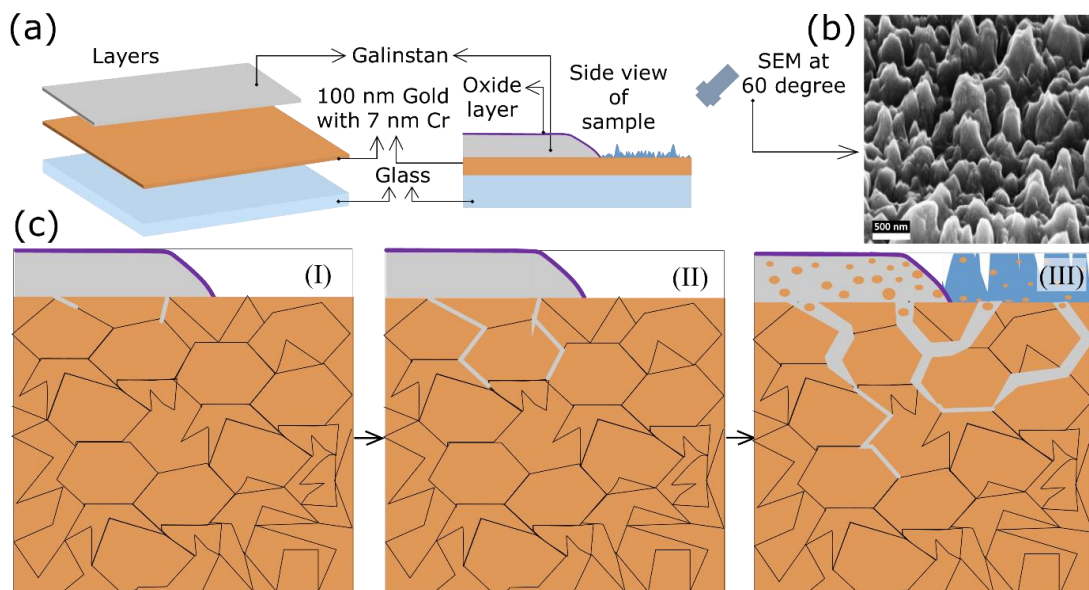


Figure 8. 17: Model of intermetallic nanostructure formation. (a) Schematic of the sample setup. (b) SEM image of the intermetallic nanostructures at a 60° view angle. (c) The proposed growing mechanism for the intermetallic nanostructures. (I) Crack initiation, (II) grain boundary penetration, and (III) intermetallic nanostructure formation. Color representations are; light blue: glass, orange: gold, gray: Galinstan, blue: intermetallic nanostructures, and purple: oxide layer. Reproduced from [449] with permission from Wiley.

8.6 Effect of temperature and humidity on intermetallic structure formation

While the focus in this work is on the time evolution of the Galinstan gold systems, some explorative experiments in regard to temperature and humidity were performed as it is known for Ga/Al systems that raising temperature can highly increase Ga penetration into grain boundaries [459]. For this, sets of samples were kept for 18h under different temperature and humidity conditions, and spread was measured afterwards (Table 8. 2). This revealed that the influence of humidity seems negligible,

but heating the substrates to elevated temperatures of 50 °C and 100 °C substantially increases spread, in particular for thicker line structures.

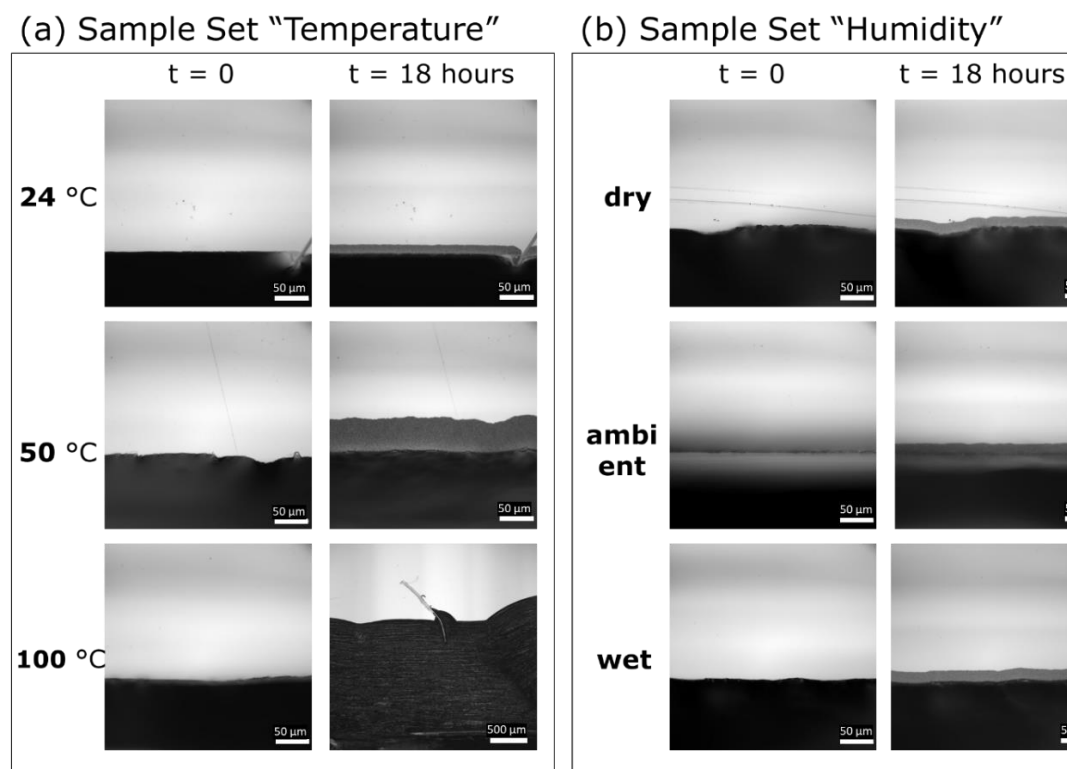


Figure 8. 18: Effect of temperature and humidity on formation of intermetallic structures. Comparison of optical microscope images of edges of printed Galinstan line pattern on Gold surface fresh sample to 18 hours aged sample. (a) sample set temperature. (b) Sample set humidity. Reproduced from [449] with permission from Wiley.

Table 8. 2: Results of spreading experiments for LM lines on the gold surface for different temperatures and humidity. Images of the samples are provided in Figure 8. 18. Reproduced from [449] with permission from Wiley.

| | Sample | Line Width (μm) | Temperature ($^{\circ}\text{C}$) | Relative Humidity (RH) | Spread (μm) |
|--------------------------|---------------|--|--|-----------------------------------|--|
| Sample Set "Temperature" | 1 | ≈ 10 | 24 | ambient ¹ | 8.36 ± 0.57 |
| | 2 | ≈ 10 | 50 | ambient ¹ | 9.18 ± 0.6 |
| | 3 | ≈ 10 | 100 | ambient ¹ | 19.07 ± 1.97 |
| | 4 | ≈ 500 | 24 | ambient ¹ | 13.45 ± 0.68 |
| | 5 | ≈ 500 | 50 | ambient ¹ | 49.72 ± 1.84 |
| | 6 | ≈ 500 | 100 | ambient ¹ | 1723.18 ± 66.07 |
| Sample Set "Humidity" | 7 | ≈ 10 | 24 | dry ² | 9.28 ± 0.31 |
| | 8 | ≈ 10 | 24 | ambient ¹ | 8.07 ± 0.34 |
| | 9 | ≈ 10 | 24 | wet ³ | 11.25 ± 0.63 |
| | 10 | ≈ 500 | 24 | dry ² | 17.27 ± 1.00 |
| | 11 | ≈ 500 | 24 | ambient ¹ | 14.89 ± 0.70 |
| | 12 | ≈ 500 | 24 | wet ³ | 16.6 ± 0.52 |

¹ Sample was exposed to an ambient lab environment, with approx. 37% r.h.

² Sample was under a dry nitrogen flow, approx. 20% r.h.

³ Sample was enclosed in the petri dish with water, leading to a saturated atmosphere of $\approx 100\%$ r.h.

8.7 Effect of encapsulation on intermetallic structure formation

Finally, another line-printed sample was encapsulated with PMMA to look for factors affecting the spread of Galinstan on gold. Here, optical microscopy images were captured with respect to time (Figure 8. 19). The PMMA encapsulation cannot prohibit LM spreading (as is expected, as the spread also propagates through the gold film bulk); however substantially slows down at least the surface visible outgrowth, probably by mechanical blocking and acting as a stabilizer for the surface.

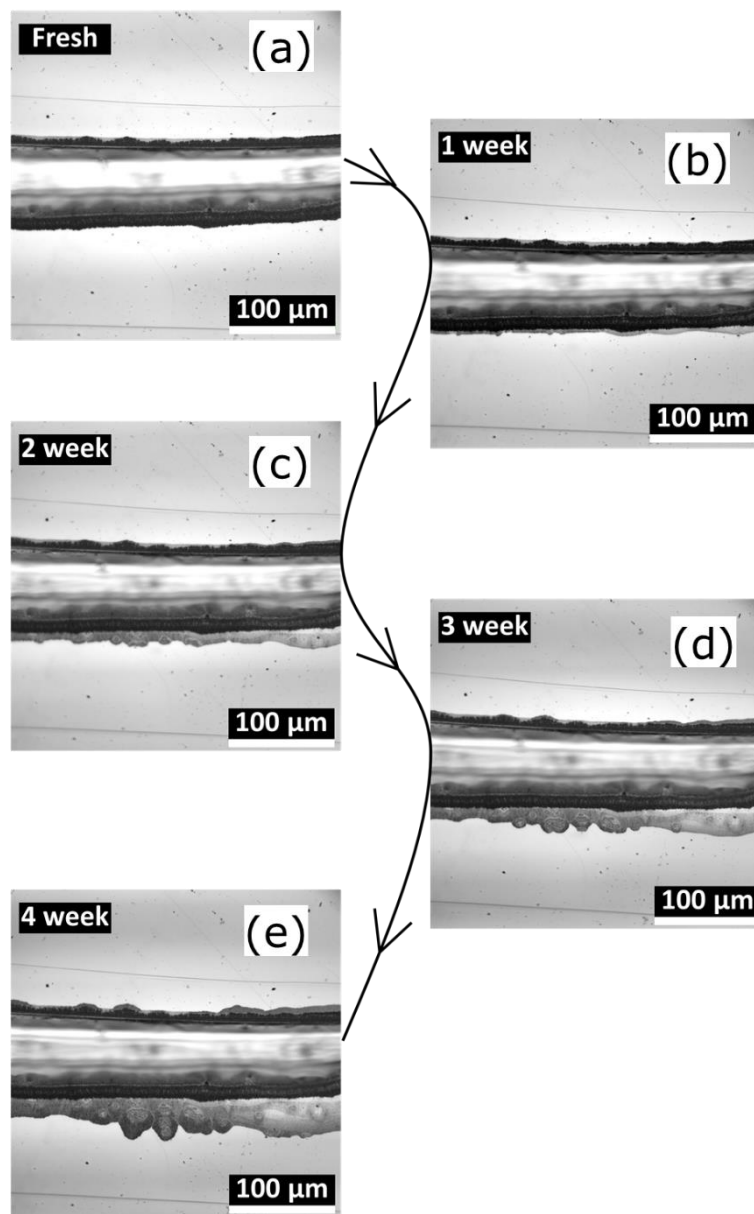


Figure 8. 19: Optical microscope images of PMMA encapsulated printed pattern on the gold surface show less penetration. (a) Fresh sample. (b) After 1 week. (c) After 2 weeks. (d) After 3 weeks. (e) After 4 weeks. The initial spread for the sample in (a) is probably induced by the high temperature during the curing of the PMMA (c.f. discussion on temperature influence on spreading and Figure 8. 18, Table 8. 2). Reproduced from [449] with permission from Wiley.

8.8 Estimation of the oxide layer

One of the most interesting properties of these gallium-based liquid metals is their tendency to spontaneously form a metal oxide on their surfaces. Even O_2 concentrations as low as 1 ppm are sufficient to form the oxide layer [99]. According to reports, this oxide layer is 1–5 nm thick [98], [473], [474]. This oxide layer acts as a passivating layer and provides stability to structures while/after

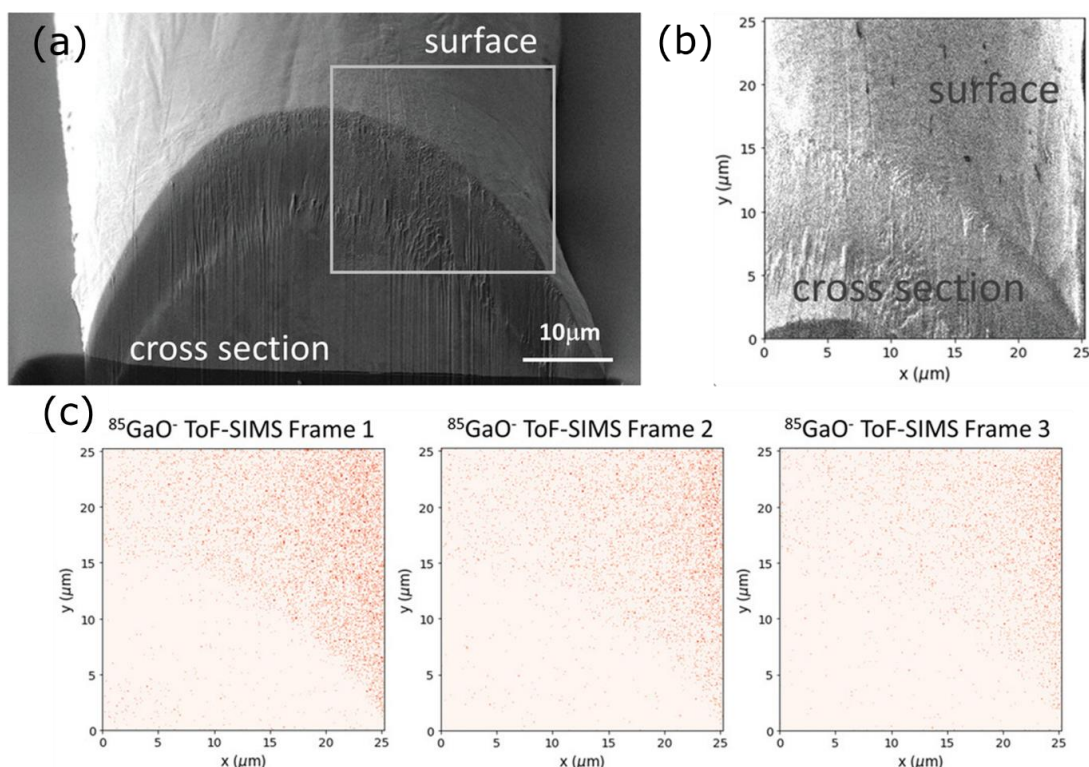


Figure 8. 20: Chemical analysis of the oxide layer on the printed LM lines. a) SEM secondary electron (SE) image of a cross-section after TOF-SIMS analysis (executed on the area indicated by grey frame). b) FIB SE image of the first frame of the TOF-SIMS analysis. c) GaO-signal of the first 3 ToF-SIMS frames indicating an oxide layer on the sample surface, while the in situ milled cross-section (not previously exposed to air) shows no sign of an oxide cover. d) Ga3d core level spectra from XPS measurement on a one-month air-exposed Galinstan sample. Reproduced from [80] with permission from Wiley.

printing on the surface that would ordinarily be unfavorable due to the extremely high surface tension ($\approx 640 \text{ mN}\cdot\text{m}^{-1}$) of bare LMs. This oxide layer can provide a rather negligible increase in contact resistance for reconfigured patterns (where there is a thin oxide layer between EGaIn and electrode pads) compared to the case of direct printing [101]. However, the oxide layer can be removed with HCl or NaOH treatment in some approaches [272], [274]. The remarkable stability of Galinstan-based LM structures, allowing even for 3D free-standing arcs (as described in chapter 4), as also demonstrated for LM droplets [100] and interconnects [101], is based on an oxide layer "skin" forming immediately on contact with oxygen from environmental air.

In order to obtain a better understanding of the oxide layer formation in printed systems and, in particular, learn about the thickness of the layer, experiments were conducted to characterize the printed LM lines with time-of-flight secondary ion mass

spectrometry (TOF-SIMS) and X-ray photoelectron spectroscopy (XPS), results shown in Figure 8. 20, Figure 8. 21.

The oxide layer can clearly be detected in TOF-SIMS measurements (Figure 8. 20a–c). For this, a cross-section of a LM line was done at $-100\text{ }^{\circ}\text{C}$ (Figure 8. 20a), and then an image area with parts of the cross-section and parts of the LM line surface (Figure 8. 20b) was mapped by TOF-SIMS (Figure 8. 20c).

While the cross-section shows no GaO^- signal (as an indicator of gallium oxide), a signal is clearly observed on the surface areas where the oxide layer is still present. During TOF-SIMS milling, the signal quickly diminishes within a few frames (Figure 8. 20c), indicating the thin nature of this layer. For further information on the oxide layer thickness, XPS measurements from a one-month air-aged Galinstan sample deposited on Si were conducted (Figure 8. 21a).

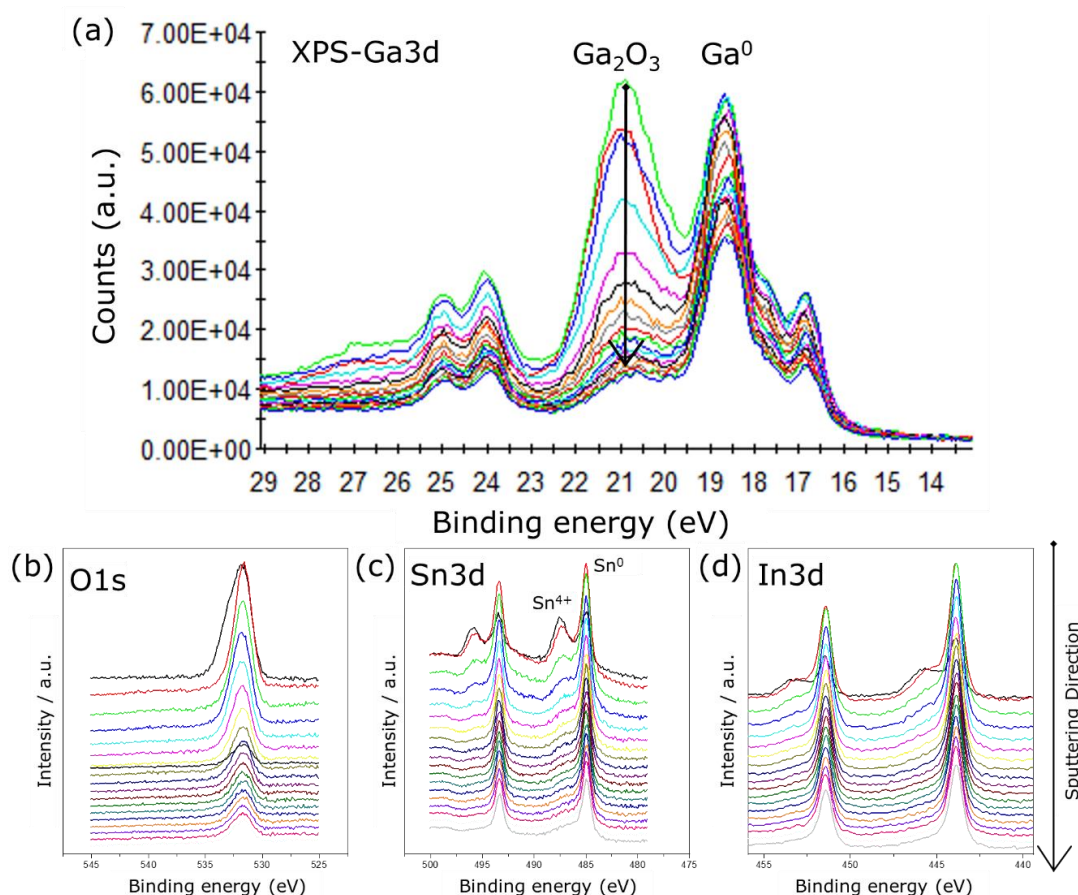


Figure 8. 21: Chemical analysis of oxide layer on the printed LM lines by XPS. Core level spectra from XPS measurement on a one-month air-exposed Galinstan sample. Core level spectra of (a) Ga3d, (b) O1s, (c) Sn3d, and (d) In3d of a sputtered depth profile on Galinstan. The graph was plotted in Origin (OriginLab, USA). Reproduced from [80] with permission from Wiley.

The Ga3d core level spectra have two high-intensity peaks at 20.9 and 18.6 eV corresponding to the Ga^{3+} and Ga^0 states of Ga [98], [475]. This clearly indicates

the Galinstan surface oxidized and formed Ga_2O_3 . Additionally, O1s In3d and Sn3d peaks are also detected on the oxidized surface of the Galinstan (see Figure 8. 21b,c,d).

To determine the thickness of the surface Ga_2O_3 layer, a sputtering depth profile was completed using 500 eV monoatomic Ar ion sputtering. The relative intensities of Ga^{3+} and Ga^{0+} states in the Ga3d core level spectra are considered for the determination of Ga_2O_3 surface layer thickness.

For the determination of Ga_2O_3 thickness following equation [476] is used:

$$t_{\text{Ga}_2\text{O}_3} = \lambda_{\text{Ga}_2\text{O}_3} \sin \theta \ln \left\{ \left[\frac{I_{\text{Ga}}^\infty}{I_{\text{Ga}_2\text{O}_3}^\infty} \left(\frac{I_{\text{Ga}_2\text{O}_3}^{\text{exp}}}{I_{\text{Ga}}^{\text{exp}}} \right) \right] + 1 \right\}$$

Where

$t_{\text{Ga}_2\text{O}_3}$: are the thickness of Ga_2O_3 .

$\lambda_{\text{Ga}_2\text{O}_3}$: inelastic mean free part of electron in Ga_2O_3 .

$\frac{I_{\text{Ga}}^\infty}{I_{\text{Ga}_2\text{O}_3}^\infty}$: Ga to Ga_2O_3 intensity ratio in their indefinite thickness.

$\frac{I_{\text{Ga}}^\infty}{I_{\text{Ga}_2\text{O}_3}^\infty}$: Ga to Ga_2O_3 intensity ratio in experiments.

θ : Angle between the plane of the sample surface and analyzer.

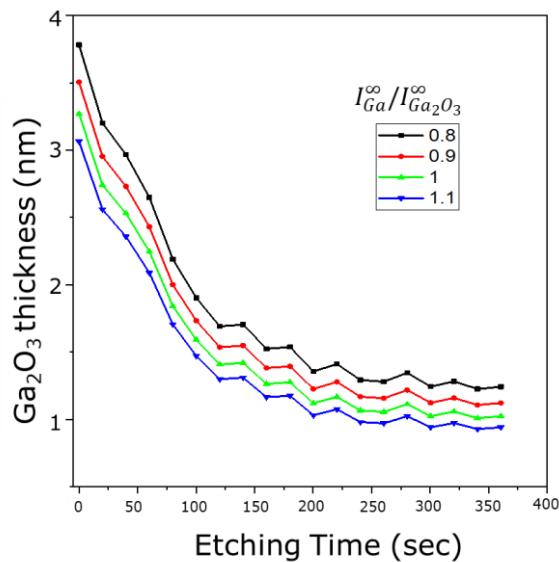


Figure 8. 22: The thickness of Ga_2O_3 over sputtering depth from Galinstan deposited on a Si substrate. Reproduced from [80] with permission from Wiley.

8. Gallium alloys and gold interfaces

Here, the $\lambda_{\text{Ga}_2\text{O}_3}$ was considered to be around 3.8 nm, obtained using the impWin software from NIST (National Institute of Standards and Technology) [477].

The $I_{\text{Ga}}^\infty/I_{\text{Ga}_2\text{O}_3}^\infty$ ratio should be obtained experimentally; however, as data on very thick films (to approximate the infinite case) is unavailable (especially for the oxide), this ratio cannot be obtained experimentally in these experiments. Therefore in these calculations, four different ratios were used to have an approximate thickness of Ga_2O_3 , which can also be seen in Figure 8. 22.

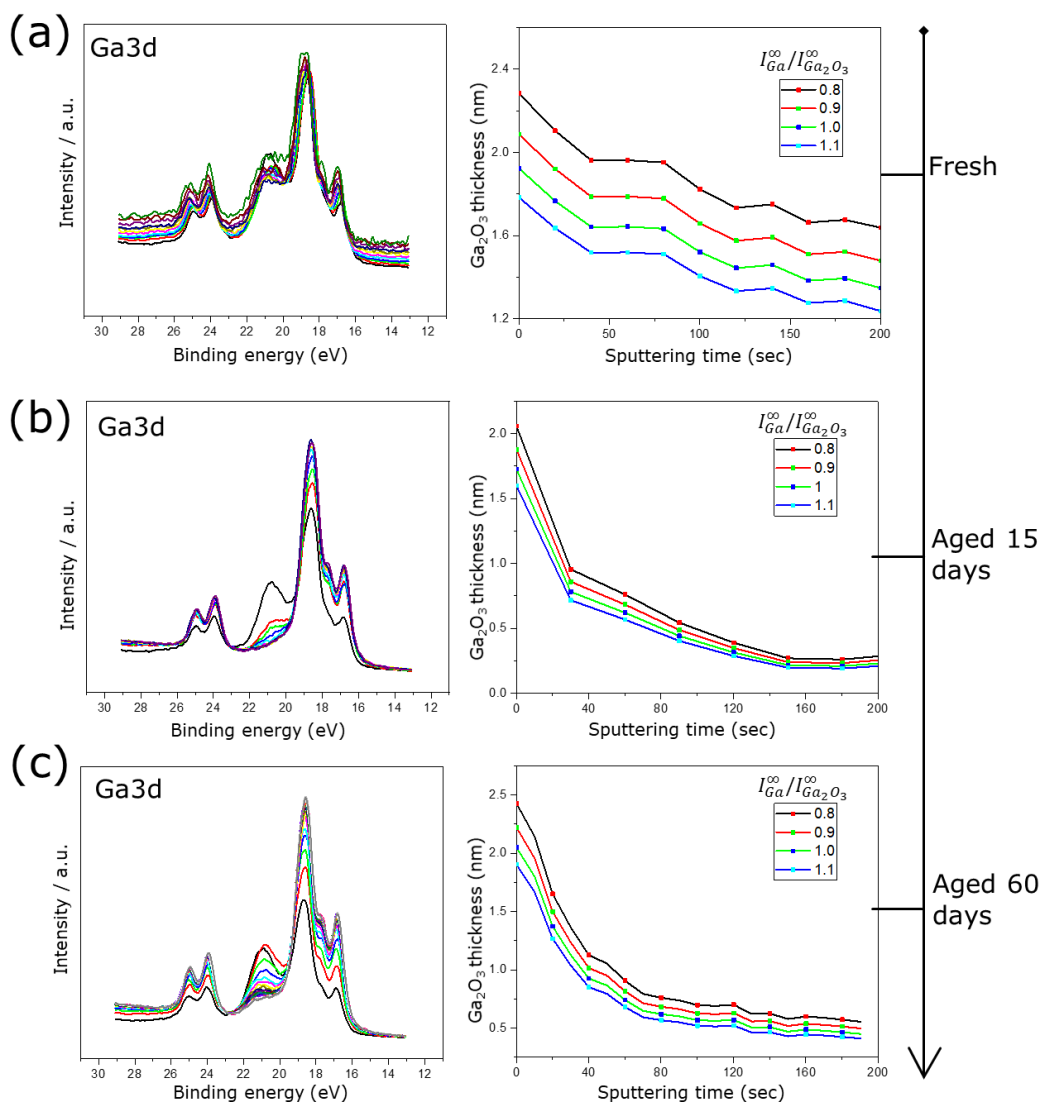


Figure 8. 23: XPS Analysis of aging Galinstan line. Ga3d core level collected from (a) fresh and aged samples for (b) 15 days and (c) 60 days on Galinstan deposited on Au substrate. The Ga_2O_3 thickness determined by sputtering depth profile XPS on fresh, 15 days, and 60 days-aged Galinstan samples. The thickness of Ga_2O_3 over layer changes from 2.0 nm to 2.5 nm in 60 days of aging in air. The graph was plotted in Origin (OriginLab, USA). Reproduced from [80] with permission from Wiley.

From the XPS data, a thickness in the range of 2.5 to 3.5 nm is obtained via modeling the data in regard to the theoretical ratio of Ga3d peak intensities in infinite thick Ga and Ga₂O₃ films. Following the evolution of the oxide layer thickness on a sample from freshly prepared up to 60 days (Figure 8. 23), there was only a minor growth of film, about 0.5 nm, in this time period. Thus, the initial oxidation of the surface limits the further oxidation of Galinstan, and the air aging has only a minimal effect on the growth of Ga₂O₃ on it. Overall, our results confirm the nanometer-sized thickness of the native oxide layer, as also estimated in other studies [473].

8.9 Electrical characterization of Galinstan-Gold contacts

To investigate the effect of time aging on the electrical properties of Galinstan-gold contacts, the total resistance was measured between the printed Galinstan pattern in between two gold pads. For this, printed (38.38 ± 2.35) μm wide Galinstan lines

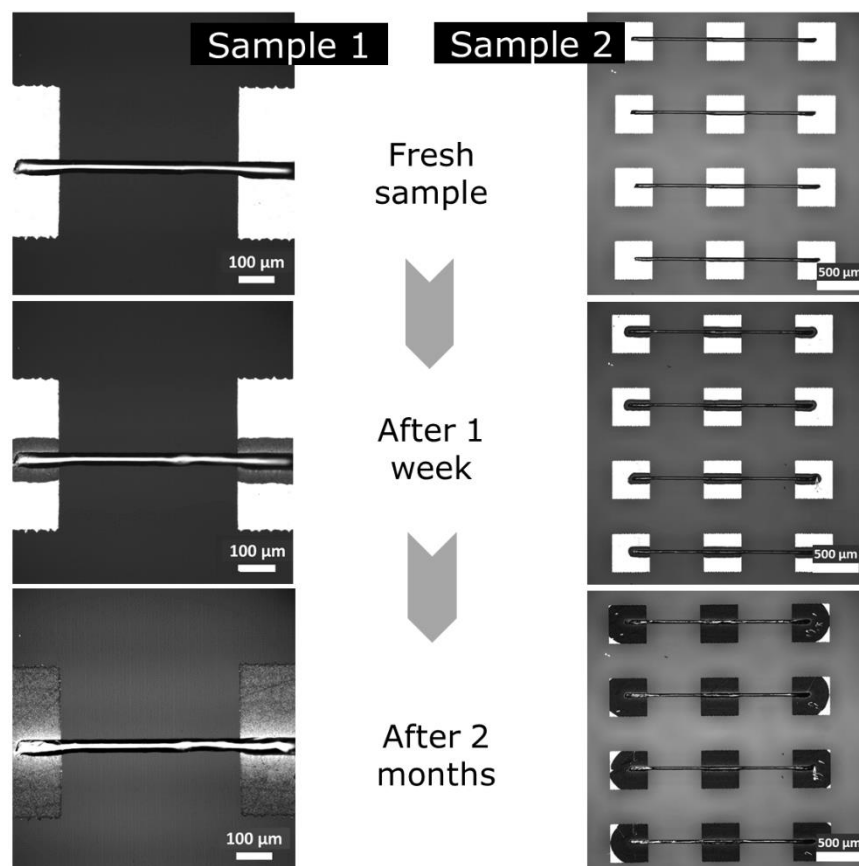


Figure 8. 24: Printed resistors as Galinstan lines between two gold pads (average width: 38.38 ± 2.35 μm), the distance between two gold pads 500 μm for sample 1 and 1620 μm for sample 2 (including 42 μm of the middle gold pad). Reproduced from [449] with permission from Wiley.

(Figure 8. 24) connecting two gold pads located at 500 μm for sample 1 and 1620 μm for sample 2 (including 420 μm of the middle gold pad).

The resistance between the pads was measured using two probes for the samples for freshly prepared samples after seven days, one month, and two months of aging time. Optical microscope images were also captured for the same intervals. As the optical microscope images show in Figure 8.24, the Galinstan starts reacting with a gold pad immediately after the printing, and after two months, the gold pads are entirely covered.

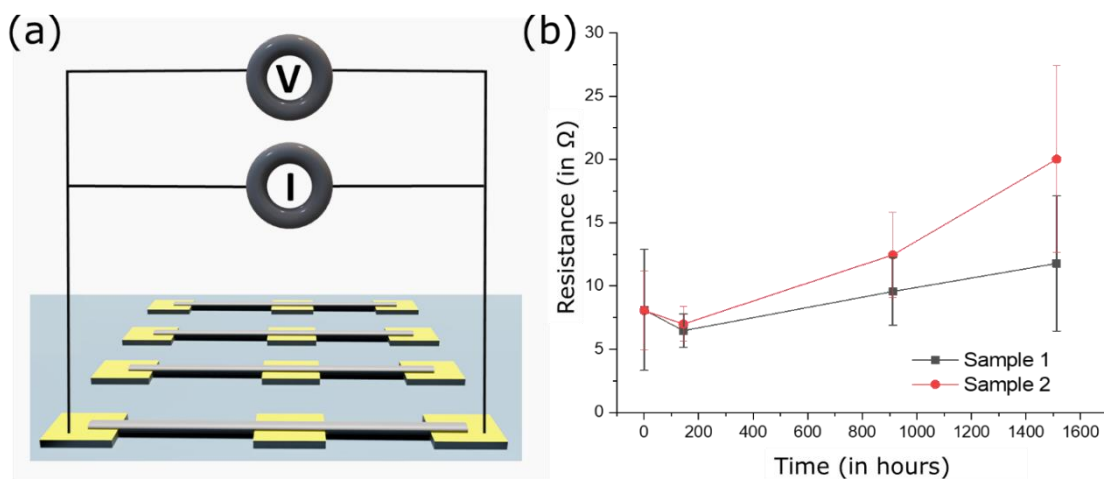


Figure 8. 25: Scheme of Au/Galinstan setup. (a) Conductivity measurement setup based upon a 2-point probe system. (b) Resistance studies with respect to time for two types of printed resistors. For each data point, the resistance was measured for 10 samples. The graph was plotted in Origin (OriginLab, USA). All error bars in graphs and error ranges reported represent one standard deviation (SD) of the reported mean. Reproduced from [449] with permission from Wiley.

The resistance measured using two probes increased with respect to air aging. The resistance for directly printed Galinstan resistors between two gold pads was (8.11 \pm 4.77), (6.47 \pm 1.32), (9.56 \pm 2.68), and (11.77 \pm 5.33) Ω for fresh, after 7 days, one month and two months aging, respectively. On the other hand, for sample 2, it was found to be (8.05 \pm 3.10), (6.99 \pm 1.36), (12.45 \pm 3.36), and (20.01 \pm 7.38) Ω for the same time intervals, respectively. Both of the data were measured for an average of 10 samples. Overall, there is only a slight difference in total resistance over time. However, there is a higher increase for sample 2, where the LM line was traversing a 420 μm additional gold pad in contrast to the direct connection of electrodes in sample 1. This could indicate an additional change in LM composition and internal structure over the middle part of the connection in sample 2, where it is in direct contact with the gold pad. Here, Au can penetrate back into the LM line itself (Figure 8. 16), potentially raising the LM lines' resistance as of the introduced phase boundaries and localized composition changes, as, e.g., also observed in Fe-loaded LMs [259].

Part IV. Summary, conclusions and outlook

9. Summary

The aim of this thesis is to explore the potential capabilities and applications of new direct writing/patterning methods to fabricate fully printed electronic devices. The methods developed include a high-resolution glass capillary-based LM additive manufacturing setup and a low-cost microplotter system. Several key challenges with these direct-write approaches are discussed, and possible solutions are implemented or outlined. Most importantly, this thesis explores the potential use of LM direct write methods for the fabrication of fully functional electronic components and devices. The thesis completes all the objectives discussed in chapter 1. The first objective was to develop a unique method to directly write LM on surfaces. The second objective was to design a low-cost, on-demand printing setup that could be used without intensive training, making it much more accessible for new users. The third objective was to use these printing methods to design LM-based microelectronic devices as resistors, diodes, and transistors. The fourth objective was to directly write microheater structures with the LM printing setup and rectify the occurring challenges and explore advantages associated with LM-based microheaters. The fifth objective was to thoroughly study the interface formed between the LM (Galinstan) and gold pads used in microelectronics devices.

Printing setups, their design, manufacturing, and application in printing microelectronic devices, as well as the electrical characterization of the resulting devices corresponding to each of these objectives, have been presented.

This thesis has several contributions to the understanding and advancement of printed electronics. The following section provides a detailed summary chapter-wise:

- Chapter 2 gives a background of printable materials and basic printing methods available in printed electronics. It discusses some common printable materials and functional inks (insulator, semiconductor, conductor inks) used in PE, along with a brief introduction to LMs and the problem associated with writing LMs. The discussion also includes the efficiency and printability of all functional inks, regardless of whether they were organic or inorganic. It also covers pre-printing steps and post-printing processes.
- Chapter 3 deals with device design, functioning, and typical characteristics of p-n diodes, field effect transistors, and microheaters. It also discusses the printed electrolyte gated FETs (EGFET)'s basic structure and functionality. It also presents a brief overview of the state-of-the-art LM-based microelectronic devices.

- Chapter 4 shows the glass capillary-based direct write system developed during the thesis based on a customized commercial nanolithography system. It shows Galinstan-based LM structures with remarkable stability (macroscale as well as microscale) with different thicknesses and widths; even 3D freestanding arcs were created with this approach. The chapter also discusses factors influencing the dimensions of the written patterns, such as the inner diameter of the capillary, the size of the capillary tip opening, and the distance between the substrate and the glass capillary tip. The minimum width of homogeneous, well-defined lines achieved in this approach is $(1.3 \pm 0.1) \mu\text{m}$, which is achieved using a tip of $2 \mu\text{m}$ opening and at a writing speed of $1000 \mu\text{m}\cdot\text{s}^{-1}$. It also shows that interspacing of LM lines can be achieved in the sub- $10 \mu\text{m}$ range without merging of lines. Challenges that arise while printing Galinstan (the LM used here) and methods to address those challenges are also discussed.
- Chapter 5 describes the design and implementation of an open-source microprinting system that allows for flexible and highly accessible on-demand microplotting on samples and devices that are otherwise hard to address with conventional spotting methodologies. The setup provides a straightforward installation, configuration, and hassle-free operation without special training and offers competitive resolution and precision. This setup can be used intuitively as direct access to the microrealm for everyone. This microplotter setup can provide printing of various aqueous solutions and solvent-based liquids in a wide viscosity range. This chapter also explores the microplotter setup's high accessibility and ease-of-use for flexible on-demand functionalization ranging from the micro- to mm scale. Furthermore, the uses of this microplotter system in model applications for printable electronics and bioactive device functionalization are demonstrated, exemplifying the broad material compatibility and flexibility for substrate geometry. For printable electronics applications, Au nanoparticle-based ink is printed on glass coverslips, and Kapton foil is then cured to make the patterns conductive. The characterization of printed patterns with optical microscopy shows that sub- $10 \mu\text{m}$ gap sizes between features could be achieved. The chapter also discusses the flexibility of this micromanipulator-based printing approach for in situ and on-demand printing of interconnects. It also demonstrates the printing capability of biomaterial inks, such as inks containing lipids (DOPC), proteins (BSA), and small bioactive molecules (biotin).
- Chapter 6 shows the fabrication of various fully printed devices based on Galinstan capillary printing. This chapter discusses the fabrication and electrical characterization of fully printed interconnect wires, resistors, p-n diodes, and transistors which are process compatible with other digital printing methods and thin film structuring methods for integration. The fully printed working p-n diodes shows currents in the order of $I_{\text{ON}} = 10^{-4} \text{ A}$ and

$I_{\text{OFF}} \approx 10^{-9}$ A (ON/OFF ratio of 10^5), translating to a current density of ≈ 2.28 A \cdot cm $^{-2}$, at an area of 100×100 μm^2 . The LM-based fully printed transistors show ON currents in the order of tens of mA, display a negative threshold voltage (V_{th}) of -0.31 V, and a current ON/OFF ratio of 1.84×10^3 . It is also observed that there is a leakage current in the order of 10^{-8} A. The chapter also shows tunable resistors that can be further encapsulated with PMMA to protect them from environmental influences without losing conductivity.

- Chapter 7 shows the direct writing of LM-based microheaters with meander structure design on glass substrates. In the fabricated microheaters, optical microscopy reveals an average LM line width of around ≈ 100 μm , with a minimum line width of 20 μm . The LM microheater structures were characterized for power consumption, response time, and heating and cooling rates. These LM microheater structures can go up to 200°C . The maximum voltage applied is 2.5 V, and the power consumption is 1.54 W. The response time while heating is around 150 seconds to reach a stable temperature. While cooling, the sample takes around 250 seconds to reach near room temperature.
- Chapter 8 describes the study of the interaction of Galinstan with solid gold surfaces correlating different techniques. Additionally, the study explores the oxide layer of Galinstan, which is the origin of the surprising stability of the printed structures. It is observed that Ga and In can penetrate from LMs into solid gold along grain boundaries due to stress (then the process is called Liquid Metal Embrittlement (LME)) and a thermodynamic driving force that reduces the interfacial energy (then referred to as grain boundary penetration (GBP)). As Ga and In spread into the Au, they form intermetallic structures. A correlated characterization system is applied that contrasts Vertical scanning interferometry (VSI) with Energy-dispersive X-ray spectroscopy (EDS) and Scanning Electron Microscopy (SEM) to assess the physical topography and chemical mapping, and it also helps to determine the spread rate. For the initial 30 hours, the spread is found to be around (32.97 ± 3.59) μm , which translates into a spread rate of around 1.1 $\mu\text{m}\cdot\text{h}^{-1}$. For the period 30 hours to 144 hours (day 6), a spread of (34.34 ± 3.30) μm is found, respectively, which signifies a spread rate of 0.3 $\mu\text{m}\cdot\text{h}^{-1}$. The intermetallic nanostructures formation in Galinstan-Gold is also observed in SEM and EDs with respect to time, which shows Ga and In start spreading into the gold surface immediately on contact. Sn penetration is not seen in initial EDS maps, and only later EDS maps after 1 week show slight signals of Sn appearing on the gold surface near the Galinstan line. It is also observed that the formation of the intermetallic nanostructures becomes visible even to the naked eye after enough time has passed. XRD of intermetallic structures suggests predominantly AuGa_2 formation. The chapter also shows the XPS study of the spreading of Galinstan on the Au surface over a period of 120 days. Here, it also became visible that the oxide layer growth on Galinstan is self-limiting,

as a stable thickness is already reached eight days after film deposition. In addition, it is found that some Au migrated to the surface of the LM film, also forming AuGa phases. In the XPS study of air-aged and HCl etched (afterward aged in Ar) samples, the sputtering depth profile shows that only the air-stored Galinstan is oxidized, while on HCl etching, the Ga_2O_3 is removed, but the formation of an even more stable GaCl_3 layer was observed. The AFM study of the intermetallic structures shows that all of the positions in the sample have similar hill structures in regard to size and height, and only minor roughness differences are observed. Additionally, an X-ray nanoCT study of a Galinstan-coated gold-wire tip of $31 \mu\text{m}^3$ volume shows a distribution of ca. 48% of intermetallic phases, 35% of Galinstan, 12% of gold, and 5% of oxygen. It also shows that the inner structure is mostly intermetallic phases and gold, Galinstan is distributed in the more external layers, and oxygen forms a thin layer on the sample surface. Based on all the results, a growing mechanism for the intermetallic nanostructures is proposed based on the penetration of Ga and In from the LM into the gold surface. Additionally, the effects of temperature and humidity on intermetallic structure formation are studied. While the influence of humidity seems negligible, heating the substrates to elevated temperatures of 50°C and 100°C substantially increases spread, in particular for thicker line structures. Other than that, this chapter also offers a better understanding of the oxide layer formation with the help of time-of-flight secondary ion mass spectrometry (TOF-SIMS) and X-ray photoelectron spectroscopy (XPS). The XPS sputtering data estimates the thickness of the oxide layer of Galinstan in the range of 2.5 to 3.5 nm.

10. Outlook

The work presented in this thesis showcased the potential of glass capillary-based direct writing of LM for fabricating functional, fully printed electronic devices. There are several directions in which this work could be extended to further realize the potential of LM direct writing for printed electronics applications. Some of the potential directions in which this research could be extended in the future are as follows:

- Update of the micromanipulator-based system

The ink/substrate range could be broadened even further by the integration of an active ink delivery system (e.g., syringe pump or microfluidic controller) into the glass capillary stylus, omitting the capillary force relying on the ink transfer mode presented here. Further control in printing could also be achieved by the inclusion of the setup within a humidity chamber if desired for certain types of inks or substrates. In general, it should be noted that the achievable minimal feature size is highly dependent on the interaction of the ink and substrate, i.e., in particular, the surface tension of ink and the surface energy of the substrate. Combining the setup with more powerful optics would also allow us to fully leverage the micromanipulator robots positioning precision, enabling not only the functionalization of hard-to-reach surfaces but also pre-existing microstructures themselves, e.g., for 3D-printed complex microscaffold structures in cell experiments [478]. It would also be conceivable to add other stylus designs allowing for multi-ink deposition, e.g., by

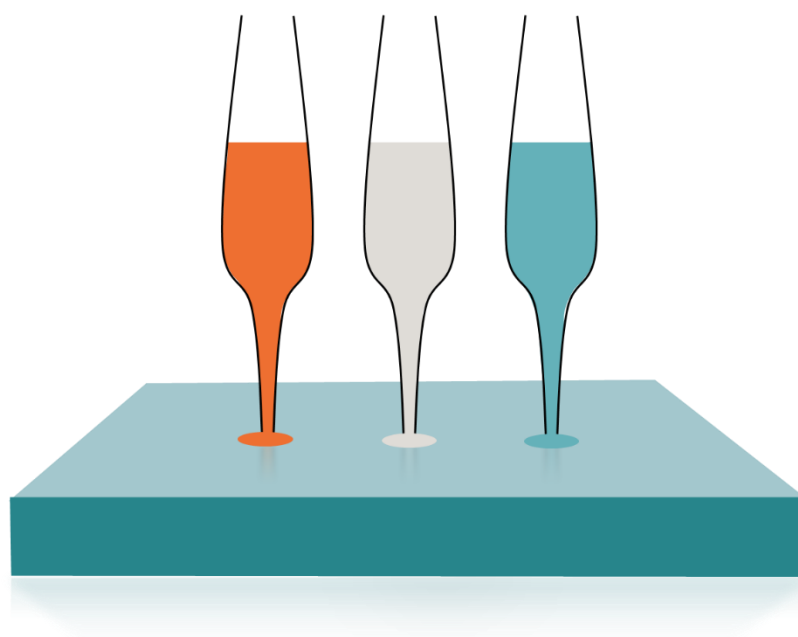


Figure 10. 1: Multi-ink deposition using parallel arrays of glass capillaries.

parallel arrays of miniaturized capillaries (as shown in Figure 10. 1), or using other printing principles as, e.g., in arrays of microchannel cantilevers [479] or miniaturized polymer pen lithography stamps [480] (thus all of these would need conformal leveling, complicating manual control).

- Fabrication of nano-meter feature LM lines

There is a very high demand from the electronics industry to fabricate features with finer resolutions than those achieved during the course of this research using 250 nm diameter nozzle openings. These can be accomplished by using techniques such as FluidFM [244], [481], [482] or with the help of using nanosized nozzles such as Polymicro Nano-Capillary Tubing (inner diameter 200nm) [483]. In these cases, high pressure would be needed to extrude the LM out of the nozzle as of the increased capillary force. All the parameters and designs should be studied to look for the possibility of upgradation/improvement and to practically accomplish nm-scale LM printing. The microheaters reported in the thesis are usually used in gas sensors, but in the future, on-demand direct fabrication and nm-resolution printing would help to accomplish in situ manipulation of samples by directly writing the desired micro/nanoheater structure around/on the sample. Applying heat stimuli to samples would help to understand sample properties and interactions in real-time at elevated temperatures. The geometry can be designed such that the sample can be in either contact with LM or covered with SiO₂ and then LM printed over it. These LM micro/nanoheaters can also be also used for other large variety of applications, such as stretchable, wearable, or implantable heating probes or for thermos control in PCR, etc.

- Improving the performance of current fully printed electronic devices

The fabricated FETs show a leakage current in the order of 10⁻⁸ A and are fabricated with a yield of ≈19%. We attribute these to the only thin film thickness of the electrolyte layer on top of the Galinstan lines so that PEDOT:PSS might penetrate the electrolyte in these areas, causing this significant leakage current. In the electrolyte layer, CSPE could be replaced with ion gel [123], [484], and the whole device can also be encapsulated to avoid any effect of moisture or the environment [485]. Overall, on further optimization of the printing process, multilayer printing, and post-processing steps, these issues, including yield, might be improved in the future.

- Extending fully printed electronic devices for fabricating electronic circuits

The device functionality achieved with only a single processing technique for various inks eases the fabrication flow and shows the great potential of LM printing, which by far exceeds its simple use as interconnect of conventional electronic devices in PE. These fully printed electronic devices can be primarily extended to flexible substrates and designed LM-based fully printed components such as inverters and ring

oscillators. In the future, these fully printed devices can be used in circuit building blocks for wearable, flexible sensors and, in particular, for bioelectronics and biomedical applications. In the latter, the devices will be in direct contact with living systems, and the favorable material properties concerning toxicity, as well as their relatively low cost of processing (enabling one-time use when needed), will be a significant advantage.

Part V. Appendix

A.1. Materials

Table A. 1: Materials used in work throughout the thesis.

| No. | Name | Catalogue Number | Supplier |
|-----|--|------------------|--------------------------------------|
| 1 | Glass pipette borosilicate | GC120TF-10 | Warner Instruments |
| 2 | Chloroform | 1.02445.1000 | Merck Group |
| 3 | 2-propanol | 6752.1 | Carl Roth GmbH |
| 4 | Acetone | 20063.296 | VWR Chemicals (avantor) |
| 5 | Ethanol | 20821.296 | VWR Chemicals (avantor) |
| 6 | Dimethyl sulfoxide | 276855-1L | Sigma-Aldrich |
| 7 | Galinstan | 200 gm pack | Strategic Elements |
| 8 | Gold nanoparticles ink | UTDAu25-IJ | UT Dots |
| 9 | Indium(III) nitrate hydrate $\text{In}(\text{NO}_3)_3 \cdot x \text{H}_2\text{O}$ | 326127-10G | Sigma Aldrich |
| 10 | Glycerol | 65516-500ML | Sigma-Aldrich |
| 11 | Copper(II) nitrate hemi(pentahydrate) $\text{Cu}(\text{NO}_3)_2 \times 2.5 \text{H}_2\text{O}$ | 223395-100G | Sigma-Aldrich |
| 12 | Propylene carbonate | 310328-500ML | Sigma-Aldrich |
| 13 | Lithium perchlorate (LiClO_4) | 431567-50G | Sigma Aldrich |
| 14 | Poly(3,4-ethylenedioxythiophene)-poly(styrenesulfonate) PEDOT:PSS 3.0-4.0% in H_2O | 655201-25G | Sigma-Aldrich |
| 15 | Ethylene glycol | 324558-100ML | Sigma-Aldrich |
| 16 | PMMA | - | Micro Chem |
| 17 | Anisole | - | Sigma-Aldrich |
| 18 | 1,2-dioleoyl-sn-glycero-3-phosphocholine (DOPC) | 850375C-25MG | Avanti Polar Lipids (USA) |
| 19 | Bovine serum albumin (BSA) | - | Invitrogen, Thermo Fisher Scientific |
| 20 | Protein A-biotin from staphylococcus aureus in phosphate-buffered saline (PBS) | - | Sigma-Aldrich |
| 21 | Rhodamine 6G | - | Sigma-Aldrich |
| 22 | Fluorescein isothiocyanate (FITC)-PEG | PG2-FCTH-1k | NANOCS |

A.1. Materials

| | | | |
|----|--|-----------------------|-------------------------------------|
| 23 | Alexa fluor 647 azide, triethylammonium salt | A10277 | Life Technologies, Thermo Fisher |
| 24 | Silver epoxy | Elecolit® 3653 10g | Panacol adhesives |
| 25 | Polytetrafluoroethylene membrane | MS-3201 | Pall Inc Acrodisc® |
| 26 | Polyvinylidene fluoride (PVDF) 13 mm syringe filter with 0.2 µm membrane | 4450T | Pall Inc Acrodisc® |

A.2. Methods and techniques

A.2.1 Glass capillary preparation

For preparing glass capillaries with varying tip and taper sizes, a Sutter Instruments P-1000 micropipette puller system (Figure A. 1) was used. This P-1000 is designed to handle 0.6-3.0 mm outer diameter aluminosilicate, borosilicate, or other lower melting point glass tubing or capillaries. Quartz glass cannot be pulled with this instrument. Throughout the thesis, glass pipettes with an outer diameter (OD) of 1.2 mm, and an inner diameter (ID) of 0.94 mm, and a length of 100 mm were used (Warner Instruments, GC120TF-10).



Figure A. 1: P-1000 micropipette puller system. (Setup at glass workshop INT)

Pulling parameters for heat, filament (fil), velocity (vel), delay (del), and pull (as shown value used in Table A. 2) were also used to produce the glass capillary with different tip and taper sizes.

Scoring the glass capillary

- I. To score the glass capillary held in one hand (on the left in Figure A. 2), the part near the shoulder of the taper of the second glass capillary (in the right hand in Figure A. 2) should be kept on the top of the desired position to break.
- II. After scoring, make sure that the scoring glass capillary is above the location of the score → push the top of the taper to break the glass capillary off at the desired position.

Table A. 2: Description of capillary pulling parameters used on the P-1000 system. Adapted from Sutter Instruments pipette cookbook 2018 [486], Sutter Instrument Company.

A.2. Methods and techniques

| Parameter | Value Description | Values used* | Increase | Decrease | Notes for Practical Use |
|-----------|--|--------------|---------------------------------|---------------------------------|--|
| Heat | This value does represent the amount of current supplied to the filament. | 540 | smaller tip with longer taper | larger tip with a shorter taper | If the heat is too high/low, there is a risk of burning the filament or damaging the puller. |
| Pull | When the glass is softened, this setting determines how much current is supplied to the solenoid that creates the hard pull. | 90 | smaller tip with longer taper | larger tip with a shorter taper | < 0 > for 3-5 mm short taper and a 1-3 μ m tip. <50-150> for microinjection needle. |
| Vel | This is the puller bar's separation rate when the glass first melts. | 100 | smaller tip with longer taper | larger tip with a shorter taper | Typical Value: <18 - 65> |
| Time | As the glass and filament are pulled through the air, this is the time it takes for the glass and filament to cool | 250 | larger tip with a shorter taper | smaller tip with longer taper | Recommended: 150 (75ms) for trough filament. 250 (125ms) for thick glass. |
| Pressure | During cooling, this is the pressure of air used. | 500 | larger tip with a shorter taper | smaller tip with longer taper | Default: 500 units (2psi) of cooling air |
| Delay | The Delay value represents how long the glass is cooled before pulling | Not Used | larger tip with a shorter taper | smaller tip with longer taper | A low Delay value of 40-90 units. A higher delay value is 100-250. |

*: Value used to make glass capillaries used in this thesis. To make glass capillaries for different tip sizes, the same capillaries were scored from the desired position, as shown in Figure A. 2.

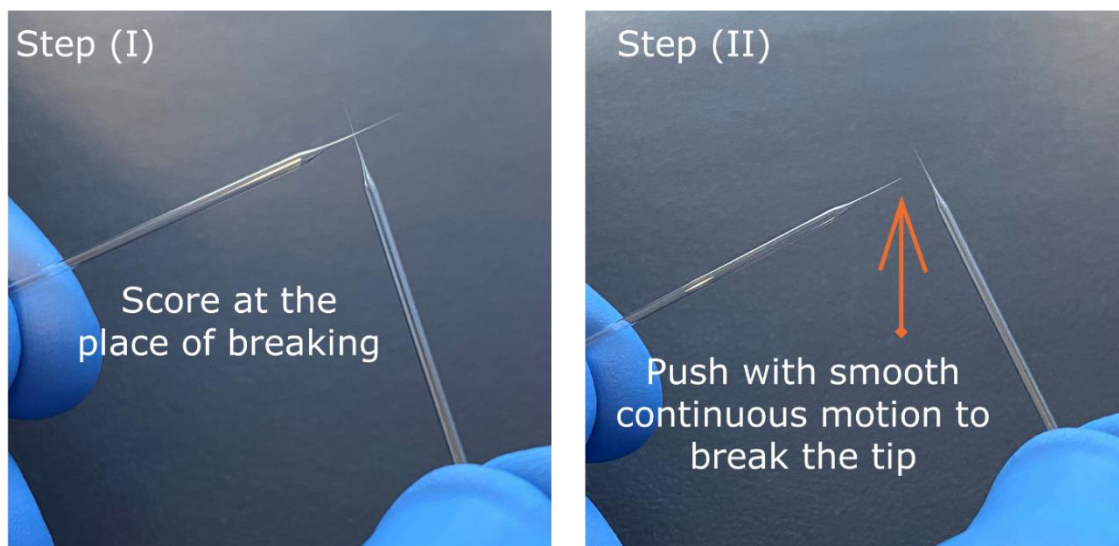


Figure A. 2: Process of breaking the Glass capillary tip for desired and larger aperture size. Adapted from Sutter Instruments pipette cookbook 2018 [486].

A.2.2 Preparation of substrates

Standard glass coverslips (size: 18mm X 18mm, from VWR Germany) were cleaned with chloroform, 2-propanol, and finally with deionized water, and later dried by blowing with nitrogen. In some cases, an ATTO B plasma-cleaner (Diener electronic GmbH, Germany, shown in Figure A. 3) was used for cleaning substrates for hydroxyl functionalization (10 sccm O₂, 0.2 mbar, 100 W, 2 minutes). Plasma cleaning is usually performed with oxygen plasma in a high-frequency plasma system, which removes organic matters and carbon from products deposited during the cleaning or handling.

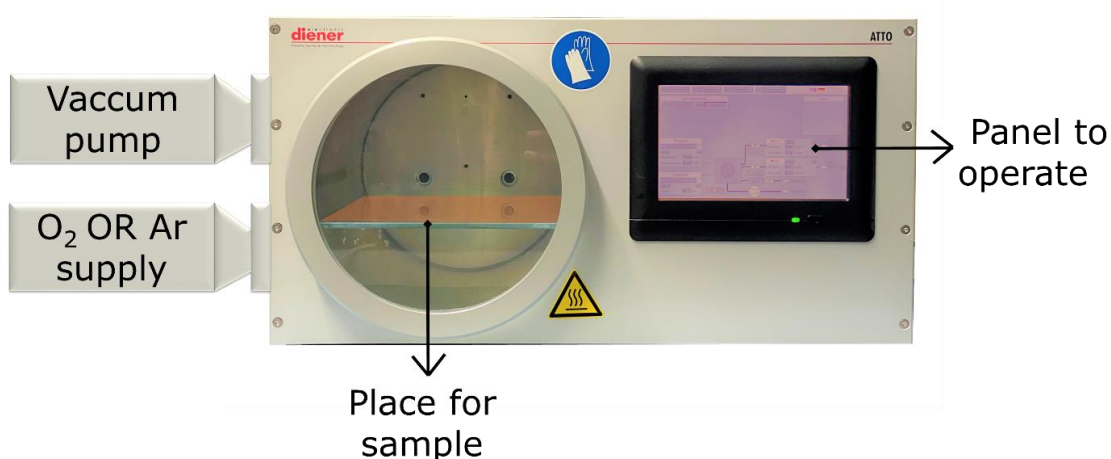


Figure A. 3: ATTO B plasma-cleaner (Diener electronic GmbH, Germany) at INT.

The surface energy is increased without damaging the material's properties. The vacuum system pumps out all removed contaminants out of the chamber.

A.2.2.1 Gold-coated substrates with e-beam evaporation

The setup with e-beam evaporation and deposition under a high vacuum capability was used to deposit a gold film onto freshly cleaned glass substrates. To improve adhesion, the glass substrate was first coated with a 7 nm Cr layer and then 150 nm Au over it. Electron beam bombardment at ultra-high vacuum temperatures heats the material to high vapor pressure and condenses it onto the substrates. It yields the smoothest, cleanest gold surfaces and can deposition as much as $100 \mu\text{m}\cdot\text{min}^{-1}$.

Instrumentation and working:

As shown in Figure A. 4, an e-beam physical vapor deposition (EBPVD) system uses an evacuated deposition chamber (at least 10^{-5} Torr), allowing electrons to pass from an electron gun to an evaporation material, which can either be an ingot or rod. These EBPVD systems can simultaneously use a variety of evaporation materials and electron guns with power ranging from tens to hundreds of kilowatts. There are three methods of generating electron beams: thermionic emission, field electron emission, and anodic arc emission. Electron beams are generated and accelerated to high kinetic energy before being directed toward evaporation materials. As soon as the electrons strike the evaporation material, their energy will be rapidly lost, and they convert their kinetic energy into other forms of energy, usually thermal energy. Melting or sublimation occurs because of this thermal energy. At high temperatures and vacuum levels, melted or solid materials will emit vapor. Surfaces can then be coated with the resulting vapor. Depending on the application, accelerating voltages can range between 3 and 40 kV. Another overview can be read here [487].

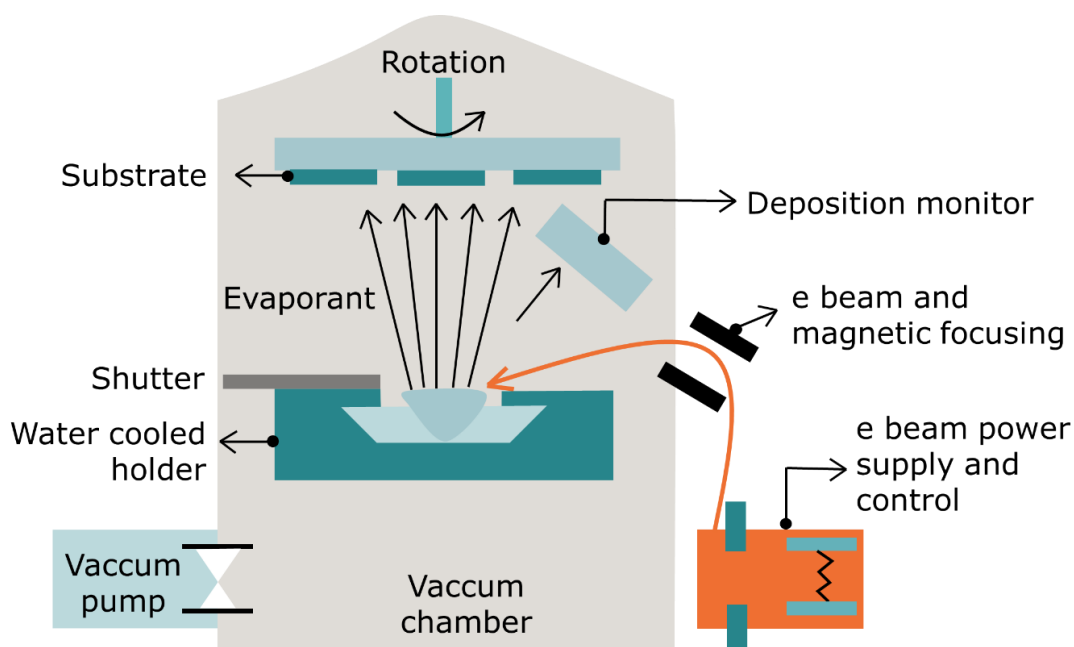


Figure A. 4: Working of e-beam physical vapor deposition (EBPVD).

A.2.2.2 Laser ablation

Laser ablation of gold-coated substrates was performed with the TRUMPF TruMicro 5000 laser ablation system to obtain contact pads with varying distances between the pads (60–550 μm). As shown in Figure A. 5, high laser flux typically results in plasma formation during the ablation process. Laser ablation usually refers to the removal of material using a pulsed laser (with certain pulse width and frequency), but continuous wave laser beams (laser remains on continuously until stopped) can also be used.

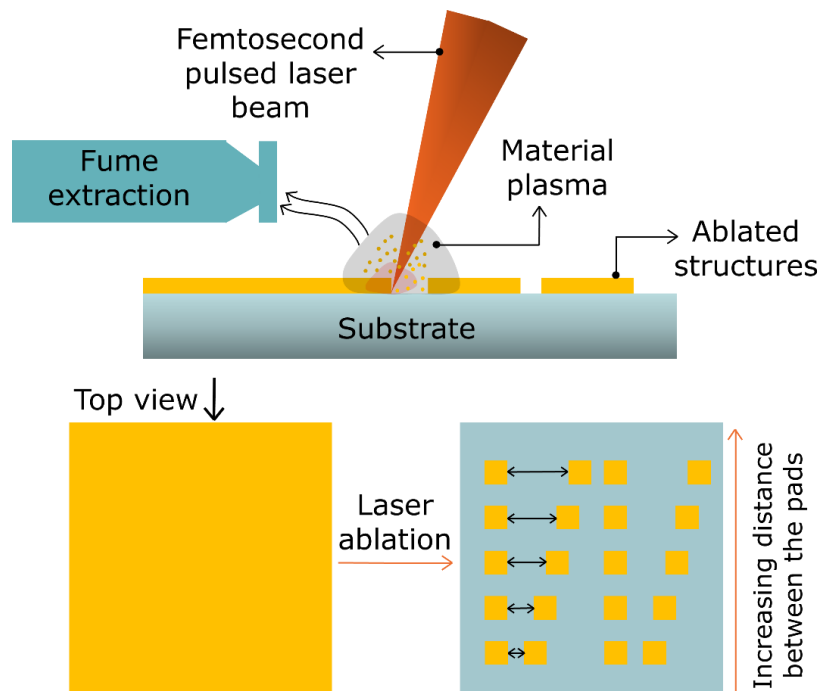


Figure A. 5: Working of laser ablation and fabrication of contact pads with varying distances between the pads (60–550 μm)

Depending on the ablation threshold of each material, laser ablation can differentiate between two or more materials when vaporizing a layer from an object. When the ablation thresholds of the materials are sufficiently different, one layer (the lower ablation threshold layer) can be removed, and at the same time, the substrate isn't ablated much. In our case, gold was ablated from a glass substrate. Lasers do not use toxic chemicals or solvents, and only a laser beam is used to vaporize the layer being removed, so they can be referred to as safe. However, in order to prevent hazardous substances from being released into the air or surrounding areas, a fume extraction system must be installed. Other than that, suitable safety glasses must always be put on while the laser is ON and during the ablation process. Detailed principles and working of laser ablation and machining can be read here [488], [489].

A.2.2.3 Focused Ion Beam (FIB) lithography

The cross-sections of Galinstan lines on silicon substrates shown in Figure 8. 5 were fabricated using a dual-focused ion beam (FIB)/scanning electron microscopy (SEM)

(Crossbeam 540, Carl Zeiss Microscopy, Oberkochen, Germany) at Heidelberg University, that was cooled to -100°C using a Leica cryo stage. Thus, solid Galinstan could be ablated with Ga^+ ions. For milling and polishing the cross-section, Ga^+ ions with an energy of 30 kV and currents of 15 nA, 3 nA, and 700 pA were used. For Figure 6. 6 and chapter 8, FIB was performed using a dual-beam Zeiss AURIGA 60 system (available at INT). For trench milling and cross-sectioning, a focused Ga^+ ion beam with a 30 kV potential was applied with distinct apertures of 20 nA to 16 nA. With the help of a Deben cryo-stage, partially cross-sections were milled and imaged under cryo-conditions at -50°C .

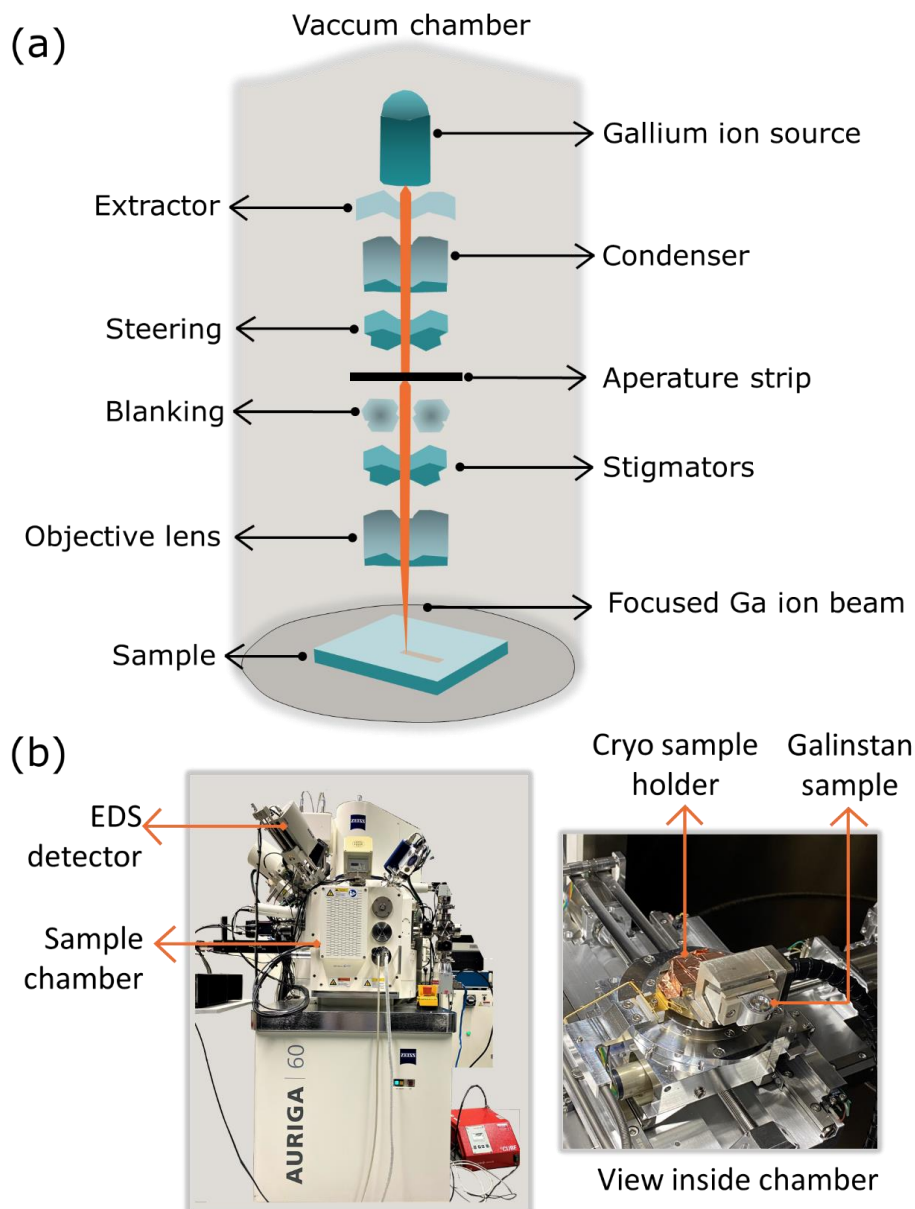


Figure A. 6: (a) Focused Ion Beam Lithography working. (b) Auriga 60 System at INT. Special cryo holder and mounted Galinstan sample.

Working of FIB:

A FIB can also be used for direct-write patterning. The FIB patterning technique is similar to electron beam lithography (EBL), but the energy carriers in FIB patterning are ions rather than electrons. Throughout the milling process, atoms are milled away and removed from the sample by an ions beam (usually Ga^+). The instrumentation includes ion source, extractor, condenser, steering, blanking stigmators, and objective lens as used to keep a beam focused at a point. An aperture is a micrometer-sized hole in a Pt or Mo substrate that shapes and constricts an ion beam. Normally, FIB is used in milling to engrave submicrometer-sized features on a surface. A FIB provides the best resolution, with a characteristic as small as 20 nanometers, but is extremely time-consuming.

As shown in Table A. 3, several factors affect the resolution, but the current applied to the probe is the most important. A high probe current produces faster milling, while a small probe current provides a sharp, fine structure in FIB. A beam's diameter is a function of the probe current, which ranges from one pA to several hundred nA. When aligned and focused, a 30kV at 1 nA FIB probe gives a spot size of approximately 200 nm. As a result of bombarding surfaces with ions, FIB patterning is an inherently destructive process with ions that causes atomic sputtering from the surface. To overcome the speed drawback of FIB, a new generation of FIB Technology called Plasma FIB (PFIB) is developed, which is very fast; it uses Xe^+ , and has a much higher maximum current, which allows it to high throughput milling for a large volume. Apertures consist of a micrometer-sized hole in a Pt or Mo substrate and are used to shape and constrict the ion beam. A detailed description of focused ion/electron beam-based nanofabrication can be studied here [490]–[494].

A.2.3 Preparation of inks

A.2.3.1 Gold nanoparticles ink

Gold structures for fully printed functional devices (reported in chapter 6) and mibots-based setup (reported in chapter 5) were printed with UTDAu25-IJ ink (from UT Dots) [495]. This ink consists of gold nanoparticles with an average size of about 4 nm dispersed in a solvent based on hydrocarbons. The gold nanoparticles in this ink are surface-stabilized and can be dissolved in nonpolar organic solvents, and the ink is stable at room temperature under atmospheric conditions. As necessary, the patterns were heated to remove hydrocarbon and organic parts from the ink based on the demand after printing.

A.2.3.2 Galinstan ink

The Galinstan ink used throughout the thesis was obtained from Strategic Elements, Germany, and used as received [496]. The name "Galinstan" comes from the combination of gallium, indium, and stannum (Latin for tin). This appears with a shiny

A.2. Methods and techniques

surface, as shown in Figure A. 7. This eutectic alloy is composed of 68% gallium, 21% indium, and 11% alloy, melting at -19°C (about -2°F), so it is liquid at RT.

Table A. 3: Description of parameters used on FIB system [491], [493], [494].

| Parameter | Value Description | Change and Effect |
|-------------------------------------|---|---|
| Acceleration voltage | influences the energy of the ions arriving at the surface of the sample | Typical from 1 to 50 keV. Higher the acceleration voltage, the faster the ions \rightarrow greater the energy \rightarrow Fast milling but damages occur. Slow milling can reduce damage. |
| Ion beam current | affects the beam spot size \rightarrow defines resolution and feature size | A higher primary beam current speeds up the sputtering process. It is, therefore, necessary to use a low current beam in order to obtain a high-resolution pattern and fine polish. |
| Spot Size of beam | Beam current and aperture size can control it | Range: 2 nm – 2 μm . More beam current gives a big spot size finally, which influences the resolution and minimum feature size |
| Dwell Time (in μs or ms) | Time the beam stays at a particular position (ion beam stops at each pixel) | Long dwell time is suitable for small structures. |
| Scan Modes | Two types of scanning modes: raster and serpentine scans. They are further divided into: standard up-and-down raster, side-to-side raster, spiral raster, serpentine pattern, or double serpentine pattern. | Raster mode: after finishing a scanning line, the beam returns to the initial point of the following line (retracing). Serpentine mode: From one line to the next, the beam moves in the opposite direction and avoids long retracements |
| Pixel Spacing | distance between the centers of two adjacent pixels | It must be small to make smooth milling. |

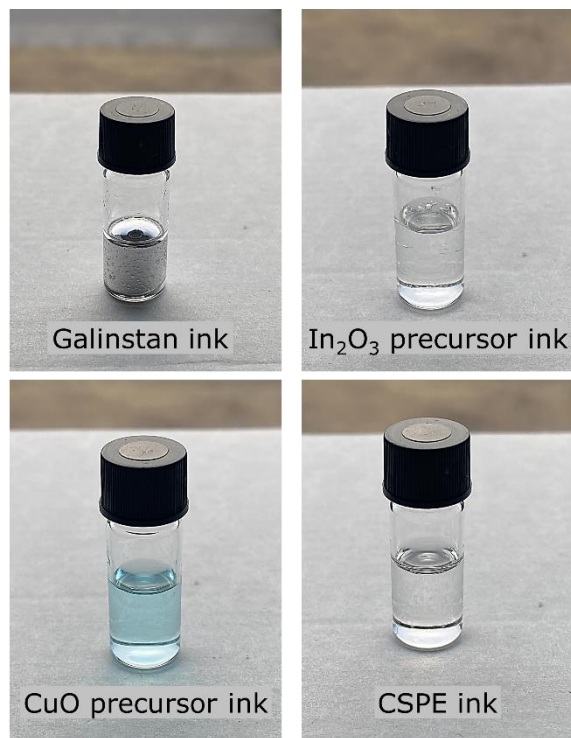


Figure A. 7: Prepared inks. Galinstan ink, In₂O₃ precursor ink, CuO precursor ink, and CSPE (Composite solid polymer electrolyte) ink.

A.2.3.3 Indium oxide precursor ink

In₂O₃ precursor ink preparation was adapted from a previous recipe [157]. A solution of 0.05 M In(NO₃)₃ × H₂O and glycerol (with a ratio of 4:1) was prepared in double-deionized water. The ink solution was stirred again at RT to achieve a homogenous mixture and further filtered with a hydrophilic 0.2 μm polyvinylidene fluoride (PVDF) syringe filter before printing.

In₂O₃ crystal structure: In₂O₃ can exist in three different crystal structures: cubic bixbyite-type (c-In₂O₃) stable under ambient conditions, hexagonal corundum-type (h-In₂O₃), and orthorhombic Rh₂O₃(II)-type structures stable only under high pressures and temperatures [497]. The crystalline structure for many of the indium oxides is the bixbyite structure and is most widely used in industry as n-type transparent conducting oxides. Cubic bixbyite-type (c-In₂O₃) is a fluorite-type structure where one-quarter of the anions are missing, and it is a periodic structure that produces "structural vacancies." Figure A. 8 represents the In₂O₃ crystalline structure, in which oxygen atoms are octahedrally coordinated around the indium cations; each indium is surrounded by six oxygen atoms and offers two structural vacancies. There can be structural vacancies along the body diagonal (b-site) or along a face diagonal (d-site). In the b-site, which represents 25% of the octahedra arrangement, all the oxygens are at the same distance from the indium at 2.18 Å. On the other hand, in the d-site, which represents 75% of the octahedra arrangement, there are two oxygens at each distance 2.13, 2.19, and 2.23 Å. The

existence of structural vacancies gives rise to two configurations: corner-sharing and edge-sharing. Corner-sharing involves sharing both an oxygen and a structural vacancy between adjacent polyhedra, resulting in the polyhedra only being joined at corners. Edge-sharing consists of sharing two oxygens between adjacent polyhedra in order to join them along their edges [498].

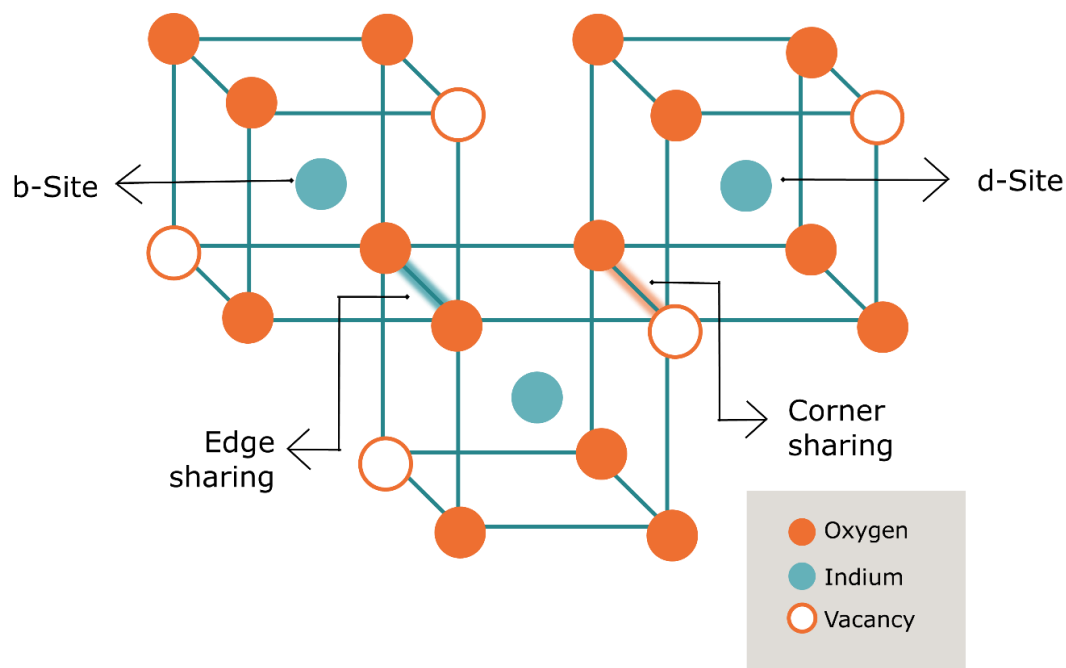


Figure A. 8: Structure of crystalline In₂O₃.

There are 32 indium atoms in an indium oxide unit cell (24 in d-sites and 8 in b-sites), surrounded by 48 oxygen atoms. The lattice parameter is approximately 10 Å. Indium oxide has an n-type carrier concentration due to the two extra electrons contributed by each oxygen vacancy [499].

In solution-processed indium oxide films, the crystallinity and the morphology of the printed films play a crucial role in electron mobility. Defects arising during the processing could mostly harm the device's characteristics. These printed films can also experience phenomena such as coffee-ring formation and crack propagation while printing, which can be solved by changing ink compositions or substrate surface energies. Owing to its high device mobility [15], indium oxide is chosen as the n-type semiconductor for fully printed electronic devices (chapter 6) in this thesis.

A.2.3.4 Copper oxide precursor ink

CuO precursor ink was prepared according to a previous report [157]: by mixing 0.1 M solutions of Cu(NO₃)₂ in 2.5 H₂O in double-deionized water. Afterward, glycerol was added in a ratio of 4:1. This CuO precursor ink was stirred at RT for proper dispersion and to prepare a homogenous solution. The ink was passed through a 0.2 μm PVDF syringe filter before printing. After printing, as soon as CuO precursors are

exposed to a hotplate at 150° C, they decompose to metallic copper, which remains predominant until 300° C, when it oxidizes to copper oxides. In p-n diode fabrication (chapter 6), the CuO film used for 400° C annealing consists primarily of CuO (90%) with a minor amount of Cu₂O (10%), a well-known p-type oxide semiconductor.

A.2.3.5 Composite solid polymer electrolyte

CSPE ink was also prepared in the same way as described previously [500]. In short, 4.29 wt% polyvinyl alcohol was dissolved in 85.71 wt% dimethyl sulfoxide (DMSO) and stirred for two hours at 90 °C for a homogenous mixing. At the same time, 1 wt% lithium perchlorate (LiClO₄) was dissolved in 9 wt% propylene carbonate and stirred for two hours at RT. Both solutions were mixed while stirring at RT. As the last step, the solution was filtered through a 0.2 μm polytetrafluoroethylene membrane.

A.2.3.6 PEDOT:PSS ink

The PEDOT:PSS ink was also prepared as previously described [500] to fabricate the top-gate in FETs and top electrode in p-n diode, 70 wt% PEDOT:PSS was stirred together with 30 wt% ethylene glycol for 2 h. Directly before printing, the ink was filtered with a 0.45 μm PVDF membrane.

A.2.4 Material characterization

In order to assess the quality, properties, and potential importance of a material in the final device, material testing and characterization are essential functions. Additionally, the dimensions of fabricated parts and printed patterns also play an important role in calculating the parameters for measuring device performance. The following section discusses different microscopic characterization methodologies, their functionality, limitations, and spectroscopic techniques used throughout the thesis.

A.2.4.1 Optical microscopy

An upright Nikon Eclipse 80i microscope loaded with a Nikon DS-Qi2 camera and a broadband excitation light source (C-HGFIE Intensilight from Nikon) was used for the imaging. The measurements of the devices were evaluated using NIS-Elements imaging software.

Working: Optical microscopes, also known as light microscopes, generate magnified images of small objects by using visible light and lenses. It may be possible to examine the object immediately through the eyepieces of a microscope after it has been placed on a stage, so it is very fast and always preferred as an initial step to characterize microstructures. In order to magnify a pattern, a mirror reflects light up through the sample into an objective lens, resulting in a first magnification. In addition to the objective lens, the eyepiece lens also functions as a magnifying glass, magnifying the image again. A variety of lighting methods can be used to illuminate

the sample. Bright-field provides a dark image against a bright background, and dark-field provides a bright image against a dark background. In order to determine the crystal orientation of metallic objects, polarised light can be used. The phase contrast technique increases image contrast and provides small details at different refractive indices.

Limitation of Optical Microscopes: Due to the wavelengths of visible light, conventional compound light microscopes can only magnify samples up to a maximum of about 1000x. As a result, two points closer than 200 nm, although it is possible to look at them, but cannot be distinguished [501]. Advanced technologies like scanning electron microscopy (SEM) and atomic force microscopy (AFM) can be used to investigate smaller structures.

A.2.4.2 Scanning electron microscope

SEM image shown in Figure 6. 5 were recorded with a dual-focused ion beam (FIB)/scanning electron microscopy (SEM) microscope (Crossbeam 540, Carl Zeiss Microscopy, Oberkochen, Germany). These experiments were performed at Heidelberg University. First, the sample was cooled down to $-100\text{ }^{\circ}\text{C}$ using a Leica cryo-stage, and later images were recorded using primary electron energy of 3 keV and a current of 500 pA by imaging SEs (topological contrast) and/or back-scattered electrons (material contrast).

The SEM imaging shown in chapter 8 was performed using a dual-beam Zeiss AURIGA 60 system (available at INT). SEM imaging was carried out using an e-beam with 5 kV and an aperture of 30 nA.

Working: SEMs produce images of samples by scanning the surface with a focused beam of electrons. Initially, electrons are generated from the electron source at the top of the column, as illustrated in Figure A. 9. Electrons are generated when their thermal energy exceeds the material's work function. The positively-charged anode accelerates and attracts them. In response to electron interactions with atoms in the sample, a variety of signals containing information about the surface composition and topography of the sample are produced. A high-resolution image can also be obtained since the entire electron column is under a high vacuum. It is possible to have other atoms and molecules present in the column in the absence of a high vacuum or sometimes while dealing with less stable materials. When these substances in the chamber interact with electrons, they cause the electron beam to deflect and, as a result, reduce the quality of the image. Additionally, the high vacuum increases the efficiency of the detectors in the column in collecting electrons.

Similar to optical microscopes, electrons are controlled by lenses. Electrons cannot pass through the glass, so electromagnetic lenses are used. In simple terms, electromagnetic lenses consist of coils of wires inside metal pole pieces. Magnetic fields are generated when current passes through coils. Electrons are extremely

sensitive to magnetic fields, so these lenses can control electrons' path inside the microscope column by adjusting the current applied to them.

As electrons travel towards the sample, they encounter two types of electromagnetic lenses: condenser lenses and objective lenses (shown in Figure A. 9). A condenser lens converges the beam first, and then the electron beam cone opens up again, and then an objective lens again converges the beam before hitting the sample. The objective lens has the primary responsibility of focusing the beam onto the sample, while the condenser lens determines the beam size, which determines the resolution. A scanning coil is also integrated into the lens system of the SEM for rastering the beam onto the sample. There is also an "aperture" (which has small holes in a metallic plate) placed between the condenser lens and the objective lens, and it allows a small

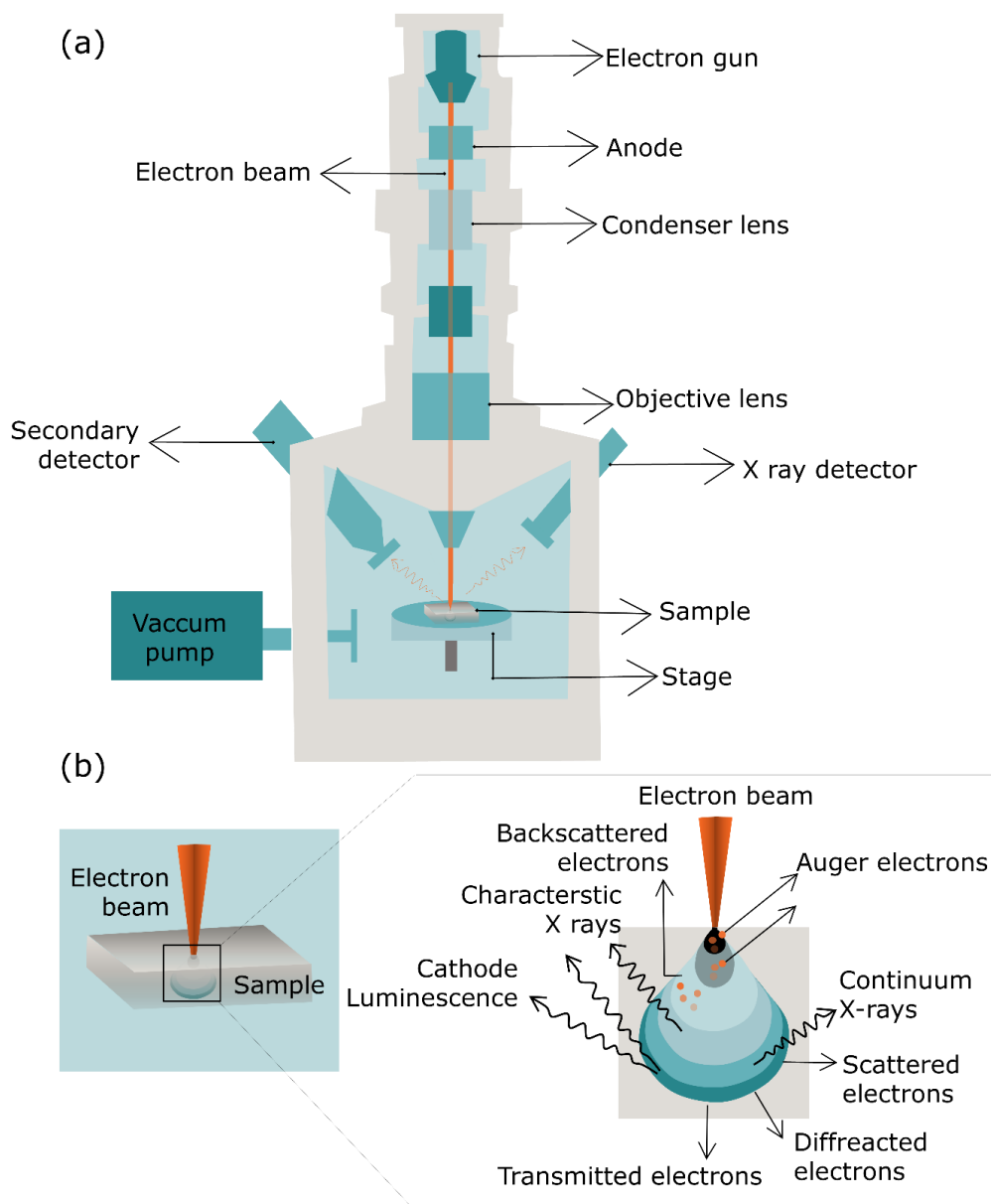


Figure A. 9: (a) SEM working and electron beam interaction with the sample. (b) Interaction of electrons within a sample.

fraction of the electron beam to reach the objective lens. Apertures and lenses operating parameters together define the beam size.

The electron beam's position and intensity are combined to produce an image by scanning it in a raster scan pattern. There are several types of signals generated by electrons within a sample (as shown in Figure A. 9b): secondary electrons (SE), reflected or back-scattered electrons (BSE), characteristic, absorbed currents (specimen currents), X-rays and light cathodoluminescence (CL) and transmitted electrons. BSE and SE are two types of electrons that are used for imaging.

Table A. 4: Commonly used signals by SEM users for imaging [502].

| Signal | Description |
|--------------------------------|---|
| Secondary electrons (SE) | In solid matter, SE has low energies (below 50 eV), which limits its mean free path. SE can only escape from the top of surfaces (a few nanometers). |
| Back-scattered electrons (BSE) | As the name suggests, BSE are electron beams reflected from a sample by elastic scattering. Due to their much higher energy, BSEs emerge from deeper locations within specimens, and the electron beam scatters more at greater depths; therefore, their resolution is lower than SE images. As BSE images can provide information about the distribution of different elements in a sample, but not its identity, as BSE intensity is strongly related to the atomic number (Z) of the specimen. Compared to lighter elements, heavier elements can deflect electrons more strongly because of their larger nuclei. Due to the higher back-scattered electrons that are emitted from the surface of heavy elements, they appear brighter in an SEM image than light elements. A specimen's crystallographic structure can also be determined using an electron back-scatter diffraction (EBSD) image formed by back-scattered electrons. |
| X Rays | Electron beams help to emit X-rays when they remove an electron from an inner shell, releasing energy to fill the shell with a higher-energy electron. By measuring the energy or wavelength of these characteristic X-rays, one can identify and measure element abundance and map their distribution in a sample using energy-dispersive X-ray spectroscopy or wavelength-dispersive X-ray spectroscopy. |

There are different types of detectors that detect BSE and SE. To maximize BSE collection, solid-state detectors are placed above samples, concentrically with the electron beam. On the other hand, Everhart-Thornley detectors are usually used to detect SE. It consists of a scintillator positioned inside a Faraday cage that is positively charged and attracts the SE to it. These scintillators accelerate electrons and convert them into light before amplification by photomultipliers. In order to increase the efficiency of detecting SE, the SE detector is angled across the electron

to increase its efficiency in detecting SEs, which in the end, creates an image of the sample. A detailed comparison of conventional Everhart-Thornley style and in-lens secondary electron detectors can be read here [503]. A detailed description of SEM can be read here [502], [504], [505].

Limitation

- Since the sample must be both vacuum and electron-beam friendly, the final resolution is affected by its chemical properties and stability in the electron beam. As a solution, AFM (described in next section) can be used, which provides atomic resolution without a vacuum requirement.

A.2.4.3 Atomic force microscopy

The atomic force microscopy (AFM) images were obtained on a Dimension Icon AFM (Bruker, Germany) in tapping mode under ambient conditions. The LM interconnects were scanned with AFM tips of a spring constant of 40 N.m^{-1} and a nominal resonance frequency of 325 kHz (MikroMasch HQ:NSC15/Al BS AFM probe tips, MikroMasch, Wetzlar, Germany). AFM images were collected with NanoScope 9.7 software and processed with the freeware tool Gwyddion (3D image shown in Figure 4. 18f).

AFM images for different positions on Galinstan spread area (as shown in Figure 8. 11) were also obtained on Dimension Icon AFM (Bruker, Germany) using tip (All-in-One-Al, Budget Sensors Ltd., 65 kHz Resonanz frequency). The AFM data were flattened via a form removal function using a least-squares 7th polynomial. These AFM images were recorded with NanoScope software and afterward processed and analyzed for a roughness analysis according to the ISO 25178 standard in MountainsMap® (Digital Surf®) software.

Working:

An AFM microscope is a non-optical surface characterization technique that uses an extremely sharp tip to measure the surface features of samples with an atomic resolution for lateral and height measurements. AFM fits in the class of scanning probe microscopy; here, a sample is scanned using the tip by raster scanning across its surface line by line. The method varies based on the operating mode.

As shown in Figure A. 10, a nanoscale tip is attached to a small cantilever. This sharp tip near the free end helps it to behave as a spring. As the tip approaches a sample, it is affected by forces present at the surface of the sample. In turn, this causes the tip of the cantilever to move, which in turn bends the entire cantilever. There is a force at work between the tip and the sample in this bending. In order to detect bending, a laser diode and a split photodetector are used. As Figure A. 10 shows, the scanning process involves directing a laser beam onto a coating on the tip, which helps reflect the laser beam. Laser beams are reflected off shiny surfaces and fall on photodetectors. As the tip encounters bumps or depressions on the sample surface, it deflects from its original position, causing the laser beam to move as well. The

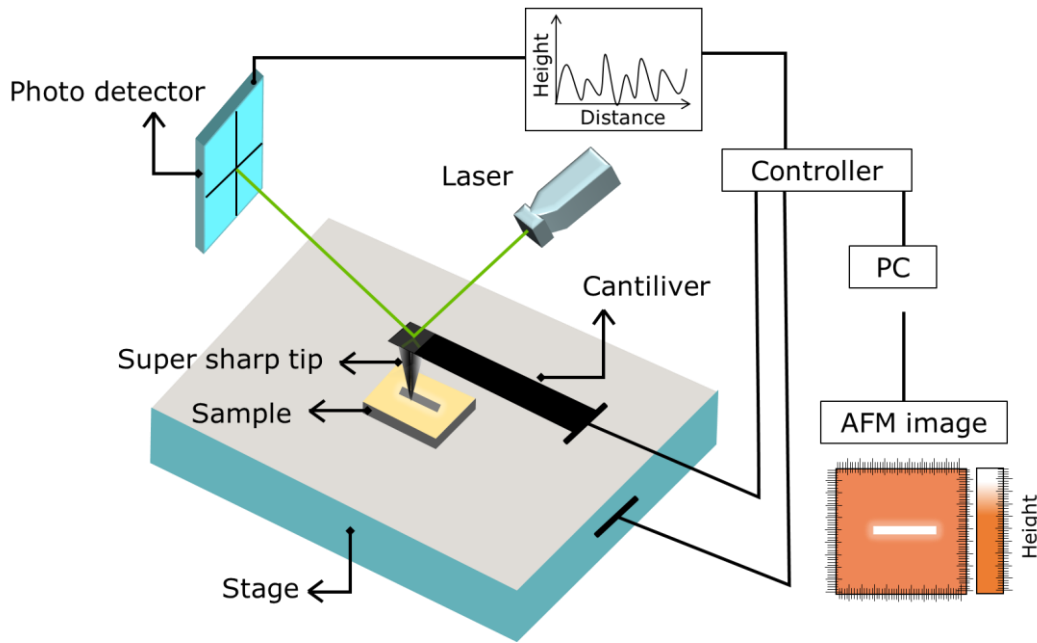


Figure A. 10: Working of atomic force microscopy.

photodetector detects movement and passes it on to a high-gain amplifier. These signals are processed by the amplifier and converted into a processable form. Finally, a computer provides a 3D profile of the surface based on the signals collected during the entire scanning process.

Generally, static (usually contact mode) and dynamic (usually tapping mode) are the two main operating modes. During contact mode, the tip is pressed onto the surface, and an electronic feedback loop monitors tip-sample interaction while maintaining constant deflection. Tapping mode protects both the tip and the sample surface from damage by limiting contact between them. A cantilever vibrates near its resonance frequency in this mode which follows a periodic movement of the tip up and down. The presence of attractive or repulsive interactions reduces this motion as it approaches the sample. Feedback loops work similarly to contact modes but maintain the amplitude of the tapping motion instead of the quasistatic deflection. Consequently, a line-by-line analysis of the sample's topography is carried out.

AFM images can also provide a lot of information about the surface, including roughness. AFMs can also be used to assess mechanical, electrical, ferroelectric- and piezoelectric-electrical, magnetic, and thermal properties. A detailed description, working principle, and applications of AFM can be read here [506]–[508].

Surface roughness measurements and analysis can also be accomplished using two widely-employed methods:

- (1) Stylus profilometer (contact method)
- (2) 3D optical profiler based on optical interferometric principles (Non-contact method)

A.2.4.4 Optical profilometry/ vertical scanning interferometry

We performed large-scale (μm -millimeter range) topography measurements with a white light vertical scanning interferometer (VSI) Contour GT-K (Bruker) using 5x magnification (pixel size $\approx 0.75 \mu\text{m}$). We processed and analyzed the topography data in MountainsMap® (Digital Surf®).

Working:

An optical profilometer is a fast technique to measure surface properties and topography non-destructively and without contacting the surface. As shown in Figure A. 11, an optical profiler is a microscope that uses a splitter and splits the light from a lamp into two paths.

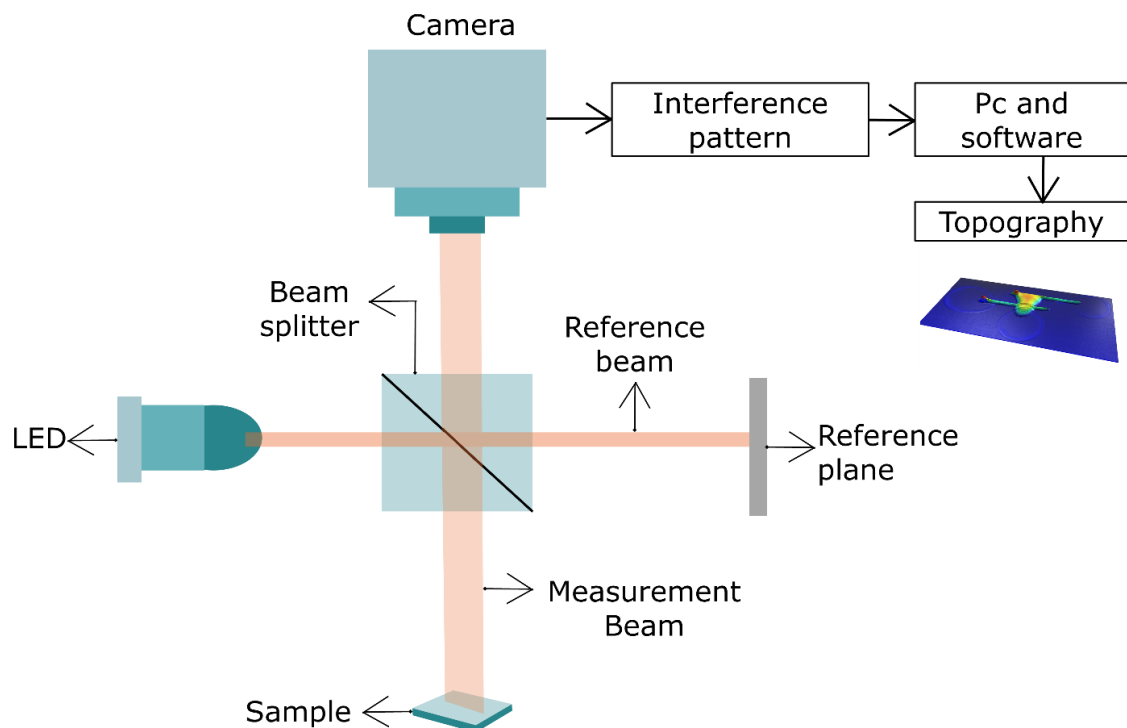


Figure A. 11: Working of optical profilometry.

For scanning, light travels along two paths, one of which is focused on the surface being tested, and the other is directed toward a mirror serving as a reference. An array detector receives recombined reflections from the two surfaces. It is possible to have interference when the path difference between the recombined beams is on the order of a few wavelengths of light or less. This interference pattern is used to determine the surface properties of the sample. An objective can have a vertical resolution of up to several angstroms, whereas lateral resolution is typically around $0.3 - 8 \mu\text{m}$, depending on the objective lens and light source used.

A.2.4.5 Stylus profilometer

Height measurements of printed interconnects/resistors were completed on a Veeco Dektak 6M Profilometer.

Working:

A stylus profilometer detects surfaces by moving a probe along the surface to measure their height. As the probe scans along the surface, the mechanical feedback loop monitors the force exerted by the sample pushing up. The feedback system helps the arm to maintain a fixed amount of torque, called the 'setpoint'. The changes in the arm holder's Z position can then help reconstruct the surface.

Limitation:

- The stylus profilometer is slower than non-contact techniques because it involves physical movements in X, Y, and Z.
- A stylus tip's size and shape can affect the measurement and limit lateral resolution.
- Despite its sensitivity and Z resolution, stylus profilometry is also sensitive to soft surfaces, and they can contaminate tip or tip and can also damage some surfaces this way.

A.2.5 Spectrometry characterization

Spectroscopy techniques are the key to understanding the atomic properties of all matter. A central principle of spectroscopy is that light has different wavelengths, and each wavelength corresponds to a different frequency. In addition to the importance of spectroscopy, each element in the periodic table emits and absorbs light at a unique frequency, consistent with the same part of the electromagnetic spectrum when diffracted. That frequency defines the light spectrum of every element in the periodic table. This section discusses some of the spectroscopic techniques used throughout the thesis, such as TOF-SIMS, EDS, and XPS.

A.2.5.1 Time-of-Flight Secondary Ion Mass Spectrometry (TOF-SIMS)

Chemical analysis of the oxide layer on Galinstan (as shown in Figure 8. 20) was completed on a ToF-SIMS analysis system (Tofwerk AG, Thun, Switzerland & Carl Zeiss Microscopy, Oberkochen, Germany) attached to the Crossbeam540. The Galinstan sample was tilted to 54° and irradiated with Ga⁺ ions (30 keV, 50 pA). Secondary ions originating from the ion-sample interaction were detected and imaged. The maps showed the spatially distributed secondary ion signal of the ToF-SIMS detector integrated over a mass/charge ratio between 84.5 and 85.5, corresponding to 85 GaO⁻ ions.

Working:

As shown in Figure A. 12, a ToF-SIMS uses a focused, pulsed particle beam (typically Cs or Ga), and a sample surface is bombarded by these primary ions of some keV energy. As a result of atomic collisions, the primary ion energy is transferred to target atoms, and a collision cascade is formed. Atoms and molecular compounds on the sample surface can overcome the surface binding energy by absorbing a portion of this energy. As a result of the soft interaction of the collision cascade with the surface molecules, even nonvolatile molecules with high masses can also escape without or with little fragmentation. Because SIMS emits particles from the top one or two

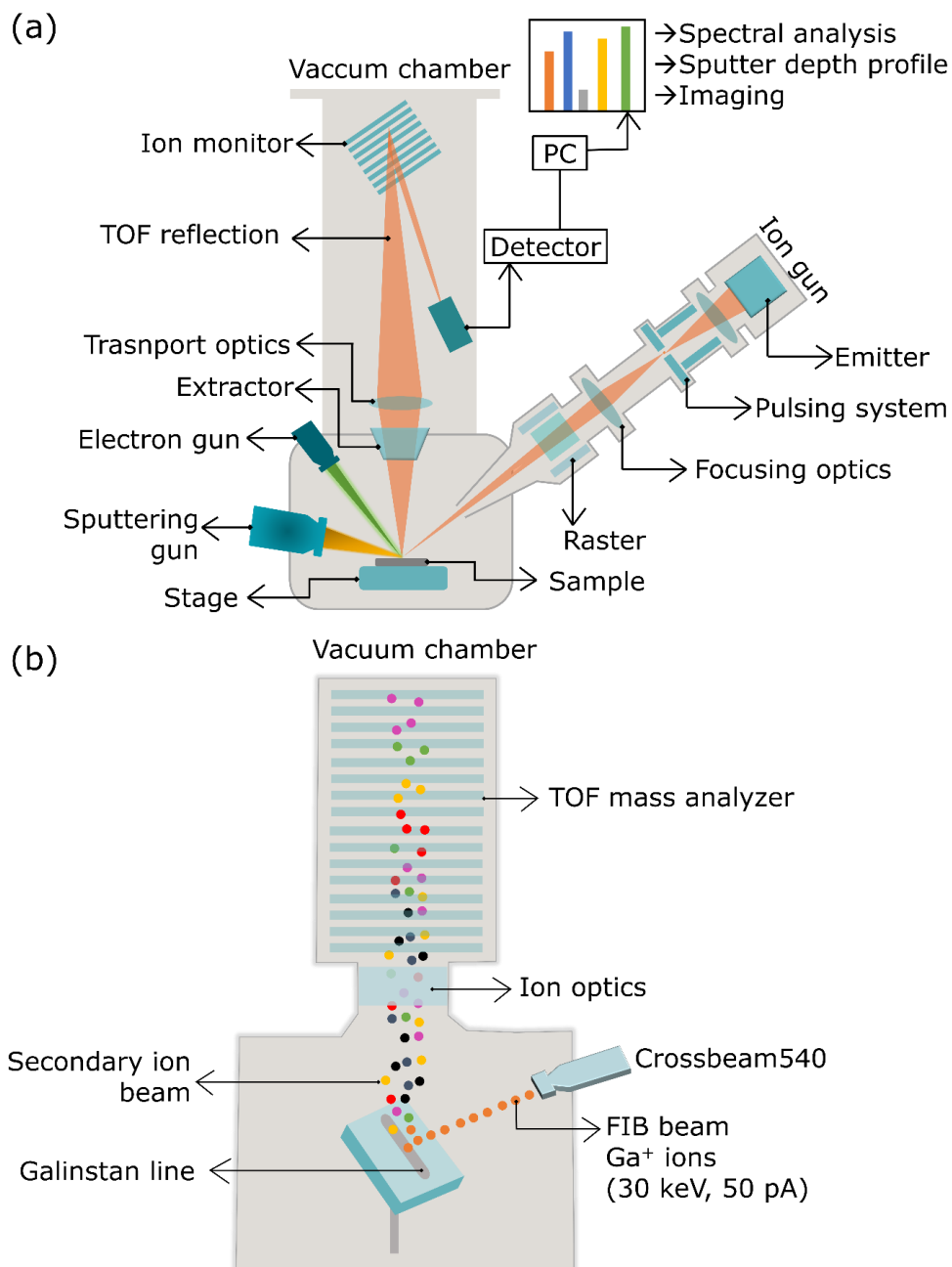


Figure A. 12: (a) Working of TOF-SIMS, and (b) beam interaction with the sample in FIB-TOF.

monolayers, the technique is very surface-sensitive. Most emitted ions have neutral charges, but a small proportion is negatively or positively charged. The generated ions are accelerated to common energy by an electrostatic field.

It is based on the fact that ions with the same energy but different masses travel at different speeds. On the way to the detector, the accelerated ions travel over a drift path. In general, lighter ions arrive at the detector faster than heavier ones because they fly at higher velocities. By analyzing the time-of-flight of ions emitted from the surface, we can determine the mass of an ion and, as a result, the elemental and molecular composition of the sample. A detailed description of the working of ToF-SIMS can be read here [509].

A.2.5.2 Energy-Dispersive X-Ray Spectroscopy (EDS)

EDS measurements reported in this thesis were done with the Zeiss Auriga 60, using an EDAX Octane Super A detector controlled by EDAX TEAM software. EDS-mappings were carried out using 5 kV and 120 pA e-beam conditions and X-ray La-signals for Ga and Mz-signals for In and Sn.

Working:

EDS analyzes material composition by identifying its elemental composition. Figure A. 13 shows a beam of electrons focused on a sample at high energy, which may excite electrons within an inner shell, ejecting them and creating an electron hole. An electron in an outer shell can fill this hole; during this process, X-rays are emitted. Energy dispersive spectrometers use X-rays to determine an element's composition by measuring the number and energy of the X-rays emitted from it. A detailed description can be read here[504].

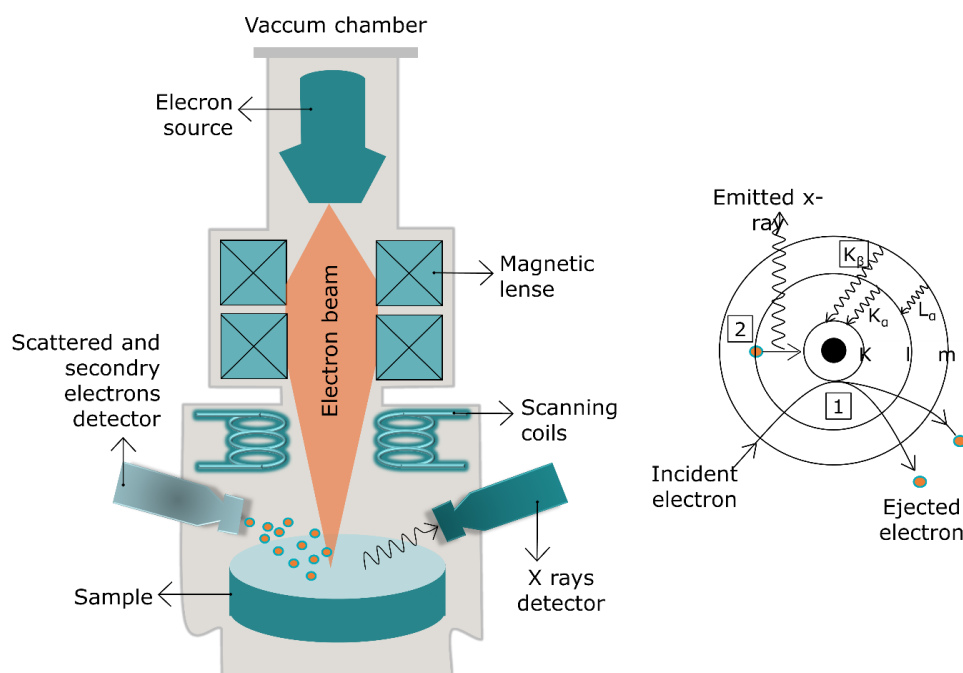


Figure A. 13: EDS working principle and instrumentation.

A.2.5.3 X-Ray Photoelectron Spectroscopy (XPS)

The XPS measurements on the Galinstan sample shown in chapter 8 were completed with a Thermofisher K-alpha system (available at IMT, KIT-CN). Monochromatic Al-ka X-ray has a photon energy of 1480.6 eV. The emitted photoelectrons were collected in the analyzer at 90° to the sample's surface. A monoatomic Ar⁺ ion with a kinetic energy of 500 eV was used for depth profile sputtering. Thermofisher's Avantage software was used for data analysis, and Origin was used to plot XPS graphs.

Working:

XPS is a spectroscopic technique for analyzing surfaces' elemental compositions and chemical states. As shown in Figure A. 14, XPS is initiated by irradiating a sample with monoenergetic soft X-rays, most commonly Mg K α or Al K α . In modern instruments, the Al K α X-ray line can be further narrowed using a monochromator (quartz crystal)[510].

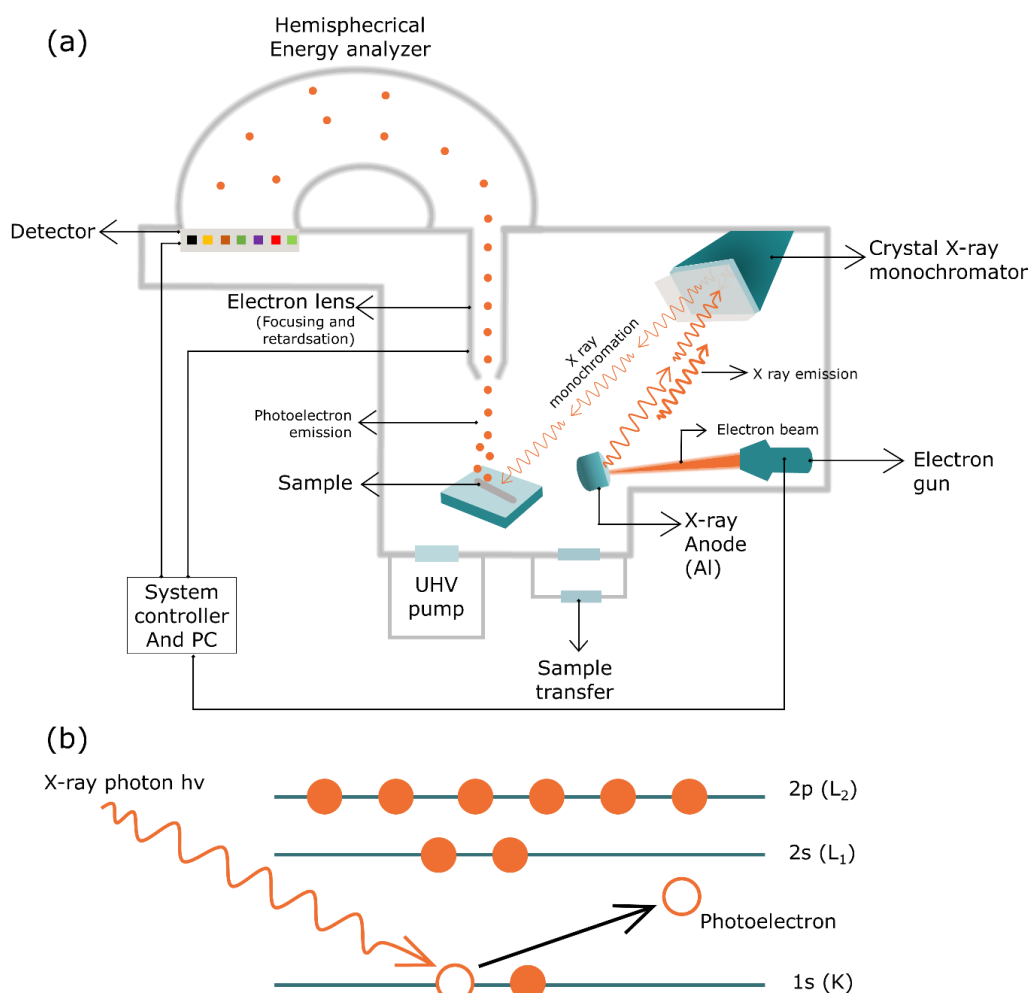


Figure A. 14: (a) XPS working, and (b) X-rays interaction with the sample, and photoelectron formation.

When X-rays are irradiated onto a sample, electrons within the sample absorb photons of a specific energy and then emerge from the sample. Electrons are counted at various kinetic energies as they are ejected, resulting in a photoelectron spectrum that contains information about the electronic states of atoms on the surface. XPS can normally reach up to depths of 10 nm. Because of its flexibility and efficacy, XPS is more popular, versatile, and useful than other techniques.

In XPS, the binding energies of the photoelectrons can be detected to determine the chemical composition of surfaces except for hydrogen and helium. It is possible to identify chemical states based on small variations in binding energies of photoelectron lines, Auger lines, satellite peaks, and multiple splitting. A detailed description of the XPS working principle and applications can be read here [510], [511].

A.2.6 Electrical Characterization

A.6.1 Electrical resistivity measurements

Resistance measurements of bare and encapsulated Galinstan interconnect (shown in Figure 6. 4 and Figure 8. 25) were conducted using an Agilent 4155C semiconductor parameter analyzer and a probe station with TRIAX probes with a current detection limit of 30 fA. Measurements were completed with voltage sweeps from -100 to $+100$ mV and a step size of $5 \mu\text{V}$; the average of 8 samples was used as a single data point.

A.2.6.2 P–N diode and FET characterization

Electrical measurements such as two-point resistance, characteristics of fully printed transistors (shown in Figure 6. 12, Figure 6. 13), and p–n diodes (shown in Figure 6. 9) were characterized at ambient conditions using Agilent 4156C semiconductor parameter analyzer and contacted through a precision probe station (SÜSS MicroTec MLC-150C). The sweep rate was $10 \text{ mV}\cdot\text{s}^{-1}$ in all cases. The devices are contacted with a source measure unit (SMU) which, as the name suggests, can simultaneously measure both source voltage and current.

A.2.7 Encapsulation of devices

The printed components were encapsulated by spin coating with PMMA (from Micro Chem dissolved in Anisol) at 4000 rpm for 60 seconds, with 10 seconds ramp-up and ramp-down times. The encapsulated components were then placed on a hot plate at $150 \text{ }^\circ\text{C}$ for 3 min to cure the PMMA.

A.2.8 Tutorial: Printing tips and safety concerns with miBots

Once the stage and USB camera is installed, the miBot can be coarsely positioned by hand in arbitrary positions. It has no mounting screws. Once the setup is thoroughly established, and all the connections are correctly working, it is safe to touch the stage and other components without gloves, safety glasses, or goggles. Care must still be

exercised when working with the miBot. Ensure that the miBots are not to be touched while operating. While placing the miBot on the surface for printing, it should be handled with care, and the rear part should be placed first and then slowly the piezo motor part. Otherwise, the piezo motor can be damaged, and it will no longer work as desired and may have diminished performance. The same gentleness should be maintained while loading the miBot with the Glass capillary tip molded in LDPE tubing. It will be better to load the glass capillary onto the robotic arm with the help of a tweezer. However, miBots can be freely moved and placed by hand once disconnected from the power supply, though these movements should be avoided as much as possible. Of course, in general, while printing and dealing with chemicals, gloves and goggles are necessary. The miBot is controllable with the miBot Remote Control or Precisio software application. The joypad connected to the computer offering direct-write control also makes the experiments at micron-scale very easy and delightful. For the overall unwrinkled movement of the miBot, the stage must be as smooth as possible. And specifically, for better control over line printing and to avoid vibration and disruption while moving the tip, the miBot should be moved in as minimal step size as possible. While printing vertically, the glass substrates were oxygen plasma cleaned to achieve proper ink transfer and adhesion.

Part VI. Index and references

Glossary

List of Abbreviations

μCP Microcontact Printing

4IR Industry 4.0

AFM Atomic force microscopy

BJT Bipolar junction transistors

BSE Back-scattered electrons (also reflected)

b-SPL Bias-induced scanning probe lithography

CAD Computer-aided design

CE Conventional electronics

CIJ continuous inkjet

CL Cathodoluminescence

CMOS Complementary Metal-Oxide-Semiconductor

c-SPL Current-induced scanning probe lithography

CVD Chemical vapor deposition

DCM Dissolutions-condensation mechanism

DOD Drop-on-demand

DPN Dip-pen nanolithography

DUV Deep ultraviolet

EA Electron affinity

EBL Electron Beam Lithography

EBPVD Electron-beam physical vapor deposition

EBS Electron back-scatter diffraction

EDAX Energy Dispersive X-Ray Analysis software to analyze EDS data

EDL Electric double layer

EDS Energy-Dispersive X-Ray Spectroscopy

EGFET Electrolyte-gated Field Effect Transistor

FET Field-effect transistors

FIB Focused Ion Beam lithography

FluidFM Fluid force microscopy

GBP grain boundary penetration

HOMO highest occupied molecular orbits

ID Inner diameter

IGFET Insulated Gate Field Effect Transistor

IoT Internet of things

IP Ionization potentials

JFET Junction field-Effect transistors

LCST Lower critical solution temperature

LDPE Low-density polyethylene

LED Light emitting diodes

LM Liquid metals

LME Liquid metal embrittlement

LUMO Lowest unoccupied molecular orbit

miBot Piezo-based manipulator from imina inc

MOD Metal-Organic decomposition

MOS Metal-Oxide-Semiconductor

MOSFET Metal Oxide Semiconductor field effect transistor

m-SPL Mechanical scanning probe lithography

MVC Micro-void coalescence

nanoCT X-ray nano computed tomography

NIST National institute of standards and technology (provided XPS databases)

NMOS Negative channel Metal-Oxide-Semiconductor

NP Nanoparticle

OD Outer diameter

OFET Organic field-effect transistor

OSC Organic semiconductor

PE Printed electronics

PMOS Positive channel Metal-Oxide-Semiconductor

PZT Piezoelectric transducers

RFID Radio-Frequency IDentification

RH Relative Humidity

SAM Self-assembled monolayers

SCCM Standard cubic centimeters per minute (unit for flow)

SD Standard deviation

SE Secondary electrons

SEM Scanning electron microscope

SESI Secondary electron secondary ion

SMU Source measure unit

SPL Scanning probe lithography

TCNL Thermochemical nanolithography

TCO Transparent conducting oxides

tc-SPL Thermochemical scanning probe lithography

t-DPN Thermal dip-pen lithography

TEC Temperature/thermal expansion coefficients

TEM Transmission electron microscopy

TFT Thin-film transistor

TOF-SIMS Time-of-Flight Secondary ion mass spectrometry

TOS Transparent oxide semiconductors

TRIAx Triaxial cable

t-SPL Thermal scanning probe lithography

USB Universal serial bus

VLSI Very Large-scale integration

VSI Vertical scanning interferometry

WD Working distance (parameter in SEM)

XPS X-Ray photoelectron spectroscopy

XRD X-Ray diffraction

Nomenclature (List of symbols)

μm Micrometer

ϵ_0 Permittivity of free space

λ Debye screening length

μ Field-Effect Mobility (in $\text{cm}^2.\text{V}^{-1}.\text{s}^{-1}$)

μ_n Electron mobility (in $\text{m}^2.\text{V}.\text{s}^{-1}$)

μ_p Hole mobility

ρ Resistivity ($\Omega.\text{cm}$)

σ Conductivity ($\Omega^{-1}.\text{cm}^{-1}$ or $\text{S}.\text{cm}^{-1}$)

A Cross-sectional area of the sample

BV_{DS} Drain Source Breakdown Voltage

C Capacitance

d Thickness of the active layer

e Charge of an electron,

G Conductivity (in $\text{S}.\text{m}^{-1}$)

g_m Transconductance

h Height of the printed interconnect/resistor

I Total current (in Amperes)

I_{DS} channel current

I_{ON}/I_{OFF} On/Off current ratio

I_s Reverse saturation current,

k Boltzmann constant

L Channel width

l Length of the printed interconnect/resistor

n Electron density,

q Charge

R Resistance (in Ω)

R_L External resistor (load)

S_a Roughness average (the mean height on the surface)

S_q Root mean square

SS Subthreshold swing

S_z Maximum Height

T Temperature

V Voltage (in Volt)

V_f Voltage applied during forward bias

V_{GS} Gate-source Bias

V_p Pinch off Voltage

V_r Voltage applied during reverse bias

V_{th} Threshold voltage, or knee voltage

w Width of the printed interconnect/resistor

W_0 Depletion width

W_f Depletion width during forward bias

W_r Depletion width during reverse bias

Materials (Chemical and elements)

ABS Acrylonitrile butadiene styrene

Ag Silver

Al Aluminium

Al₂O₃ Aluminum oxide

Au Gold

AZO Aluminum-doped Zinc Oxide

BDOPV Benzodifurandione-based oligo(p-phenylenevinylene)

BSA Bovine serum albumin

BTBT 2,7-dioctyl[1]benzothieno[3,2-b][1]benzothiophene

CdZnTe Cadmium zinc telluride

CIGS Cu(In,Ga)Se₂

Cl Chlorine

CNT Carbon nanotube

CPS Cyclopentasiloxane

Cr Chromium

CsClO₄ Cesium perchlorate

Cu(NO₃)₂ Copper(II) nitrate

Cu Copper

Cu₂O Copper(I) oxide

CuO Copper(II) oxide

DEME diethyl-N-methyl-N-(2-methoxyethyl)ammonium

DMF Dimethylformamide

DMSO Dimethyl sulfoxide

DOPC 1,2-dioleoyl-sn-glycero-3-phosphocholine

DPP N-alkyl diketopyrrolo-pyrrole

DTT Dithienylthieno[3,2-b]thiophene

EG Ethylene glycol

EGaIn Eutectic gallium-indium

EMIM 1-ethyl-3-methylimidazolium

FAP trifluorotris(pentafluoroethyl)phosphate

FITC Fluorescein isothiocyanate fluorescent dye

Ga₂O₃ Gallium oxide

GaCl₃ Gallium trichloride

Galinstan Ga-In-Sn alloy

H₂O Water

HCl Hydrochloric acid

HfO₂ Hafnium oxide

HgCdTe Mercury cadmium telluride

In(NO₃)₃ × H₂O Indium(III) nitrate hydrate

In Indium

In₂O₃ Indium(III)-oxide

InZnO Indium zinc oxide

ITO indium tin oxide

LiClO₄ Lithium perchlorate

LM/Zinc Liquid metal-Zinc

NaDDBS Sodium dodecyl benzene sulfonate

NaOH Sodium hydroxide

NiO Nickel(II) oxide

NMP N-methyl-2-pyrrolidone

P(VDFHFP) Poly(vinylidene-co-hexafluoropropylene)

PBS Phosphate-buffered saline

PbSe Lead selenide

PCDTPT Poly[4-(4,4-dihexadecyl-4H-cyclopenta[1,2-b:5,4-b']dithiophen-2-yl)-alt [1,2,5]thiadiazolo[3,4-c]pyridine]

PDMS Polydimethylsiloxane

PEDOT/PSS Poly(3,4-ethylenedioxythiophene)-poly(styrenesulfonate)

PEDOT Poly(3,4-ethylenedioxythiophene)

PEE Poly(ether-block-ester)

PEG Poly(ethylene glycol)

PEGDA Poly(ethylene glycol) diacrylate

PEO Poly(ethylene oxide)

PET Polyethylene terephthalate

PI Polyimide

PMMA Poly(methyl methacrylate)

PNIPAM Poly(N-isopropylacrylamide)

PP Polypropylene

PQT-12 Poly(3,3'''-didodecylquaterthiophene)

PS Polystyrene

PS-PEO-PS Poly(styrene-block-ethylene oxide-block-styrene)

PS-PMMA-PS Poly-(styrene-b-methyl methacrylateb-styrene)

Pt Platinum

PTFE Polytetrafluoroethylene

PVAL Polyvinyl alcohol

PVC Polyvinyl chloride

PE Polyethene

PS Polystyrene

PVDF Polyvinylidene fluoride

PVP Poly(N-vinylpyrrolidone)

Rh₂O₃ Rhodium(III) oxide

Rhodamine 6G Rhodamine 6G fluorescent dye

SDS Sodium dodecyl sulfate

Si Silicon

SiO₂ Silicon oxide

Sn Tin

SOS-N3 Poly[(styrene-r-vinylbenzylazide)-b-ethylene oxideb-(styrene-r-vinylbenzylazide)]

Ta₂O₅ Tantalum oxide

TCB Tetracyanoborate

TFSI trifluoromethylsulfonylimide

Ti Titanium

TiO₂ Titanium oxide

W Tungsten

Y₂O₃ Yttrium oxide

List of Figures

| | |
|---|----|
| Figure 1. 1: A semi-log plot showing the evolution of transistor counts on integrated chips from 1971 to 2020 with respect to Moore's Law, which states the number of transistors on an IC chip doubles approximately every two years. Reprint from [2,3] under license CC-BY-4.0..... | 3 |
| Figure 1. 2: Comparison of conventional electronic device manufacturing vs. printed electronics. Conventional electronics manufacturing involves a lot of complex steps, and it is based on subtractive methods; on the other hand, printed electronics is based on direct writing, thus can be (in comparison) simple and fast. | 5 |
| Figure 2. 1: Classification of materials based on the band gap. | 16 |
| Figure 2. 2: Classification of some insulators/dielectrics materials. | 19 |
| Figure 2. 3: Semiconductor energy band diagrams for (a) intrinsic, (b) n-type, and | 22 |
| Figure 2. 4: Structure of PEDOT:PSS. | 29 |
| Figure 2. 5: Laser-based selective sintering technologies. | 32 |
| Figure 2. 6: Conductivity comparison of different liquid metal composites. A:[99], [253], B:[253], C:[257], D:[258], E:[259], F:[260], G:[261], H:[262], I:[263], J:[264], and K:[265]. | 34 |
| Figure 2. 8: Scheme outlining the oxide layer surrounding the LM core. | 36 |
| Figure 2. 9: Effect of oxide layer on wetting and contact angle. | 37 |
| Figure 2. 10: Schematic diagram of inkjet printing. (a) Continuous mode; (b) DOD mode (c) Dimatix Materials Printer DMP-2850 at INT (d) components of cartridge. | 38 |
| Figure 2. 11: Resistless lithography, such as screen printing and stencil (shadow mask) lithography workflow. | 41 |
| Figure 2. 12: (a) Microcontact printing process and (b) problems during printing such as stamp collapse and ink filling up the trenches. | 42 |
| Figure 2. 13: Classification of SPL methods. Adapted from [41] with permission from Springer Nature, copyright 2014. | 44 |
| Figure 2. 14: Schematics of microchannel cantilever spotting (μ CS) technique. ... | 46 |
| Figure 2. 15: FluidFM-based additive manufacturing (3D metal printing) that does not need post-processing steps. FluidFM cantilever (inset). Here CE: Counter Electrode, RE: Reference Electrode, and WE: Working Electrode. | 47 |
| Figure 2. 16: Comparison of different printing methods. | 49 |

| | | |
|---------------|---|----|
| Figure 3. 1: | (a) The circuit symbol, where the triangle corresponds to the p side. (b) Physical diode orientation indicating the cathode. | 51 |
| Figure 3. 2: | A p–n junction. | 51 |
| Figure 3. 3: | (a) A p-n junction at zero bias and formation of the depletion region. (b) Energy band diagram of a p-n junction in zero bias state under thermal equilibrium..... | 52 |
| Figure 3. 4: | A p-n junction at zero bias, forward bias, and reverse bias. W_0 , W_f , and W_r represent the width of the depletion region, respectively. I is current. V , V_f , and V_r represent the applied voltage, respectively. . | 54 |
| Figure 3. 5: | I–V characteristic of the p-n diode. (a) Shows the ideal I–V characteristics. (b) I-V characteristics of the real p-n junction diode | 57 |
| Figure 3. 6: | Classification of transistors. | 59 |
| Figure 3. 7: | Typical transfer characteristics of (a) n-type, (b) p-type, and (c) ambipolar transistor..... | 59 |
| Figure 3. 8: | Basic layer structures of printed FET: (a) bottom-gate; (b) top-gate; (c) side-gate; (d) liquid-gate. | 60 |
| Figure 3. 9: | An electrolyte-gated organic field-effect transistor. | 61 |
| Figure 3. 10: | Schematics of EGFETs (a) in-plane gate (also called displaced-gate) and (b) top gate configuration..... | 62 |
| Figure 3. 11: | Schematic diagram of the working principle of an n-type MOSFET in different bias conditions. (a) Cross-section view (without gate voltage). MOSFET is driven by gate voltage: (b) Triode region, (c) Channel pinch-off region, and (d) Saturation region..... | 63 |
| Figure 3. 12: | Typical I-V characteristics of the n-type MOSFET. (a) Output curve. (b) Transfer curve. (c), (d), (e) Different regions of output characteristics curve. | 66 |
| Figure 3. 13: | The I_{DS} vs. V_{GS} curve for threshold voltage (V_{th}) value extraction... | 68 |
| Figure 3. 14: | Log I_{DS} vs. V_{GS} curve to estimate the SS , I_{ON} , and I_{OFF} | 69 |
| Figure 3. 15: | Schematic transfer characteristics (log I_{DS} vs. V_{GS}) show hysteresis for n-type FET..... | 70 |
| Figure 3. 16: | A resistive microheater structure and material properties..... | 73 |
| Figure 3. 17: | Different microheater designs. | 74 |

Figure 4. 1: Schematic depicting the printing setup, which consists of a high-precision positioning stage, an optical microscope for monitoring the process, and a stationary holder for a glass capillary, which is further attached to a syringe pump. As illustrated in the inset, the positioning

| | |
|--|----|
| stage can be moved appropriately in the x, y, and z directions in order to write an LM line onto the substrate. Reproduced from [80] with permission from Wiley..... | 82 |
| Figure 4. 2:Setup components (a) Cutaway figure showing different parts of the NLP-2000 system. (Adapted from NLP-2000 getting started guide received with the system) (b) Customized glass capillary static holder. | 82 |
| Figure 4. 3:Actual image of the printing process: glass capillary mounted in the fixed holder, positioned over a glass sample used as substrate. The glass capillary is connected to the pump via LDPE tubing. The microscope image on the left shows a glass capillary tip while printing. Adapted from [80] with permission from Wiley..... | 83 |
| Figure 4. 4: View from the optical microscope while printing. | 83 |
| Figure 4. 5:Galinstan printing steps. (a) User interface and steps for the writing of LM with NLP 2000. (b) Steps after the "print" command is executed from the user interface. (I) Approach the starting point of the pattern. (II) Contact with the substrate. (III) Start the pre-programmed stage movements to form the desired pattern. | 84 |
| Figure 4. 6:Microscopy image of a freshly prepared glass capillary prior to opening up the tip aperture. Reproduced from [80] with permission from Wiley..... | 85 |
| Figure 4. 7:Resulting line widths versus tip opening size. The blue diamonds show average line widths obtained from 10 different capillaries. The yellow circles show the distribution of obtained lines, and the error bars represent the standard deviation (SD). The dashed line is a polynomial fit for guiding the eye ($y = 0.0144x^2 - 0.2945x + 27.363$, $R^2 = 0.9184$). Reproduced from [80] with permission from Wiley. | 86 |
| Figure 4. 8:Line printing with Galinstan. (a) The letters INT are patterned in macroscale on a glass substrate. (b) Different widths of Galinstan lines are achieved by tuning writing velocity. (c) Printed Galinstan grid structures. (d) Microwell structures. (e) The parallel Galinstan lines demonstrate conformity and reproducibility in writing. (f) AFM image of a printed Galinstan line. Adapted from [80] with permission from Wiley..... | 88 |
| Figure 4. 9:Optical micrograph of a single printed Galinstan line with a width of $(1.3 \pm 0.1) \mu\text{m}$. For analysis, the greyscale image was thresholded at an intensity of 150, and then the diameter of the wire | |

was measured at 10 randomly selected sites along the line. The orange overlay has a thickness of $1.3\mu\text{m}$ for direct scale. Reproduced from [80] with permission from Wiley. 88

Figure 4. 10: Optical micrograph of parallel lines with different interspacing in between. The minimal line distances achievable with the setup in experiments is about $6.3\mu\text{m}$ spacing; overall, the minimal line distance is well below the $10\text{-}\mu\text{m}$ threshold. Reproduced from [80] with permission from Wiley. 89

Figure 4. 11: SEM images of 3D prints. (a) Galinstan line arching over another previously printed line. (b) Interconnect arching over the substrate. Adapted from [80] with permission from Wiley. 89

Figure 4. 12: Droplet formation on the glass capillary tip. 90

Figure 4. 13: Droplet printing at the place of line formation..... 91

Figure 4. 14: Printing lines with different interspacing. Printing lines next to each other in close proximity (around $10\mu\text{m}$) might merge. Reproduced from [80] with permission from Wiley. 91

Figure 5. 1: An overview of the printing setup: (a) a schematic representation and (b) a photo of the actual setup. The setup comprises a printing stage with a USB webcam above the sample area and an arm-mounted micromanipulator carrying a glass capillary. The micromanipulator is connected to the computer via a control unit and can be controlled by handheld controllers, while a webcam displays the positioning of the capillary over the sample. Reproduced from [412] with permission from AIP..... 94

Figure 5. 2: An illustration showing the capillary stylus and printing process. (a) Close-up photo of a glass capillary stylus mounted on a micromanipulator. (b) Photography of the capillary during the ink loading process in the ink reservoir. Reproduced from [412] with permission from AIP..... 96

Figure 5. 3: Printing steps. (a) Glass capillary tip approaching the substrate under software control. (b) Upon contact with the substrate, the glass capillary nozzles transfer ink to the substrate. (c) Moving the tip mounted on the miBot according to the desired structure or pattern. (d), (e), (f) An illustration of writing dots, lines, and arbitrary curves, respectively. Figures (d), (e), and (f) are reproduced from [412] with permission from AIP..... 97

Figure 5. 4: Schematics of the interaction during the writing process. θ_a is the approaching angle between the glass capillary tip and substrate. Reproduced from [412] with permission from AIP. 98

| | | |
|--------------|---|-----|
| Figure 5. 5: | Various issues while printing lines of a printed line on a substrate. (a) ink holding onto the glass capillary, moving along with the tip; (b) the line breaks up into microdots; (c) a non-homogeneous line.... | 99 |
| Figure 5. 6: | "Hard-to-access" surfaces printability examples. (a) The design scheme for 3D-printed substrate holders for demonstration of vertical printing capabilities. (b) A photograph of the vertical printing setup with an ink-filled capillary and a micromanipulator in place. (c) The complex holder structure demonstrates the ability of this printing setup to reach places where regular printers cannot reach. (d) An actual photo of the multilevel printing, again with a micromanipulator and an ink-filled capillary. Reproduced from [412] with permission from AIP. | 100 |
| Figure 5. 7: | Examples of gold patterns on glass and Kapton substrates. (a) Photography of macroscopic letters "INT" printed on a glass substrate. Bright-field microscopy images of (b) side-by-side printed dots on a glass substrate with a gap distance of sub-10 μm , (c) microdots on a glass substrate, (d) line structures of different widths on a glass substrate, (e) microdots on a Kapton substrate, and (f) line structures on a Kapton substrate. Reproduced from [412] with permission from AIP. | 101 |
| Figure 5. 8: | In situ and on-demand connector writing. (a) The schematic workflow: The silver-epoxy paste electrodes are structured on a glass chip and recessed into a metal cube, which serves as a model device. After the wiring is done on the microplotter, Au-NP connector lines are written between the electrodes to close the circuit. The device is then cured in a furnace to make the printed pattern conductive. Finally, the LED and the power supply can be connected to demonstrate the function of the created circuit. (b) Actual photographs of the writing process. (c) An image of the fine gold connector lines printed by the microplotter. (d) The final photograph shows the circuit after curing and assembly of the LED and power supply. It demonstrates a fully functional circuit. Adapted from [412] with permission from AIP. | 102 |
| Figure 5. 9: | Fluorescence microscopy images of the deposited bioink pattern. Different spot configurations were plotted with ink 1 (a) and (d), ink 2 (b) and (e), and ink 3 (c) and (f). Red channel: Texas Red filter set (Y-2E/C, Nikon, Ex.: 540–580 nm, Em.: 600–660 nm), green channel: FITC filter set (B-2E/C, Nikon, Ex.: 465–495 nm, Em.: 515–555 nm), and purple channel: Cy5 filter set (AHF F41-008, Nikon, Ex.: 590–650 nm, Em.: 662–738 nm). Reproduced from [412] with permission from AIP. | 105 |
| Figure 6. 1: | Fabrication of interconnects. | 108 |

Figure 6. 2: Optical micrograph of a typical LM resistor structure. (a) Planar resistor structure (b) Stereo microscope image of freestanding interconnect. Reproduced from [81] with permission from Wiley. 108

Figure 6. 3: A schematic of the Galinstan line printed over two gold pads shows the distance between the gold pads, which defines the length l of the resistor structure, the width of the LM line defines w , and the height h . Adapted from [81] with permission from Wiley. 109

Figure 6. 4: Graph of specific resistance ρ for resistor structures of different lengths. The graph was plotted in Origin (OriginLab, USA). All error bars in graphs and error ranges reported represent one standard deviation (SD) of the reported mean. Reproduced from [81] with permission from Wiley..... 109

Figure 6. 5: Combination of focused Ion Beam for lithography and scanning electron microscope (FIB-SEM) analysis of a Galinstan line printed on a gold pad. (a) Sample description. (b) SEM secondary electron (SE, left) and (c) backscattered electron (BSE, right two) images of a cross-section through a Galinstan line show good contact between Galinstan and gold while the entire assembly lifted off the Si substrate during freezing (left of the arrow in BSE image) due to the larger thermal expansion coefficients of gold and Galinstan. Fabricated using a dual-focused ion beam (FIB)/scanning electron microscopy (SEM) (Crossbeam 540, Carl Zeiss Microscopy, Oberkochen, Germany) at Heidelberg University. Adapted from [81] with permission from Wiley. 110

Figure 6. 6: EDS analysis of Galinstan line at room temperature. (a) Fresh cross-section of a printed Galinstan line shortly after milling with the FIB at room temperature. Multiple lines in the lower half of the image show drifting artifacts produced by the Ga-ion beam during milling, and image contrast reveal "wetting" of the complete cross-section with Galinstan (b) EDS-maps of detected elements, used energy lines in brackets. The displayed maps confirm the "wetting" process. Performed using a dual-beam Zeiss AURIGA 60 system (available at INT). Reproduced from [81] with permission from Wiley..... 111

Figure 6. 7: Workflow for the construction of a fully printed diode by combining capillary and inkjet printing. Adapted from [81] with permission from Wiley. 113

Figure 6. 8: Optical micrograph of a typical printed diode (left) and the corresponding schematic (right). Adapted from [81] with permission from Wiley. 114

Figure 6. 9: Typical I–V characteristics of the printed diode in linear (top) and log-scale (bottom). Reproduced from [81] with permission from Wiley. 115

| | |
|---|-----|
| Figure 6. 10: Workflow for the construction of a fully printed FET by combining capillary printed Galinstan lines and inkjet printing for the materials In ₂ O ₃ , PEDOT:PSS, and electrolyte. Adapted from [81] with permission from Wiley. | 117 |
| Figure 6. 11: Optical micrograph of a typical printed FET (left) and the corresponding schematic (right). Adapted from [1] with permission from Wiley. | 118 |
| Figure 6. 12: I-V characteristics of the FET for the voltage applied to (a) ground/source (top) and (b) drain/source (bottom), respectively. Reproduced from [1] with permission from Wiley. | 118 |
| Figure 6. 13: Characterization of fully printed transistors with Au electrodes. Transfer characteristics of the transistor operating in (a) normally-OFF mode and (b) in normally-ON mode. Reproduced from [1] with permission from Wiley. | 119 |
| | |
| Figure 7. 1: Example of different LM microheaters with different designs and structure sizes (line width) obtained by tuning writing parameters. | 121 |
| Figure 7. 2: Optical microscope images of different microheater structures on glass were used in this study. | 122 |
| Figure 7. 3: A thermogram showing the temperature distribution for a typical microheater structure (bottom) and the corresponding design (top). | 123 |
| Figure 7. 4: Set up to measure resistance measurement at various temperatures. | 124 |
| Figure 7. 5: Electrical resistance of LM microheaters of the design (devices shown in Figure 7. 4). This plot is in accordance with previously reported Resistivity vs. Temperature data from [434]. | 124 |
| Figure 7. 6: Optical microscope images of a LM microheater structures part right after printing (left) and after heating (right). | 125 |
| Figure 7. 7: (a) Schematics of electromigration in LM printed line. Adapted with permission from Springer Nature [435]. (b) Schematics of LM line break-up within the heating channel induced by voids. Adapted with permission from MDPI [108]. | 126 |
| Figure 7. 8: Microheater based on continuous injection of LM in encapsulated microchannels. | 127 |
| Figure 7. 9: Printing multiple layers on top of each other increases the pattern's height and provides more temperature-stable structures. | 127 |
| Figure 7. 10: (a) Photo and optical microscope image of P-T_sample1 and 2. Line width: (108.49 ± 4.54) μm (b) Recorded maximum surface temperature with respect to the power applied. (c) shows the heating and cooling cycles for both LM microheaters where a voltage of 1.5V and 2 V are applied, resulting in a 0.92 W and 1.54 W power | |

| | | |
|---------------|---|-----|
| | consumption in LM microheaters P-T_Sample 1 and 2, respectively. | 128 |
| Figure 7. 11: | Microheater for microvalve application. (a) Scheme of device fabrication. (b) Schematics of the complete setup. (c) Actual photograph of the setup. Microscope images of the PNIPAM barrier and adjacent QD liquid (d) in bright field and (e) in fluorescence with FITC filter (B-2E/C, Nikon, Ex.: 465–495 nm, Em.: 515–555 nm). (f) shows a fluorescent image of the microchannel after triggering the PNIPAM valve by heating, allowing the fluorescent QDs to diffuse into the other parts of the channel. | 132 |
| Figure 8. 1: | Sample preparation and characterization description. Reproduced from [449] with permission from Wiley..... | 136 |
| Figure 8. 2: | Galinstan spread correlated study with Scanning Electron Microscopy (SEM), Energy-dispersive X-ray spectroscopy (EDS), and Vertical scanning interferometry (VSI) for the sample with respect to time. Reproduced from [449] with permission from Wiley. | 137 |
| Figure 8. 3: | SEM and VSI overlay of printed Galinstan line. The overlay was generated using the colocalization feature of MountainsMap (Digital Surf, France). Reproduced from [449] with permission from Wiley. | 138 |
| Figure 8. 4: | Spread distances from the Galinstan line. Fitting the spread S dependence of time t , assuming the free-space diffusion process [457] results in $S(t) = (5 \pm 0.63) \sqrt{t}$. EDS/VSI images from the same sample positions were used to quantify the spread. In each image, the perpendicular distance of 15 random points at the spread front to the LM line was measured. The fit was done in Origin (OriginLab, USA). All error bars in graphs and error ranges reported represent one standard deviation (SD) of the reported mean. Reproduced from [449] with permission from Wiley. | 139 |
| Figure 8. 5: | Intermetallic nanostructures formation in Galinstan-Gold. (a) SEM image at a 60-degree angle (closed view in inset), scale bar: 100 μm . (b) SEM image shows an apparent border between the intermetallic nanostructures products and the bare gold surface just after 7 hours of printing Galinstan on the gold surface. (c) EDS map edge of Galinstan line printed on the gold surface, acquired at 10 kV, 120 pA, Working distance (WD) = 5mm. Reproduced from [449] with permission from Wiley..... | 140 |
| Figure 8. 6: | EDS map for Galinstan, intermetallic nanostructure, and Au surface for freshly prepared sample for different time scales. 4 hours, 54 hours, 178 hours (1 week), 2 weeks, and 4 weeks. SEM image elemental overlay, Au signal, Ga signal, In signal, and Sn signal. Adapted from [449] with permission from Wiley..... | 141 |

-
- Figure 8. 7: Photo of LM sample on a gold-coated surface showing the light grey/blue color shades appearing on both sides due to Ga and In penetration into the gold film. The LM was applied to the film by the doctor blading without any contact or scratching of the gold film. The image is captured 190 days after the sample preparation. Reproduced from [449] with permission from Wiley.142
- Figure 8. 8: XRD analysis of LM sample. Potential peak positions corresponding to metallic Au (in blue) and Au-Ga alloys (AuGa₂ in red) are marked in the graph. Overall the pattern of peaks clearly indicates the presence of intermetallic AuGa₂, but AuIn₂ and AuSn₂ might be masked by peak overlaps. Keeping in mind additionally the (relative to Ga) low concentration of In and Sn indicated in the EDS measurements (Figure 8. 6), the intermetallic phase is expected to be predominantly AuGa₂. Reproduced from [449] with permission from Wiley.143
- Figure 8. 9: Line scan on a LM line on a homogeneously Au-coated substrate at 8, 14, and 120 days after printing. (a) Core level maps of Au4f, Ga2p, In3d, and Sn3d. The map's color code from blue to red is the lowest to highest intensity of the peak along the Y-axis. Point 4 (dark grey line), shows the starting point of the LM line. (b) Scheme on the sample and scan positions. (c), (d) High-resolution core-level spectra of Au4f, Ga3d, In3d, and Sn3d orbitals for a LM line (at the position marked in (b)) on Au for fresh, 8 days, 14 days, and 120 days after deposition. Reproduced from [449] with permission from Wiley. .144
- Figure 8. 10: High-resolution XPS spectra of Ga3d, C1s, O1s, and Cl2p orbitals for fresh/before sputtering and after sputtering with Ar+ Galinstan samples (a) air aged and (b) HCl etched and stored in Ar. The black line represents the first spectra (recorded before sputtering), and the red line represents the final spectra (after the sputtering experiment). Reproduced from [449] with permission from Wiley.146
- Figure 8. 11: Correlated SEM and AFM measurements on LM spread. (a) Optical microscopy image showing different shades of intermetallic nanostructure products. (b) SEM image of the edge of the intermetallic nanostructures band with the adjacent bare gold surface. (c) SEM imaging at a 60° angle (scale bar 1 μm) and corresponding AFM images for different positions. (d) Profile extraction from AFM images of positions. Reproduced from [449] with permission from Wiley.147
- Figure 8. 12: EDS map for Galinstan, Galinstan-Au products, and Au surface, which constitutes different shades; these shades were seen in the optical microscope as well as InLens signal in SEM, not seen in the SESI (Secondary electron secondary ion) signal. (a) SEM image (SESI signal). (b) Elemental Overlay. (c) Au signal. (d) Ga signal. (e) In signal. (f) Sn signal. (g) SEM InLens signal image for the same spot

- as (a). (SESI: Secondary electron secondary ion) Reproduced from [449] with permission from Wiley..... 149
- Figure 8. 13: A time-lapse optical microscope image shows bands, which can be correlated to vacuum cycles (when performing XPS) and air spread, where the corresponding width of the band increases in width with longer measuring and aging times. The grey spread area was influenced by high vacuum, and the black spread area is normal air aging. Reproduced from [449] with permission from Wiley. 149
- Figure 8. 14: FIB cross-section at 54 degrees showing nanostructures around 500 nm high (FIB cross-section depth 1 μm , width: 4 μm , milling current is 30kV:600pA) and EDS map at 54 degrees of FIB cross-section into the intermetallic nanostructures. For the fresh sample, the thickness of the gold layer was around 100 nm, with 7nm of Cr as the adhesion layer. (a), (b) SEM image. (c) Si Signal. (d) Au signal. (e) Ga signal. (f) In signal. (g) Sn signal. Reproduced from [449] with permission from Wiley..... 150
- Figure 8. 15: EDS map for LM line and adjacent intermetallic nanostructures at 60° view angle. (a) SEM image. (b) Elemental Overlay. (c) Au signal. (d) Ga signal. (e) In signal. (f) Sn signal. The Au-signal in the LM line indicates a back-propagation of Au from the substrate into the LM itself. Reproduced from [449] with permission from Wiley. 151
- Figure 8. 16: (a) NanoCT sample preparation. (b) NanoCT scan process. (c) NanoCT 2D slices and volumetric reconstruction of a nanoCT scan were performed 53 days after dipping a gold wire into the Galinstan. (as shown in (a)) of a gold, wire dipped into Galinstan. Side view slice of the sample in (I) grayscale (lighter gray indicates denser material) and (II) color map. The white dashed line in (II) indicates the cut for the top view (III). Reproduced from [449] with permission from Wiley. 152
- Figure 8. 17: Model of intermetallic nanostructure formation. (a) Schematic of the sample setup. (b) SEM image of the intermetallic nanostructures at a 60° view angle. (c) The proposed growing mechanism for the intermetallic nanostructures. (I) Crack initiation, (II) grain boundary penetration, and (III) intermetallic nanostructure formation. Color representations are; light blue: glass, orange: gold, gray: Galinstan, blue: intermetallic nanostructures, and purple: oxide layer. Reproduced from [449] with permission from Wiley. 153
- Figure 8. 18: Effect of temperature and humidity on formation of intermetallic structures. Comparison of optical microscope images of edges of printed Galinstan line pattern on Gold surface fresh sample to 18 hours aged sample. (a) sample set temperature. (b) Sample set humidity. Reproduced from [449] with permission from Wiley... 154
- Figure 8. 19: Optical microscope images of PMMA encapsulated printed pattern on the gold surface show less penetration. (a) Fresh sample. (b) After 1

- week. (c) After 2 weeks. (d) After 3 weeks. (e) After 4 weeks. The initial spread for the sample in (a) is probably induced by the high temperature during the curing of the PMMA (c.f. discussion on temperature influence on spreading and Figure 8. 18, Table 8. 2). Reproduced from [449] with permission from Wiley.....156
- Figure 8. 20: Chemical analysis of the oxide layer on the printed LM lines. a) SEM secondary electron (SE) image of a cross-section after TOF-SIMS analysis (executed on the area indicated by grey frame). b) FIB SE image of the first frame of the TOF-SIMS analysis. c) GaO-signal of the first 3 ToF-SIMS frames indicating an oxide layer on the sample surface, while the in situ milled cross-section (not previously exposed to air) shows no sign of an oxide cover. d) Ga3d core level spectra from XPS measurement on a one-month air-exposed Galinstan sample. Reproduced from [81] with permission from Wiley.157
- Figure 8. 21: Chemical analysis of oxide layer on the printed LM lines by XPS. Core level spectra from XPS measurement on a one-month air-exposed Galinstan sample. Core level spectra of (a) Ga3d, (b) O1s, (c) Sn3d, and (d) In3d of a sputtered depth profile on Galinstan. The graph was plotted in Origin (OriginLab, USA). Reproduced from [81] with permission from Wiley.158
- Figure 8. 22: The thickness of Ga₂O₃ over sputtering depth from Galinstan deposited on a Si substrate. Reproduced from [81] with permission from Wiley.159
- Figure 8. 23: XPS Analysis of aging Galinstan line. Ga3d core level collected from (a) fresh and aged samples for (b) 15 days and (c) 60 days on Galinstan deposited on Au substrate. The Ga₂O₃ thickness determined by sputtering depth profile XPS on fresh, 15 days, and 60 days-aged Galinstan samples. The thickness of Ga₂O₃ over layer changes from 2.0 nm to 2.5 nm in 60 days of aging in air. The graph was plotted in Origin (OriginLab, USA). Reproduced from [81] with permission from Wiley.160
- Figure 8. 24: Printed resistors as Galinstan lines between two gold pads (average width: $38.38 \pm 2.35 \mu\text{m}$), the distance between two gold pads 500 μm for sample 1 and 1620 μm for sample 2 (including 42 μm of the middle gold pad). Reproduced from [449] with permission from Wiley.161
- Figure 8. 25: Scheme of Au/Galinstan setup. (a) Conductivity measurement setup based upon a 2-point probe system. (b) Resistance studies with respect to time for two types of printed resistors. For each data point, the resistance was measured for 10 samples. The graph was plotted in Origin (OriginLab, USA). All error bars in graphs and error ranges reported represent one standard deviation (SD) of the reported mean. Reproduced from [449] with permission from Wiley.162

| | |
|--|-----|
| Figure 10. 1: Multi-ink deposition using parallel arrays of glass capillaries. | 169 |
| Figure A. 1: P-1000 micropipette puller system. (Setup at glass workshop INT) | 177 |
| Figure A. 2: Process of breaking the Glass capillary tip for desired and larger aperture size. Adapted from Sutter Instruments pipette cookbook 2018 [486]. | 179 |
| Figure A. 3: ATTO B plasma-cleaner (Diener electronic GmbH, Germany) at INT. | 179 |
| Figure A. 4: Working of e-beam physical vapor deposition (EBPVD). | 180 |
| Figure A. 5: Working of laser ablation and fabrication of contact pads with varying distances between the pads (60–550 μm)..... | 181 |
| Figure A. 6: (a) Focused Ion Beam Lithography working. (b) Auriga 60 System at INT. Special cryo holder and mounted Galinstan sample. | 182 |
| Figure A. 7: Prepared inks. Galinstan ink, In_2O_3 precursor ink, CuO precursor ink, and CSPE (Composite solid polymer electrolyte) ink. | 185 |
| Figure A. 8: Structure of crystalline In_2O_3 | 186 |
| Figure A. 9: (a) SEM working and electron beam interaction with the sample. (b) Interaction of electrons within a sample. | 189 |
| Figure A. 10: Working of atomic force microscopy. | 192 |
| Figure A. 11: Working of optical profilometry. | 193 |
| Figure A. 12: (a) Working of TOF-SIMS, and (b) beam interaction with the sample in FIB-TOF. | 195 |
| Figure A. 13: EDS working principle and instrumentation. | 196 |
| Figure A. 14: (a) XPS working, and (b) X-rays interaction with the sample, and photoelectron formation. | 197 |

List of Tables

| | |
|--|-----|
| Table 1.1: Difference between conventional fabrication in electronics and printed electronics..... | 4 |
| Table 2.1: Comparison of general trends for different properties of organic and inorganic materials..... | 17 |
| Table 2. 2: Properties of various organic and inorganic gate dielectrics used in printed electronics..... | 18 |
| Table 2. 3: Common electrolytes used in printed electronics..... | 21 |
| Table 2. 4: The intrinsic mobility of commonly inorganic semiconductors in printed electronics. | 23 |
| Table 2. 5: The intrinsic motilities of commonly organic semiconductors in printed electronics. | 26 |
| Table 2. 6: Common conductive inks used in printed electronics with their respective reported conductivity. | 27 |
| Table 2. 7: Physical properties of common liquid metals. Reproduced from [100,254] with permission from IEEE and RSC..... | 34 |
| Table 2. 8: Comparison of different printing methods [115,234,344]..... | 48 |
| Table 3. 1: Comparison of forward and reverse biased p-n diode. | 55 |
| Table 4. 1: Summary of a few scientific reports based on LM use for application. According to the ink used method of LM deposition, application reported, and year of publication of the report. | 76 |
| Table 5. 1: Components of the printing setup. Reproduced from [412] with permission from AIP..... | 95 |
| Table 5. 2: Ink formulations. Reproduced from [412] with permission from AIP..... | 104 |
| Table 6. 1: Comparison of fully printed p-n diodes. | 115 |
| Table 7 1: Comparison of previously reported printed microheaters and LM-based microheaters with current work. | 130 |
| Table 8. 1: Surface roughness for the positions in shades where the roughness average (Sa) represents the mean height on the surface, and the root mean square (Sq) indicates the standard deviation from the mean height. All reported values were calculated from the whole area of the recorded AFM images in MountainsMap (Digital Surf, France). Reproduced from [449] with permission from Wiley. | 148 |

List of Tables

Table 8. 2: Results of spreading experiments for LM lines on the gold surface for different temperatures and humidity. Images of the samples are provided in Figure 8.18. Reproduced from [449] with permission from Wiley. 154

Table A. 1: Materials used in work throughout the thesis. 175

Table A. 2: Description of capillary pulling parameters used on the P-1000 system. Adapted from Sutter Instruments pipette cookbook 2018 [486]. 177

Table A. 3: Description of parameters used on FIB system [491,493,494]. 184

Table A. 4: Commonly used signals by SEM users for imaging [502]. 190

Bibliography

- [1] A. W. Colombo *et al.*, "A 70-Year Industrial Electronics Society Evolution through Industrial Revolutions: The Rise and Flourishing of Information and Communication Technologies," *IEEE Industrial Electronics Magazine*, vol. 15, no. 1, pp. 115–126, Mar. 2021, doi: 10.1109/MIE.2020.3028058.
- [2] "Moore's Law: The number of transistors per microprocessor." <https://ourworldindata.org/grapher/transistors-per-microprocessor> (accessed Oct. 15, 2022).
- [3] G. E. Moore, "Cramming more components onto integrated circuits." <https://newsroom.intel.com/wp-content/uploads/sites/11/2018/05/moores-law-electronics.pdf> (accessed Aug. 30, 2022).
- [4] G. E. Moore, "Cramming more components onto integrated circuits, Reprinted from Electronics, volume 38, number 8, April 19, 1965, pp.114 ff.," *IEEE Solid-State Circuits Society Newsletter*, vol. 11, no. 3, pp. 33–35, Feb. 2009, doi: 10.1109/N-SSC.2006.4785860.
- [5] "The Story of the Intel® 4004." <https://www.intel.com/content/www/us/en/history/museum-story-of-intel-4004.html> (accessed Aug. 30, 2022).
- [6] "Apple unveils M1 Ultra, the world's most powerful chip for a personal computer - Apple." <https://www.apple.com/newsroom/2022/03/apple-unveils-m1-ultra-the-worlds-most-powerful-chip-for-a-personal-computer/> (accessed Aug. 30, 2022).
- [7] N. Z. Haron and S. Hamdioui, "Why is CMOS scaling coming to an END?," *Proceedings - 2008 3rd International Design and Test Workshop, IDT 2008*, pp. 98–103, 2008, doi: 10.1109/IDT.2008.4802475.
- [8] M. Heacock *et al.*, "E-waste and harm to vulnerable populations: A growing global problem," *Environ Health Perspect*, vol. 124, no. 5, pp. 550–555, May 2016, doi: 10.1289/EHP.1509699.
- [9] R. A. Patil and S. Ramakrishna, "A comprehensive analysis of e-waste legislation worldwide," *Environmental Science and Pollution Research*, vol. 27, no. 13, pp. 14412–14431, May 2020, doi: 10.1007/S11356-020-07992-1/FIGURES/3.
- [10] R. Y. Zhong, X. Xu, E. Klotz, and S. T. Newman, "Intelligent Manufacturing in the Context of Industry 4.0: A Review," *Engineering*, vol. 3, no. 5, pp. 616–630, Oct. 2017, doi: 10.1016/J.ENG.2017.05.015.
- [11] "7 Ways the Printing Press Changed the World - HISTORY." <https://www.history.com/news/printing-press-renaissance> (accessed Oct. 06, 2022).
- [12] H. Shirakawa, E. J. Louis, A. G. MacDiarmid, C. K. Chiang, and A. J. Heeger, "Synthesis of electrically conducting organic polymers: halogen derivatives of polyacetylene, (CH)_x," *J Chem Soc Chem Commun*, no. 16, pp. 578–580, Jan. 1977, doi: 10.1039/C39770000578.
- [13] F. Ebisawa, T. Kurokawa, and S. Nara, "Electrical properties of polyacetylene/polysiloxane interface," *J Appl Phys*, vol. 54, no. 6, p. 3255, Aug. 1998, doi: 10.1063/1.332488.

- [14] A. Tsumura, H. Koezuka, and T. Ando, "Macromolecular electronic device: Field-effect transistor with a polythiophene thin film," *Appl Phys Lett*, vol. 49, no. 18, p. 1210, Jun. 1998, doi: 10.1063/1.97417.
- [15] S. K. Garlapati, M. Divya, B. Breitung, R. Kruk, H. Hahn, and S. Dasgupta, "Printed Electronics Based on Inorganic Semiconductors: From Processes and Materials to Devices," *Advanced Materials*, vol. 30, no. 40, p. 1707600, Oct. 2018, doi: 10.1002/ADMA.201707600.
- [16] E. Sowade, H. Kang, K. Y. Mitra, O. J. Weiß, J. Weber, and R. R. Baumann, "Roll-to-roll infrared (IR) drying and sintering of an inkjet-printed silver nanoparticle ink within 1 second," *J Mater Chem C Mater*, vol. 3, no. 45, pp. 11815–11826, Nov. 2015, doi: 10.1039/C5TC02291F.
- [17] J. Liu *et al.*, "Fully stretchable active-matrix organic light-emitting electrochemical cell array," *Nature Communications 2020 11:1*, vol. 11, no. 1, pp. 1–11, Jul. 2020, doi: 10.1038/s41467-020-17084-w.
- [18] C. L. Baumbauer *et al.*, "Printed, flexible, compact UHF-RFID sensor tags enabled by hybrid electronics," *Scientific Reports 2020 10:1*, vol. 10, no. 1, pp. 1–12, Oct. 2020, doi: 10.1038/s41598-020-73471-9.
- [19] Y. F. Wang *et al.*, "Fully Printed PEDOT:PSS-based Temperature Sensor with High Humidity Stability for Wireless Healthcare Monitoring," *Scientific Reports 2020 10:1*, vol. 10, no. 1, pp. 1–8, Feb. 2020, doi: 10.1038/s41598-020-59432-2.
- [20] S. Harada, K. Kanao, Y. Yamamoto, T. Arie, S. Akita, and K. Takei, "Fully printed flexible fingerprint-like three-Axis tactile and slip force and temperature sensors for artificial skin," *ACS Nano*, vol. 8, no. 12, pp. 12851–12857, Dec. 2014, doi: 10.1021/nn506293y.
- [21] T. Sekine *et al.*, "Fully Printed Wearable Vital Sensor for Human Pulse Rate Monitoring using Ferroelectric Polymer," *Scientific Reports 2018 8:1*, vol. 8, no. 1, pp. 1–10, Mar. 2018, doi: 10.1038/s41598-018-22746-3.
- [22] K. Fukuda *et al.*, "Fully-printed high-performance organic thin-film transistors and circuitry on one-micron-thick polymer films," *Nature Communications 2014 5:1*, vol. 5, no. 1, pp. 1–8, Jun. 2014, doi: 10.1038/ncomms5147.
- [23] T. Minamiki *et al.*, "Flexible organic thin-film transistor immunosensor printed on a one-micron-thick film," *Communications Materials 2021 2:1*, vol. 2, no. 1, pp. 1–8, Jan. 2021, doi: 10.1038/s43246-020-00112-z.
- [24] P. He *et al.*, "Fully printed high performance humidity sensors based on two-dimensional materials," *Nanoscale*, vol. 10, no. 12, pp. 5599–5606, Mar. 2018, doi: 10.1039/C7NR08115D.
- [25] E. Bihar, S. Wustoni, A. M. Pappa, K. N. Salama, D. Baran, and S. Inal, "A fully inkjet-printed disposable glucose sensor on paper," *npj Flexible Electronics 2018 2:1*, vol. 2, no. 1, pp. 1–8, Dec. 2018, doi: 10.1038/s41528-018-0044-y.
- [26] E. Song, R. P. Tortorich, T. H. da Costa, and J. W. Choi, "Inkjet printing of conductive polymer nanowire network on flexible substrates and its application in chemical sensing," *Microelectron Eng*, vol. 145, pp. 143–148, Sep. 2015, doi: 10.1016/J.MEE.2015.04.004.
- [27] J. B. Andrews, J. A. Cardenas, C. J. Lim, S. G. Noyce, J. Mullett, and A. D. Franklin, "Fully Printed and Flexible Carbon Nanotube Transistors for Pressure Sensing in Automobile Tires," *IEEE Sens J*, vol. 18, no. 19, pp. 7875–7880, Oct. 2018, doi: 10.1109/JSEN.2018.2842139.

-
- [28] M. Colina, P. Serra, J. M. Fernández-Pradas, L. Sevilla, and J. L. Morenza, "DNA deposition through laser induced forward transfer," *Biosens Bioelectron*, vol. 20, no. 8, pp. 1638–1642, Feb. 2005, doi: 10.1016/J.BIOS.2004.08.047.
- [29] J. A. Barron, H. D. Young, D. D. Dlott, M. M. Darfler, D. B. Krizman, and B. R. Ringeisen, "Printing of protein microarrays via a capillary-free fluid jetting mechanism," *Proteomics*, vol. 5, no. 16, pp. 4138–4144, Nov. 2005, doi: 10.1002/PMIC.200401294.
- [30] J. Bian *et al.*, "Laser Transfer, Printing, and Assembly Techniques for Flexible Electronics," *Adv Electron Mater*, vol. 5, no. 7, p. 1800900, Jul. 2019, doi: 10.1002/AELM.201800900.
- [31] M. Horák, K. Bukvišová, V. Švarc, J. Jaskowiec, V. Křápek, and T. Šikola, "Comparative study of plasmonic antennas fabricated by electron beam and focused ion beam lithography," *Scientific Reports 2018 8:1*, vol. 8, no. 1, pp. 1–8, Jun. 2018, doi: 10.1038/s41598-018-28037-1.
- [32] A. Angelin, U. Bog, R. Kumar, C. M. Niemeyer, and M. Hirtz, "Writing Behavior of Phospholipids in Polymer Pen Lithography (PPL) for Bioactive Micropatterns," *Polymers 2019, Vol. 11, Page 891*, vol. 11, no. 5, p. 891, May 2019, doi: 10.3390/POLYM11050891.
- [33] I. N. Lee *et al.*, "Large-area Scanning Probe Nanolithography Facilitated by Automated Alignment and Its Application to Substrate Fabrication for Cell Culture Studies," *JoVE (Journal of Visualized Experiments)*, vol. 2018, no. 136, p. e56967, Jun. 2018, doi: 10.3791/56967.
- [34] V. N. Morozov and T. Y. Morozova, "Electrospray deposition as a method for mass fabrication of mono- and multicomponent microarrays of biological and biologically active substances," *Anal Chem*, vol. 71, no. 15, pp. 3110–3117, 1999, doi: 10.1021/ac981412h.
- [35] X. Chen *et al.*, "Multi-metal 4D printing with a desktop electrochemical 3D printer," *Scientific Reports 2019 9:1*, vol. 9, no. 1, pp. 1–9, Mar. 2019, doi: 10.1038/s41598-019-40774-5.
- [36] P. Rath, M. Hirtz, G. Lewes-Malandrakis, D. Brink, C. Nebel, and W. H. P. Pernice, "Diamond Nanophotonic Circuits Functionalized by Dip-pen Nanolithography," *Adv Opt Mater*, vol. 3, no. 3, pp. 328–335, Mar. 2015, doi: 10.1002/ADOM.201400434.
- [37] M. Hirtz, A. Oikonomou, T. Georgiou, H. Fuchs, and A. Vijayaraghavan, "Multiplexed biomimetic lipid membranes on graphene by dip-pen nanolithography," *Nature Communications 2013 4:1*, vol. 4, no. 1, pp. 1–8, Oct. 2013, doi: 10.1038/ncomms3591.
- [38] H. Wagner, M. K. Brinks, M. Hirtz, A. Schäfer, L. Chi, and A. Studer, "Chemical Surface Modification of Self-Assembled Monolayers by Radical Nitroxide Exchange Reactions," *Chemistry – A European Journal*, vol. 17, no. 33, pp. 9107–9112, Aug. 2011, doi: 10.1002/CHEM.201100543.
- [39] G. Liu *et al.*, "Development of Dip-Pen Nanolithography (DPN) and Its Derivatives," *Small*, vol. 15, no. 21, p. 1900564, May 2019, doi: 10.1002/SMLL.201900564.
- [40] R. D. Piner, J. Zhu, F. Xu, S. Hong, and C. A. Mirkin, "'Dip-pen' nanolithography," *Science (1979)*, vol. 283, no. 5402, pp. 661–663, Jan. 1999, doi: 10.1126/science.283.5402.661.

- [41] R. Garcia, A. W. Knoll, and E. Riedo, "Advanced scanning probe lithography," *Nature Nanotechnology* 2014 9:8, vol. 9, no. 8, pp. 577–587, Aug. 2014, doi: 10.1038/nnano.2014.157.
- [42] S. A. M. Carnally and L. S. Wong, "Harnessing catalysis to enhance scanning probe nanolithography," *Nanoscale*, vol. 6, no. 10, pp. 4998–5007, Apr. 2014, doi: 10.1039/C4NR00618F.
- [43] J. Fernández-Salmerón, A. Rivadeneyra, F. Martínez-Martí, L. F. Capitán-Vallvey, A. J. Palma, and M. A. Carvajal, "Passive UHF RFID Tag with Multiple Sensing Capabilities," *Sensors* 2015, Vol. 15, Pages 26769-26782, vol. 15, no. 10, pp. 26769–26782, Oct. 2015, doi: 10.3390/S151026769.
- [44] V. Subramanian *et al.*, "Progress toward development of all-printed RFID tags: Materials, processes, and devices," *Proceedings of the IEEE*, vol. 93, no. 7, pp. 1330–1338, 2005, doi: 10.1109/JPROC.2005.850305.
- [45] M. Mäntysalo and P. Mansikkamäki, "An inkjet-deposited antenna for 2.4 GHz applications," *AEU - International Journal of Electronics and Communications*, vol. 63, no. 1, pp. 31–35, Jan. 2009, doi: 10.1016/J.AEUE.2007.10.004.
- [46] S. Kim, "Inkjet-Printed Electronics on Paper for RF Identification (RFID) and Sensing," *Electronics* 2020, Vol. 9, Page 1636, vol. 9, no. 10, p. 1636, Oct. 2020, doi: 10.3390/ELECTRONICS9101636.
- [47] I. I. Labiano and A. Alomainy, "Flexible inkjet-printed graphene antenna on Kapton," *Flexible and Printed Electronics*, vol. 6, no. 2, p. 025010, Jun. 2021, doi: 10.1088/2058-8585/AC0AC1.
- [48] M. Bhattacharjee, F. Nikbakhtnasrabadi, and R. Dahiya, "Printed Chipless Antenna as Flexible Temperature Sensor," *IEEE Internet Things J*, vol. 8, no. 6, pp. 5101–5110, Mar. 2021, doi: 10.1109/JIOT.2021.3051467.
- [49] S. Y. Y. Leung and D. C. C. Lam, "Performance of printed polymer-based RFID antenna on curvilinear surface," *IEEE Transactions on Electronics Packaging Manufacturing*, vol. 30, no. 3, pp. 200–205, Jul. 2007, doi: 10.1109/TEPM.2007.901181.
- [50] A. Falco, J. F. Salmerón, F. C. Loghin, P. Lugli, and A. Rivadeneyra, "Fully Printed Flexible Single-Chip RFID Tag with Light Detection Capabilities," *Sensors* 2017, Vol. 17, Page 534, vol. 17, no. 3, p. 534, Mar. 2017, doi: 10.3390/S17030534.
- [51] J. V. Voutilainen, T. Happonen, J. Hakkinen, and T. Fabritius, "All silk-screen printed polymer-based remotely readable temperature sensor," *IEEE Sens J*, vol. 15, no. 2, pp. 723–733, Feb. 2015, doi: 10.1109/JSEN.2014.2350077.
- [52] P. Lall, K. Goyal, and J. Narangaparambil, "Accuracy, Hysteresis and Extended Time Stability of Additively Printed Temperature and Humidity Sensors," *Proceedings - Electronic Components and Technology Conference*, vol. 2020-June, pp. 1070–1080, Jun. 2020, doi: 10.1109/ECTC32862.2020.00173.
- [53] M. Soni, M. Bhattacharjee, M. Ntagios, and R. Dahiya, "Printed Temperature Sensor Based on PEDOT: PSS-Graphene Oxide Composite," *IEEE Sens J*, vol. 20, no. 14, pp. 7525–7531, Jul. 2020, doi: 10.1109/JSEN.2020.2969667.
- [54] D. Barmpakos and G. Kaltsas, "A Review on Humidity, Temperature and Strain Printed Sensors—Current Trends and Future Perspectives," *Sensors* 2021, Vol. 21, Page 739, vol. 21, no. 3, p. 739, Jan. 2021, doi: 10.3390/S21030739.

-
- [55] X. Wang *et al.*, "An all-printed wireless humidity sensor label," *Sens Actuators B Chem*, vol. 166–167, pp. 556–561, May 2012, doi: 10.1016/J.SNB.2012.03.009.
- [56] M. U. Khan, G. Hassan, M. Awais, and J. Bae, "All printed full range humidity sensor based on Fe₂O₃," *Sens Actuators A Phys*, vol. 311, p. 112072, Aug. 2020, doi: 10.1016/J.SNA.2020.112072.
- [57] J. Gao, J. Siden, H. E. Nilsson, and M. Gulliksson, "Printed humidity sensor with memory functionality for passive RFID tags," *IEEE Sens J*, vol. 13, no. 5, pp. 1824–1834, 2013, doi: 10.1109/JSEN.2013.2244034.
- [58] D. Zymelka, K. Togashi, and T. Kobayashi, "Carbon-based printed strain sensor array for remote and automated structural health monitoring," *Smart Mater Struct*, vol. 29, no. 10, p. 105022, Sep. 2020, doi: 10.1088/1361-665X/ABA81C.
- [59] B. Thompson and H. S. Yoon, "Aerosol-printed strain sensor using PEDOT:PSS," *IEEE Sens J*, vol. 13, no. 11, pp. 4256–4263, 2013, doi: 10.1109/JSEN.2013.2264482.
- [60] D. Zymelka, K. Togashi, and T. Kobayashi, "Concentric Array of Printed Strain Sensors for Structural Health Monitoring," *Sensors 2020, Vol. 20, Page 1997*, vol. 20, no. 7, p. 1997, Apr. 2020, doi: 10.3390/S20071997.
- [61] V. Correia *et al.*, "All-printed piezoresistive sensor matrix with organic thin-film transistors as a switch for crosstalk reduction," *ACS Appl Electron Mater*, vol. 2, no. 5, pp. 1470–1477, 2020, doi: 10.1021/acsaelm.0c00214.
- [62] J. DeGraff, R. Liang, M. Q. Le, J. F. Capsal, F. Ganet, and P. J. Cottinet, "Printable low-cost and flexible carbon nanotube buckypaper motion sensors," *Mater Des*, vol. 133, pp. 47–53, Nov. 2017, doi: 10.1016/J.MATDES.2017.07.048.
- [63] Y. Wei, R. Torah, K. Yang, S. Beeby, and J. Tudor, "Screen printing of a capacitive cantilever-based motion sensor on fabric using a novel sacrificial layer process for smart fabric applications," *Meas Sci Technol*, vol. 24, no. 7, p. 075104, Jun. 2013, doi: 10.1088/0957-0233/24/7/075104.
- [64] S. Ali, S. Khan, and A. Bermak, "All-Printed Human Activity Monitoring and Energy Harvesting Device for Internet of Thing Applications," *Sensors 2019, Vol. 19, Page 1197*, vol. 19, no. 5, p. 1197, Mar. 2019, doi: 10.3390/S19051197.
- [65] Y. Guo *et al.*, "Degradable and Fully Recyclable Dynamic Thermoset Elastomer for 3D-Printed Wearable Electronics," *Adv Funct Mater*, vol. 31, no. 9, p. 2009799, Feb. 2021, doi: 10.1002/ADFM.202009799.
- [66] T. Hassinen, K. Eiroma, T. Mäkelä, and V. Ermolov, "Printed pressure sensor matrix with organic field-effect transistors," *Sens Actuators A Phys*, vol. 236, pp. 343–348, Dec. 2015, doi: 10.1016/J.SNA.2015.11.007.
- [67] L. W. Lo, H. Shi, H. Wan, Z. Xu, X. Tan, and C. Wang, "Inkjet-Printed Soft Resistive Pressure Sensor Patch for Wearable Electronics Applications," *Adv Mater Technol*, vol. 5, no. 1, p. 1900717, Jan. 2020, doi: 10.1002/ADMT.201900717.
- [68] L. Mo *et al.*, "Full printed flexible pressure sensor based on microcapsule controllable structure and composite dielectrics," *Flexible and Printed Electronics*, vol. 6, no. 1, p. 014001, Mar. 2021, doi: 10.1088/2058-8585/ABE842.

- [69] H. Shi *et al.*, "Screen-Printed Soft Capacitive Sensors for Spatial Mapping of Both Positive and Negative Pressures," *Adv Funct Mater*, vol. 29, no. 23, p. 1809116, Jun. 2019, doi: 10.1002/ADFM.201809116.
- [70] A. Albrecht *et al.*, "Screen-printed capacitive pressure sensors with high sensitivity and accuracy on flexible substrates," *Flexible and Printed Electronics*, vol. 7, no. 3, p. 035005, Jul. 2022, doi: 10.1088/2058-8585/AC812D.
- [71] M. L. Seol, J. W. Han, D. il Moon, K. J. Yoon, C. S. Hwang, and M. Meyyappan, "All-printed triboelectric nanogenerator," *Nano Energy*, vol. 44, pp. 82–88, Feb. 2018, doi: 10.1016/J.NANOEN.2017.11.067.
- [72] L. Grande, V. T. Chundi, D. Wei, C. Bower, P. Andrew, and T. Ryhänen, "Graphene for energy harvesting/storage devices and printed electronics," *Particuology*, vol. 10, no. 1, pp. 1–8, Feb. 2012, doi: 10.1016/J.PARTIC.2011.12.001.
- [73] L. Zhang *et al.*, "Ambient Inkjet-Printed High-Efficiency Perovskite Solar Cells: Manipulating the Spreading and Crystallization Behaviors of Picoliter Perovskite Droplets," *Solar RRL*, vol. 5, no. 5, p. 2100106, May 2021, doi: 10.1002/SOLR.202100106.
- [74] F. Nickel *et al.*, "Mechanically robust, ITO-free, 4.8% efficient, all-solution processed organic solar cells on flexible PET foil," *Solar Energy Materials and Solar Cells*, vol. 130, pp. 317–321, Nov. 2014, doi: 10.1016/J.SOLMAT.2014.07.005.
- [75] M. Hatala *et al.*, "Screen-printed conductive carbon layers for dye-sensitized solar cells and electrochemical detection of dopamine," *Chemical Papers*, vol. 75, no. 8, pp. 3817–3829, Aug. 2021, doi: 10.1007/S11696-021-01601-2/TABLES/5.
- [76] D. Janczak *et al.*, "Stretchable and Washable Electroluminescent Display Screen-Printed on Textile," *Nanomaterials 2019, Vol. 9, Page 1276*, vol. 9, no. 9, p. 1276, Sep. 2019, doi: 10.3390/NANO9091276.
- [77] J. Kawahara *et al.*, "Flexible active matrix addressed displays manufactured by printing and coating techniques," *J Polym Sci B Polym Phys*, vol. 51, no. 4, pp. 265–271, Feb. 2013, doi: 10.1002/POLB.23213.
- [78] D. E. Schwartz *et al.*, "Flexible hybrid electronic circuits and systems," *IEEE J Emerg Sel Top Circuits Syst*, vol. 7, no. 1, pp. 27–37, Mar. 2017, doi: 10.1109/JETCAS.2016.2612623.
- [79] H. Yan *et al.*, "A high-mobility electron-transporting polymer for printed transistors," *Nature 2009 457:7230*, vol. 457, no. 7230, pp. 679–686, Jan. 2009, doi: 10.1038/nature07727.
- [80] N. Hussain *et al.*, "High-Resolution Capillary Printing of Eutectic Gallium Alloys for Printed Electronics," *Adv Mater Technol*, vol. 6, no. 11, p. 2100650, Nov. 2021, doi: 10.1002/ADMT.202100650.
- [81] J. Zhao *et al.*, "Ambipolar deep-subthreshold printed-carbon-nanotube transistors for ultralow-voltage and ultralow-power electronics," *ACS Nano*, vol. 14, no. 10, pp. 14036–14046, Oct. 2020, doi: 10.1021/acsnano.0c06619.
- [82] D. E. Schwartz and T. N. Ng, "Comparison of static and dynamic printed organic shift registers," *IEEE Electron Device Letters*, vol. 34, no. 2, pp. 271–273, 2013, doi: 10.1109/LED.2012.2233709.

-
- [83] T. N. Ng *et al.*, "Pulsed voltage multiplier based on printed organic devices," *Flexible and Printed Electronics*, vol. 1, no. 1, p. 015002, Dec. 2015, doi: 10.1088/2058-8585/1/1/015002.
- [84] R. Kamali-Sarvestani, B. Martin, and L. Brayden, "Design and fabrication of ink-jet printed logic gates using SWCNT-FET for flexible circuit applications," *Proceedings - IEEE International Symposium on Circuits and Systems*, vol. 2019-May, 2019, doi: 10.1109/ISCAS.2019.8702776.
- [85] S. Singh, Y. Takeda, H. Matsui, and S. Tokito, "Flexible PMOS Inverter and NOR Gate Using Inkjet-Printed Dual-Gate Organic Thin Film Transistors," *IEEE Electron Device Letters*, vol. 41, no. 3, pp. 409–412, Mar. 2020, doi: 10.1109/LED.2020.2969275.
- [86] H. Matsui, K. Hayasaka, Y. Takeda, R. Shiwaku, J. Kwon, and S. Tokito, "Printed 5-V organic operational amplifiers for various signal processing," *Scientific Reports 2018 8:1*, vol. 8, no. 1, pp. 1–9, Jun. 2018, doi: 10.1038/s41598-018-27205-7.
- [87] H. Sun, Y. Xu, and Y. Y. Noh, "Flexible Organic Amplifiers," *IEEE Trans Electron Devices*, vol. 64, no. 5, pp. 1944–1954, May 2017, doi: 10.1109/TED.2017.2667704.
- [88] M. Hassan *et al.*, "Significance of Flexible Substrates for Wearable and Implantable Devices: Recent Advances and Perspectives," *Adv Mater Technol*, vol. 7, no. 3, p. 2100773, Mar. 2022, doi: 10.1002/ADMT.202100773.
- [89] N. Jürgensen, M. Pietsch, X. Hai, S. Schliske, and G. Hernandez-Sosa, "Green ink formulation for inkjet printed transparent electrodes in OLEDs on biodegradable substrates," *Synth Met*, vol. 282, p. 116930, Dec. 2021, doi: 10.1016/J.SYNTHMET.2021.116930.
- [90] M. Atreya, K. Dikshit, G. Marinick, J. Nielson, C. Bruns, and G. L. Whiting, "Poly(lactic acid)-Based Ink for Biodegradable Printed Electronics with Conductivity Enhanced through Solvent Aging," *ACS Appl Mater Interfaces*, vol. 12, no. 20, pp. 23494–23501, May 2020, doi: 10.1021/acsami.0c05196.
- [91] Y. Lin *et al.*, "Routes towards manufacturing biodegradable electronics with polycaprolactone (PCL) via direct light writing and electroless plating," *Flexible and Printed Electronics*, vol. 7, no. 2, p. 025006, May 2022, doi: 10.1088/2058-8585/AC6B6E.
- [92] "Flexible, Printed and Organic Electronics 2020-2030: Forecasts, Technologies, Markets: IDTechEx." <https://www.idtechex.com/en/research-report/flexible-printed-and-organic-electronics-2020-2030-forecasts-technologies-markets/687> (accessed Sep. 09, 2022).
- [93] Y. C. Sun, G. Boero, and J. Brugger, "Stretchable Conductors Fabricated by Stencil Lithography and Centrifugal Force-Assisted Patterning of Liquid Metal," *ACS Appl Electron Mater*, vol. 3, no. 12, pp. 5423–5432, Dec. 2021, doi: 10.1021/ACSAELM.1C00884/ASSET/IMAGES/LARGE/EL1C00884_0004.JPEG.
- [94] O. Vazquez-Mena, G. Villanueva, V. Savu, K. Sidler, M. A. F. van den Boogaart, and J. Brugger, "Metallic nanowires by full wafer stencil lithography," *Nano Lett*, vol. 8, no. 11, pp. 3675–3682, Nov. 2008, doi: 10.1021/NL801778T/SUPPL_FILE/NL801778T_SI_001.PDF.
- [95] M. gu Kim, D. K. Brown, and O. Brand, "Nanofabrication for all-soft and high-density electronic devices based on liquid metal," *Nature Communications 2020 11:1*, vol. 11, no. 1, pp. 1–11, Feb. 2020, doi: 10.1038/s41467-020-14814-y.

- [96] A. Tabatabai, A. Fassler, C. Usiak, and C. Majidi, "Liquid-phase gallium-indium alloy electronics with microcontact printing," *Langmuir*, vol. 29, no. 20, pp. 6194–6200, May 2013, doi: 10.1021/la401245d.
- [97] J. W. Boley, E. L. White, G. T. C. Chiu, and R. K. Kramer, "Direct Writing of Gallium-Indium Alloy for Stretchable Electronics," *Adv Funct Mater*, vol. 24, no. 23, pp. 3501–3507, Jun. 2014, doi: 10.1002/ADFM.201303220.
- [98] F. Scharmann *et al.*, "Viscosity effect on GaInSn studied by XPS," *Surface and Interface Analysis*, vol. 36, no. 8, pp. 981–985, Aug. 2004, doi: 10.1002/SIA.1817.
- [99] T. Liu, P. Sen, and C. J. Kim, "Characterization of nontoxic liquid-metal alloy galinstan for applications in microdevices," *Journal of Microelectromechanical Systems*, vol. 21, no. 2, pp. 443–450, Apr. 2012, doi: 10.1109/JMEMS.2011.2174421.
- [100] C. Ladd *et al.*, "3D Printing of Free Standing Liquid Metal Microstructures," *Advanced Materials*, vol. 25, no. 36, pp. 5081–5085, Sep. 2013, doi: 10.1002/ADMA.201301400.
- [101] Y. G. Park, H. S. An, J. Y. Kim, and J. U. Park, "High-resolution, reconfigurable printing of liquid metals with three-dimensional structures," *Sci Adv*, vol. 5, no. 6, 2019, doi: 10.1126/SCIADV.AAW2844.
- [102] A. Hacohen, H. R. Jessel, A. Richter-Levin, and O. Shefi, "Patterning of Particles and Live Cells at Single Cell Resolution," *Micromachines 2020, Vol. 11, Page 505*, vol. 11, no. 5, p. 505, May 2020, doi: 10.3390/MI11050505.
- [103] T. H. da Costa and J. W. Choi, "Low-cost and customizable inkjet printing for microelectrodes fabrication," *Micro and Nano Systems Letters*, vol. 8, no. 1, pp. 1–6, Dec. 2020, doi: 10.1186/S40486-020-0104-7/FIGURES/6.
- [104] B. Y. Ahn *et al.*, "Omnidirectional printing of flexible, stretchable, and spanning silver microelectrodes," *Science (1979)*, vol. 323, no. 5921, pp. 1590–1593, Mar. 2009, doi: 10.1126/SCIENCE.1168375.
- [105] G. M. Gratson, M. Xu, and J. A. Lewis, "Direct writing of three-dimensional webs," *Nature 2004 428:6981*, vol. 428, no. 6981, pp. 386–386, Mar. 2004, doi: 10.1038/428386a.
- [106] J. Je and J. Lee, "Design, fabrication, and characterization of liquid metal microheaters," *Journal of Microelectromechanical Systems*, vol. 23, no. 5, pp. 1156–1163, Oct. 2014, doi: 10.1109/JMEMS.2014.2307358.
- [107] L. Zhang *et al.*, "A Performance-Enhanced Liquid Metal-Based Microheater with Parallel Ventilating Side-Channels," *Micromachines 2020, Vol. 11, Page 133*, vol. 11, no. 2, p. 133, Jan. 2020, doi: 10.3390/MI11020133.
- [108] T. Sato, K. Yamagishi, M. Hashimoto, and E. Iwase, "Method to Reduce the Contact Resistivity between Galinstan and a Copper Electrode for Electrical Connection in Flexible Devices," *ACS Appl Mater Interfaces*, vol. 13, no. 15, pp. 18247–18254, Apr. 2021, doi: 10.1021/ACSAMI.1C00431.
- [109] Z. Cui, *Printed Electronics: Materials, Technologies and Applications*. Singapore: John Wiley & Sons Singapore Pte. Ltd, 2016. doi: 10.1002/9781118920954.
- [110] Edited by, M. Caironi, and Y.-Y. Noh, *Large area and flexible electronics*. Wiley-VCH, 2015. Accessed: Sep. 09, 2022. ISBN: 978-3-527-67999-7.

-
- [111] Y. Sun and J. A. Rogers, "Inorganic Semiconductors for Flexible Electronics," *Advanced Materials*, vol. 19, no. 15, pp. 1897–1916, Aug. 2007, doi: 10.1002/ADMA.200602223.
- [112] C. S. Buga and J. C. Viana, "A Review on Materials and Technologies for Organic Large-Area Electronics," *Adv Mater Technol*, vol. 6, no. 6, p. 2001016, Jun. 2021, doi: 10.1002/ADMT.202001016.
- [113] M. Berggren, D. Nilsson, and N. D. Robinson, "Organic materials for printed electronics," *Nature Materials 2007 6:1*, vol. 6, no. 1, pp. 3–5, Jan. 2007, doi: 10.1038/nmat1817.
- [114] J. Wiklund *et al.*, "A Review on Printed Electronics: Fabrication Methods, Inks, Substrates, Applications and Environmental Impacts," *Journal of Manufacturing and Materials Processing 2021, Vol. 5, Page 89*, vol. 5, no. 3, p. 89, Aug. 2021, doi: 10.3390/JMMP5030089.
- [115] Z. Cui *et al.*, "Inorganic Printable Electronic Materials," *Printed Electronics*, pp. 54–105, Apr. 2016, doi: 10.1002/9781118920954.CH3.
- [116] B. Nketia-Yawson, Y.-Y. Noh, B. Nketia-Yawson, and Y.-Y. Noh, "Recent Progress on High-Capacitance Polymer Gate Dielectrics for Flexible Low-Voltage Transistors," *Adv Funct Mater*, vol. 28, no. 42, p. 1802201, Oct. 2018, doi: 10.1002/ADFM.201802201.
- [117] P. K. Nayak, M. N. Hedhili, D. Cha, and H. N. Alshareef, "High performance In₂O₃ thin film transistors using chemically derived aluminum oxide dielectric," *Appl Phys Lett*, vol. 103, no. 3, p. 033518, Jul. 2013, doi: 10.1063/1.4816060.
- [118] A. Matavž, B. Malič, and V. Bobnar, "Inkjet printing of metal-oxide-based transparent thin-film capacitors," *J Appl Phys*, vol. 122, no. 21, p. 214102, Dec. 2017, doi: 10.1063/1.5000432.
- [119] G. Vescio, J. López-Vidrier, R. Leghrib, A. Cornet, and A. Cirera, "Flexible inkjet printed high-k HfO₂-based MIM capacitors," *J Mater Chem C Mater*, vol. 4, no. 9, pp. 1804–1812, Feb. 2016, doi: 10.1039/C5TC03307A.
- [120] K. Song, W. Yang, Y. Jung, S. Jeong, and J. Moon, "A solution-processed yttrium oxide gate insulator for high-performance all-solution-processed fully transparent thin film transistors," *J Mater Chem*, vol. 22, no. 39, pp. 21265–21271, Sep. 2012, doi: 10.1039/C2JM34162J.
- [121] J. A. Amick, G. L. Schnable, and J. L. Vossen, "Deposition techniques for dielectric films on semiconductor devices," *Journal of Vacuum Science and Technology*, vol. 14, no. 5, p. 1053, Jun. 1998, doi: 10.1116/1.569412.
- [122] Y. Y. Illarionov *et al.*, "Insulators for 2D nanoelectronics: the gap to bridge," *Nature Communications 2020 11:1*, vol. 11, no. 1, pp. 1–15, Jul. 2020, doi: 10.1038/s41467-020-16640-8.
- [123] J. H. Cho *et al.*, "Printable ion-gel gate dielectrics for low-voltage polymer thin-film transistors on plastic," *Nature Materials 2008 7:11*, vol. 7, no. 11, pp. 900–906, Oct. 2008, doi: 10.1038/nmat2291.
- [124] B. Kumar, B. K. Kaushik, and Y. S. Negi, "Perspectives and challenges for organic thin film transistors: Materials, devices, processes and applications," *Journal of Materials Science: Materials in Electronics*, vol. 25, no. 1, pp. 1–30, Jan. 2014, doi: 10.1007/S10854-013-1550-2.
- [125] B. Wang, W. Huang, L. Chi, M. Al-Hashimi, T. J. Marks, and A. Facchetti, "High-k Gate Dielectrics for Emerging Flexible and Stretchable Electronics," *Chem*

- Rev, vol. 118, no. 11, pp. 5690–5754, Jun. 2018, doi: 10.1021/ACS.CHEMREV.8B00045.
- [126] M. J. Panzer, C. R. Newman, and C. D. Frisbie, "Low-voltage operation of a pentacene field-effect transistor with a polymer electrolyte gate dielectric," *Appl Phys Lett*, vol. 86, no. 10, p. 103503, Feb. 2005, doi: 10.1063/1.1880434.
- [127] A. R. V. Benvenho, W. S. Machado, I. Cruz-Cruz, and I. A. Hümmelgen, "Study of poly(3-hexylthiophene)/cross-linked poly(vinyl alcohol) as semiconductor/insulator for application in low voltage organic field effect transistors," *J Appl Phys*, vol. 113, no. 21, p. 214509, Jun. 2013, doi: 10.1063/1.4809285.
- [128] J. Li, Z. Sun, and F. Yan, "Solution Processable Low-Voltage Organic Thin Film Transistors with High-k Relaxor Ferroelectric Polymer as Gate Insulator," *Advanced Materials*, vol. 24, no. 1, pp. 88–93, Jan. 2012, doi: 10.1002/ADMA.201103542.
- [129] J. Sannigrahi, D. Bhadra, and B. K. Chaudhuri, "Crystalline graphite oxide/PVDF nanocomposite gate dielectric: Low-voltage and high field effect mobility thin-film transistor," *physica status solidi (a)*, vol. 210, no. 3, pp. 546–552, Mar. 2013, doi: 10.1002/PSSA.201228661.
- [130] J. Jang *et al.*, "Fully Inkjet-Printed Transparent Oxide Thin Film Transistors Using a Fugitive Wettability Switch," *Adv Electron Mater*, vol. 1, no. 7, p. 1500086, Jul. 2015, doi: 10.1002/AELM.201500086.
- [131] M. Esro, G. Vourlias, C. Somerton, W. I. Milne, and G. Adamopoulos, "High-Mobility ZnO Thin Film Transistors Based on Solution-processed Hafnium Oxide Gate Dielectrics," *Adv Funct Mater*, vol. 25, no. 1, pp. 134–141, Jan. 2015, doi: 10.1002/ADFM.201402684.
- [132] X. Wu, F. Fei, Z. Chen, W. Su, and Z. Cui, "A new nanocomposite dielectric ink and its application in printed thin-film transistors," *Compos Sci Technol*, vol. 94, pp. 117–122, Apr. 2014, doi: 10.1016/J.COMPSCITECH.2014.01.024.
- [133] A. S. Paramane and K. S. Kumar, "A Review on Nanocomposite Based Electrical Insulations," *Transactions on Electrical and Electronic Materials*, vol. 17, no. 5, pp. 239–251, Oct. 2016, doi: 10.4313/TEEM.2016.17.5.239.
- [134] F. C. Chen, C. W. Chu, J. He, Y. Yang, and J. L. Lin, "Organic thin-film transistors with nanocomposite dielectric gate insulator," *Appl Phys Lett*, vol. 85, no. 15, p. 3295, Oct. 2004, doi: 10.1063/1.1806283.
- [135] W. Wu, "Inorganic nanomaterials for printed electronics: a review," *Nanoscale*, vol. 9, no. 22, pp. 7342–7372, Jun. 2017, doi: 10.1039/C7NR01604B.
- [136] X. Wu, F. Fei, Z. Chen, W. Su, and Z. Cui, "A new nanocomposite dielectric ink and its application in printed thin-film transistors," *Compos Sci Technol*, vol. 94, pp. 117–122, Apr. 2014, doi: 10.1016/J.COMPSCITECH.2014.01.024.
- [137] R. Gupta, B. Badel, P. Gupta, D. G. Bucknall, D. Flynn, and K. Pancholi, "Flexible Low-Density Polyethylene-BaTiO₃Nanoparticle Composites for Monitoring Leakage Current in High-Tension Equipment," *ACS Appl Nano Mater*, vol. 4, no. 3, pp. 2413–2422, Mar. 2021, doi: 10.1021/ACSANM.0C02719.
- [138] P. Kim *et al.*, "High energy density nanocomposites based on surface-modified BaTiO₃ and a ferroelectric polymer," *ACS Nano*, vol. 3, no. 9, pp. 2581–2592, Sep. 2009, doi: 10.1021/NN9006412.

-
- [139] M. Z. Saleem and M. Akbar, "Review of the Performance of High-Voltage Composite Insulators," *Polymers* 2022, Vol. 14, Page 431, vol. 14, no. 3, p. 431, Jan. 2022, doi: 10.3390/POLYM14030431.
- [140] A. Marras, I. de Munari, D. Vescovi, and P. Ciampolini, "Impact of gate-leakage currents on CMOS circuit performance," *Microelectronics Reliability*, vol. 45, no. 3–4, pp. 499–506, Mar. 2005, doi: 10.1016/J.MICROREL.2004.09.006.
- [141] K. H. Lee, S. Zhang, T. P. Lodge, and C. D. Frisbie, "Electrical impedance of spin-coatable ion gel films," *Journal of Physical Chemistry B*, vol. 115, no. 13, pp. 3315–3321, Apr. 2011, doi: 10.1021/JP110166U.
- [142] S. Hyun Kim *et al.*, "Electrolyte-Gated Transistors for Organic and Printed Electronics," *Advanced Materials*, vol. 25, no. 13, pp. 1822–1846, Apr. 2013, doi: 10.1002/ADMA.201202790.
- [143] M. J. Panzer and C. D. Frisbie, "High Carrier Density and Metallic Conductivity in Poly(3-hexylthiophene) Achieved by Electrostatic Charge Injection," *Adv Funct Mater*, vol. 16, no. 8, pp. 1051–1056, May 2006, doi: 10.1002/ADFM.200600111.
- [144] H. Feng, X. Lu, W. Wang, N. G. Kang, and J. W. Mays, "Block Copolymers: Synthesis, Self-Assembly, and Applications," *Polymers* 2017, Vol. 9, Page 494, vol. 9, no. 10, p. 494, Oct. 2017, doi: 10.3390/POLYM9100494.
- [145] E. Quartarone, P. Mustarelli, and A. Magistris, "PEO-based composite polymer electrolytes," *Solid State Ion*, vol. 110, no. 1–2, pp. 1–14, Jul. 1998, doi: 10.1016/S0167-2738(98)00114-3.
- [146] L. M. Dumitru, K. Manoli, M. Magliulo, L. Sabbatini, G. Palazzo, and L. Torsi, "Plain poly(acrylic acid) gated organic field-effect transistors on a flexible substrate," *ACS Appl Mater Interfaces*, vol. 5, no. 21, pp. 10819–10823, Nov. 2013, doi: 10.1021/AM403008B.
- [147] S. Rahi, V. Raghuvanshi, P. Saxena, G. Konwar, and S. P. Tiwari, "High Performance Flexible Transistors With Polyelectrolyte/Polymer Bilayer Dielectric," *IEEE Trans Electron Devices*, vol. 69, no. 4, pp. 2002–2008, Apr. 2022, doi: 10.1109/TED.2022.3148700.
- [148] T. Fujimoto and K. Awaga, "Electric-double-layer field-effect transistors with ionic liquids," *Physical Chemistry Chemical Physics*, vol. 15, no. 23, pp. 8983–9006, May 2013, doi: 10.1039/C3CP50755F.
- [149] S. M. Sze and K. K. Ng, *Physics of Semiconductor Devices*. John Wiley & Sons, Inc., 2006. doi: 10.1002/0470068329.
- [150] C. Vahlas, B. Caussat, P. Serp, and G. N. Angelopoulos, "Principles and applications of CVD powder technology," *Materials Science and Engineering: R: Reports*, vol. 53, no. 1–2, pp. 1–72, Jul. 2006, doi: 10.1016/J.MSER.2006.05.001.
- [151] S. Niesar *et al.*, "Defect reduction in silicon nanoparticles by low-temperature vacuum annealing," *Appl Phys Lett*, vol. 96, no. 19, p. 193112, May 2010, doi: 10.1063/1.3428359.
- [152] E. Drahi *et al.*, "Recovering Functional Properties of Solution Processed Silicon Thin-Films," *Energy Procedia*, vol. 10, pp. 144–148, Jan. 2011, doi: 10.1016/J.EGYPRO.2011.10.167.
- [153] J. Wem Lee *et al.*, "Fabrication and characterization of entirely inkjet-printed polysilicon thin film transistors," *Flexible and Printed Electronics*, vol. 6, no. 1, p. 015001, Jan. 2021, doi: 10.1088/2058-8585/ABD29E.

- [154] T. Masuda *et al.*, "Inkjet Printing of Liquid Silicon," *Macromol Rapid Commun*, vol. 41, no. 23, p. 2000362, Dec. 2020, doi: 10.1002/MARC.202000362.
- [155] K. Nomura, H. Ohta, K. Ueda, T. Kamiya, M. Hirano, and H. Hosono, "Thin-film transistor fabricated in single-crystalline transparent oxide semiconductor," *Science (1979)*, vol. 300, no. 5623, pp. 1269–1272, May 2003, doi: 10.1126/SCIENCE.1083212.
- [156] Antonio. Facchetti and T. J. Marks, Eds., *Transparent electronics: from synthesis to applications*. Wiley, 2010. Accessed: Aug. 30, 2022. ISBN: 978-0-470-71059-3.
- [157] S. K. Garlapati *et al.*, "Ink-Jet Printed CMOS Electronics from Oxide Semiconductors," *Small*, vol. 11, no. 29, pp. 3591–3596, Aug. 2015, doi: 10.1002/SMLL.201403288.
- [158] L. Petti *et al.*, "Metal oxide semiconductor thin-film transistors for flexible electronics," *Appl Phys Rev*, vol. 3, no. 2, p. 021303, Jun. 2016, doi: 10.1063/1.4953034.
- [159] H. Hosono, "Recent progress in transparent oxide semiconductors: Materials and device application," *Thin Solid Films*, vol. 515, no. 15, pp. 6000–6014, May 2007, doi: 10.1016/J.TSF.2006.12.125.
- [160] J. Leppäniemi, K. Eiroma, H. Majumdar, and A. Alastalo, "Far-UV Annealed Inkjet-Printed In₂O₃ Semiconductor Layers for Thin-Film Transistors on a Flexible Polyethylene Naphthalate Substrate," *ACS Appl Mater Interfaces*, vol. 9, no. 10, pp. 8774–8782, Mar. 2017, doi: 10.1021/ACSAMI.6B14654.
- [161] J. Perelaer *et al.*, "Printed electronics: the challenges involved in printing devices, interconnects, and contacts based on inorganic materials," *J Mater Chem*, vol. 20, no. 39, pp. 8446–8453, Sep. 2010, doi: 10.1039/C0JM00264J.
- [162] W. J. Scheideler *et al.*, "Low-Temperature-Processed Printed Metal Oxide Transistors Based on Pure Aqueous Inks," *Adv Funct Mater*, vol. 27, no. 14, p. 1606062, Apr. 2017, doi: 10.1002/ADFM.201606062.
- [163] J. Woo Park, B. Ha Kang, H. Jae Kim, J. W. Park, B. H. Kang, and H. J. Kim, "A Review of Low-Temperature Solution-Processed Metal Oxide Thin-Film Transistors for Flexible Electronics," *Adv Funct Mater*, vol. 30, no. 20, p. 1904632, May 2020, doi: 10.1002/ADFM.201904632.
- [164] A. S. Dahiya, D. Shakthivel, Y. Kumaresan, A. Zumeit, A. Christou, and R. Dahiya, "High-performance printed electronics based on inorganic semiconducting nano to chip scale structures," *Nano Convergence 2020 7:1*, vol. 7, no. 1, pp. 1–25, Oct. 2020, doi: 10.1186/S40580-020-00243-6.
- [165] S. K. Garlapati *et al.*, "Electrolyte-gated, high mobility inorganic oxide transistors from printed metal halides," *ACS Appl Mater Interfaces*, vol. 5, no. 22, pp. 11498–11502, Nov. 2013, doi: 10.1021/AM403131J.
- [166] X. Du, R. T. Frederick, Y. Li, Z. Zhou, W. F. Stickle, and G. S. Herman, "Amorphous In-Ga-Zn-O thin-film transistors fabricated by microcontact printing," *Journal of Vacuum Science & Technology B, Nanotechnology and Microelectronics: Materials, Processing, Measurement, and Phenomena*, vol. 33, no. 5, p. 052208, Sep. 2015, doi: 10.1116/1.4929984.
- [167] Z. Liu *et al.*, "Contact printing of horizontally aligned Zn₂GeO₄ and In₂Ge₂O₇ nanowire arrays for multi-channel field-effect transistors and their photoresponse performances," *J Mater Chem C Mater*, vol. 1, no. 1, pp. 131–137, Nov. 2012, doi: 10.1039/C2TC00055E.

-
- [168] G. Chen *et al.*, "Single-Crystalline p-Type Zn₃As₂ Nanowires for Field-Effect Transistors and Visible-Light Photodetectors on Rigid and Flexible Substrates," *Adv Funct Mater*, vol. 23, no. 21, pp. 2681–2690, Jun. 2013, doi: 10.1002/ADFM.201202739.
- [169] J. Yu, G. Liu, A. Liu, Y. Meng, B. Shin, and F. Shan, "Solution-processed p-type copper oxide thin-film transistors fabricated by using a one-step vacuum annealing technique," *J Mater Chem C Mater*, vol. 3, no. 37, pp. 9509–9513, Sep. 2015, doi: 10.1039/C5TC02384J.
- [170] A. Liu *et al.*, "Solution Combustion Synthesis: Low-Temperature Processing for p-Type Cu:NiO Thin Films for Transparent Electronics," *Advanced Materials*, vol. 29, no. 34, p. 1701599, Sep. 2017, doi: 10.1002/ADMA.201701599.
- [171] A. Liu *et al.*, "Hole mobility modulation of solution-processed nickel oxide thin-film transistor based on high-k dielectric," *Appl Phys Lett*, vol. 108, no. 23, p. 233506, Jun. 2016, doi: 10.1063/1.4953460.
- [172] F. Y. Gan and I. Shih, "Preparation of thin-film transistors with chemical bath deposited CdSe and CdS thin films," *IEEE Trans Electron Devices*, vol. 49, no. 1, pp. 15–18, 2002, doi: 10.1109/16.974742.
- [173] B. Walker *et al.*, "Solution-processed CdS transistors with high electron mobility," *RSC Adv*, vol. 4, no. 7, pp. 3153–3157, Dec. 2013, doi: 10.1039/C3RA44436H.
- [174] T. Carey *et al.*, "Inkjet Printed Circuits with 2D Semiconductor Inks for High-Performance Electronics," *Adv Electron Mater*, vol. 7, no. 7, p. 2100112, Jul. 2021, doi: 10.1002/AELM.202100112.
- [175] D. v. Talapin and C. B. Murray, "PbSe nanocrystal solids for n- and p-channel thin film field-effect transistors," *Science (1979)*, vol. 310, no. 5745, pp. 86–89, Oct. 2005, doi: 10.1126/SCIENCE.1116703.
- [176] H. J. Yun, J. Lim, J. Roh, D. C. J. Neo, M. Law, and V. I. Klimov, "Solution-processable integrated CMOS circuits based on colloidal CuInSe₂ quantum dots," *Nature Communications 2020 11:1*, vol. 11, no. 1, pp. 1–10, Oct. 2020, doi: 10.1038/s41467-020-18932-5.
- [177] F. Hetsch, N. Zhao, S. v. Kershaw, and A. L. Rogach, "Quantum dot field effect transistors," *Materials Today*, vol. 16, no. 9, pp. 312–325, Sep. 2013, doi: 10.1016/J.MATTOD.2013.08.011.
- [178] S. Lu and A. D. Franklin, "Printed carbon nanotube thin-film transistors: progress on printable materials and the path to applications," *Nanoscale*, vol. 12, no. 46, pp. 23371–23390, Dec. 2020, doi: 10.1039/D0NR06231F.
- [179] Y. Lee *et al.*, "Semiconducting carbon nanotube network thin-film transistors with enhanced inkjet-printed source and drain contact interfaces," *Appl Phys Lett*, vol. 111, no. 17, p. 173108, Oct. 2017, doi: 10.1063/1.5009656.
- [180] C. Pintossi and L. Sangaletti, *Semiconducting Carbon Nanotubes: Properties, Characterization and Selected Applications*. Springer, Cham, 2016. doi: 10.1007/978-3-319-25340-4_10.
- [181] A. Kamyshny and S. Magdassi, "Conductive Nanomaterials for Printed Electronics," *Small*, vol. 10, no. 17, pp. 3515–3535, Sep. 2014, doi: 10.1002/SMLL.201303000.
- [182] H. Matsui, Y. Takeda, and S. Tokito, "Flexible and printed organic transistors: From materials to integrated circuits," *Org Electron*, vol. 75, p. 105432, Dec. 2019, doi: 10.1016/J.ORGEL.2019.105432.

- [183] M. T. Greiner and Z. H. Lu, "Thin-film metal oxides in organic semiconductor devices: their electronic structures, work functions and interfaces," *NPG Asia Materials* 2013 5:7, vol. 5, no. 7, pp. e55–e55, Jul. 2013, doi: 10.1038/am.2013.29.
- [184] W. Brütting, Ed., *Physics of Organic Semiconductors*. John Wiley and Sons, 2006. doi: 10.1002/3527606637.
- [185] V. Coropceanu, J. Cornil, D. A. da Silva Filho, Y. Olivier, R. Silbey, and J. L. Brédas, "Charge transport in organic semiconductors," *Chem Rev*, vol. 107, no. 4, pp. 926–952, Apr. 2007, doi: 10.1021/CR050140X.
- [186] C. G. Zhan, J. A. Nichols, and D. A. Dixon, "Ionization potential, electron affinity, electronegativity, hardness, and electron excitation energy: Molecular properties from density functional theory orbital energies," *Journal of Physical Chemistry A*, vol. 107, no. 20, pp. 4184–4195, May 2003, doi: 10.1021/JP0225774.
- [187] S. Kola, J. Sinha, and H. E. Katz, "Organic transistors in the new decade: Toward n-channel, printed, and stabilized devices," *J Polym Sci B Polym Phys*, vol. 50, no. 15, pp. 1090–1120, Aug. 2012, doi: 10.1002/POLB.23054.
- [188] K. Liu, B. Ouyang, X. Guo, Y. Guo, and Y. Liu, "Advances in flexible organic field-effect transistors and their applications for flexible electronics," *npj Flexible Electronics* 2022 6:1, vol. 6, no. 1, pp. 1–19, Jan. 2022, doi: 10.1038/s41528-022-00133-3.
- [189] X. Zhan *et al.*, "Rylene and Related Diimides for Organic Electronics," *Advanced Materials*, vol. 23, no. 2, pp. 268–284, Jan. 2011, doi: 10.1002/ADMA.201001402.
- [190] S. Griggs, A. Marks, H. Bristow, and I. McCulloch, "n-Type organic semiconducting polymers: stability limitations, design considerations and applications," *J Mater Chem C Mater*, vol. 9, no. 26, pp. 8099–8128, Jul. 2021, doi: 10.1039/D1TC02048J.
- [191] W. Tang *et al.*, "Recent progress in printable organic field effect transistors," *J Mater Chem C Mater*, vol. 7, no. 4, pp. 790–808, Jan. 2019, doi: 10.1039/C8TC05485A.
- [192] H. Minemawari *et al.*, "Inkjet printing of single-crystal films," *Nature* 2011 475:7356, vol. 475, no. 7356, pp. 364–367, Jul. 2011, doi: 10.1038/nature10313.
- [193] J. Li *et al.*, "A stable solution-processed polymer semiconductor with record high-mobility for printed transistors," *Scientific Reports* 2012 2:1, vol. 2, no. 1, pp. 1–9, Oct. 2012, doi: 10.1038/srep00754.
- [194] H.-R. Tseng *et al.*, "High-Mobility Field-Effect Transistors Fabricated with Macroscopic Aligned Semiconducting Polymers," *Advanced Materials*, vol. 26, no. 19, pp. 2993–2998, May 2014, doi: 10.1002/ADMA.201305084.
- [195] M. Chu *et al.*, "Halogenated Tetraazapentacenes with Electron Mobility as High as 27.8 cm² V⁻¹ s⁻¹ in Solution-Processed n-Channel Organic Thin-Film Transistors," *Advanced Materials*, vol. 30, no. 38, p. 1803467, Sep. 2018, doi: 10.1002/ADMA.201803467.
- [196] J. H. Dou *et al.*, "Fine-Tuning of Crystal Packing and Charge Transport Properties of BDOPV Derivatives through Fluorine Substitution," *J Am Chem Soc*, vol. 137, no. 50, pp. 15947–15956, Dec. 2015, doi: 10.1021/JACS.5B11114.

-
- [197] Q. Huang and Y. Zhu, "Printing Conductive Nanomaterials for Flexible and Stretchable Electronics: A Review of Materials, Processes, and Applications," *Adv Mater Technol*, vol. 4, no. 5, p. 1800546, May 2019, doi: 10.1002/ADMT.201800546.
- [198] X. Wang, M. Jiang, Z. Zhou, J. Gou, and D. Hui, "3D printing of polymer matrix composites: A review and prospective," *Compos B Eng*, vol. 110, pp. 442–458, Feb. 2017, doi: 10.1016/J.COMPOSITESB.2016.11.034.
- [199] N. Ibrahim, J. O. Akindoyo, and M. Mariatti, "Recent development in silver-based ink for flexible electronics," *Journal of Science: Advanced Materials and Devices*, vol. 7, no. 1, p. 100395, Mar. 2022, doi: 10.1016/J.JSAMD.2021.09.002.
- [200] V. Abhinav K, V. K. Rao R, P. S. Karthik, and S. P. Singh, "Copper conductive inks: synthesis and utilization in flexible electronics," *RSC Adv*, vol. 5, no. 79, pp. 63985–64030, Jul. 2015, doi: 10.1039/C5RA08205F.
- [201] S. Magdassi, M. Grouchko, and A. Kamyshny, "Copper Nanoparticles for Printed Electronics: Routes Towards Achieving Oxidation Stability," *Materials 2010, Vol. 3, Pages 4626-4638*, vol. 3, no. 9, pp. 4626–4638, Sep. 2010, doi: 10.3390/MA3094626.
- [202] D. Li, D. Sutton, A. Burgess, D. Graham, and P. D. Calvert, "Conductive copper and nickel lines via reactive inkjet printing," *J Mater Chem*, vol. 19, no. 22, pp. 3719–3724, Jun. 2009, doi: 10.1039/B820459D.
- [203] D. Adner, F. M. Wolf, S. Möckel, J. Perelaer, U. S. Schubert, and H. Lang, "Copper(II) ethylene glycol carboxylates as precursors for inkjet printing of conductive copper patterns," *Thin Solid Films*, vol. 565, pp. 143–148, Aug. 2014, doi: 10.1016/J.TSF.2014.06.054.
- [204] W. Cui, W. Lu, Y. Zhang, G. Lin, T. Wei, and L. Jiang, "Gold nanoparticle ink suitable for electric-conductive pattern fabrication using in ink-jet printing technology," *Colloids Surf A Physicochem Eng Asp*, vol. 358, no. 1–3, pp. 35–41, Apr. 2010, doi: 10.1016/J.COLSURFA.2010.01.023.
- [205] H. Hong, J. Hu, and X. Yan, "UV Curable Conductive Ink for the Fabrication of Textile-Based Conductive Circuits and Wearable UHF RFID Tags," *ACS Appl Mater Interfaces*, vol. 11, no. 30, pp. 27318–27326, Jul. 2019, doi: 10.1021/ACSAMI.9B06432.
- [206] K. Pan *et al.*, "Sustainable production of highly conductive multilayer graphene ink for wireless connectivity and IoT applications," *Nature Communications 2018 9:1*, vol. 9, no. 1, pp. 1–10, Dec. 2018, doi: 10.1038/s41467-018-07632-w.
- [207] G. C. Pidcock and M. in het Panhuis, "Extrusion Printing of Flexible Electrically Conducting Carbon Nanotube Networks," *Adv Funct Mater*, vol. 22, no. 22, pp. 4790–4800, Nov. 2012, doi: 10.1002/ADFM.201200724.
- [208] T. Horii, Y. Li, Y. Mori, and H. Okuzaki, "Correlation between the hierarchical structure and electrical conductivity of PEDOT/PSS," *Polymer Journal 2015 47:10*, vol. 47, no. 10, pp. 695–699, Jul. 2015, doi: 10.1038/pj.2015.48.
- [209] N. Kim *et al.*, "Highly Conductive PEDOT:PSS Nanofibrils Induced by Solution-Processed Crystallization," *Advanced Materials*, vol. 26, no. 14, pp. 2268–2272, Apr. 2014, doi: 10.1002/ADMA.201304611.
- [210] W. Yang, E. J. W. List-Kratochvil, and C. Wang, "Metal particle-free inks for printed flexible electronics," *J Mater Chem C Mater*, vol. 7, no. 48, pp. 15098–15117, Dec. 2019, doi: 10.1039/C9TC05463D.

- [211] Shlomo. Magdassi and Alexander. Kamyshny, Eds., *Nanomaterials for 2D and 3D Printing*. John Wiley & Sons, Incorporated, 2017, ISBN: 978-3-527-33819-1.
- [212] S. Park, M. Vosguerichian, and Z. Bao, "A review of fabrication and applications of carbon nanotube film-based flexible electronics," *Nanoscale*, vol. 5, no. 5, pp. 1727–1752, Feb. 2013, doi: 10.1039/C3NR33560G.
- [213] D. S. Hecht, L. Hu, and G. Irvin, "Emerging Transparent Electrodes Based on Thin Films of Carbon Nanotubes, Graphene, and Metallic Nanostructures," *Advanced Materials*, vol. 23, no. 13, pp. 1482–1513, Apr. 2011, doi: 10.1002/ADMA.201003188.
- [214] Y. Z. N. Htwe and M. Mariatti, "Printed graphene and hybrid conductive inks for flexible, stretchable, and wearable electronics: Progress, opportunities, and challenges," *Journal of Science: Advanced Materials and Devices*, vol. 7, no. 2, p. 100435, Jun. 2022, doi: 10.1016/J.JSAMD.2022.100435.
- [215] L. Pei and Y. F. Li, "Rapid and efficient intense pulsed light reduction of graphene oxide inks for flexible printed electronics," *RSC Adv*, vol. 7, no. 81, pp. 51711–51720, Nov. 2017, doi: 10.1039/C7RA10416B.
- [216] F. Torrisi *et al.*, "Inkjet-printed graphene electronics," *ACS Nano*, vol. 6, no. 4, pp. 2992–3006, Apr. 2012, doi: 10.1021/NN2044609.
- [217] C. O'Mahony, E. Ul Haq, C. Sillien, and S. A. M. Tofail, "Rheological Issues in Carbon-Based Inks for Additive Manufacturing," *Micromachines 2019, Vol. 10, Page 99*, vol. 10, no. 2, p. 99, Jan. 2019, doi: 10.3390/MI10020099.
- [218] J. Song and H. Zeng, "Transparent Electrodes Printed with Nanocrystal Inks for Flexible Smart Devices," *Angewandte Chemie International Edition*, vol. 54, no. 34, pp. 9760–9774, Aug. 2015, doi: 10.1002/ANIE.201501233.
- [219] A. Kamyshny and S. Magdassi, "Conductive nanomaterials for 2D and 3D printed flexible electronics," *Chem Soc Rev*, vol. 48, no. 6, pp. 1712–1740, Mar. 2019, doi: 10.1039/C8CS00738A.
- [220] C. Cano-Raya, Z. Z. Denchev, S. F. Cruz, and J. C. Viana, "Chemistry of solid metal-based inks and pastes for printed electronics – A review," *Appl Mater Today*, vol. 15, pp. 416–430, Jun. 2019, doi: 10.1016/J.APMT.2019.02.012.
- [221] K. Namsheer and C. S. Rout, "Conducting polymers: a comprehensive review on recent advances in synthesis, properties and applications," *RSC Adv*, vol. 11, no. 10, pp. 5659–5697, Jan. 2021, doi: 10.1039/D0RA07800J.
- [222] M. N. Gueye, A. Carella, J. Faure-Vincent, R. Demadrille, and J. P. Simonato, "Progress in understanding structure and transport properties of PEDOT-based materials: A critical review," *Prog Mater Sci*, vol. 108, p. 100616, Feb. 2020, doi: 10.1016/J.PMATSCI.2019.100616.
- [223] E. M. Thomas, P. H. Nguyen, S. D. Jones, M. L. Chabiny, and R. A. Segalman, "Electronic, Ionic, and Mixed Conduction in Polymeric Systems," <https://doi.org/10.1146/annurev-matsci-080619-110405>, vol. 51, pp. 1–20, Jul. 2021, doi: 10.1146/ANNUREV-MATSCI-080619-110405.
- [224] R. Balint, N. J. Cassidy, and S. H. Cartmell, "Conductive polymers: Towards a smart biomaterial for tissue engineering," *Acta Biomater*, vol. 10, no. 6, pp. 2341–2353, Jun. 2014, doi: 10.1016/J.ACTBIO.2014.02.015.
- [225] L. Groenendaal, F. Jonas, D. Freitag, H. Pielartzik, and J. R. Reynolds, "Poly(3,4-ethylenedioxythiophene) and Its Derivatives: Past, Present, and Future**", doi: 10.1002/(SICI)1521-4095(200004)12:7.

-
- [226] X. Zhang, W. Yang, H. Zhang, M. Xie, and X. Duan, "PEDOT:PSS: From conductive polymers to sensors," *Nanotechnology and Precision Engineering*, vol. 4, no. 4, p. 045004, Nov. 2021, doi: 10.1063/10.0006866.
- [227] J. Y. Kim, J. H. Jung, D. E. Lee, and J. Joo, "Enhancement of electrical conductivity of poly(3,4-ethylenedioxythiophene)/poly(4-styrenesulfonate) by a change of solvents," *Synth Met*, vol. 126, no. 2–3, pp. 311–316, Feb. 2002, doi: 10.1016/S0379-6779(01)00576-8.
- [228] J. Ouyang, "'Secondary doping' methods to significantly enhance the conductivity of PEDOT:PSS for its application as transparent electrode of optoelectronic devices," *Displays*, vol. 34, no. 5, pp. 423–436, Dec. 2013, doi: 10.1016/J.DISPLA.2013.08.007.
- [229] Z. Li *et al.*, "A nonionic surfactant simultaneously enhancing wetting property and electrical conductivity of PEDOT:PSS for vacuum-free organic solar cells," *Solar Energy Materials and Solar Cells*, vol. 137, pp. 311–318, Jun. 2015, doi: 10.1016/J.SOLMAT.2015.02.024.
- [230] D. Amoabeng and S. S. Velankar, "A review of conductive polymer composites filled with low melting point metal alloys," *Polym Eng Sci*, vol. 58, no. 6, pp. 1010–1019, Jun. 2018, doi: 10.1002/PEN.24774.
- [231] D. Pejak Simunec and A. Sola, "Emerging Research in Conductive Materials for Fused Filament Fabrication: A Critical Review," *Adv Eng Mater*, vol. 24, no. 7, p. 2101476, Jul. 2022, doi: 10.1002/ADEM.202101476.
- [232] D. Li *et al.*, "Printable Transparent Conductive Films for Flexible Electronics," *Advanced Materials*, vol. 30, no. 10, p. 1704738, Mar. 2018, doi: 10.1002/ADMA.201704738.
- [233] J. Lemarchand *et al.*, "Challenges, Prospects, and Emerging Applications of Inkjet-Printed Electronics: A Chemist's Point of View," *Angewandte Chemie International Edition*, vol. 61, no. 20, p. e202200166, May 2022, doi: 10.1002/ANIE.202200166.
- [234] C. G. Jothi Prakash and R. Prasanth, "Approaches to design a surface with tunable wettability: a review on surface properties," *Journal of Materials Science 2020 56:1*, vol. 56, no. 1, pp. 108–135, Sep. 2020, doi: 10.1007/S10853-020-05116-1.
- [235] Y. Aleeva and B. Pignataro, "Recent advances in upscalable wet methods and ink formulations for printed electronics," *J Mater Chem C Mater*, vol. 2, no. 32, pp. 6436–6453, Jul. 2014, doi: 10.1039/C4TC00618F.
- [236] K. Yvon and N. Fabrice, Eds., *Printed Electronics: Technologies, Applications and Challenges – Nova Science Publishers*. 2017, ISBN: 978-1-53612-797-3.
- [237] D. J. Lee, S. H. Park, S. Jang, H. S. Kim, J. H. Oh, and Y. W. Song, "Pulsed light sintering characteristics of inkjet-printed nanosilver films on a polymer substrate," *Journal of Micromechanics and Microengineering*, vol. 21, no. 12, p. 125023, Nov. 2011, doi: 10.1088/0960-1317/21/12/125023.
- [238] R. German, *Sintering: From Empirical Observations to Scientific Principles*. Elsevier Inc., 2014. doi: 10.1016/C2012-0-00717-X.
- [239] I. Reinhold *et al.*, "Argon plasma sintering of inkjet printed silver tracks on polymer substrates," *J Mater Chem*, vol. 19, no. 21, pp. 3384–3388, May 2009, doi: 10.1039/B823329B.
- [240] J. Perelaer, R. Jani, M. Grouchko, A. Kamyshny, S. Magdassi, and U. S. Schubert, "Plasma and Microwave Flash Sintering of a Tailored Silver

- Nanoparticle Ink, Yielding 60% Bulk Conductivity on Cost-Effective Polymer Foils," *Advanced Materials*, vol. 24, no. 29, pp. 3993–3998, Aug. 2012, doi: 10.1002/ADMA.201200899.
- [241] E. Saleh *et al.*, "3D Inkjet Printing of Electronics Using UV Conversion," *Adv Mater Technol*, vol. 2, no. 10, p. 1700134, Oct. 2017, doi: 10.1002/ADMT.201700134.
- [242] C. van Nesselroy, C. Shen, T. Zambelli, and D. Momotenko, "Electrochemical 3D printing of silver and nickel microstructures with FluidFM," *Addit Manuf*, vol. 53, p. 102718, May 2022, doi: 10.1016/J.ADDMA.2022.102718.
- [243] X. Chen *et al.*, "A Low Cost Desktop Electrochemical Metal 3D Printer," *Adv Mater Technol*, vol. 2, no. 10, p. 1700148, Oct. 2017, doi: 10.1002/ADMT.201700148.
- [244] L. Hirt *et al.*, "Template-Free 3D Microprinting of Metals Using a Force-Controlled Nanopipette for Layer-by-Layer Electrodeposition," *Advanced Materials*, vol. 28, no. 12, pp. 2311–2315, Mar. 2016, doi: 10.1002/ADMA.201504967.
- [245] S. C. Ligon, R. Liska, J. Stampfl, M. Gurr, and R. Mülhaupt, "Polymers for 3D Printing and Customized Additive Manufacturing," *Chem Rev*, vol. 117, no. 15, pp. 10212–10290, Aug. 2017, doi: 10.1021/ACS.CHEMREV.7B00074.
- [246] M. Rafiee, R. D. Farahani, and D. Therriault, "Multi-Material 3D and 4D Printing: A Survey," *Advanced Science*, vol. 7, no. 12, p. 1902307, Jun. 2020, doi: 10.1002/ADVS.201902307.
- [247] H. Y. Jeong, E. Lee, S. C. An, Y. Lim, and Y. C. Jun, "3D and 4D printing for optics and metaphotonics," *Nanophotonics*, vol. 9, no. 5, pp. 1139–1160, May 2020, doi: 10.1515/NANOPH-2019-0483.
- [248] H. W. Tan, Y. Y. C. Choong, C. N. Kuo, H. Y. Low, and C. K. Chua, "3D printed electronics: Processes, materials and future trends," *Prog Mater Sci*, vol. 127, p. 100945, Jun. 2022, doi: 10.1016/J.PMATSCI.2022.100945.
- [249] D. v. Baker, C. Bao, and W. S. Kim, "Highly Conductive 3D Printable Materials for 3D Structural Electronics," *ACS Appl Electron Mater*, vol. 3, no. 6, pp. 2423–2433, Jun. 2021, doi: 10.1021/ACSAELM.1C00296.
- [250] C. K. Chua, W. Y. Yeong, H. Y. Low, T. Tran, and H. W. Tan, *3D printing and additive manufacturing of electronics: Principles and applications*, vol. 3. World Scientific Publishing Co., 2021. doi: 10.1142/11773.
- [251] M. D. Dickey, R. C. Chiechi, R. J. Larsen, E. A. Weiss, D. A. Weitz, and G. M. Whitesides, "Eutectic Gallium-Indium (EGaIn): A Liquid Metal Alloy for the Formation of Stable Structures in Microchannels at Room Temperature," *Adv Funct Mater*, vol. 18, no. 7, pp. 1097–1104, Apr. 2008, doi: 10.1002/ADFM.200701216.
- [252] S. A. Ozkan and B. Uslu, "From mercury to nanosensors: Past, present and the future perspective of electrochemistry in pharmaceutical and biomedical analysis," *J Pharm Biomed Anal*, vol. 130, pp. 126–140, Oct. 2016, doi: 10.1016/J.JPBA.2016.05.006.
- [253] K. Khoshmanesh *et al.*, "Liquid metal enabled microfluidics," *Lab Chip*, vol. 17, no. 6, pp. 974–993, Mar. 2017, doi: 10.1039/C7LC00046D.
- [254] J. A. Rogers, T. Someya, and Y. Huang, "Materials and mechanics for stretchable electronics," *Science (1979)*, vol. 327, no. 5973, pp. 1603–1607, Mar. 2010, doi: 10.1126/SCIENCE.1182383.

-
- [255] O. Parlak, A. Salleo, and A. Turner, Eds, *Wearable bioelectronics*, ISBN: 9780081024089.
- [256] T. Liu, P. Sen, and C. J. Kim, "Characterization of liquid-metal Galinstan® for droplet applications," *Proceedings of the IEEE International Conference on Micro Electro Mechanical Systems (MEMS)*, pp. 560–563, 2010, doi: 10.1109/MEMSYS.2010.5442440.
- [257] Y. Sohn and K. Chu, "Flexible hybrid conductor comprising eutectic Ga-In liquid metal and Ag nanowires for the application of electronic skin," *Mater Lett*, vol. 265, p. 127223, Apr. 2020, doi: 10.1016/J.MATLET.2019.127223.
- [258] Y. G. Park, H. Kim, S. Y. Park, J. Y. Kim, and J. U. Park, "Instantaneous and Repeatable Self-Healing of Fully Metallic Electrodes at Ambient Conditions," *ACS Appl Mater Interfaces*, vol. 11, no. 44, pp. 41497–41505, Nov. 2019, doi: 10.1021/ACSAMI.9B12417.
- [259] R. Guo *et al.*, "Magnetic Liquid Metal (Fe-EGaIn) Based Multifunctional Electronics for Remote Self-Healing Materials, Degradable Electronics, and Thermal Transfer Printing," *Advanced Science*, vol. 6, no. 20, p. 1901478, Oct. 2019, doi: 10.1002/ADVS.201901478.
- [260] N. Ning *et al.*, "Highly stretchable liquid metal/polyurethane sponge conductors with excellent electrical conductivity stability and good mechanical properties," *Compos B Eng*, vol. 179, p. 107492, Dec. 2019, doi: 10.1016/J.COMPOSITESB.2019.107492.
- [261] G. Chen, H. Wang, R. Guo, M. Duan, Y. Zhang, and J. Liu, "Superelastic EGaIn Composite Fibers Sustaining 500% Tensile Strain with Superior Electrical Conductivity for Wearable Electronics," *ACS Appl Mater Interfaces*, vol. 12, no. 5, pp. 6112–6118, Feb. 2020, doi: 10.1021/ACSAMI.9B23083.
- [262] M. Ou, W. Qiu, K. Huang, H. Feng, and S. Chu, "Ultrastretchable Liquid Metal Electrical Conductors Built-in Cloth Fiber Networks for Wearable Electronics," *ACS Appl Mater Interfaces*, vol. 12, no. 6, pp. 7673–7678, Feb. 2020, doi: 10.1021/ACSAMI.9B17634.
- [263] Y. Huang, B. Yu, L. Zhang, N. Ning, and M. Tian, "Highly Stretchable Conductor by Self-Assembling and Mechanical Sintering of a 2D Liquid Metal on a 3D Polydopamine-Modified Polyurethane Sponge," *ACS Appl Mater Interfaces*, vol. 11, no. 51, pp. 48321–48330, Dec. 2019, doi: 10.1021/ACSAMI.9B15776.
- [264] Y. Peng, H. Liu, T. Li, and J. Zhang, "Hybrid Metallic Foam with Superior Elasticity, High Electrical Conductivity, and Pressure Sensitivity," *ACS Appl Mater Interfaces*, vol. 12, no. 5, pp. 6489–6495, Feb. 2020, doi: 10.1021/ACSAMI.9B20652.
- [265] M. Liao, H. Liao, J. Ye, P. Wan, and L. Zhang, "Polyvinyl Alcohol-Stabilized Liquid Metal Hydrogel for Wearable Transient Epidermal Sensors," *ACS Appl Mater Interfaces*, vol. 11, no. 50, pp. 47358–47364, Dec. 2019, doi: 10.1021/ACSAMI.9B16675.
- [266] Y. Lin, Y. Liu, J. Genzer, and M. D. Dickey, "Shape-transformable liquid metal nanoparticles in aqueous solution," *Chem Sci*, vol. 8, no. 5, pp. 3832–3837, May 2017, doi: 10.1039/C7SC00057J.
- [267] C. Chiew, M. J. Morris, and M. H. Malakooti, "Functional liquid metal nanoparticles: synthesis and applications," *Mater Adv*, vol. 2, no. 24, pp. 7799–7819, Dec. 2021, doi: 10.1039/D1MA00789K.

- [268] C. Pan *et al.*, "A Liquid-Metal-Elastomer Nanocomposite for Stretchable Dielectric Materials," *Advanced Materials*, vol. 31, no. 23, p. 1900663, Jun. 2019, doi: 10.1002/ADMA.201900663.
- [269] E. J. Markvicka, M. D. Bartlett, X. Huang, and C. Majidi, "An autonomously electrically self-healing liquid metal-elastomer composite for robust soft-matter robotics and electronics," *Nature Materials* 2018 17:7, vol. 17, no. 7, pp. 618–624, May 2018, doi: 10.1038/s41563-018-0084-7.
- [270] S. Chen, H. Z. Wang, R. Q. Zhao, W. Rao, and J. Liu, "Liquid Metal Composites," *Matter*, vol. 2, no. 6, pp. 1446–1480, Jun. 2020, doi: 10.1016/J.MATT.2020.03.016.
- [271] A. R. Jacob, D. P. Parekh, M. D. Dickey, and L. C. Hsiao, "Interfacial Rheology of Gallium-Based Liquid Metals," *Langmuir*, vol. 35, no. 36, pp. 11774–11783, Sep. 2019, doi: 10.1021/ACS.LANGMUIR.9B01821.
- [272] D. Kim *et al.*, "Recovery of nonwetting characteristics by surface modification of gallium-based liquid metal droplets using hydrochloric acid vapor," *ACS Appl Mater Interfaces*, vol. 5, no. 1, pp. 179–185, Jan. 2013, doi: 10.1021/AM302357T.
- [273] R. J. Larsen, M. D. Dickey, G. M. Whitesides, and D. A. Weitz, "Viscoelastic properties of oxide-coated liquid metals," *J Rheol (N Y N Y)*, vol. 53, no. 6, p. 1305, Jan. 2010, doi: 10.1122/1.3236517.
- [274] S. Handschuh-Wang, Y. Chen, L. Zhu, and X. Zhou, "Analysis and Transformations of Room-Temperature Liquid Metal Interfaces – A Closer Look through Interfacial Tension," *ChemPhysChem*, vol. 19, no. 13, pp. 1584–1592, Jul. 2018, doi: 10.1002/CPHC.201800129.
- [275] I. D. Joshipura *et al.*, "Are Contact Angle Measurements Useful for Oxide-Coated Liquid Metals?," *Langmuir*, vol. 37, no. 37, pp. 10914–10923, Sep. 2021, doi: 10.1021/ACS.LANGMUIR.1C01173.
- [276] K. Doudrick *et al.*, "Different shades of oxide: From nanoscale wetting mechanisms to contact printing of gallium-based liquid metals," *Langmuir*, vol. 30, no. 23, pp. 6867–6877, Jun. 2014, doi: 10.1021/LA5012023.
- [277] R. Adam Bilodeau, D. Y. Zemlyanov, R. K. Kramer, R. A. Bilodeau, R. K. Kramer, and D. Y. Zemlyanov, "Liquid Metal Switches for Environmentally Responsive Electronics," *Adv Mater Interfaces*, vol. 4, no. 5, p. 1600913, Mar. 2017, doi: 10.1002/ADMI.201600913.
- [278] S. Liu, S. N. Reed, M. J. Higgins, M. S. Titus, and R. Kramer-Bottiglio, "Oxide rupture-induced conductivity in liquid metal nanoparticles by laser and thermal sintering," *Nanoscale*, vol. 11, no. 38, pp. 17615–17629, Oct. 2019, doi: 10.1039/C9NR03903A.
- [279] Y. Khan, A. Thielens, S. Muin, J. Ting, C. Baumbauer, and A. C. Arias, "A New Frontier of Printed Electronics: Flexible Hybrid Electronics," *Advanced Materials*, vol. 32, no. 15, p. 1905279, Apr. 2020, doi: 10.1002/ADMA.201905279.
- [280] M. A. Shah, D. G. Lee, B. Y. Lee, and S. Hur, "Classifications and Applications of Inkjet Printing Technology: A Review," *IEEE Access*, vol. 9, pp. 140079–140102, 2021, doi: 10.1109/ACCESS.2021.3119219.
- [281] J. G. Edited by Korvink, P. J. Smith, and D.-Y. Shin, *Inkjet-based Micromanufacturing*. Accessed: Sep. 10, 2022, ISBN: 978-3-527-31904-6.

-
- [282] P. Calvert, "Inkjet printing for materials and devices," *Chemistry of Materials*, vol. 13, no. 10, pp. 3299–3305, 2001, doi: 10.1021/CM0101632.
- [283] E. Tekin, P. J. Smith, and U. S. Schubert, "Inkjet printing as a deposition and patterning tool for polymers and inorganic particles," *Soft Matter*, vol. 4, no. 4, pp. 703–713, Mar. 2008, doi: 10.1039/B711984D.
- [284] B. Derby, "Inkjet Printing of Functional and Structural Materials: Fluid Property Requirements, Feature Stability, and Resolution," *Annual Review of Materials Research*, vol. 40, pp. 395–414, Jul. 2010, doi: 10.1146/ANNUREV-MATSCI-070909-104502.
- [285] B. J. de Gans, P. C. Duineveld, and U. S. Schubert, "Inkjet Printing of Polymers: State of the Art and Future Developments," *Advanced Materials*, vol. 16, no. 3, pp. 203–213, Feb. 2004, doi: 10.1002/ADMA.200300385.
- [286] L. Nayak, S. Mohanty, S. K. Nayak, and A. Ramadoss, "A review on inkjet printing of nanoparticle inks for flexible electronics," *J Mater Chem C Mater*, vol. 7, no. 29, pp. 8771–8795, Jul. 2019, doi: 10.1039/C9TC01630A.
- [287] G. Cummins and M. P. Y. Desmulliez, "Inkjet printing of conductive materials: A review," *Circuit World*, vol. 38, no. 4, pp. 193–213, 2012, doi: 10.1108/03056121211280413.
- [288] D. Kim, J. H. Yoo, Y. Lee, W. Choi, K. Yoo, and J. B. J. Lee, "Gallium-based liquid metal inkjet printing," *Proceedings of the IEEE International Conference on Micro Electro Mechanical Systems (MEMS)*, pp. 967–970, 2014, doi: 10.1109/MEMSYS.2014.6765804.
- [289] G. Li, X. Wu, and D. W. Lee, "A galinstan-based inkjet printing system for highly stretchable electronics with self-healing capability," *Lab Chip*, vol. 16, no. 8, pp. 1366–1373, Apr. 2016, doi: 10.1039/C6LC00046K.
- [290] N. Lazarus, S. S. Bedair, and I. M. Kierzewski, "Ultrafine pitch stencil printing of liquid metal alloys," *ACS Appl Mater Interfaces*, vol. 9, no. 2, pp. 1178–1182, Jan. 2017, doi: 10.1021/ACSAMI.6B13088.
- [291] S. H. Jeong, A. Hagman, K. Hjort, M. Jobs, J. Sundqvist, and Z. Wu, "Liquid alloy printing of microfluidic stretchable electronics," *Lab Chip*, vol. 12, no. 22, pp. 4657–4664, Oct. 2012, doi: 10.1039/C2LC40628D.
- [292] A. G. Kelly, D. Finn, A. Harvey, T. Hallam, and J. N. Coleman, "All-printed capacitors from graphene-BN-graphene nanosheet heterostructures," *Appl Phys Lett*, vol. 109, no. 2, p. 023107, Jul. 2016, doi: 10.1063/1.4958858.
- [293] R. W. Kay, S. Stoyanov, G. P. Glinski, C. Bailey, and M. P. Y. Desmulliez, "Ultrafine pitch stencil printing for a low cost and low temperature flip-chip assembly process," *IEEE Transactions on Components and Packaging Technologies*, vol. 30, no. 1, pp. 129–136, Mar. 2007, doi: 10.1109/TCAPT.2007.892085.
- [294] R. Kay and M. Desmulliez, "A review of stencil printing for microelectronic packaging," *Soldering and Surface Mount Technology*, vol. 24, no. 1, pp. 38–50, 2012, doi: 10.1108/09540911211198540.
- [295] O. Vazquez-Mena, L. Gross, S. Xie, L. G. Villanueva, and J. Brugger, "Resistless nanofabrication by stencil lithography: A review," *Microelectron Eng*, vol. 132, pp. 236–254, Jan. 2015, doi: 10.1016/J.MEE.2014.08.003.
- [296] H. A. Biebuyck, N. B. Larsen, E. Delamarche, and B. Michel, "Lithography beyond light: Microcontact printing with monolayer resists," *IBM J Res Dev*, vol. 41, no. 1–2, pp. 159–170, 1997, doi: 10.1147/RD.411.0159.

- [297] F. Huo, Z. Zheng, G. Zheng, L. R. Giam, H. Zhang, and C. A. Mirkin, "Polymer pen lithography," *Science (1979)*, vol. 321, no. 5896, pp. 1658–1660, Sep. 2008, doi: 10.1126/SCIENCE.1162193.
- [298] T. W. Odom, J. C. Love, D. B. Wolfe, K. E. Paul, and G. M. Whitesides, "Improved pattern transfer in soft lithography using composite stamps," *Langmuir*, vol. 18, no. 13, pp. 5314–5320, Jun. 2002, doi: 10.1021/LA020169L.
- [299] H. Schmid and B. Michel, "Siloxane polymers for high-resolution, high-accuracy soft lithography," *Macromolecules*, vol. 33, no. 8, pp. 3042–3049, Apr. 2000, doi: 10.1021/MA982034L.
- [300] J. C. Cau, L. Ludovic, N. Marie, L. Adriana, and P. Vincent, "Magnetic field assisted microcontact printing: A new concept of fully automated and calibrated process," *Microelectron Eng*, vol. 110, pp. 207–214, Oct. 2013, doi: 10.1016/J.MEE.2013.03.164.
- [301] J. M. Hong, F. M. Ozkeskin, and J. Zou, "A micromachined elastomeric tip array for contact printing with variable dot size and density," *Journal of Micromechanics and Microengineering*, vol. 18, no. 1, p. 015003, Nov. 2007, doi: 10.1088/0960-1317/18/1/015003.
- [302] F. Brinkmann *et al.*, "Interdigitated Multicolored Bioink Micropatterns by Multiplexed Polymer Pen Lithography," *Small*, vol. 9, no. 19, pp. 3266–3275, Oct. 2013, doi: 10.1002/SMLL.201203183.
- [303] G. Arrabito *et al.*, "Configurable Low-Cost Plotter Device for Fabrication of Multi-Color Sub-Cellular Scale Microarrays," *Small*, vol. 10, no. 14, pp. 2870–2876, Jul. 2014, doi: 10.1002/SMLL.201303390.
- [304] D. C. Trimbach, M. Al-Hussein, W. H. de Jeu, M. Decré, D. J. Broer, and C. W. M. Bastiaansen, "Hydrophilic elastomers for microcontact printing of polar inks," *Langmuir*, vol. 20, no. 11, pp. 4738–4742, May 2004, doi: 10.1021/LA049716O/.
- [305] "KRATON™ D1102 K Polymer".
- [306] "KRATON™ G (SEBS AND SEBS OE) - Kraton Corporation." https://kraton.com/products/KRATON_G.php (accessed Aug. 30, 2022).
- [307] T. Kaufmann and B. J. Ravoo, "Stamps, inks and substrates: polymers in microcontact printing," *Polym Chem*, vol. 1, no. 4, pp. 371–387, May 2010, doi: 10.1039/B9PY00281B.
- [308] D. Qin, Y. Xia, and G. M. Whitesides, "Soft lithography for micro- and nanoscale patterning," *Nature Protocols 2010 5:3*, vol. 5, no. 3, pp. 491–502, Feb. 2010, doi: 10.1038/nprot.2009.234.
- [309] Y. Xia and G. M. Whitesides, "SOFT LITHOGRAPHY," *Annual Review of Materials Science*, vol. 28, no. 1, pp. 153–184, Nov. 2003, doi: 10.1146/ANNUREV.MATSCI.28.1.153.
- [310] A. Perl, D. N. Reinhoudt, and J. Huskens, "Microcontact Printing: Limitations and Achievements," *Advanced Materials*, vol. 21, no. 22, pp. 2257–2268, Jun. 2009, doi: 10.1002/ADMA.200801864.
- [311] E. P. Yalcintas, K. B. Ozutemiz, T. Cetinkaya, L. Dalloro, C. Majidi, and O. B. Ozdoganlar, "Soft Electronics Manufacturing Using Microcontact Printing," *Adv Funct Mater*, vol. 29, no. 51, p. 1906551, Dec. 2019, doi: 10.1002/ADFM.201906551.

-
- [312] R. Szoszkiewicz *et al.*, "High-speed, sub-15 nm feature size thermochemical nanolithography," *Nano Lett*, vol. 7, no. 4, pp. 1064–1069, Apr. 2007, doi: 10.1021/NL070300F.
- [313] M. Jaschke and H. J. Butt, "Deposition of Organic Material by the Tip of a Scanning Force Microscope," *Langmuir*, vol. 11, no. 4, pp. 1061–1064, Apr. 1995, doi: 10.1021/LA00004A004.
- [314] K. Salaita, Y. Wang, and C. A. Mirkin, "Applications of dip-pen nanolithography," *Nature Nanotechnology 2007 2:3*, vol. 2, no. 3, pp. 145–155, Feb. 2007, doi: 10.1038/nnano.2007.39.
- [315] P. E. Sheehan, L. J. Whitman, W. P. King, and B. A. Nelson, "Nanoscale deposition of solid inks via thermal dip pen nanolithography," *Appl Phys Lett*, vol. 85, no. 9, p. 1589, Aug. 2004, doi: 10.1063/1.1785860.
- [316] Y. K. Ryu Cho *et al.*, "Sub-10 Nanometer Feature Size in Silicon Using Thermal Scanning Probe Lithography," *ACS Nano*, vol. 11, no. 12, pp. 11890–11897, Dec. 2017, doi: 10.1021/ACS.NANO.7B06307.
- [317] Y. K. Ryu and R. Garcia, "Advanced oxidation scanning probe lithography," *Nanotechnology*, vol. 28, no. 14, p. 142003, Mar. 2017, doi: 10.1088/1361-6528/AA5651.
- [318] D. M. Burland *et al.*, "Modification of hydrogen-passivated silicon by a scanning tunneling microscope operating in air," *Appl Phys Lett*, vol. 56, no. 20, p. 2001, Jun. 1998, doi: 10.1063/1.102999.
- [319] M. Kaestner, M. Hofer, and I. W. Rangelow, "Nanolithography by scanning probes on calixarene molecular glass resist using mix-and-match lithography," *Journal of Micro/Nanolithography, MEMS, And MOEMS*, vol. 12, no. 3, p. 031111, Aug. 2013, doi: 10.1117/1.JMM.12.3.031111.
- [320] H. O. Jacobs, S. A. Campbell, and M. G. Steward, "Approaching Nanoxerography: The Use of Electrostatic Forces to Position Nanoparticles with 100 nm Scale Resolution," *Advanced Materials*, vol. 14, no. 21, pp. 1553–1557, Nov. 2002, doi: 10.1002/1521-4095(20021104)14:21<1553::AID-ADMA1553>3.0.CO;2-9.
- [321] K. Wilder, C. F. Quate, B. Singh, and D. F. Kyser, "Electron beam and scanning probe lithography: A comparison," *Journal of Vacuum Science & Technology B: Microelectronics and Nanometer Structures Processing, Measurement, and Phenomena*, vol. 16, no. 6, p. 3864, Dec. 1998, doi: 10.1116/1.590425.
- [322] J. Xu *et al.*, "Microfabricated Quill-Type Surface Patterning Tools for the Creation of Biological Micro/Nano Arrays," *Biomedical Microdevices 2004 6:2*, vol. 6, no. 2, pp. 117–123, Jun. 2004, doi: 10.1023/B:BMMD.0000031748.13353.10.
- [323] "Nano eNabler™ Molecular Printing System - BioForce Nanosciences." <https://bioforcenano.com/product/nano-enabler-molecular-printing-system/> (accessed Sep. 09, 2022).
- [324] "Surface Patterning Tools Archives - BioForce Nanosciences." <https://bioforcenano.com/product-category/surface-patterning-tools-accessories/surface-patterning-tools/> (accessed Sep. 09, 2022).
- [325] P. Belaubre *et al.*, "Fabrication of biological microarrays using microcantilevers," *Appl Phys Lett*, vol. 82, no. 18, p. 3122, Apr. 2003, doi: 10.1063/1.1565685.

- [326] J. Atwater *et al.*, "Combinatorial Synthesis of Macromolecular Arrays by Microchannel Cantilever Spotting (μ CS)," *Advanced Materials*, vol. 30, no. 31, p. 1801632, Aug. 2018, doi: 10.1002/ADMA.201801632.
- [327] S. M. M. Dadfar, S. Sekula-Neuner, U. Bog, V. Trouillet, and M. Hirtz, "Site-Specific Surface Functionalization via Microchannel Cantilever Spotting (μ CS): Comparison between Azide-Alkyne and Thiol-Alkyne Click Chemistry Reactions," *Small*, vol. 14, no. 21, p. 1800131, May 2018, doi: 10.1002/SMLL.201800131.
- [328] S. M. M. Dadfar, S. Sekula-Neuner, V. Trouillet, and M. Hirtz, "Protein Microarray Immobilization via Epoxide Ring-Opening by Thiol, Amine, and Azide," *Adv Mater Interfaces*, vol. 8, no. 10, p. 2002117, May 2021, doi: 10.1002/ADMI.202002117.
- [329] S. Mohammad Mahdi Dadfar, S. Sekula-Neuner, V. Trouillet, and M. Hirtz, "A Comparative Study of Thiol-Terminated Surface Modification by Click Reactions: Thiol-yne Coupling versus Thiol-ene Michael Addition," *Adv Mater Interfaces*, vol. 5, no. 24, p. 1801343, Dec. 2018, doi: 10.1002/ADMI.201801343.
- [330] S. Das, R. Kumar, D. Parbat, S. Sekula-Neuner, M. Hirtz, and U. Manna, "Covalently Modulated and Transiently Visible Writing: Rational Association of Two Extremes of Water Wettabilities," *ACS Appl Mater Interfaces*, vol. 12, no. 2, pp. 2935–2943, Jan. 2020, doi: 10.1021/ACSAMI.9B17470.
- [331] M. Hirtz, S. Varey, H. Fuchs, and A. Vijayaraghavan, "Attoliter Chemistry for Nanoscale Functionalization of Graphene," *ACS Appl Mater Interfaces*, vol. 8, no. 49, pp. 33371–33376, Dec. 2016, doi: 10.1021/ACSAMI.6B06065.
- [332] C. Zhong, C. Hu, R. Kumar, V. Trouillet, F. Biedermann, and M. Hirtz, "Cucurbit[*n*]uril-Immobilized Sensor Arrays for Indicator-Displacement Assays of Small Bioactive Metabolites," *ACS Appl Nano Mater*, vol. 4, no. 5, pp. 4676–4687, May 2021, doi: 10.1021/ACSANM.1C00293.
- [333] V. K. S. Yadav, S. Raveesh, T. T. Daniel, and R. Paily, "Microcantilever Printed Back-to-Back ZnO Single-Nanowire Schottky Diodes," *IEEE Trans Electron Devices*, vol. 67, no. 8, pp. 3309–3314, Aug. 2020, doi: 10.1109/TED.2020.3002733.
- [334] V. K. S. Yadav, T. T. Daniel, and R. P. Paily, "Gas Sensors Based on Drop-Casted ZnO Nanowires and Micro-Cantilever Printed Ag Contacts," *IEEE Sens J*, vol. 20, no. 9, pp. 4951–4958, May 2020, doi: 10.1109/JSEN.2020.2964600.
- [335] V. K. S. Yadav, G. Natu, and R. P. Paily, "Fabrication and electrical characterization of printed microresistors of silver nanoparticles using microcantilever-based printing technology," *IEEE Trans Compon Packaging Manuf Technol*, vol. 10, no. 1, pp. 57–64, Jan. 2020, doi: 10.1109/TCPMT.2019.2954079.
- [336] V. K. S. Yadav, G. Natu, and R. Paily, "Analysis of Superfine-Resolution Printing of Polyaniline and Silver Microstructures for Electronic Applications," *IEEE Trans Compon Packaging Manuf Technol*, vol. 8, no. 9, pp. 1678–1685, Sep. 2018, doi: 10.1109/TCPMT.2018.2854629.
- [337] A. Meister *et al.*, "FluidFM: Combining atomic force microscopy and nanofluidics in a universal liquid delivery system for single cell applications and beyond," *Nano Lett*, vol. 9, no. 6, pp. 2501–2507, Jun. 2009, doi: 10.1021/NL901384X.

-
- [338] R. R. Grüter, J. Vörös, and T. Zambelli, "FluidFM as a lithography tool in liquid: spatially controlled deposition of fluorescent nanoparticles," *Nanoscale*, vol. 5, no. 3, pp. 1097–1104, Jan. 2013, doi: 10.1039/C2NR33214K.
- [339] "FluidFM ® Application Note 00819 Spotting and lithography with FluidFM", Accessed: Aug. 30, 2022. [Online]. Available: www.nanosurf.com
- [340] "FluidFM technology | Cytosurge AG." <https://www.cytosurge.com/technology> (accessed Aug. 30, 2022).
- [341] P. Dörig *et al.*, "Force-controlled spatial manipulation of viable mammalian cells and micro-organisms by means of FluidFM technology," *Appl Phys Lett*, vol. 97, no. 2, p. 023701, Jul. 2010, doi: 10.1063/1.3462979.
- [342] O. Guillaume-Gentil, E. Potthoff, D. Ossola, C. M. Franz, T. Zambelli, and J. A. Vorholt, "Force-controlled manipulation of single cells: from AFM to FluidFM," *Trends Biotechnol*, vol. 32, no. 7, pp. 381–388, Jul. 2014, doi: 10.1016/J.TIBTECH.2014.04.008.
- [343] C. Müller-Renno, D. Remmel, M. Braun, K. Boonrod, G. Krczal, and C. Ziegler, "Producing Plant Virus Patterns with Defined 2D Structure," *physica status solidi (a)*, vol. 218, no. 18, p. 2100259, Sep. 2021, doi: 10.1002/PSSA.202100259.
- [344] D. Jin Kang *et al.*, "Printable conductive inks used for the fabrication of electronics: an overview," *Nanotechnology*, vol. 32, no. 50, p. 502009, Oct. 2021, doi: 10.1088/1361-6528/ABEFFF.
- [345] T. v. Neumann and M. D. Dickey, "Liquid Metal Direct Write and 3D Printing: A Review," *Adv Mater Technol*, vol. 5, no. 9, p. 2000070, Sep. 2020, doi: 10.1002/ADMT.202000070.
- [346] C. T. Sah, R. N. Noyce, and W. Shockley, "Carrier Generation and Recombination in P-N Junctions and P-N Junction Characteristics," *Proceedings of the IRE*, vol. 45, no. 9, pp. 1228–1243, 1957, doi: 10.1109/JRPROC.1957.278528.
- [347] P. Horowitz and W. Hill, *The Art of Electronics 3rd edition*. 2017, ISBN: 9780521809269.
- [348] R. L. Boylestad and L. Nashelsky, *Electronic Devices and Circuit Theory*. 2013. Accessed: Aug. 30, 2022, ISBN: 978-1-292-03806-3.
- [349] S. J. G. Gift and B. Maundy, *Electronic Circuit Design and Application*. Springer International Publishing, 2021. doi: 10.1007/978-3-030-46989-4.
- [350] J. Bardeen and W. H. Brattain, "The transistor, a semi-conductor triode [14]," *Physical Review*, vol. 74, no. 2, pp. 230–231, Jul. 1948, doi: 10.1103/PHYSREV.74.230.
- [351] "1956 Nobel Prize in Physics - John Bardeen, Walter H Brattain and William Shockley - Nokia Bell Labs." <https://www.bell-labs.com/about/awards/1956-nobel-prize-physics/#gref> (accessed Oct. 02, 2022).
- [352] F. Torricelli *et al.*, "Electrolyte-gated transistors for enhanced performance bioelectronics," *Nature Reviews Methods Primers 2021 1:1*, vol. 1, no. 1, pp. 1–24, Oct. 2021, doi: 10.1038/s43586-021-00065-8.
- [353] W. Huang *et al.*, "Dielectric materials for electrolyte gated transistor applications," *J Mater Chem C Mater*, vol. 9, no. 30, pp. 9348–9376, Aug. 2021, doi: 10.1039/D1TC02271G.

- [354] B. Razavi, *Design of analog CMOS integrated circuits*, Second. Tata McGraw-Hill Education, 2017.
- [355] C. A. Vu and W. Y. Chen, "Field-Effect Transistor Biosensors for Biomedical Applications: Recent Advances and Future Prospects," *Sensors 2019, Vol. 19, Page 4214*, vol. 19, no. 19, p. 4214, Sep. 2019, doi: 10.3390/S19194214.
- [356] L. Li, S. Wang, Y. Xiao, and Y. Wang, "Recent Advances in Immobilization Strategies for Biomolecules in Sensors Using Organic Field-Effect Transistors," *Transactions of Tianjin University*, vol. 26, no. 6, pp. 424–440, Dec. 2020, doi: 10.1007/S12209-020-00234-Y.
- [357] L. Torsi, M. Magliulo, K. Manoli, and G. Palazzo, "Organic field-effect transistor sensors: a tutorial review," *Chem Soc Rev*, vol. 42, no. 22, pp. 8612–8628, Oct. 2013, doi: 10.1039/C3CS60127G.
- [358] D. Wang, V. Noël, and B. Piro, "Electrolytic Gated Organic Field-Effect Transistors for Application in Biosensors—A Review," *Electronics 2016, Vol. 5, Page 9*, vol. 5, no. 1, p. 9, Feb. 2016, doi: 10.3390/ELECTRONICS5010009.
- [359] L. Liao and Z. Cui, Eds., *Solution Processed Metal Oxide Thin Films for Electronic Applications*. Elsevier, 2020. doi: 10.1016/B978-0-12-814930-0.00007-4.
- [360] X. Hong and L. Liao, "Metal oxide dielectrics," *Solution Processed Metal Oxide Thin Films for Electronic Applications*, pp. 31–39, Jan. 2020, doi: 10.1016/B978-0-12-814930-0.00003-7.
- [361] H. Sirringhaus, N. Tessler, and R. H. Friend, "Integrated optoelectronic devices based on conjugated polymers," *Science (1979)*, vol. 280, no. 5370, pp. 1741–1744, Jun. 1998, doi: 10.1126/SCIENCE.280.5370.1741.
- [362] Z. E. Jeroish, K. S. Bhuvaneshwari, F. Samsuri, and V. Narayanamurthy, "Microheater: material, design, fabrication, temperature control, and applications—a role in COVID-19," *Biomed Microdevices*, vol. 24, no. 1, pp. 1–49, Mar. 2022, doi: 10.1007/S10544-021-00595-8.
- [363] S. Joy and J. K. Antony, "Design and Simulation of a Micro Hotplate Using COMSOL Multiphysics for MEMS Based Gas Sensor," *Proceedings - 2015 5th International Conference on Advances in Computing and Communications, ICACC 2015*, pp. 465–468, Mar. 2016, doi: 10.1109/ICACC.2015.108.
- [364] S. Ali *et al.*, "Flexible Capacitive Pressure Sensor Based on PDMS Substrate and Ga-In Liquid Metal," *IEEE Sens J*, vol. 19, no. 1, pp. 97–104, Jan. 2019, doi: 10.1109/JSEN.2018.2877929.
- [365] M. M. Ali *et al.*, "Eutectic Ga-In liquid metal based flexible capacitive pressure sensor," *Proceedings of IEEE Sensors*, Jan. 2017, doi: 10.1109/ICSENS.2016.7808515.
- [366] K. Kim *et al.*, "Highly Sensitive and Wearable Liquid Metal-Based Pressure Sensor for Health Monitoring Applications: Integration of a 3D-Printed Microbump Array with the Microchannel," *Adv Healthc Mater*, vol. 8, no. 22, p. 1900978, Nov. 2019, doi: 10.1002/ADHM.201900978.
- [367] C. Pan *et al.*, "Visually Imperceptible Liquid-Metal Circuits for Transparent, Stretchable Electronics with Direct Laser Writing," *Advanced Materials*, vol. 30, no. 12, p. 1706937, Mar. 2018, doi: 10.1002/ADMA.201706937.
- [368] X. Peng Hao *et al.*, "Self-Shaping Soft Electronics Based on Patterned Hydrogel with Stencil-Printed Liquid Metal," *Adv Funct Mater*, vol. 31, no. 47, p. 2105481, Nov. 2021, doi: 10.1002/ADFM.202105481.

-
- [369] B. Ma *et al.*, "A Versatile Approach for Direct Patterning of Liquid Metal Using Magnetic Field," *Adv Funct Mater*, vol. 29, no. 28, p. 1901370, Jul. 2019, doi: 10.1002/ADFM.201901370.
- [370] H. Ota *et al.*, "3D printed 'earable' smart devices for real-time detection of core body temperature," *ACS Sens*, vol. 2, no. 7, pp. 990–997, Jul. 2017, doi: 10.1021/ACSSENSORS.7B00247.
- [371] K. Bugra Ozutemiz *et al.*, "EGaIn–Metal Interfacing for Liquid Metal Circuitry and Microelectronics Integration," *Adv Mater Interfaces*, vol. 5, no. 10, p. 1701596, May 2018, doi: 10.1002/ADMI.201701596.
- [372] H. Ota *et al.*, "Application of 3D Printing for Smart Objects with Embedded Electronic Sensors and Systems," *Adv Mater Technol*, vol. 1, no. 1, p. 1600013, Apr. 2016, doi: 10.1002/ADMT.201600013.
- [373] C. B. Cooper *et al.*, "Stretchable Capacitive Sensors of Torsion, Strain, and Touch Using Double Helix Liquid Metal Fibers," *Adv Funct Mater*, vol. 27, no. 20, p. 1605630, May 2017, doi: 10.1002/ADFM.201605630.
- [374] Y. Gao *et al.*, "Wearable Microfluidic Diaphragm Pressure Sensor for Health and Tactile Touch Monitoring," *Advanced Materials*, vol. 29, no. 39, p. 1701985, Oct. 2017, doi: 10.1002/ADMA.201701985.
- [375] J. H. So, J. Thelen, A. Qusba, G. J. Hayes, G. Lazzi, and M. D. Dickey, "Reversibly Deformable and Mechanically Tunable Fluidic Antennas," *Adv Funct Mater*, vol. 19, no. 22, pp. 3632–3637, Nov. 2009, doi: 10.1002/ADFM.200900604.
- [376] Z. Xie, R. Avila, Y. Huang, and J. A. Rogers, "Flexible and Stretchable Antennas for Biointegrated Electronics," *Advanced Materials*, vol. 32, no. 15, p. 1902767, Apr. 2020, doi: 10.1002/ADMA.201902767.
- [377] M. Cosker, L. Lizzi, F. Ferrero, R. Staraj, and J. M. Ribero, "Realization of 3-D flexible antennas using liquid metal and additive printing technologies," *IEEE Antennas Wirel Propag Lett*, vol. 16, pp. 971–974, 2017, doi: 10.1109/LAWP.2016.2615568.
- [378] M. Kubo *et al.*, "Stretchable Microfluidic Radiofrequency Antennas," *Advanced Materials*, vol. 22, no. 25, pp. 2749–2752, Jul. 2010, doi: 10.1002/ADMA.200904201.
- [379] G. Li, X. Wu, and D. W. Lee, "Selectively plated stretchable liquid metal wires for transparent electronics," *Sens Actuators B Chem*, vol. 221, pp. 1114–1119, Dec. 2015, doi: 10.1016/J.SNB.2015.07.062.
- [380] C. Etienne Palleau *et al.*, "Self-Healing Stretchable Wires for Reconfigurable Circuit Wiring and 3D Microfluidics," *Advanced Materials*, vol. 25, no. 11, pp. 1589–1592, Mar. 2013, doi: 10.1002/ADMA.201203921.
- [381] Z. Zhang *et al.*, "Liquid metal-created macroporous composite hydrogels with self-healing ability and multiple sensations as artificial flexible sensors," *J Mater Chem A Mater*, vol. 9, no. 2, pp. 875–883, Jan. 2021, doi: 10.1039/D0TA09730F.
- [382] S. H. Jeong, K. Hjort, and Z. Wu, "Tape Transfer Atomization Patterning of Liquid Alloys for Microfluidic Stretchable Wireless Power Transfer," *Scientific Reports 2015 5:1*, vol. 5, no. 1, pp. 1–7, Feb. 2015, doi: 10.1038/srep08419.
- [383] G. Mao *et al.*, "Soft electromagnetic actuators," *Sci Adv*, vol. 6, no. 26, Jun. 2020, doi: 10.1126/SCIADV.ABC0251.

- [384] T. N. Do *et al.*, "Miniature Soft Electromagnetic Actuators for Robotic Applications," *Adv Funct Mater*, vol. 28, no. 18, p. 1800244, May 2018, doi: 10.1002/ADFM.201800244.
- [385] S. W. Jin *et al.*, "Stretchable Loudspeaker using Liquid Metal Microchannel," *Scientific Reports 2015 5:1*, vol. 5, no. 1, pp. 1–13, Jul. 2015, doi: 10.1038/srep11695.
- [386] M. D. Dickey, "Stretchable and Soft Electronics using Liquid Metals," *Advanced Materials*, vol. 29, no. 27, p. 1606425, Jul. 2017, doi: 10.1002/ADMA.201606425.
- [387] S. Zhu *et al.*, "Ultrastretchable Fibers with Metallic Conductivity Using a Liquid Metal Alloy Core," *Adv Funct Mater*, vol. 23, no. 18, pp. 2308–2314, May 2013, doi: 10.1002/ADFM.201202405.
- [388] H. Zhu, S. Wang, M. Zhang, T. Li, G. Hu, and D. Kong, "Fully solution processed liquid metal features as highly conductive and ultrastretchable conductors," *npj Flexible Electronics 2021 5:1*, vol. 5, no. 1, pp. 1–8, Sep. 2021, doi: 10.1038/s41528-021-00123-x.
- [389] G. Li, F. Sun, H. Chen, Y. Jin, A. Zhang, and J. Du, "High-Efficiency Large-Area Printed Multilayer Liquid Metal Wires for Stretchable Biomedical Sensors with Recyclability," *ACS Appl Mater Interfaces*, vol. 13, no. 48, pp. 56961–56971, Dec. 2021, doi: 10.1021/ACSAMI.1C17514.
- [390] Q. Wang *et al.*, "Fast Fabrication of Flexible Functional Circuits Based on Liquid Metal Dual-Trans Printing," *Advanced Materials*, vol. 27, no. 44, pp. 7109–7116, Nov. 2015, doi: 10.1002/ADMA.201502200.
- [391] B. A. Gozen, A. Tabatabai, O. B. Ozdoganlar, and C. Majidi, "High-Density Soft-Matter Electronics with Micron-Scale Line Width," *Advanced Materials*, vol. 26, no. 30, pp. 5211–5216, Aug. 2014, doi: 10.1002/ADMA.201400502.
- [392] J. Yang, Y. Yang, Z. He, B. Chen, and J. Liu, "A Personal Desktop Liquid-Metal Printer as a Pervasive Electronics Manufacturing Tool for Society in the Near Future," *Engineering*, vol. 1, no. 4, pp. 506–512, Dec. 2015, doi: 10.15302/J-ENG-2015042.
- [393] S. Zhang, B. Wang, J. Jiang, K. Wu, C. F. Guo, and Z. Wu, "High-Fidelity Conformal Printing of 3D Liquid Alloy Circuits for Soft Electronics," *ACS Appl Mater Interfaces*, vol. 11, no. 7, pp. 7148–7156, Feb. 2019, doi: 10.1021/ACSAMI.8B20595.
- [394] R. C. Ordonez *et al.*, "Rapid Fabrication of Graphene Field-Effect Transistors with Liquid-metal Interconnects and Electrolytic Gate Dielectric Made of Honey," *Scientific Reports 2017 7:1*, vol. 7, no. 1, pp. 1–9, Aug. 2017, doi: 10.1038/s41598-017-10043-4.
- [395] J. B. Andrews *et al.*, "Patterned Liquid Metal Contacts for Printed Carbon Nanotube Transistors," *ACS Nano*, vol. 12, no. 6, pp. 5482–5488, Jun. 2018, doi: 10.1021/ACS.NANO.8B00909.
- [396] M. Wang, X. Feng, X. Wang, S. Hu, C. Zhang, and H. Qi, "Facile gelation of a fully polymeric conductive hydrogel activated by liquid metal nanoparticles," *J Mater Chem A Mater*, vol. 9, no. 43, pp. 24539–24547, Nov. 2021, doi: 10.1039/D1TA07254D.
- [397] M. Wang *et al.*, "Stencil Printing of Liquid Metal upon Electrospun Nanofibers Enables High-Performance Flexible Electronics," *ACS Nano*, vol. 15, no. 12, pp. 19364–19376, Dec. 2021, doi: 10.1021/ACS.NANO.1C05762.

-
- [398] K. Chu *et al.*, "Smart Passivation Materials with a Liquid Metal Microcapsule as Self-Healing Conductors for Sustainable and Flexible Perovskite Solar Cells," *Adv Funct Mater*, vol. 28, no. 22, p. 1800110, May 2018, doi: 10.1002/ADFM.201800110.
- [399] J. Y. Zhu, S. Y. Tang, K. Khoshmanesh, and K. Ghorbani, "An Integrated Liquid Cooling System Based on Galinstan Liquid Metal Droplets," *ACS Appl Mater Interfaces*, vol. 8, no. 3, pp. 2173–2180, Jan. 2016, doi: 10.1021/ACSAMI.5B10769.
- [400] M. Zadan, M. H. Malakooti, and C. Majidi, "Soft and Stretchable Thermoelectric Generators Enabled by Liquid Metal Elastomer Composites," *ACS Appl Mater Interfaces*, vol. 12, no. 15, pp. 17921–17928, Apr. 2020, doi: 10.1021/ACSAMI.9B19837.
- [401] U. Pierre Claver and G. Zhao, "Recent Progress in Flexible Pressure Sensors Based Electronic Skin," *Adv Eng Mater*, vol. 23, no. 5, p. 2001187, May 2021, doi: 10.1002/ADEM.202001187.
- [402] X. Wang *et al.*, "Printed Conformable Liquid Metal e-Skin-Enabled Spatiotemporally Controlled Bioelectromagnetics for Wireless Multisite Tumor Therapy," *Adv Funct Mater*, vol. 29, no. 51, p. 1907063, Dec. 2019, doi: 10.1002/ADFM.201907063.
- [403] T. Lu, E. J. Markvicka, Y. Jin, and C. Majidi, "Soft-Matter Printed Circuit Board with UV Laser Micropatterning," *ACS Appl Mater Interfaces*, vol. 9, no. 26, pp. 22055–22062, Jul. 2017, doi: 10.1021/ACSAMI.7B05522.
- [404] Y. Ren, X. Sun, and J. Liu, "Advances in Liquid Metal-Enabled Flexible and Wearable Sensors," *Micromachines 2020, Vol. 11, Page 200*, vol. 11, no. 2, p. 200, Feb. 2020, doi: 10.3390/MI11020200.
- [405] Y. G. Park, G. Y. Lee, J. Jang, S. M. Yun, E. Kim, and J. U. Park, "Liquid Metal-Based Soft Electronics for Wearable Healthcare," *Adv Healthc Mater*, vol. 10, no. 17, p. 2002280, Sep. 2021, doi: 10.1002/ADHM.202002280.
- [406] Y. R. Jeong *et al.*, "A skin-attachable, stretchable integrated system based on liquid GaInSn for wireless human motion monitoring with multi-site sensing capabilities," *NPG Asia Materials 2017 9:10*, vol. 9, no. 10, pp. e443–e443, Oct. 2017, doi: 10.1038/am.2017.189.
- [407] Z. N. Zhao *et al.*, "Liquid Metal Enabled Flexible Electronic System for Eye Movement Tracking," *IEEE Sens J*, vol. 18, no. 6, pp. 2592–2598, Mar. 2018, doi: 10.1109/JSEN.2018.2796121.
- [408] R. Guo and J. Liu, "Implantable liquid metal-based flexible neural microelectrode array and its application in recovering animal locomotion functions," *Journal of Micromechanics and Microengineering*, vol. 27, no. 10, p. 104002, Sep. 2017, doi: 10.1088/1361-6439/AA891C.
- [409] X. Wang, Y. Zhang, R. Guo, H. Wang, B. Yuan, and J. Liu, "Conformable liquid metal printed epidermal electronics for smart physiological monitoring and simulation treatment," *Journal of Micromechanics and Microengineering*, vol. 28, no. 3, p. 034003, Feb. 2018, doi: 10.1088/1361-6439/AAA80F.
- [410] Q. Zhang, Y. Gao, and J. Liu, "Atomized spraying of liquid metal droplets on desired substrate surfaces as a generalized way for ubiquitous printed electronics," *Appl Phys A Mater Sci Process*, vol. 116, no. 3, pp. 1091–1097, Dec. 2014, doi: 10.1007/S00339-013-8191-4.

- [411] A. Fassler and C. Majidi, "Soft-matter capacitors and inductors for hyperelastic strain sensing and stretchable electronics," *Smart Mater Struct*, vol. 22, no. 5, p. 055023, Apr. 2013, doi: 10.1088/0964-1726/22/5/055023.
- [412] N. Hussain, M. Jan Nazami, C. Ma, and M. Hirtz, "High-precision tabletop microplotter for flexible on-demand material deposition in printed electronics and device functionalization," *Review of Scientific Instruments*, vol. 92, no. 12, p. 125104, Dec. 2021, doi: 10.1063/5.0061331.
- [413] "Electronic Devices Failure Analysis, November 2019 Digital Version available at edfas.org." <https://static.asminternational.org/EDFA/201911/> (accessed Sep. 10, 2022).
- [414] W. Geng *et al.*, "Ohmic contact on single ZnO nanowires grown by MOCVD," *physica status solidi (c)*, vol. 10, no. 10, pp. 1292–1296, Oct. 2013, doi: 10.1002/PSSC.201200984.
- [415] M. Power and G. Z. Yang, "Direct laser written passive micromanipulator end-effector for compliant object manipulation," *IEEE International Conference on Intelligent Robots and Systems*, vol. 2015-December, pp. 790–797, Dec. 2015, doi: 10.1109/IROS.2015.7353462.
- [416] E. F. Arkan, D. Sacchetto, I. Yildiz, Y. Leblebici, and B. E. Alaca, "Monolithic integration of Si nanowires with metallic electrodes: NEMS resonator and switch applications," *Journal of Micromechanics and Microengineering*, vol. 21, no. 12, p. 125018, Nov. 2011, doi: 10.1088/0960-1317/21/12/125018.
- [417] D. Thuau, C. Ayela, P. Poulin, and I. Dufour, "Highly piezoresistive hybrid MEMS sensors," *Sens Actuators A Phys*, vol. 209, pp. 161–168, Mar. 2014, doi: 10.1016/J.SNA.2014.01.037.
- [418] "In Operando Equipments - EDEN Instruments | In Situ NanoCharacterization Solutions." <https://www.eden-instruments.com/en/in-operando-equipments/> (accessed Aug. 30, 2022).
- [419] M. Hunstig, "Piezoelectric Inertia Motors—A Critical Review of History, Concepts, Design, Applications, and Perspectives," *Actuators 2017, Vol. 6, Page 7*, vol. 6, no. 1, p. 7, Feb. 2017, doi: 10.3390/ACT6010007.
- [420] "NANO - Imina Technologies SA Semiconductor Nanoprobing Solutions for Electron Microscopes." <https://imina.ch/en/products/nano-robotics-solutions-electron-microscopes#specifications> (accessed Sep. 08, 2022).
- [421] "Manipulator MiBot - PIK Instruments." <https://pik-instruments.pl/en/science/electron-microscopy/imina/manipulator-mibot/> (accessed Sep. 08, 2022).
- [422] E. Lin, A. Sikand, J. Wickware, Y. Hao, and R. Derda, "Peptide microarray patterning for controlling and monitoring cell growth," *Acta Biomater*, vol. 34, pp. 53–59, Apr. 2016, doi: 10.1016/J.ACTBIO.2016.01.028.
- [423] S. Sekula *et al.*, "Multiplexed Lipid Dip-Pen Nanolithography on Subcellular Scales for the Templating of Functional Proteins and Cell Culture," *Small*, vol. 4, no. 10, pp. 1785–1793, Oct. 2008, doi: 10.1002/SMLL.200800949.
- [424] S. Sekula *et al.*, "Allergen Arrays for Antibody Screening and Immune Cell Activation Profiling Generated by Parallel Lipid Dip-Pen Nanolithography," *Small*, vol. 8, no. 4, pp. 585–591, Feb. 2012, doi: 10.1002/SMLL.201101694.
- [425] F. Brinkmann *et al.*, "A Versatile Microarray Platform for Capturing Rare Cells," *Scientific Reports 2015 5:1*, vol. 5, no. 1, pp. 1–11, Oct. 2015, doi: 10.1038/srep15342.

-
- [426] H. Y. Liu *et al.*, "Evaluation of Microfluidic Ceiling Designs for the Capture of Circulating Tumor Cells on a Microarray Platform," *Adv Biosyst*, vol. 4, no. 2, p. 1900162, Feb. 2020, doi: 10.1002/ADBI.201900162.
- [427] N. B. Morley, J. Burris, L. C. Cadwallader, and M. D. Nornberg, "GaInSn usage in the research laboratory," *Review of Scientific Instruments*, vol. 79, no. 5, p. 056107, May 2008, doi: 10.1063/1.2930813.
- [428] S. Cheng and Z. Wu, "Microfluidic electronics," *Lab Chip*, vol. 12, no. 16, pp. 2782–2791, Jul. 2012, doi: 10.1039/C2LC21176A.
- [429] G. Cadilha Marques *et al.*, "Fabrication and Modeling of pn-Diodes Based on Inkjet Printed Oxide Semiconductors," *IEEE Electron Device Letters*, vol. 41, no. 1, pp. 187–190, Jan. 2020, doi: 10.1109/LED.2019.2956346.
- [430] D. Yamamoto, M. Shiomi, T. Arie, S. Akita, and K. Takei, "All-Solution-Based Heterogeneous Material Formation for p-n Junction Diodes," *ACS Appl Mater Interfaces*, vol. 11, no. 1, pp. 1021–1025, Jan. 2019, doi: 10.1021/ACSAMI.8B15900.
- [431] G. C. Marques *et al.*, "Electrolyte-gated FETs based on oxide semiconductors: Fabrication and modeling," *IEEE Trans Electron Devices*, vol. 64, no. 1, pp. 279–285, Jan. 2017, doi: 10.1109/TED.2016.2621777.
- [432] G. Cadilha Marques *et al.*, "Digital power and performance analysis of inkjet printed ring oscillators based on electrolyte-gated oxide electronics," *Appl Phys Lett*, vol. 111, no. 10, p. 102103, Sep. 2017, doi: 10.1063/1.4991919.
- [433] X. Feng, C. Punckt, G. C. Marques, M. Hefenbrock, M. B. Tahoori, and J. Aghassi-Hagmann, "Impact of Intrinsic Capacitances on the Dynamic Performance of Printed Electrolyte-Gated Inorganic Field Effect Transistors," *IEEE Trans Electron Devices*, vol. 66, no. 8, pp. 3365–3370, Aug. 2019, doi: 10.1109/TED.2019.2919933.
- [434] Y. Plevachuk, V. Sklyarchuk, S. Eckert, G. Gerbeth, and R. Novakovic, "Thermophysical properties of the liquid Ga-In-Sn eutectic alloy," *J Chem Eng Data*, vol. 59, no. 3, pp. 757–763, Mar. 2014, doi: 10.1021/JE400882Q.
- [435] R. Ma, C. Guo, Y. Zhou, and J. Liu, "Electromigration Induced Break-up Phenomena in Liquid Metal Printed Thin Films," *Journal of Electronic Materials* 2014 43:11, vol. 43, no. 11, pp. 4255–4261, Aug. 2014, doi: 10.1007/S11664-014-3366-0.
- [436] H. O. Michaud and S. P. Lacour, "Liquid electromigration in gallium-based biphasic thin films," *APL Mater*, vol. 7, no. 3, p. 031504, Feb. 2019, doi: 10.1063/1.5059380.
- [437] P. Bhattacharyya, "Technological journey towards reliable microheater development for MEMS gas sensors: a review," *IEEE Transactions on Device and Materials Reliability*, vol. 14, no. 2, pp. 589–599, 2014, doi: 10.1109/TDMR.2014.2311801.
- [438] B. Wang *et al.*, "Liquid Metal Microscale Deposition enabled High Resolution and Density Epidermal Microheater for Localized Ectopic Expression in *Drosophila*," *Adv Mater Technol*, vol. 7, no. 3, p. 2100903, Mar. 2022, doi: 10.1002/ADMT.202100903.
- [439] A. A. Vasiliev, A. v. Nisan, and N. N. Samotaev, "Aerosol/Ink Jet Printing Technology for High-Temperature MEMS Sensors," *Proceedings 2017, Vol. 1, Page 617*, vol. 1, no. 4, p. 617, Aug. 2017, doi: 10.3390/PROCEEDINGS1040617.

- [440] Z. X. Cai, X. Y. Zeng, and J. Duan, "Fabrication of platinum microheater on alumina substrate by micro-pen and laser sintering," *Thin Solid Films*, vol. 519, no. 11, pp. 3893–3896, Mar. 2011, doi: 10.1016/J.TSF.2011.01.240.
- [441] J. L. Lin, M. H. Wu, C. Y. Kuo, K. da Lee, and Y. L. Shen, "Application of indium tin oxide (ITO)-based microheater chip with uniform thermal distribution for perfusion cell culture outside a cell incubator," *Biomed Microdevices*, vol. 12, no. 3, pp. 389–398, Jun. 2010, doi: 10.1007/S10544-010-9395-4.
- [442] S. K. Tiwari, S. Bhat, and K. K. Mahato, "Design and fabrication of screen printed microheater," *Microsystem Technologies*, vol. 24, no. 8, pp. 3273–3281, Aug. 2018, doi: 10.1007/S00542-018-3821-6.
- [443] K. M. Byers, L. K. Lin, T. J. Moehling, L. Stanciu, and J. C. Linnes, "Versatile printed microheaters to enable low-power thermal control in paper diagnostics," *Analyst*, vol. 145, no. 1, pp. 184–196, Dec. 2019, doi: 10.1039/C9AN01546A.
- [444] D. Mitra, R. Thalheim, and R. Zichner, "Inkjet Printed Heating Elements Based on Nanoparticle Silver Ink with Adjustable Temperature Distribution for Flexible Applications," *physica status solidi (a)*, vol. 218, no. 17, p. 2100257, Sep. 2021, doi: 10.1002/PSSA.202100257.
- [445] L. Zhang *et al.*, "A Performance-Enhanced Liquid Metal-Based Microheater with Parallel Ventilating Side-Channels," *Micromachines (Basel)*, vol. 11, no. 2, Feb. 2020, doi: 10.3390/MI11020133.
- [446] H. Tokuyama, N. Ishihara, and S. Sakohara, "Effects of synthesis-solvent on swelling and elastic properties of poly(N-isopropylacrylamide) hydrogels," *Eur Polym J*, vol. 43, no. 12, pp. 4975–4982, Dec. 2007, doi: 10.1016/J.EURPOLYMJ.2007.09.016.
- [447] A. Halperin, M. Kröger, and F. M. Winnik, "Poly(N-isopropylacrylamide) Phase Diagrams: Fifty Years of Research," *Angewandte Chemie International Edition*, vol. 54, no. 51, pp. 15342–15367, Dec. 2015, doi: 10.1002/ANIE.201506663.
- [448] M. Heskins and J. E. Guillet, "Solution Properties of Poly(N-isopropylacrylamide)," *Journal of Macromolecular Science: Part A - Chemistry*, vol. 2, no. 8, pp. 1441–1455, Dec. 2006, doi: 10.1080/10601326808051910.
- [449] N. Hussain *et al.*, "Correlated Study of Material Interaction Between Capillary Printed Eutectic Gallium Alloys and Gold Electrodes," *Small*, p. 2202987, Sep. 2022, doi: 10.1002/SMLL.202202987.
- [450] M. J. Cordill, O. Glushko, and B. Putz, "Electro-mechanical testing of conductive materials used in flexible electronics," *Front Mater*, vol. 3, p. 11, Feb. 2016, doi: 10.3389/FMATS.2016.00011.
- [451] J. E. Norkett, M. D. Dickey, and V. M. Miller, "A Review of Liquid Metal Embrittlement: Cracking Open the Disparate Mechanisms," *Metall Mater Trans A Phys Metall Mater Sci*, vol. 52, no. 6, pp. 2158–2172, Jun. 2021, doi: 10.1007/S11661-021-06256-Y.
- [452] E. E. Glickman, "Dissolution condensation mechanism of stress corrosion cracking in liquid metals: Driving force and crack kinetics," *Metall Mater Trans A Phys Metall Mater Sci*, vol. 42, no. 2, pp. 250–266, Feb. 2011, doi: 10.1007/S11661-010-0429-6.
- [453] W. Ludwig, E. Pereiro-López, and D. Bellet, "In situ investigation of liquid Ga penetration in Al bicrystal grain boundaries: grain boundary wetting or liquid metal embrittlement?," *Acta Mater*, vol. 53, no. 1, pp. 151–162, Jan. 2005, doi: 10.1016/J.ACTAMAT.2004.09.012.

-
- [454] "On some remarkable changes produced in iron and steel by the action of hydrogen and acids," *Proceedings of the Royal Society of London*, vol. 23, no. 156–163, pp. 168–179, Dec. 1875, doi: 10.1098/rspl.1874.0024.
- [455] J. Sun, Y. Zhang, A. Lyckegaard, F. Bachmann, E. M. Lauridsen, and D. Juul Jensen, "Grain boundary wetting correlated to the grain boundary properties: A laboratory-based multimodal X-ray tomography investigation," *Scr Mater*, vol. 163, pp. 77–81, Apr. 2019, doi: 10.1016/j.scriptamat.2019.01.007.
- [456] K. L. Dorsey, N. Lazarus, K. L. Dorsey, and N. Lazarus, "Lifetime of Liquid Metal Wires for Stretchable Devices," *Adv Mater Technol*, vol. 6, no. 4, p. 2001100, Apr. 2021, doi: 10.1002/ADMT.202001100.
- [457] B. Chen *et al.*, "Dynamics and control of gold-encapped gallium arsenide nanowires imaged by 4D electron microscopy," *Proc Natl Acad Sci U S A*, vol. 114, no. 49, pp. 12876–12881, Dec. 2017, doi: 10.1073/PNAS.1708761114.
- [458] R. C. Hugo and R. G. Hoagland, "The kinetics of gallium penetration into aluminum grain boundaries—in situ TEM observations and atomistic models," *Acta Mater*, vol. 48, no. 8, pp. 1949–1957, May 2000, doi: 10.1016/S1359-6454(99)00463-2.
- [459] H. S. Nam and D. J. Srolovitz, "Effect of material properties on liquid metal embrittlement in the Al–Ga system," *Acta Mater*, vol. 57, no. 5, pp. 1546–1553, Mar. 2009, doi: 10.1016/J.ACTAMAT.2008.11.041.
- [460] D. A. Molodov, U. Czubayko, G. Gottstein, L. S. Shvindlerman, B. Straumal, and W. Gust, "Acceleration of grain boundary motion in Al by small additions of Ga," *Philosophical Magazine Letters*, vol. 72, no. 6, pp. 361–368, 2006, doi: 10.1080/09500839508242475.
- [461] N. Tsutsui and H. Koizumi, "Intergranular/transgranular fracture in the liquid metal embrittlement of polycrystalline zinc," *Procedia Structural Integrity*, vol. 13, pp. 849–854, Jan. 2018, doi: 10.1016/J.PROSTR.2018.12.162.
- [462] C. Cretu and E. van der Lingen, "Coloured gold alloys," *Gold Bulletin 1999 32:4*, vol. 32, no. 4, pp. 115–126, 1999, doi: 10.1007/BF03214796.
- [463] K. E. Saeger and J. Rodies, "The colour of gold and its alloys," *Gold Bulletin 1977 10:1*, vol. 10, no. 1, pp. 10–14, Mar. 1977, doi: 10.1007/BF03216519.
- [464] J. Wang, Y. J. Liu, L. B. Liu, H. Y. Zhou, and Z. P. Jin, "Thermodynamic assessment of the Au–Ga binary system," *Calphad*, vol. 35, no. 2, pp. 242–248, Jun. 2011, doi: 10.1016/J.CALPHAD.2010.10.009.
- [465] C. Shen, K. Hu, L. Fan, and H. Zhang, "Thermodynamic Reassessment of the Au–In Binary System Supported with First-Principles Calculations," *J Phase Equilibria Diffus*, vol. 42, no. 4, pp. 479–488, Aug. 2021, doi: 10.1007/S11669-021-00910-Z.
- [466] J. Clarysse, A. Moser, O. Yarema, V. Wood, and M. Yarema, "Size- And composition-controlled intermetallic nanocrystals via amalgamation seeded growth," *Sci Adv*, vol. 7, no. 31, Jul. 2021, doi: 10.1126/SCIADV.ABG1934.
- [467] J. Tang, X. Zhao, J. Li, R. Guo, Y. Zhou, and J. Liu, "Gallium-Based Liquid Metal Amalgams: Transitional-State Metallic Mixtures (TransM2ixes) with Enhanced and Tunable Electrical, Thermal, and Mechanical Properties," *ACS Appl Mater Interfaces*, vol. 9, no. 41, pp. 35977–35987, Oct. 2017, doi: 10.1021/ACSAMI.7B10256.

- [468] J. Tang *et al.*, "Oscillatory bifurcation patterns initiated by seeded surface solidification of liquid metals," *Nature Synthesis* 2022 1:2, vol. 1, no. 2, pp. 158–169, Feb. 2022, doi: 10.1038/s44160-021-00020-1.
- [469] N. H. Turner and A. M. Single, "Determination of peak positions and areas from wide-scan XPS spectra," *Surface and Interface Analysis*, vol. 15, no. 3, pp. 215–222, Mar. 1990, doi: 10.1002/SIA.740150305.
- [470] Y. L. Loo, J. W. P. Hsu, R. L. Willett, K. W. Baldwin, K. W. West, and J. A. Rogers, "High-resolution transfer printing on GaAs surfaces using alkane dithiol monolayers," *Journal of Vacuum Science & Technology B: Microelectronics and Nanometer Structures Processing, Measurement, and Phenomena*, vol. 20, no. 6, p. 2853, Dec. 2002, doi: 10.1116/1.1523405.
- [471] S. C. Ghosh, M. C. Biesinger, R. R. Lapierre, and P. Kruse, "X-ray photoelectron spectroscopic study of the formation of catalytic gold nanoparticles on ultraviolet-ozone oxidized GaAs(100) substrates," *J Appl Phys*, vol. 101, no. 11, p. 114322, Jun. 2007, doi: 10.1063/1.2743729.
- [472] A. A. Maradudin, "The Design of Randomly Rough Surfaces That Scatter Waves in a Specified Manner," pp. 467–488, 2007, doi: 10.1007/978-0-387-35659-4_17.
- [473] Z. J. Farrell and C. Tabor, "Control of Gallium Oxide Growth on Liquid Metal Eutectic Gallium/Indium Nanoparticles via Thiolation," *Langmuir*, vol. 34, no. 1, pp. 234–240, Jan. 2018, doi: 10.1021/ACS.LANGMUIR.7B03384.
- [474] L. Cademartiri *et al.*, "Electrical resistance of Ag TS-S(CH₂)_n-1CH₃/Ga₂O₃/EGaIn tunneling junctions," *Journal of Physical Chemistry C*, vol. 116, no. 20, pp. 10848–10860, May 2012, doi: 10.1021/JP212501S.
- [475] C. C. Surdu-Bob, S. O. Saied, and J. L. Sullivan, "An X-ray photoelectron spectroscopy study of the oxides of GaAs," *Appl Surf Sci*, vol. 183, no. 1–2, pp. 126–136, Nov. 2001, doi: 10.1016/S0169-4332(01)00583-9.
- [476] J. R. Shallenberger *et al.*, "Oxide thickness determination by XPS, AES, SIMS, RBS and TEM," *Proceedings of the International Conference on Ion Implantation Technology*, vol. 1, pp. 79–82, 1999, doi: 10.1109/IIT.1999.812056.
- [477] "NIST Standard Reference Database 71 | NIST." <https://www.nist.gov/srd/nist-standard-reference-database-71> (accessed Aug. 30, 2022).
- [478] R. Zierold *et al.*, "Toward brain-on-a-chip: Human induced pluripotent stem cell-derived guided neuronal networks in tailor-made 3d nanoprinted microscaffolds," *ACS Nano*, vol. 14, no. 10, pp. 13091–13102, Oct. 2020, doi: 10.1021/ACS.NANO.0C04640.
- [479] J. Xu, M. Lynch, S. Nettikadan, C. Mosher, S. Vegasandra, and E. Henderson, "Microfabricated 'Biomolecular Ink Cartridges'—Surface patterning tools (SPTs) for the printing of multiplexed biomolecular arrays," *Sens Actuators B Chem*, vol. 113, no. 2, pp. 1034–1041, Feb. 2006, doi: 10.1016/J.SNB.2005.03.113.
- [480] F. Brinkmann *et al.*, "Micropatterning: Interdigitated Multicolored Bioink Micropatterns by Multiplexed Polymer Pen Lithography (Small 19/2013)," *Small*, vol. 9, no. 19, pp. 3265–3265, Oct. 2013, doi: 10.1002/SMLL.201370119.
- [481] L. Hirt, A. Reiser, R. Spolenak, and T. Zambelli, "Additive Manufacturing of Metal Structures at the Micrometer Scale," *Advanced Materials*, vol. 29, no. 17, p. 1604211, May 2017, doi: 10.1002/ADMA.201604211.

-
- [482] R. R. Grüter, B. Dielacher, L. Hirt, J. Vörös, and T. Zambelli, "Patterning gold nanoparticles in liquid environment with high ionic strength for local fabrication of up to 100 μm long metallic interconnections," *Nanotechnology*, vol. 26, no. 17, p. 175301, Apr. 2015, doi: 10.1088/0957-4484/26/17/175301.
- [483] "Molex Connector Part Number - 106815-0033." https://www.molex.com/molex/products/part-detail/capillary_tubing/1068150033 (accessed Aug. 30, 2022).
- [484] A. Facchetti, "Gels excel," *Nature Materials* 2008 7:11, vol. 7, no. 11, pp. 839–840, Nov. 2008, doi: 10.1038/nmat2310.
- [485] C. M. Homenick *et al.*, "Fully Printed and Encapsulated SWCNT-Based Thin Film Transistors via a Combination of R2R Gravure and Inkjet Printing," *ACS Appl Mater Interfaces*, vol. 8, no. 41, pp. 27900–27910, Oct. 2016, doi: 10.1021/ACSAMI.6B06838.
- [486] "Sutter Instruments Pipette Cookbook 2018 (P-97 & P-1000 Micropipette Pullers)." <https://www.sutter.com/PDFs/cookbook.pdf> (accessed Sep. 10, 2022).
- [487] Yap, Y.K., Zhang, D, Physical Vapor Deposition. In: Bhushan, B. (eds) Encyclopedia of Nanotechnology. Dordrecht: Springer, 2015. doi: 10.1007/978-94-017-9780-1_362-3.
- [488] A. K. Dubey and V. Yadava, "Laser beam machining—A review," *Int J Mach Tools Manuf*, vol. 48, no. 6, pp. 609–628, May 2008, doi: 10.1016/J.IJMACHTOOLS.2007.10.017.
- [489] S. Ravi-Kumar, B. Lies, H. Lyu, and H. Qin, "Laser Ablation of Polymers: A Review," *Procedia Manuf*, vol. 34, pp. 316–327, Jan. 2019, doi: 10.1016/J.PROMFG.2019.06.155.
- [490] A. A. Tseng, "Recent developments in micromilling using focused ion beam technology," *Journal of Micromechanics and Microengineering*, vol. 14, no. 4, p. R15, Jan. 2004, doi: 10.1088/0960-1317/14/4/R01.
- [491] I. Utke, S. Moshkalev, and P. Russell, Eds., *Nanofabrication Using Focused Ion and Electron Beams*. Oxford University Press, 2011. Accessed: Aug. 30, 2022. [Online]. Available: <https://global.oup.com/academic/product/nanofabrication-using-focused-ion-and-electron-beams-9780199734214>
- [492] J. S. Lee, R. T. Hill, A. Chilkoti, and W. L. Murphy, "Surface Patterning," *Biomater Sci*, pp. 553–573, Jan. 2020, doi: 10.1016/B978-0-12-816137-1.00037-4.
- [493] T. L. Mabe, J. G. Ryan, and J. Wei, "Functional thin films and nanostructures for sensors," *Fundamentals of Nanoparticles: Classifications, Synthesis Methods, Properties and Characterization*, pp. 169–213, Jan. 2018, doi: 10.1016/B978-0-323-51255-8.00007-0.
- [494] F. S. Jamaludin, M. F. Mohd Sabri, and S. M. Said, "Controlling parameters of focused ion beam (FIB) on high aspect ratio micro holes milling," *Microsystem Technologies*, vol. 19, no. 12, pp. 1873–1888, Dec. 2013, doi: 10.1007/S00542-013-1912-Y.
- [495] "UT Dots, Ink UTDAu25-IJ ." <https://utdots.com/products> (accessed Aug. 31, 2022).
- [496] "Galinstan - Strategic Elements." <https://www.strategic-elements.com/produkte/galinstan-1/> (accessed Aug. 31, 2022).

- [497] D. Liu *et al.*, "Large-scale synthesis of hexagonal corundum-type In₂O₃ by ball milling with enhanced lithium storage capabilities," *J Mater Chem A Mater*, vol. 1, no. 17, pp. 5274–5278, Apr. 2013, doi: 10.1039/C3TA00182B.
- [498] D. B. Buchholz *et al.*, "The structure and properties of amorphous indium oxide," *Chemistry of Materials*, vol. 26, no. 18, pp. 5401–5411, Sep. 2014, doi: 10.1021/CM502689X.
- [499] H. Kim *et al.*, "Electrical, optical, and structural properties of indium–tin–oxide thin films for organic light-emitting devices," *J Appl Phys*, vol. 86, no. 11, p. 6451, Nov. 1999, doi: 10.1063/1.371708.
- [500] G. C. Marques *et al.*, "Influence of Humidity on the Performance of Composite Polymer Electrolyte-Gated Field-Effect Transistors and Circuits," *IEEE Trans Electron Devices*, vol. 66, no. 5, pp. 2202–2207, May 2019, doi: 10.1109/TED.2019.2903456.
- [501] A. Demming, "Optical microscopy – how small can it go? – Physics World," 2020. <https://physicsworld.com/a/optical-microscopy-how-small-can-it-go/> (accessed Aug. 31, 2022).
- [502] A. Ul-Hamid, *A Beginners' Guide to Scanning Electron Microscopy*. Springer International Publishing, 2018. doi: 10.1007/978-3-319-98482-7.
- [503] B. J. Griffin, "A comparison of conventional Everhart-Thornley style and in-lens secondary electron detectors—a further variable in scanning electron microscopy," *Scanning*, vol. 33, no. 3, pp. 162–173, May 2011, doi: 10.1002/SCA.20255.
- [504] J. I. Goldstein *et al.*, *Scanning Electron Microscopy and X-ray Microanalysis*. Boston, MA: Springer US, 2003. doi: 10.1007/978-1-4615-0215-9.
- [505] Antonis Nanakoudis, "What is SEM? Scanning Electron Microscopy Explained," 2019. <https://www.thermofisher.com/blog/materials/what-is-sem-scanning-electron-microscopy-explained/> (accessed Sep. 10, 2022).
- [506] G. Haugstad, *Atomic force microscopy: understanding basic modes and advanced applications*. 2012.
- [507] R. García and R. Pérez, "Dynamic atomic force microscopy methods," *Surf Sci Rep*, vol. 47, no. 6–8, pp. 197–301, Sep. 2002, doi: 10.1016/S0167-5729(02)00077-8.
- [508] F. J. Giessibl, "Advances in atomic force microscopy," *Rev Mod Phys*, vol. 75, no. 3, p. 949, Jul. 2003, doi: 10.1103/RevModPhys.75.949.
- [509] A. Prasad, N. v. Salim, M. Mozetič, L. Kailas, and S. Thomas, "Time-of-flight secondary ion mass spectrometric analysis of polymer surfaces: A review," *J Appl Polym Sci*, vol. 139, no. 23, p. 52286, Jun. 2022, doi: 10.1002/APP.52286.
- [510] D. R. Baer and S. Thevuthasan, "Characterization of Thin Films and Coatings," *Handbook of Deposition Technologies for Films and Coatings: Science, Applications and Technology*, pp. 749–864, Jan. 2010, doi: 10.1016/B978-0-8155-2031-3.00016-8.
- [511] Paul van der Heide, *X-ray Photoelectron Spectroscopy: An introduction to Principles and Practices* | Wiley. 2012. Accessed: Sep. 10, 2022. [Online]. Available: <https://www.wiley.com/en-gb/X+ray+Photoelectron+Spectroscopy:+An+introduction+to+Principles+and+Practices-p-9781118062531>

Part VII. Personal details

Personal data

Education

| From | To | Degree | Institute |
|-------------|---------------|---|--|
| May 2018 | December 2022 | Doctoral student | Department of Electrical Engineering Information Technology, Karlsruhe Institute of Technology Germany |
| August 2009 | May 2015 | Undergraduate (B.Tech in Nanotechnology) Postgraduate (M.Tech in Nanotechnology) | Centre for Converging Technologies University of Rajasthan, Jaipur, INDIA |

Research experience

| From | To | Position | Institute |
|---------------|---------------|---|--|
| May 2018 | today | Doctoral student | Institute of Nanotechnology Karlsruhe Institute of Technology Germany |
| April 2017 | May 2017 | Karlsruhe House of Young Scientist (KHYS) aspirant | Institute of Nanotechnology Karlsruhe Institute of Technology Germany |
| December 2015 | April 2017 | Project Assistant Junior Research Fellow (JRF) at DST INSPIRE Project, Government of India | Indian Institute of Technology – Ropar, India |
| August 2014 | February 2015 | Project Intern | Indian Institute of Technology – Ropar, India |

Peer-reviewed journal publications

During PhD phase

- **N. Hussain**, T. Scherer, C. Das, J. Heuer, R. Debastiani, P. Gumbsch, J. Aghassi-Hagmann and M. Hirtz, "Correlated Study of Material Interaction Between Capillary Printed Eutectic Gallium Alloys and Gold Electrodes," *Small*, page 2202987 (2022).

- S. Das, R. Kumar, B. Yang, S. Bag, E. Sauter, **N. Hussain**, M. Hirtz, and U. Manna, "Multiplexed Covalent Patterns on Double-Reactive Porous Coating," *Chemistry – An Asian Journal*, vol. 17, page e202200157 (2022).
- R. Jemai, M. A. Djebbi, **N. Hussain**, B. Yang, M. Hirtz, V. Trouillet, H. Ben Rhaïem, and A. Ben Haj Amara, "Activated Porous Carbon Supported Pd and ZnO Nanocatalysts for Trace Sensing of Carbaryl Pesticide in Water and Food Products," *New Journal Chemistry*, vol 46, page 13880 (2022).
- **N. Hussain**, M. Jan Nazami, C. Ma, and M. Hirtz, "High-Precision Tabletop Microplotter for Flexible on-Demand Material Deposition in Printed Electronics and Device Functionalization," *Review of Scientific Instruments*, vol. 92, page 125104 (2021).
- **N. Hussain**, T. Fu, G. Marques, C. Das, T. Scherer, U. Bog, L. Berner, I. Wacker, R. R. Schröder, J. Aghassi-Hagmann, and M. Hirtz, "High-Resolution Capillary Printing of Eutectic Gallium Alloys for Printed Electronics," *Advanced Materials Technologies*, vol. 6, no. 11, page 2100650-1-11 (2021).
- C. Das, W. Zia, C. Mortan, **N. Hussain**, M. Saliba, J. Ingo Flege, and M. Kot, "Top-Down Approach to Study Chemical and Electronic Properties of Perovskite Solar Cells: Sputtered Depth Profiling Versus Tapered Cross-Sectional Photoelectron Spectroscopies," *Solar RRL*, vol. 5, page 2100298 (2021).

During Master/Bachelor

- P. Joshi, **N. Hussain**, S. R. Ali, Rishu, and V. K. Bhardwaj, "Enhanced Activity of Trinuclear Zn (II) Complexes towards Phosphate Ester Bond Cleavage by Introducing Three-Metal Cooperativity," *New Journal Chemistry*, 42, (2018).
- **N. Hussain**, P. Joshi, S. R. Ali, and V. K. Bhardwaj, "Comparative Structure Activity Relationship for Heterogeneous Phosphatase-like Catalytic Activities of One-Dimensional Cu (II) Coordination Polymers," *RSC Advances*, vol. 6 (66), page 61528 (2016).
- **N. Hussain** and V. K. Bhardwaj, "The Influence of Different Coordination Environments on One-Dimensional Cu (II) Coordination Polymers for the Photo-Degradation of Organic Dyes," *Dalton Transactions*, vol. 45 (18), page 7697 (2016).

Prospective publication

- **N. Hussain**, A. Scholz, T. Spratte, C. Selhuber-Unkel, M. Hirtz and J. Aghassi-Hagmann, "Direct writing of liquid metal microheaters for microvalve applications," 2022.

Conference oral presentations

- **N. Hussain**, ..., M. Hirtz and J. Aghassi-Hagmann, "High-Resolution Capillary Printing of Eutectic Gallium Alloys for Printed Electronics," The 65th International Conference on Electron, Ion, and Photon Beam Technology and Nanofabrication *EIPBN-2022*, New Orleans, USA. (Presented online)
- **N. Hussain**, ..., M. Hirtz and J. Aghassi-Hagmann "High-Resolution Capillary Printing of Eutectic Gallium Alloys for Printed Electronics," *MNE-2022*, Leuven, Belgium.

Posters

- **N. Hussain**, U. Bog, H Fuchs, and M. Hirtz, "Liquid Metal based printed electronics by scanning probe lithography," in 50th IFF Spring School on Scattering 2019, in Jülich, Germany.